Engineering Materials

Qing Xie *Editor*

Electrical Materials

Performance Improvement, Recent Advances and Engineering Applications

Springer

Engineering Materials

This series provides topical information on innovative, structural and functional materials and composites with applications in optical, electrical, mechanical, civil, aeronautical, medical, bio- and nano-engineering. The individual volumes are complete, comprehensive monographs covering the structure, properties, manufacturing process and applications of these materials. This multidisciplinary series is devoted to professionals, students and all those interested in the latest developments in the Materials Science field, that look for a carefully selected collection of high quality review articles on their respective field of expertise.

Indexed at Compendex (2021) and Scopus (2022)

Qing Xie
Editor

Electrical Materials

Performance Improvement, Recent Advances and Engineering Applications

Springer

Editor
Qing Xie
Department of Electric Power Engineering
North China Electric Power University
Baoding, China

With Contributions by
Peng Wang
School of Energy, Power and Mechanical Engineering
North China Electric Power University
Baoding, China

Jun Xie
Department of Electrical Engineering
North China Electric Power University
Baoding, China

Yiyi Zhang
School of Electrical Engineering
Guanxi University China
Guangxi, China

ISSN 1612-1317 ISSN 1868-1212 (electronic)
Engineering Materials
ISBN 978-981-99-9049-8 ISBN 978-981-99-9050-4 (eBook)
https://doi.org/10.1007/978-981-99-9050-4

© The Editor(s) (if applicable) and The Author(s), under exclusive license to Springer Nature Singapore Pte Ltd. 2024

This work is subject to copyright. All rights are solely and exclusively licensed by the Publisher, whether the whole or part of the material is concerned, specifically the rights of translation, reprinting, reuse of illustrations, recitation, broadcasting, reproduction on microfilms or in any other physical way, and transmission or information storage and retrieval, electronic adaptation, computer software, or by similar or dissimilar methodology now known or hereafter developed.
The use of general descriptive names, registered names, trademarks, service marks, etc. in this publication does not imply, even in the absence of a specific statement, that such names are exempt from the relevant protective laws and regulations and therefore free for general use.
The publisher, the authors, and the editors are safe to assume that the advice and information in this book are believed to be true and accurate at the date of publication. Neither the publisher nor the authors or the editors give a warranty, expressed or implied, with respect to the material contained herein or for any errors or omissions that may have been made. The publisher remains neutral with regard to jurisdictional claims in published maps and institutional affiliations.

This Springer imprint is published by the registered company Springer Nature Singapore Pte Ltd.
The registered company address is: 152 Beach Road, #21-01/04 Gateway East, Singapore 189721, Singapore

Paper in this product is recyclable.

Contents

Study on the Construction Method of Epoxy Resin Crosslinking Model

Kexin Fu, Qing Xie, Jingxuan Song, and Guowei Xia

1 Introduction

The application of molecular dynamics (MD) simulation method in the field of polymers has developed rapidly and has become a mature research tool [1]. Due to the complex structure of epoxy cured material, which is different from linear polymers, it is a three-dimensional network structure formed by the reaction of epoxy oligomers with curing agents [2]. Therefore, how to obtain an accurate molecular model of epoxy resin crosslinking network is a key problem in the application of MD simulation method in epoxy resin research.

In order to obtain an accurate epoxy resin crosslinking network model, the development of its construction method has gone through two main stages: one-step crosslinking method and iterative crosslinking method. The one-step crosslinking method is to crosslink the reactive sites within a certain cut-off distance to form an epoxy resin crosslinking network [3, 4]. It is characterized by a small number of model molecules and low network conversion rate or crosslinking density. The iterative crosslinking method, in which a system equilibrium is performed after the formation of a crosslinked bond, followed by a continuation of the crosslinking reaction until the end of the crosslinking, is characterized by a high network conversion rate or crosslink density [5–7]. Compared with the one-step crosslinking method, the iterative crosslinking method is more in line with the actual polymer model and has received more attention from scholars. Wu and Xu [5] used "active" molecular fragments of Bisphenol A diglycidyl ether (DGEBA) and IPD for modelling. When the truncation distance was 4–10 Å and the distance between the two reaction sites was minimum, a crosslinking bond was formed between the two reaction sites. After the formation of the crosslinking bond, energy minimization and MD simulation are performed to eliminate the unreasonable structure and interaction caused by the

---

K. Fu · Q. Xie (✉) · J. Song · G. Xia
Department of Electrical Engineering, North China Electric Power University, Baoding, China
e-mail: xq_ncepu@126.com

Q. Xie (ed.), *Electrical Materials*, Engineering Materials,
https://doi.org/10.1007/978-981-99-9050-4_1

formation of new construction. Then, the above process is repeated until the conversion is within the experimental value. This method can achieve a high conversion rate, but the calculation time is long. Varshney et al. [6] and Wu et al. [5] used “active” molecular fragments for modelling. Within a certain truncation distance, all potential non-crosslinked reaction pairs were identified and crosslinked bonds were formed. Next, a multi-step relaxation process is used to relax the new topology generated by the introduction of new bonds, angles, dihedral angles, etc. Then the bonding and relaxation processes are repeated until the crosslinking reaction is completed. This method can effectively improve the computational efficiency.

To further improve computational efficiency and avoid manual operation errors, more and more researchers are using computer modelling with the help of scripting programs. Xin et al. [8] wrote an epoxy resin crosslinking reaction program in Perl language based on the iterative crosslinking method and compared it with experimental data to verify the validity of the model. The algorithmic flow of the crosslinking procedure is shown in Fig. 1. Liu [9] wrote an epoxy resin crosslinking reaction program in Perl language, refined the iterative process and investigated the structure–property relationship of epoxy resin.

In recent years, the iterative crosslinking method based on the use of scripting procedures for epoxy crosslinking calculations has been widely used, but the constructed epoxy resin crosslinking systems are all epoxy-amine curing systems. However, the epoxy resin systems for high voltage insulation used in electrical insulation are epoxy-anhydride curing systems with different cross-linking mechanisms. The rapid acquisition of an accurate and realistic epoxy-anhydride crosslinking model is the basis for the study of existing resins and the development of new resins.

2 Design Principle of Epoxy Resin Crosslinking Model Based on Iterative Crosslinking Method

2.1 Reaction Mechanism of Anhydride Curing Epoxy Resin

The main reactions of anhydride with epoxy resin in the absence of accelerator are as follows, as shown in Fig. 2: (a) The hydroxyl group in the epoxy resin first opens the anhydride ring to form a carboxylic acid with an ester chain; (b) The carboxylic acid reacts with the epoxy group in the epoxy resin to form a secondary hydroxyl group; (c) The generated hydroxyl group reacts with another anhydride group, while reaction (d) takes place simultaneously; (e) The generated secondary hydroxyl group reacts with another epoxy group, ultimately forming a three-dimensional crosslinked network of epoxy resin.

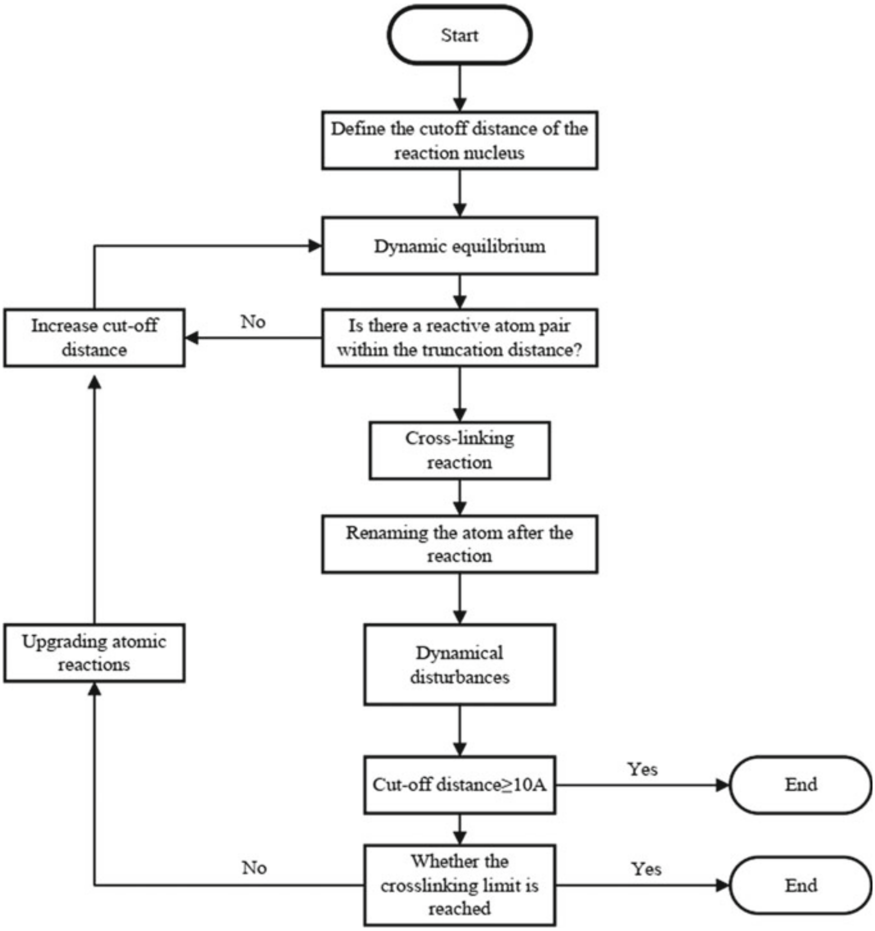

Fig. 1 Flowchart of a perl-based scripting program [10]

2.2 *Design Principles of Epoxy Resin Crosslinking Model*

The mechanism of the epoxy resin anhydride curing reaction shows that the crosslinking reaction is the alternating ring-opening polymerization of curing agent and epoxy compound [2]. It has also been shown that the homopolymerization of epoxy groups can also occur in the presence of catalysts or excessive epoxy at high temperatures [10]. The curing temperature of epoxy resin for high voltage insulation is below 473.15 K, and the epoxy resin is not excessive. The curing reaction mechanism of epoxy anhydride does not include homopolymerization. Therefore, in this paper, the construction of an epoxy-anhydride crosslinking system was implemented using a Perl-based scripting program based on the reaction mechanism of anhydride-cured epoxy resins (Fig. 2). First, the pre-crosslinking model is processed:

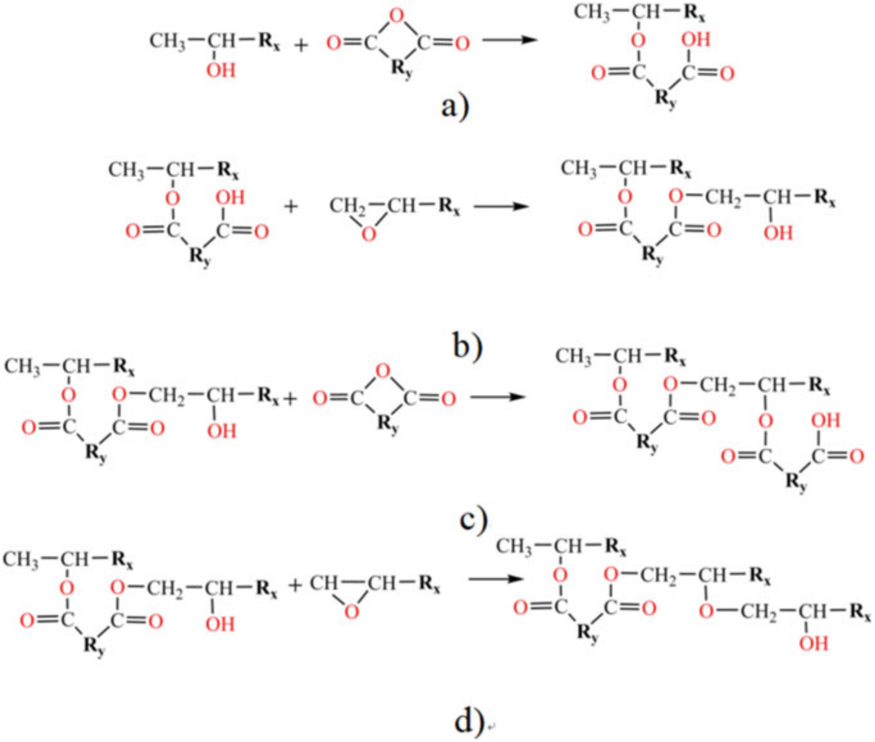

Fig. 2 Reaction mechanism diagram of epoxy resin cured by anhydride

(1) A model of the epoxy resin, the curing agent monomer and a molecular model of the carboxylic acid-containing monoester structure generated by the ring-opening reaction of the epoxy resin with the curing agent (as shown in Fig. 2a and hereinafter referred to as the primary crosslinked structure) were constructed. Labelling the epoxy resin with the C atom in CH_2 in the epoxy group and one C atom in the anhydride group of the primary crosslinked structure as reaction atom R_1 and the O atom in –OH in the carboxyl group of the primary crosslinked structure as reaction atom R_2.

(2) The molecular model of the monomer and primary cross-linked structure constructed in (1) is used to construct an amorphous model of the epoxy-anhydride system at a specific value of the molar ratio of the epoxy group to the anhydride group, which is ready for use after equilibration in MD. Then, in order to simplify the script, the following design was made in the script program while ensuring the accuracy of the epoxy-anhydride crosslinking model: labelling the O atom in the carboxyl and hydroxyl groups generated by the reaction as the reaction atom R_2, with R_1 and R_2 being the reaction atom pair; Suppose that each reactive group has the same activity; The reaction is diffusion controlled and

each reaction is carried out simultaneously. Finally, the automatic crosslinking program flow chart is shown in Fig. 3.

The flowchart is described as follows:

(1) For the amorphous model of the epoxy-anhydride system with labelled reaction atoms, first set the cross-linking temperature *T*, the target crosslinking degree *TCD*, and the range of cut-off radius for the formation of crosslinked bonds.
(2) The radius of the current stage is R_n, the maximum truncation radius is R_max, and the distance between the reaction atom pairs is calculated as d. If $\mathrm{d} < R_\mathrm{n}$, the atomic pair generates a new crosslinked bond according to the reaction principle, followed by a 50 ps NPT molecular dynamics equilibrium to ensure the rationality of the new structure; If $\mathrm{d} > R_\mathrm{n}$ then proceed to step (3);

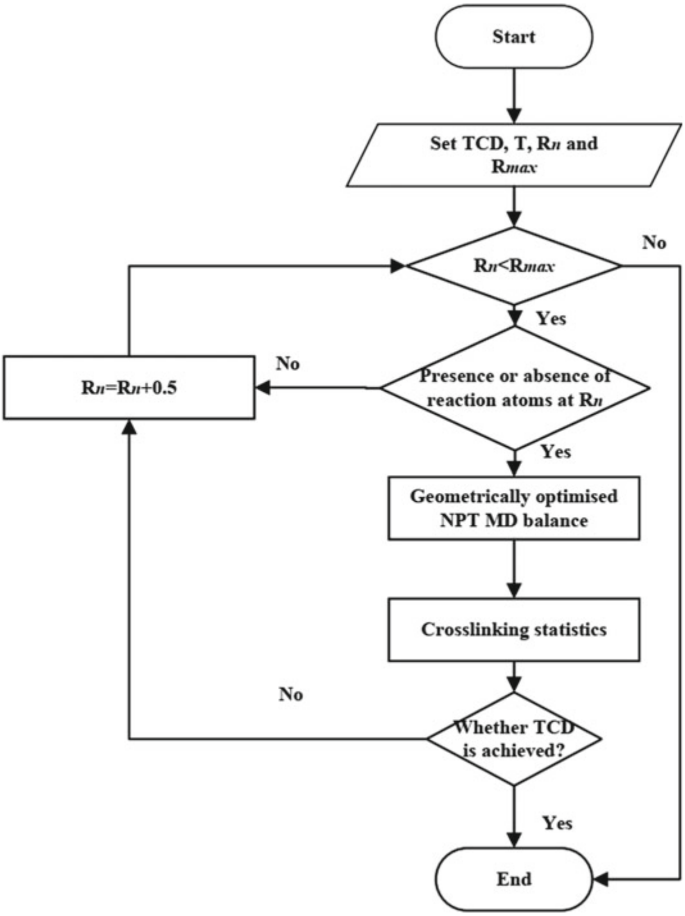

Fig. 3 Flow chart of automatic crosslinking reaction program

(3) Set $R_n = R_n + 0.5$ Å and repeat step (2). Until R_n is greater than R_{max} or the target crosslinking degree is reached, the crosslinking process is completed.

3 Epoxy-Anhydride Crosslinking Model Construction

The crosslinking network model of DGEBA/methyl-tetrahydrophthalic anhydride (MTHPA) was constructed, which can be decomposed into two main stages: (1) Constructing an amorphous model; (2) Based on the mechanism of anhydride curing reaction, the formation of DGEBA/MTHPA crosslinking network was realized by using the automatic crosslinking program written in Perl language.

In the first step, the core module "Materials Visualizer" in "Materials Studio 7.0" software is used to construct the molecular models of DGEBA and MTHPA monomers and the molecular model of DGEBA-MTHPA primary crosslinking structure. Considering that the actual average degree of polymerisation of DGEBA in the experiments ranges from 0.1 to 0.2 [11], the degree of polymerisation is set to 0 when building the molecular model of DGEBA. The molecular model is then geometrically optimized and the reaction atoms are labelled. The molecular formulas and molecular structure diagrams of epoxy resin DGEBA, curing agent MTHPA and primary crosslinking structure DGEBA-MTHPA are shown in Figs. 4 and 5. Subsequently, the "Amorphous Cell" module was used to construct 10 amorphous models containing 8 DGEBAs, 18 MTHPAs and 2 DGEBA-MTHPAs (the molar ratio of epoxy group to anhydride group is 1:1). Periodic boundary conditions are used to eliminate boundary effects, and the model construction temperature is 300 K and the density is 0.6 g/cm^3.

In the second step, Geometry Optimization in the Forcite module is used to optimize the structure of all amorphous models, selecting the structure with the lowest energy for further MD. In order to eliminate the stresses generated during the modelling process and make the model more realistic, MD simulations of NVT at

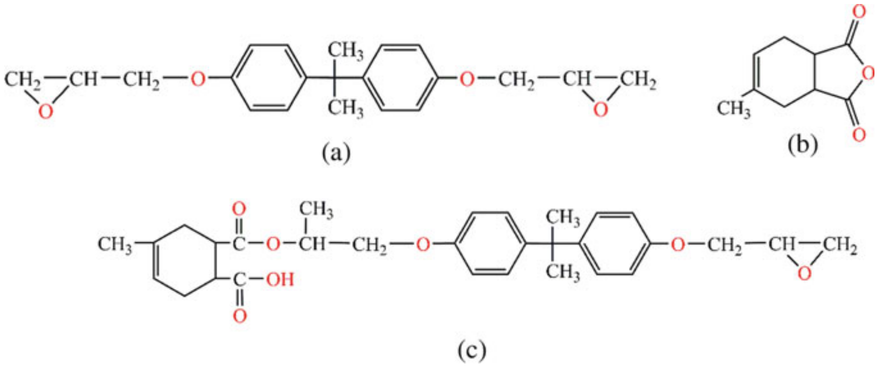

Fig. 4 Molecular formula of epoxy resin, curing agent and primary crosslinking structure: **a** DGEBA, **b** MTHPA, **c** DGEBA-MTHPA Primary crosslinked structure

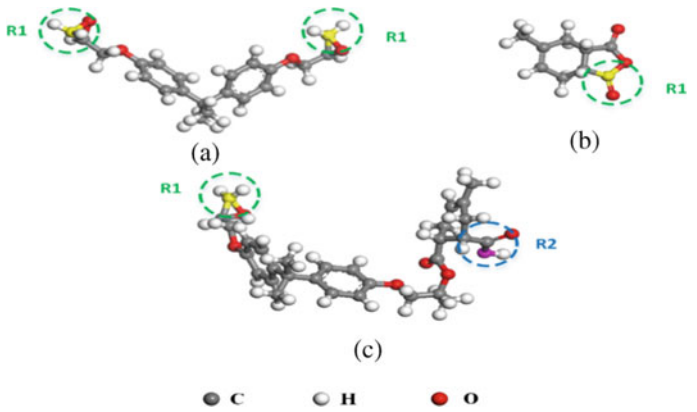

Fig. 5 Molecular model of epoxy resin, curing agent and primary crosslinked structure: **a** DGEBA, **b** MTHPA, **c** DGEBA-MTHPA primary crosslinked structure

100 ps and NPT at 200 ps are performed sequentially, with the temperature of 300 K and the pressure of 1 atmosphere. The COMPASS force field is selected for dynamic process, Andersen [12] and Berendsen [13] methods are used for temperature and pressure control respectively, and the van der Waals and electrostatic interaction calculation methods are Atom-based and Ewald methods respectively.

The third step is to embed the general program script of epoxy resin/anhydride curing agent automatic crosslinking reaction in “Materials Studio 7.0”, which is compiled according to the anhydride curing reaction mechanism and the design principle of epoxy-anhydride system crosslinking method. Set the target cross-linking degree (taking 89% crosslinking degree as an example), set the temperature at 300 K, and set the truncation radius and maximum truncation radius at 3.5 Å and 7.5 Å respectively. The epoxy-anhydride crosslinking model at the target crosslinking degree can be obtained by running the crosslinking program. The molecular structures of the DGEBA/MTHPA amorphous and crosslinked models are shown in Fig. 6. Taking the crosslinking degree of 89% as an example, the basic parameters of the system before and after crosslinking are shown in Table 1.

In the fourth step, after optimizing the structure of the obtained epoxy-anhydride crosslinking model, MD simulation of NVT and NPT ensemble was carried out successively at 600 K, and the simulation parameters are consistent with the previous paper. Finally, the 600 K crosslinked-anhydride model is “annealed” to cool it down: The crosslinked models are simulated at 600 K for 100 ps NVT and 200 ps NPT respectively and are heated up to 600 K and then cooled down by “annealing” from 600 to 300 K, with a temperature interval of 20 K and a kinetic equilibrium time of 100 ps at each temperature. Then the crosslinked structure models of epoxy-anhydride at different temperatures are output for the subsequent calculation of structure and performance parameters.

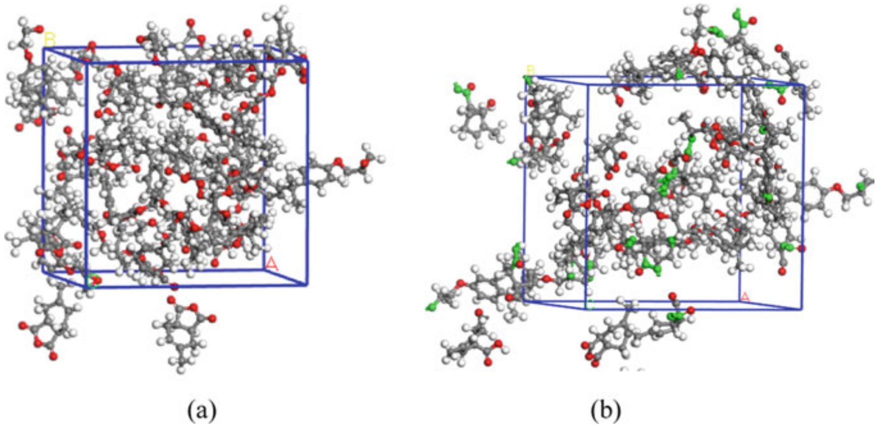

(a) (b)

Fig. 6 DGEBA/MTHPA molecular model: **a** Amorphous model, **b** crosslinked model

Table 1 Basic parameters of the DGEBA/MTHPA(DM) system before and after crosslinking

System	Number of monomer molecules			Amorphous models		Crosslinked model (89%)		System shrinkage
				Volume	Density	Volume	Density	
DM	DGEBA	MTHPA	DGEBA-MTHPA	Å^3	g/cm^3	Å^3	g/cm^3	%
	8	18	2	9782.61	1.143	9693.98	1.153	0.91%

4 Epoxy-Anhydride Crosslinking Model Applications

4.1 Preferred Epoxy Resin Monomer for High Voltage Insulation

There are many types of epoxy resins and curing agents, and the curing products of different epoxy resins and curing agents have complex structures and vary greatly in thermodynamic properties. Therefore, the selection and matching of epoxy resin and curing agent base materials, as well as the correlation between the microstructure of epoxy materials and their macroscopic properties, are of great research significance. In this section, DGEBA, dicyclopentadienyl alicyclic epoxy resin (DCPDE), MTHPA and maleic anhydride (MA) anhydride curing agents are selected as monomers to construct crosslinking structure models of four epoxy resin systems: DGEBA/MTHPA, DGEBA/MA, DCPDE/MTHPA and DCPDE/MA. The effect of the crosslinking degree on the microstructure and thermodynamic properties of epoxy has been investigated by MD simulations. Multiple parameters of the four epoxy crosslinking systems are compared, and the correlation between the microstructure and thermodynamic properties of the epoxy resin substrates is

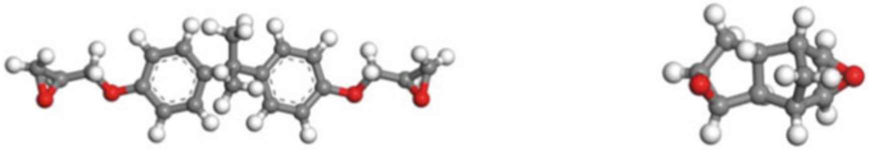

(a) DGEBA (b) DCPDE

(c) MTHPA (d) MA

Fig. 7 Molecular structure of epoxy resins and curing agents

constructed. The molecular structures of the epoxy resins DGEBA, DCPDE and the anhydride curing agents MTHPA and MA are given in Fig. 7 (Table 2).

The microstructure of a material is intrinsically important in influencing its performance. Analyzing structural parameters and predicting macroscopic performance is crucial for the optimization of epoxy resins and curing agents. Therefore, in this section, relevant parameters such as free volume, mean square displacement, glass transition temperature, coefficient of thermal expansion and modulus are calculated for the four epoxy resin systems.

The basic calculations used to characterize the structural and performance parameters are based on the following.

(1) Free volume ratio

According to the free volume theory, the volume V_T of liquid and solid substances consists of two parts: one is the volume V_0 occupied by molecules, and the other is the unoccupied volume V_{f}, namely the free volume. That is:

$$V_T = V_0 + V_f \tag{1}$$

Table 2 Basic parameters of the 4-group crosslinking model

Models	Volume (Å^3)	Density (g/cm^3)	Number of atoms
DGEBA/MTHPA	47,985.63	1.17	4726
DGEBA/MA	35,213.85	1.27	2137
DCPDE/MA	22,575.40	1.33	3410
DCPDE/MTHPA	34,853.13	1.18	3360

The free volume is dispersed within the material in the form of "pores" and provides space for the molecules to move so that the molecular chains can move. Free volume is one of the important microscopic features of polymeric materials which is often used to explain the glass transition of epoxy resins, and has a correlation with mechanical properties. Direct comparisons of free volume values are of little significance due to the differences in volume between the different crosslinking models. This book introduces the free volume ratio (FFV) to compare the free volume characteristics of different systems, which is defined as:

$$FFV = \frac{V_f}{V_0 + V_f} \times 100\% \tag{2}$$

(2) Mean square displacement

During the MD process, the position of the molecule in the model is constantly changing and the mean square displacement (MSD) of the molecule characterizes the ability of the molecule to move in the model. The mean square displacement of a molecule is defined as:

$$MSD = \left\langle |R(t) - R(0)|^2 \right\rangle \tag{3}$$

where $R(t)$ and $R(0)$ respectively represent the displacement vector of any atom i in the system at time t and at the initial moment, respectively. For a system with N atoms, the mean square displacement can be expressed as:

$$MSD = \sum_{i=0}^{N-1} \left[|\boldsymbol{R}_i(t) - \boldsymbol{R}_i(0)|^2 \right] \tag{4}$$

(3) Glass transition temperature

Glass transition is a transition that can occur in both amorphous polymers and amorphous regions of crystalline polymers. According to the free volume theory, the glass transition temperature (T_g) is a transition temperature at which the polymer chain segments transition from freezing to moving, which macroscopically shows that the material changes from glass state to rubber state and loses its high stiffness. Therefore, T_g is the highest temperature of epoxy resin as an insulating support material. In general, an increase in temperature will lead to a decrease in the density of the material, and the curve of polymer density with temperature will show an inflection point at the T_g temperature value. Therefore, the information such as density and temperature of the model under each crosslinking degree during the "annealing" cooling process can be extracted and the T_g of epoxy resin can be predicted by the temperature corresponding to the inflection point of the density curve with temperature. The specific method is shown in Fig. 8, where linear fitting is performed on the

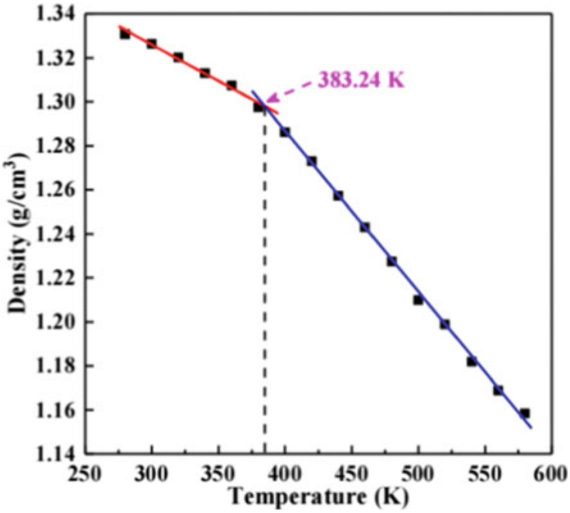

Fig. 8 Density-temperature fitting curves for epoxy resin crosslinking systems

density values on both sides of the inflection point, and the intersection of the two lines is T_g.

(4) Coefficient of thermal expansion

The Coefficient of thermal expansion (CTE) is one of the main physical properties of a material and can be used to calculate the internal stress due to thermal expansion, and is an important indicator of the thermal stability of a material. Its calculation formula is:

$$CTE = \frac{1}{V_0}\left(\frac{\partial V}{\partial T}\right)_P \tag{5}$$

where V_0 is the volume of the initial system, here taken as the volume of the system at 300 K, and P is taken as one standard atmospheric pressure. Epoxy resins correspond to different states (glassy and rubbery) before and after the glass transition and their CTE can change abruptly. A linear fit to the volume-temperature data before and after the glass transition, respectively, gives the rate of change of volume with temperature in both states. As shown in Fig. 9.

(5) *Modulus*

MD simulations enable the static normal strain method to be used to calculate the mechanical properties of crosslinked systems, that is, to analyze the stress and strain of a three-dimensional epoxy system with slight deformation, and then obtain its mechanical properties related parameters such as bulk modulus, shear modulus, Young's modulus, Poisson's ratio, etc. The process can be described as follows: a small strain is applied to the system, causing the model to undergo uniaxial tensile

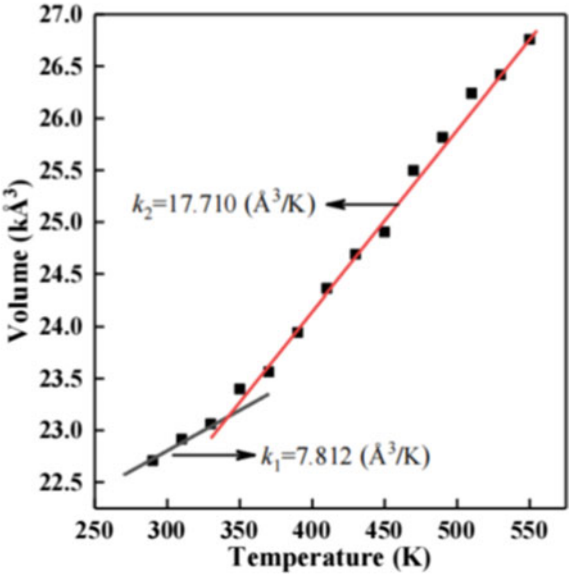

Fig. 9 Volume-temperature fitting curves for epoxy resin crosslinking systems

and compressive deformation along the x, y, and z axes, respectively, i.e., shear deformations in the xy, xz, and yz planes, respectively, and the stiffness matrix C_{ij} can be obtained from the model's response to the strain, which can be described as follows for isotropic materials.

$$C_{ij} = \begin{bmatrix} \lambda + 2\mu & \lambda & \lambda & 0 & 0 & 0 \\ \lambda & \lambda + 2\mu & \lambda & 0 & 0 & 0 \\ \lambda & \lambda & \lambda + 2\mu & 0 & 0 & 0 \\ 0 & 0 & 0 & \mu & 0 & 0 \\ 0 & 0 & 0 & 0 & \mu & 0 \\ 0 & 0 & 0 & 0 & 0 & \mu \end{bmatrix} \tag{6}$$

where λ and μ are elastic constants which can be derived from the relevant elements in the stiffness matrix.

$$\begin{cases} \lambda = \frac{1}{6}(C_{12} + C_{13} + C_{21} + C_{23} + C_{31} + C_{32}) \\ \mu = \frac{1}{3}(C_{44} + C_{55} + C_{66}) \end{cases} \tag{7}$$

The bulk modulus K, Young's modulus E, shear modulus G and other mechanical properties of epoxy system can be obtained from elastic constants λ and μ. The calculation methods are as follows:

$$\begin{cases} E = \mu \dfrac{3\lambda + 2\mu}{\lambda + \mu} \\ G = \mu \\ K = \lambda + \dfrac{2}{3}\mu \end{cases} \tag{8}$$

The results of the structural properties of the four groups of epoxy resin systems involved in the calculations are shown in Fig. 10.

The thermodynamic properties of the four groups of epoxy crosslinking models are different. The T_g of the four systems with 90% crosslinking is DGEBA/MA > DCPDE/MTHPA > DCPDE/MA > DGEBA/MTHPA in descending order; the CTE in the glassy state is DCPDE/MA < DGEBA/MA < DCPDE/MTHPA < DGEBA/MTHPA. The DGEBA/MTHPA system has low modulus and the worst mechanical properties; The DCPDE/MTHPA system is the most resistant to shear stresses and the DCPDE/MA system is the best in terms of tensile and compressive stresses. In addition, there is a certain correlation between the microscopic and thermodynamic properties of the epoxy resin base material. There is a positive correlation between FFV and the chain segment kinematic properties of epoxy resins; generally lower FFV and weaker chain segment kinematic models have better thermodynamic properties.

4.2 Study of the Effect of Polymerisation on the Structural Properties of Epoxy Resins

DGEBA is usually a mixture of homologues with different molecular sizes (chain length, molecular weight and polymerization degree). However, most of the current simulation studies have focused on the case where the polymerization degree of DGEBA is 0 and the effect of polymerization degree on the performance of crosslinked epoxy resins has been rarely studied. Previous experimental studies have confirmed that different molecular weights do have an effect on the properties of the cured product. Therefre, it is particularly important to investigate the effects of different polymerization degrees on the structure and properties of epoxy resins at the simulation level.

In this section, DGEBA, a bisphenol A epoxy resin with a polymerization degree of 1 and 2, is used as the base material for the epoxy resin, and MTHPA is used as the curing agent (the molecular structure of the monomer is shown in Fig. 11). The epoxy resins are mixed in different proportions to study the effect of different polymerization levels on the performance of the crosslinked epoxy resin system.

To investigate the effect of polymerization on the performance of crosslinked epoxy resin systems, four types of ratios of 8:2, 6:4, 5:5 and 3:7 are determined for DGEBA (n = 1) and DGEBA (n = 2). Combining the actual epoxy resin with the reaction mass ratio of the curing agent, the molar ratio of the epoxy resin mixed

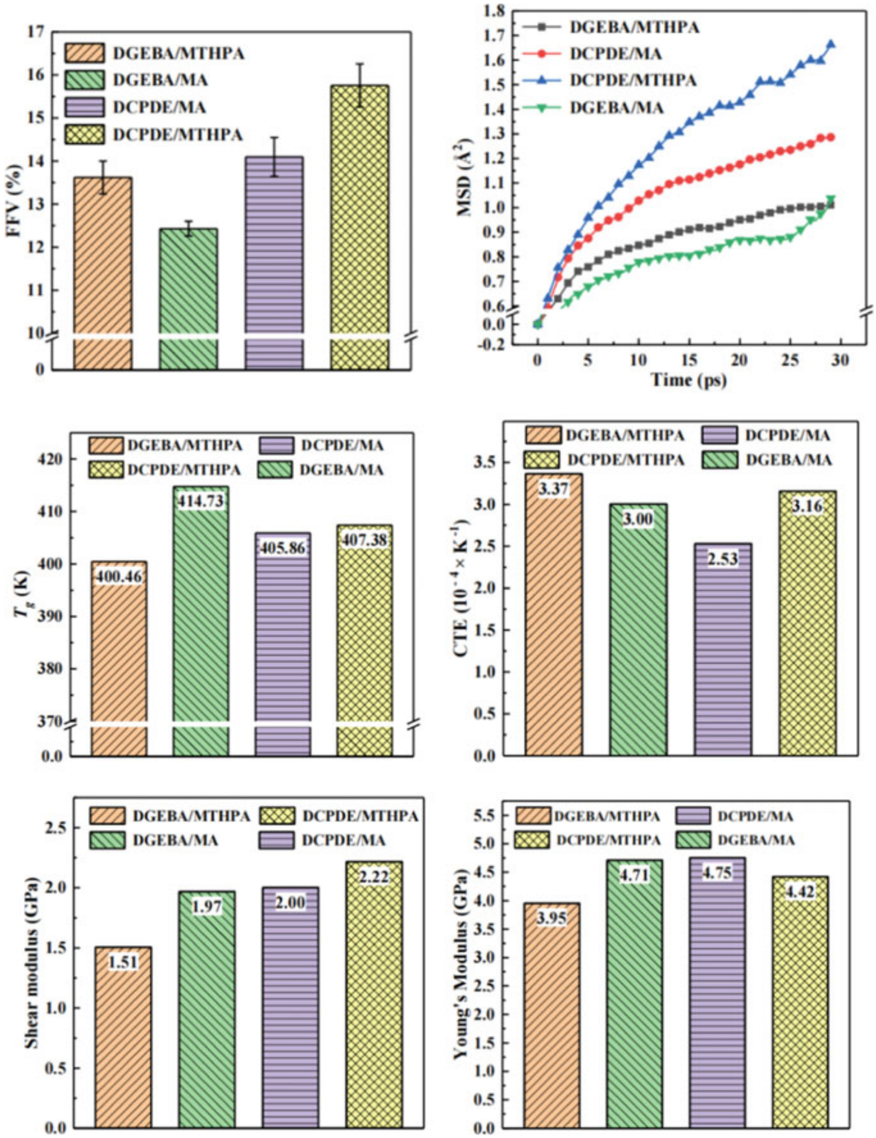

Fig. 10 Properties of four epoxy-crosslinked systems: *FFV*, *MSD*, T_g, *CTE* and modulus

with the anhydride curing agent in this section is epoxy resin: curing agent = 1:2. Therefore, the total number of DGEBA molecules is selected as 30 and MTHPA as 60. And the following molecular models are constructed respectively: (1) DGEBA (n = 1):DGEBA (n = 2):MTHPA = 24:6:60; (2) DGEBA (n = 1):DGEBA (n = 2):MTHPA = 18:12:60; (3) DGEBA (n = 1):DGEBA (n = 2):MTHPA = 15:15:60; (4) DGEBA (n = 1):DGEBA (n = 2):MTHPA = 9:21:60.

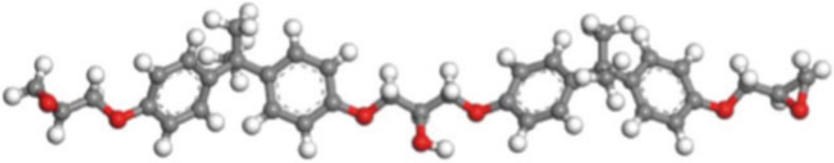

（a）DGEBA（n=1）

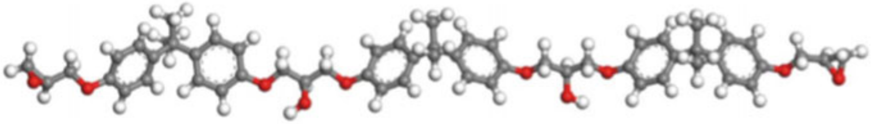

（b）DGEBA（n=2）

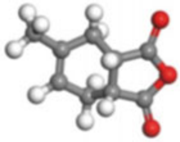

（c）MTHPA

Fig. 11 Molecular structures of monomers of DGEBA and MTHPA with different degrees of polymerization

FFV, *MSD*, T_g, *CTE* and modulus are calculated for different polymerization proportioning models respectively.

Figure 12 reveals the effect of different polymerization degrees on the thermodynamic properties of crosslinked epoxy resins. It is found that as the average molecular weight increased, the T_g of the system first increased and when it exceeded a certain value, T_g decreased to the initial level. The change in average molecular weight has a significant improvement on the glassy *CTE* of the system, while the effect on the rubbery *CTE* is not significant. The increase of average molecular weight will have a more significant improvement on the mechanical properties of the system. When the ratio is 6:4 in the polymerization degree model, the increase in each elastic modulus is the largest.

4.3 Study on the Effect of Capping Agents on the Structural Properties of Epoxy Resins

In this section, DGEBA (0 degree of polymerization) is selected as the epoxy resin matrix. MTHPA is the curing agent and ethyl salicylate (ES) is the capping agent. The molecular structural formulae and primary crosslinking structures are shown in Figs. 13, 14 and 15.

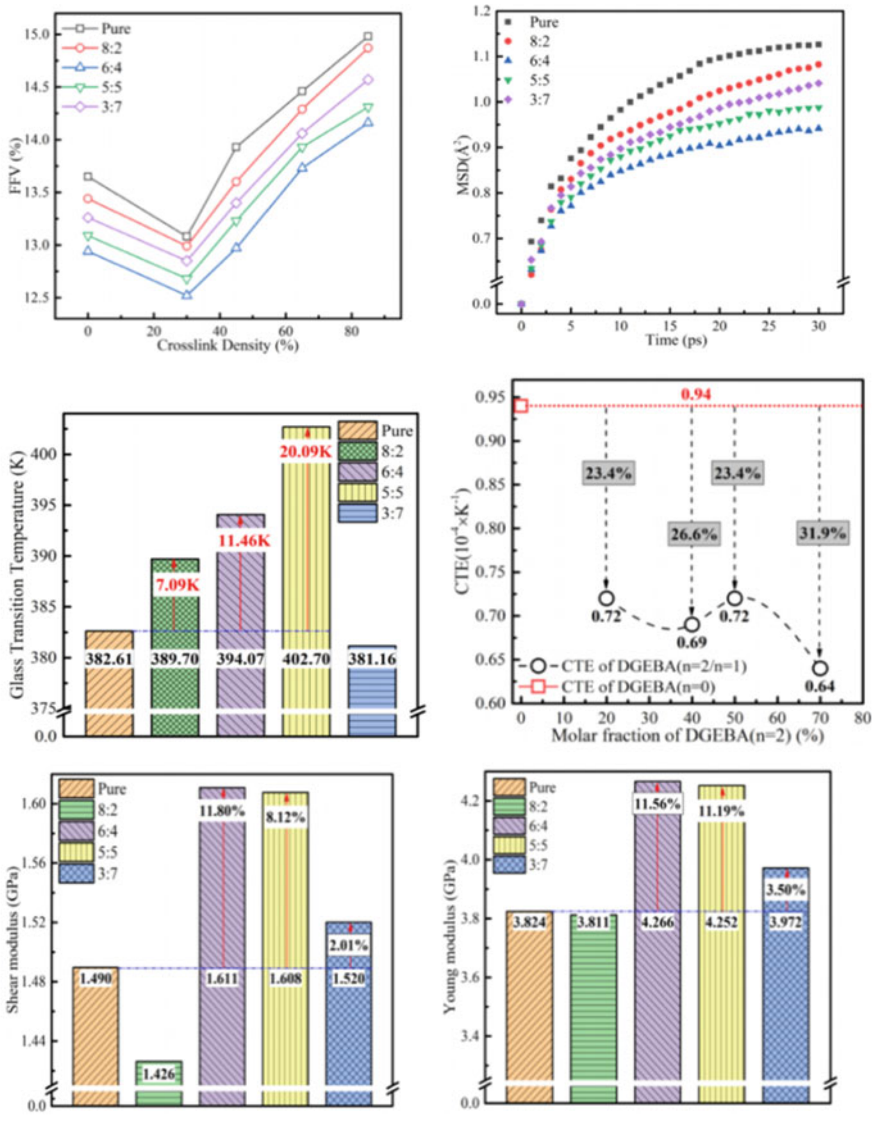

Fig. 12 *FFV*, *MSD*, T_g, *CTE* and Modulus of epoxy resin crosslinking systems with different polymerization degrees

In this section, four cases of capping agent ES with 2, 4, 6 and 8% mass fraction of epoxy resin are selected. The components of the system are shown in Table 3.

The cohesion energy density (CED), hydrogen bonding number, *FFV*, *MSD*, T_g, *CTE* and modulus are calculated for different capping agent proportioning models respectively (Fig. 16).

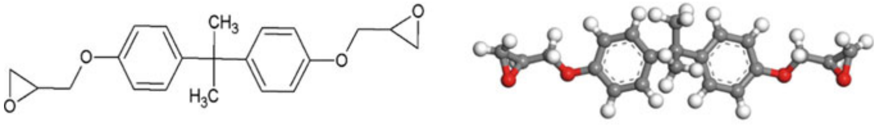

(a) DGEBA constitutional formula (b) DGEBA monomer molecule

(c) MTHPA structural formula (d) MTHPA monomer molecule

Fig. 13 Molecular structure formula of epoxy resin and curing agent

Fig. 14 Molecular structure formula and molecular model of capping agent

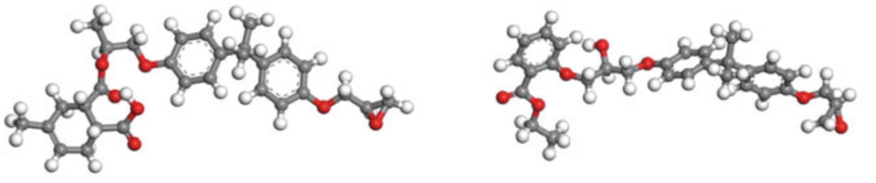

(a) DGEBA-MTHPA primary crosslinking molecular model (b) DGEBA-ES primary crosslinked molecular model

Fig. 15 Primary crosslinked molecular model

Table 3 Amorphous model components for different mass fraction systems

ES content (wt%)	Epoxy resin/strip	Curing agent/strip	One cross-linked molecule/strip	
	DGEBA	MTHPA	DGEBA-MTHPA	DGEBA-ES
2	61	136	10	4
4	56	131	10	9
6	50	125	10	15
8	44	119	10	21

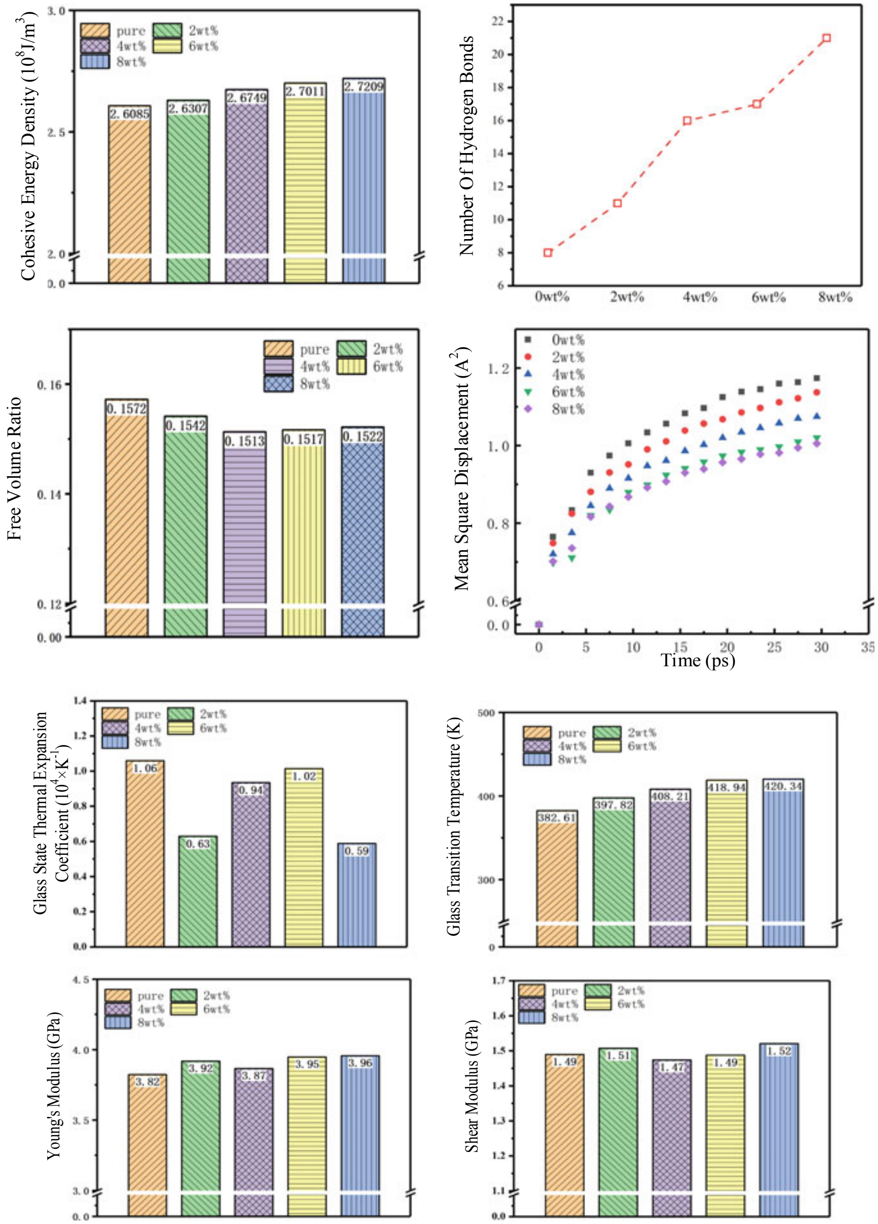

Fig. 16 CED, hydrogen bonding number, *FFV*, *MSD*, T_g, *CTE* and Modulus of different capping agent epoxy resin crosslinking systems

The results indicate that:

(1) With the increase of end-capping agent content, CED and FFV show an upward trend, which is also related to the benzene ring and double bond contained in ES. The order of FFV is pure > 2 wt% > 8 wt% > 6 wt% > 4 wt%, and the order of MSD is 8 wt% < 6 wt% < 4 wt% < 2 wt% < pure, which is due to the synergistic effect of the ES polar group with the methyl group. The number of hydrogen bonds increased with the increase of capping agent content, and the final number remain unchanged.
(2) With the increase of the content of the capping agent, the T_g of the epoxy resin is obviously increased, and the increase is gradually reduced. The thermal expansion coefficients of the ES systems with capping agents are all lower than those of the pure systems; and the trend is to increase and then decrease.
(3) After adding the capping agent ES, the Young's modulus of each system increases, and the size relationship is the same as the mean square displacement of each system. The bulk modulus and shear modulus of each system do not increase or decrease significantly with the increase of capping agent content.

4.4 Study of the Effect of Matrix Fluorination on the Properties of Epoxy Resins

In this section, bisphenol A epoxy resin DGEBA is used as epoxy substrate and MTHPA is used as an anhydride curing agent. Four monomers, diglycidyl trifluoromethylaniline (DGTFA), dodecafluoroheptanol (FTOH), 4 (-1,1,1,3,3,3-hexafluoro-2-hydroxy-2-propyl) phenol (HFIP) and hexafluorobisphenol A (BPAF), are selected as fluorine-modified reagents to fluorinate the epoxy resin matrix. The molecular formulae of the epoxy resin, curing agent and fluorinated monomer are shown in Fig. 17.

Firstly, the effect of the fluorination method on the structure and properties of the epoxy crosslinking system is investigated. The molecular models of the four groups of fluorinated resins with different matrix fluorination methods and the number of molecules contained in the blank group are shown in Tables 4.

CED, T_g, thermal conductivity and modulus are calculated for the models with different fluorination methods respectively.

(1) CED calculation analysis

Calculations of the cohesive energy density of different fluorinated epoxy systems are carried out at room temperature and the results are shown in Table 5.

The table shows that the epoxy system with the physical fluorination method has the lowest cohesive energy density of 113.26 J cm^{-3}, which indicates that the interaction force of the molecular chain segments of this epoxy system is weak. Among the fluorine-containing systems of the three chemical fluorination methods, the CED of the system using the median fluorinated fluorine-containing monomer is relatively high. Further comparison shows that the BPAF/DGEBA epoxy system

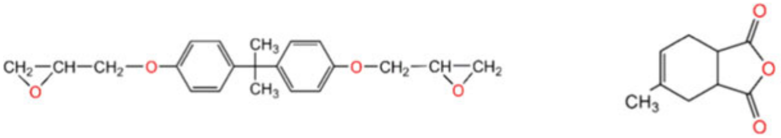

（a） DGEBA （b） MTHPA

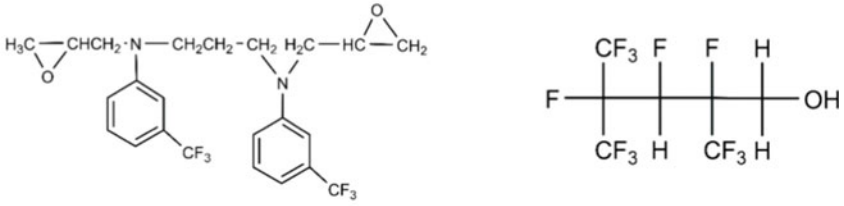

（c） DGTFA （d） FTOH

（e） HFIP （f） BPAF

Fig. 17 Molecular structure formula of epoxy resin, curing agent and fluorinated monomer

Table 4 Components of epoxy resin and hardener in the amorphous model

Fluorinated epoxy systems	Number of molecular strips of epoxy substrate		Substrate fluorination		
	DGEBA	MTHPA	Fluorinated monomers	Number of molecules	Fluoridation method
Pure	50	100	–	–	Unfluorinated
DGTEA/DGEBA	50	100	DGTFA	10	Physical co-mingling
FTOH/DGEBA	50	100	FTOH	10	End-site fluorination
HFIP/DGEBA	50	100	HEIP	10	Median fluoride
BPAF/DGEBA	50	100	BPAF	10	Median fluoride

Table 5 Cohesive energy density of resin systems with different fluorination methods

Epoxy systems	Fluoridation method	CED/J cm^3
Pure	Unfluorinated	130.03
DGTEA/DGEBA	Physical co-mingling	113.26
FTOH/DGEBA	End-site fluorination	118.94
HFIP/DGEBA	Median fluoride	135.34
BPAF/DGEBA	Median fluoride	141.69

has the highest cohesion energy density of 141.69 J cm^{-3}, which indicates that the intermolecular forces in the chain segments of this epoxy system are relatively strong and the interaction forces in the crosslinked network are high.

The analysis shows that the physical fluorination is a simple blending of the fluorinated monomer with the epoxy matrix, with no chemical bonding between the fluorinated monomer and the DGEBA molecule. Therefore, the intermolecular interaction force is weak and the CED of the system is relatively low, resulting in poor compatibility of lend phase and uneven dispersion of the two phases, thus compromising the overall performance of the fluorinated epoxy system. After chemical fluorination, the fluorine-containing segments are grafted into the epoxy resin network system by chemical reaction between the fluorination reagent and the epoxy group on the epoxy matrix. The obtained fluorine-containing epoxy system has stronger intermolecular force, more stable product structure, and relatively high CED parameters.

(2) Synergistic reversal barrier analysis

The essence of molecular segment flexibility is the ease of single bond rotation, which can be expressed by the cooperative torsion barrier of single bond with representative position in molecular segment during rotation. The larger the synergistic torsional potential at key locations for monoliths with approximate molecular structure, the less flexible their corresponding chain segments are.

From the CED calculations, it is clear that the CED values of BPAF/DGEBA and HFIP/DGEBA fluorinated epoxy resin systems are similar. This section therefore further calculates the torsional energy barriers for the chain segments of these two fluorinated monomer-containing molecules. The conformational behavior of the molecular structure is used to compare the information on the local structure and the flexibility of the molecular chain segments in the crosslinked network of the epoxy resin. The conformational analysis of the molecular chain segments of the two fluorinated monomers, HFIP and BPAF, is shown in Fig. 18. Figure 19 gives the calculation results of the co-twisting energy barriers at key bonding positions for HFIP and BPAF monomer molecules. The figure shows that the torsional energy barrier at the two hydroxyl positions of BPAF is 1131.36 kcal/mol higher than the energy barrier of the HFIP monomer molecule. This indicates that BPAF molecular chain segments require more energy to rotate around a single bond and that their molecular chains are more rigid. The analysis suggests that the two fluorinated monomers with similar structures at both ends, the BPAF molecule contains two benzene rings, which bring about a greater spatial resistance, resulting in a less free molecular conformation. Therefore the torsional energy barrier of the BPAF monomer molecule is calculated to be higher and it can be assumed that the BPAF/DGEBA epoxy system is more rigid.

(3) Performance calculation analysis

The results for T_g, thermal conductivity and modulus are shown in Fig. 20.

The analysis of the T_g calculation results shows that after fluorination of the epoxy resin, the introduction of fluorine elements and CF_3 groups will effectively improve the heat resistance of the epoxy resin, while the T_g enhancement of the

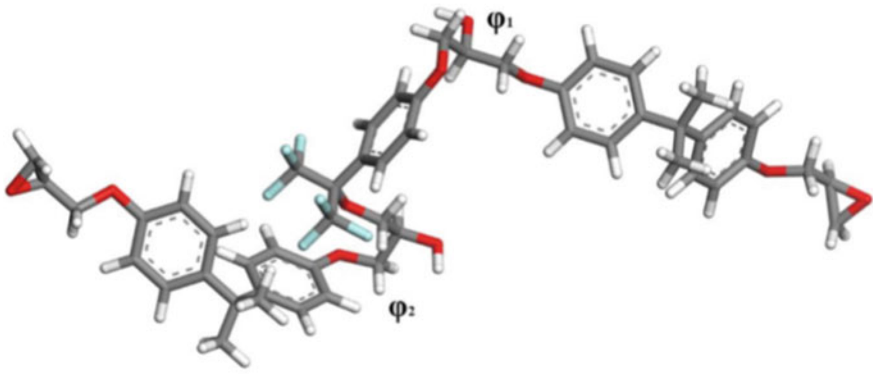

(a) Schematic diagram of HFIP key positions

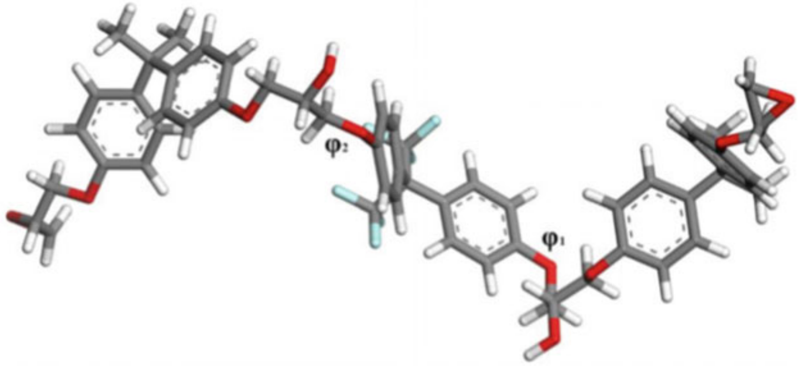

(b) Schematic diagram of BPAF key positions

Fig. 18 Schematic diagram of the bonding of HFIP and BPAF

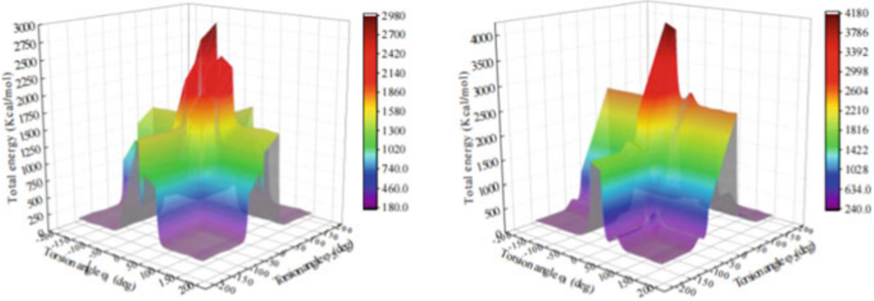

(a) HFIP Collaborative Twisting Energy Barrier

(b) BPAF Collaborative Twisting Energy Barrier

Fig. 19 Calculated results of the synergistic torsional energy barrier

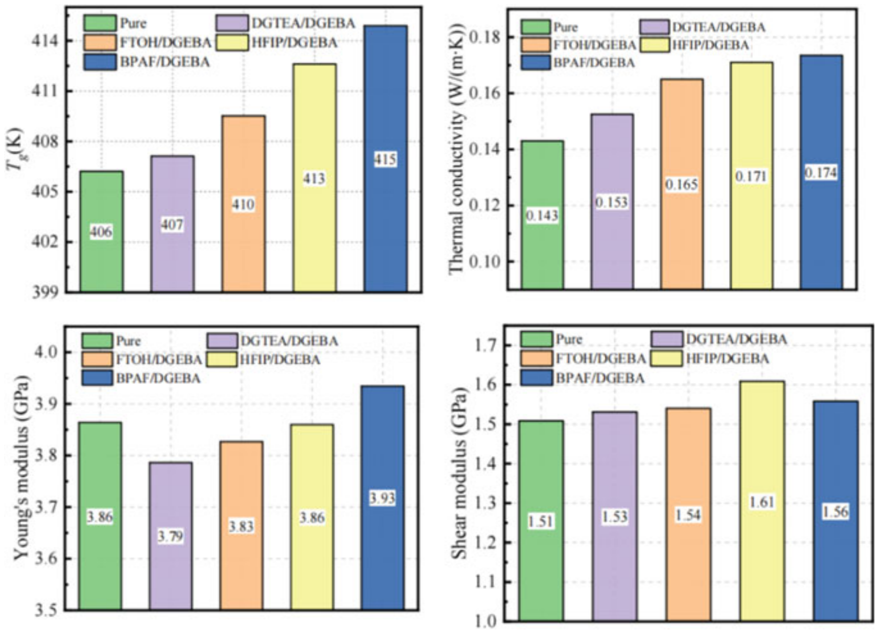

Fig. 20 T_g, thermal conductivity and modulus of epoxy systems with different fluorination methods

system by fluorinating the resin by physical blending is relatively low, and the T_g enhancement by chemical grafting fluorination is better. The highest T_g enhancement for the DGEBA/MTHPA epoxy system is achieved by the neutral fluorination of BPAF. Combined with the calculation results of micro parameters, it can be found that for the analysis of crosslinking network structure parameters, the system with relatively high polymer CED has relatively strong intermolecular interaction forces and a higher glass transition temperature. From the perspective of the fluorinated monomer configuration, the higher the molecular chain segment co-twisting energy barrier, the more rigid the molecular chain segment and the higher the T_g of the corresponding fluorinated system. Therefore, the glass transition temperature of the BPAF/DGEBA fluorinated resin system is the highest.

The analysis of the thermal conductivity calculations concluded that the epoxy resin material mainly relies on internal phonons for thermal conductivity. When the heat generated by the external environment is transferred to the epoxy molecular chain segments, it will cause the atoms to vibrate, thus enabling the transfer of heat. In the case of fluorinated resins with physical fluorination, the interaction between the fluorinated monomer and DGEBA is weaker, the molecular chain segments are more mobile, the atoms vibrate more vigorously when heated, the phonon excitation number increases and the average phonon free range decreases, so the thermal conductivity of the system is relatively low. The use of dodecafluoroheptanol chemical graft fluorination increases the number of branched molecular chain segments within the epoxy system, and studies have shown that the conformation of the chain segments containing branched chains on the main chain disrupts the symmetry and regularity of the polymer system to a certain extent, resulting in increased energy and more violent atomic vibrations within the crosslinked network. This constrains the average free range of phonons to a certain extent and thus affects the thermal conductivity of the system. The higher thermal conductivity of BPAF/DGEBA compared to the HFIP/DGEBA system may be due to the two benzene rings on the main chain of BPAF, the higher torsional energy barrier of the monomer and the higher energy required to rotate the molecular chain segments. The molecular chain conformation is more stable and the atomic vibrations are weaker, resulting in a higher thermal conductivity.

The modal analysis concluded that the fluorinated modifier can significantly improve the elastic modulus of epoxy resin due to the shorter C–F bond length and higher bond energy in the fluorocarbon chain structure after fluorination modification can significantly improve the elastic modulus of epoxy resin due to the shorter C–F bond length and higher bond energy in the fluorocarbon chain structure after fluorination modification.

References

1. Sun, Y.G., Guo, Y.F., Yang, H.: A molecular dynamics study of crosslinked epoxy networks: construction of atomistic models. Mol. Simul. **46**(2), 121–127 (2020)
2. Chen, P., Liu, S.P., Wang, D.Z., et al.: Epoxy Resin and Its Applications. Chemical Industry Press (2011)
3. Yarovsky, I., Evans, E.: Computer simulation of structure and properties of crosslinked polymers: application to epoxy resins. Polymer **43**(3), 963–969 (2002)
4. Gou, J., Minaie, B., Wang, B., et al.: Computational and experimental study of interfacial bonding of single-walled nanotube reinforced composites. Comput. Mater. Sci. **31**(3), 225–236 (2004)
5. Wu, C., Xu, W.: Atomistic molecular modelling of crosslinked epoxy resin. Polymer **47**(16), 6004–6009 (2006)
6. Varshney, V., Patnaik, S.S., Roy, A.K., et al.: A molecular dynamics study of epoxy-based networks: cross-linking procedure and prediction of molecular and material properties. Macromolecules **41**(18), 6837–6842 (2008)
7. Yang, H., Yu, K., Mu, X.M., et al.: A molecular dynamics study of bond exchange reactions in covalent adaptable networks. Soft Matter **11**(31), 6305–6317 (2015)
8. Xin, D.R., Han, Q.: Investigation of moisture diffusion in cross-linked epoxy moulding compound by molecular dynamics simulation. Mol. Simul. **39**(4), 322–329 (2013)
9. Liu, W.S.: Structure and Properties of Crosslinked Epoxy Resin TGDDM: A Molecular Dynamics Simulation. North University of China (2016)
10. Komarov, P.V., Chiu, Y.T., Chen, S.M., et al.: Highly cross-linked epoxy resins: an atomistic molecular dynamics simulation combined with a mapping/reverse mapping procedure. Macromolecules **40**(22), 8104–8113 (2007)

11. Wang, D.Z.: Production and Application of Epoxy Resin. Chemical Industry Press, Beijing (2001)
12. Andersen, C.H.: Molecular dynamics simulations at constant pressure and/or temperature. J. Chem. Phys. **4**(72), 2384–2393 (1980)
13. Berendsen, H.J., Postma, J., Van Gunsteren, et al.: Molecular dynamics with coupling to an external bath. J. Chem. Phys. **8**(81), 3684–3690 (1984)

Study of Model Construction Methods for Epoxy Resin Composites

Qijun Duan, Qing Xie, Yuyao Zhong, and Jun Xie

1 Model Construction and Performance Study of SiO_2/EP Composites

The addition of nanomaterials to the epoxy resin (EP) matrix can significantly improve the comprehensive performance of the material. In recent years, many scholars have conducted numerous studies on nano-modification to improve the thermal property, mechanical property, electrical property and other aspects of EP. These studies mainly focus on the effects of filler type, particle size, shape and dosage on the performance of EP composites. SiO_2 is the most commonly used additive filler in EP insulating materials, but there is no clear conclusion on the mechanism of improving polymer performance. Moreover, molecular simulation plays an important role in revealing the mechanism of interaction between nanoparticles and matrix. Nevertheless, there are few molecular dynamics studies researching on the effect of nano-SiO_2 size on EP. In this section, DGEBA, MTHPA and nano-SiO_2 are used as EP matrix, curing agent and filler respectively. Different molecular models of nano-SiO_2 EP composites are constructed based on molecular dynamics. And the effects of filler particle size, morphology, content and surface modification on the microstructure and macroscopic properties of nanocomposite epoxy resins are studied.

Q. Duan · Q. Xie (✉) · Y. Zhong · J. Xie
Department of Electrical Engineering, North China Electric Power University, Baoding, China
e-mail: xq_ncepu@126.com

Q. Xie (ed.), *Electrical Materials*, Engineering Materials,
https://doi.org/10.1007/978-981-99-9050-4_2

1.1 Study on the Effect of SiO_2 Particle Size on the Structure and Properties of Its Epoxy Composites

1. Construction of SiO_2 monomer molecules

Molecular models of SiO_2 crystals can be imported from MS material library. In this section, the typical cell model of SiO_2 quartz crystal is selected as shown in Fig. 1. This cell model is used to construct molecular models of spherical SiO_2 with radius of 6.5 Å, 7.6 Å, 8.8 Å and 10 Å respectively, which are oxidized according to the actual process, as shown in Fig. 2.

Nanofillers are introduced according to the crosslinking model construction method mentioned above. Each model is filled with only one nano-SiO_2 particle to simulate a well-dispersed nanocomposite epoxy system, with the filling mass fraction of SiO_2 in each system being maintained to be 6.5%. The model components of SiO_2 nanocomposite systems with various particle sizes are given in Table 1.

After running the crosslinking procedure, molecular models with crosslinking degrees of 10, 34, 67 and 96% were selected from each composite system. Among these selections, molecular models with four crosslinking degrees of 8.8 Å particle size composite system are displayed in Fig. 3, and the crosslinking points are marked with spherical atoms. It can be seen from the figure that in addition to the crosslinking of DGEBA and MTHPA, the hydroxyl groups on the surface of SiO_2 are also involved in the curing reaction of EP.

The variation trends of FFV, T_g and modulus of epoxy composites with different particle sizes according to the crosslinking density are then analyzed.

(1) FFV analysis

Figure 4 presents the variation of FFV with crosslinking degree of each system. It can be seen from the figure that the addition of nano-SiO_2 results in a significant decrease in FFV compared to pure epoxy, which is due to the fact that the nanoparticles occupy some of the small pores and a considerable portion of the space in the epoxy resin, resulting in a smaller range of segment motion and a decrease in FFV. When the crosslinking degree is lower ($\leq$34%), the FFV does not change obviously

Fig. 1 Molecular model of SiO_2 cell

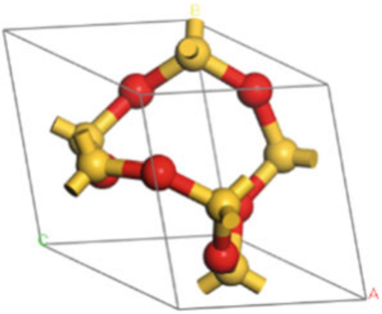

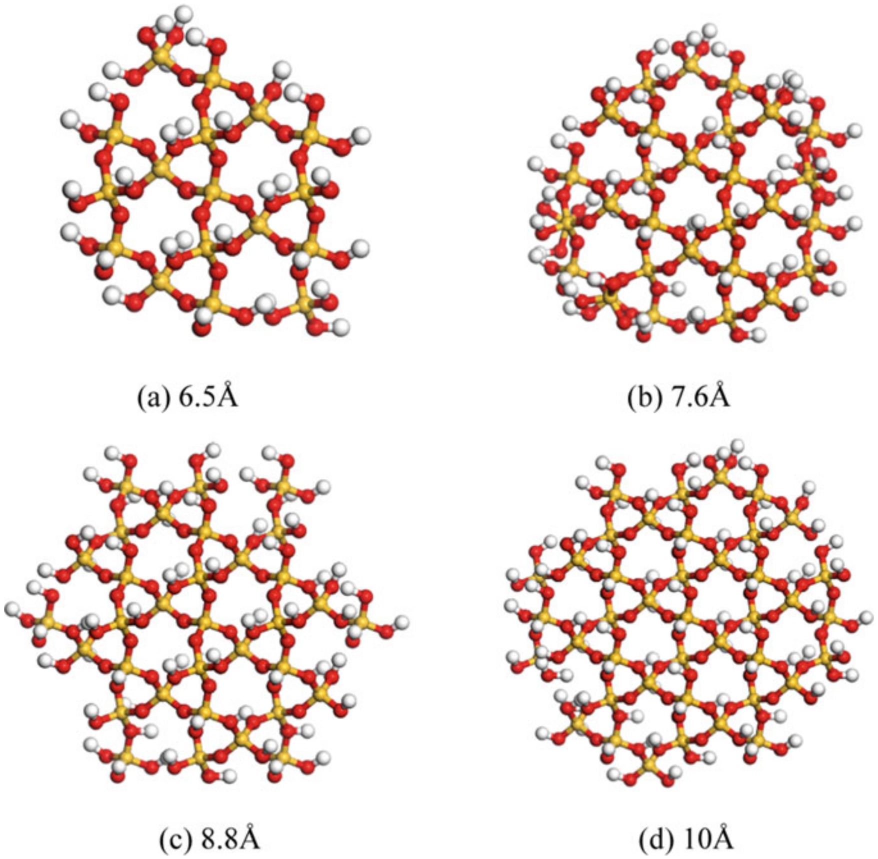
(a) 6.5Å
(b) 7.6Å
(c) 8.8Å
(d) 10Å

Fig. 2 Molecular models of SiO_2 with different particle sizes

Table 1 Model components of SiO_2 nanocomposite systems with different particle sizes

SiO_2 (Å)	DGEBA	MTHPA	DGEBA-MTHPA	Atomic number	SiO_2 mass fraction/ %
6.5	40	90	10	4838	6.5
7.6	65	146	16	7823	6.5
8.8	88	199	23	10,708	6.5
10	124	288	40	15,830	6.5

with the particle size. And with the increase of crosslinking degree, FFV decreased with decreasing particle size. This may be due to the fact that SiO_2 is bonded to the system molecules when a more complete cross-linked network is formed, and the interaction force between small particle size nano-SiO_2 and the matrix is stronger. According to previous studies by scholars, the mechanical properties of polymers

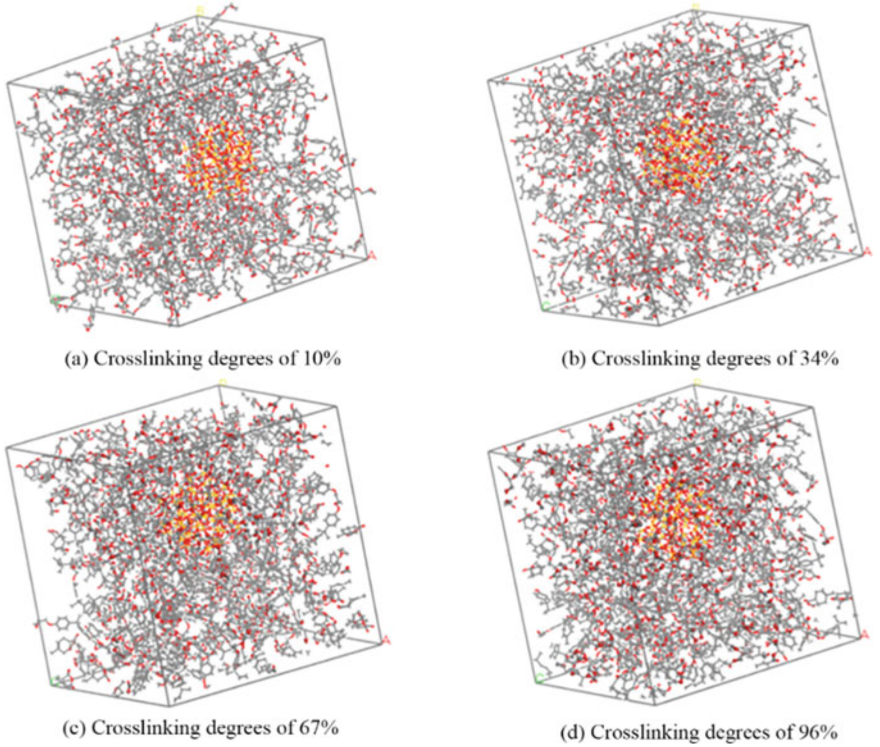
(a) Crosslinking degrees of 10%
(b) Crosslinking degrees of 34%
(c) Crosslinking degrees of 67%
(d) Crosslinking degrees of 96%

Fig. 3 Molecular models of 8.8 Å nanocomposite epoxy with different crosslinking degrees

have a certain dependence on the free volume. The smaller the free volume is, the better the properties are. It can be predicted that the mechanical properties of the system with filler are better than those of the pure epoxy system. Furthermore, when the crosslinking degree is higher, the smaller the particle size is, the better the mechanical properties are.

(2) T_g analysis

As shown in Fig. 5, T_g of the pure epoxy system is higher than that of the filler-containing system at the beginning of crosslinking. While the opposite result is shown as the crosslinking degree increased. Because when the system molecules completed a certain stacking, the filler is bonded to the resin matrix and curing agent, and the filler forms an interface layer with the matrix, which increases the T_g. From the filler particle size, the variation trend of T_g with particle size is not obvious at low crosslinking degree. However, when the crosslinking degree is ≥67%, the T_g of the composites basically increases with the decrease of the filler particle size. Moreover, when the crosslinking degree reached 96%, the T_g of the 6.5 Å system is particularly large. This shows that when the filler and polymer are bonded to a certain extent, the interfacial bonding force between the filler with small particle size and the matrix

Fig. 4 Variation of FFV for each system

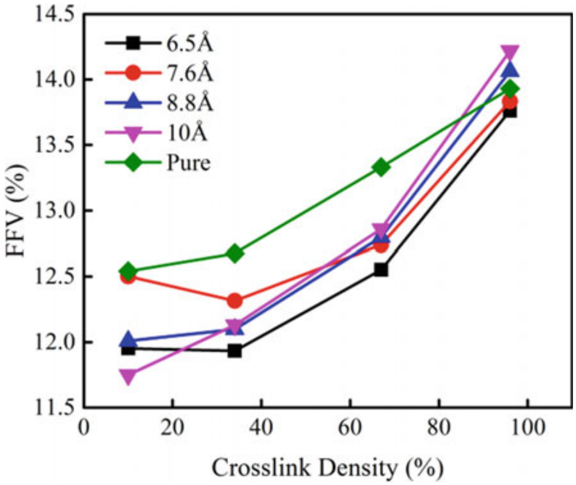

Fig. 5 T_g value of pure epoxy and filler containing system

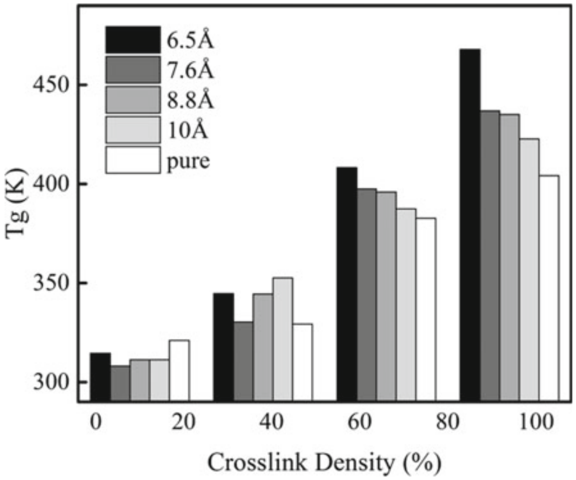

is stronger, which is more conducive to the formation of a stable and high-rigidity system.

(3) Analysis of the modulus

It can be seen from Fig. 6 that the elastic modulus value of each system increases with the increase of crosslinking degree. Meanwhile, comprehensive static mechanical properties of the filler system were significantly superior to those of the pure epoxy system. Moreover, when the crosslinking degree is ≥67%, the smaller the particle size of SiO_2, the higher each modulus value of the composite system. This is owing to the fact that, on the one hand, due to the large modulus of nano-SiO_2, adding SiO_2 can remarkably upgrade the mechanical properties of matrix. On the other hand, when

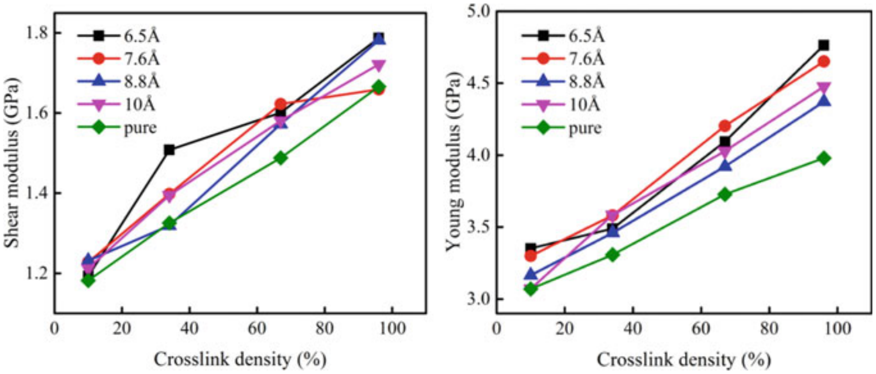

Fig. 6 Mechanical properties of nanocomposite system and pure epoxy system

the crosslinking reaches a certain degree, the bonding force between the nano-SiO_2 and matrix gets strengthened and enlarges with the reduction of the filler particle size. Thus, the general mechanical properties presented by the small particle size composite system are better. Besides, combined with the previous analysis, it can be concluded that when the crosslinking degree is $\geq 67\%$, the modulus values of the system and the slopes of the FFV and MSD curves are negatively correlated.

In addition, this section also analyzes the effect of temperature on mechanical properties. As displayed in Fig. 7, the variation of elastic modulus with temperature at 300, 350, 400, 450 and 500 K for each composite system at a crosslinking degree of 67% was investigated at 50 K intervals. It can be noticed from the figure that the shear modulus and Young's modulus of each system reduced continuously as the temperature increased and the modulus value of each system decreased most within the temperature range where T_g is located. When the temperature is lower (<350 K), two moduli of the composite system are both higher than those of the pure epoxy system. However, with the increase of temperature, the modulus values of the composite system decrease faster. When the temperature exceeds 400 K, the shear modulus of 10 and 8.8 Å particle size composite system is inferior to that of pure epoxy system. In addition, the reduction in modulus is also severe for the 6.5 and 7.6 Å particle size systems. Nevertheless, their modulus value is still higher than that of the pure epoxy system at this temperature owing to their obvious bonding enhancement effect. When the temperature reaches 500 K, the overall modulus value of the composite system is lower than that of the pure epoxy system.

In general, the modulus value of the filler system is more sensitive to temperature shifts at the crosslinking degree of 67%. In particular, the 6.5 Å composite system experienced the most remarkable falling range in each modulus value with increasing temperature after the glass transition. It suggests that the unique nano small size effect of the system after the glass transition might gradually collapse at high temperature, and the combination between filler and matrix is sharply weakened. For the whole temperature range from 300 to 500 K, 10 Å system and pure epoxy system exhibited better heat resistance and their CTE are also relatively small under this condition.

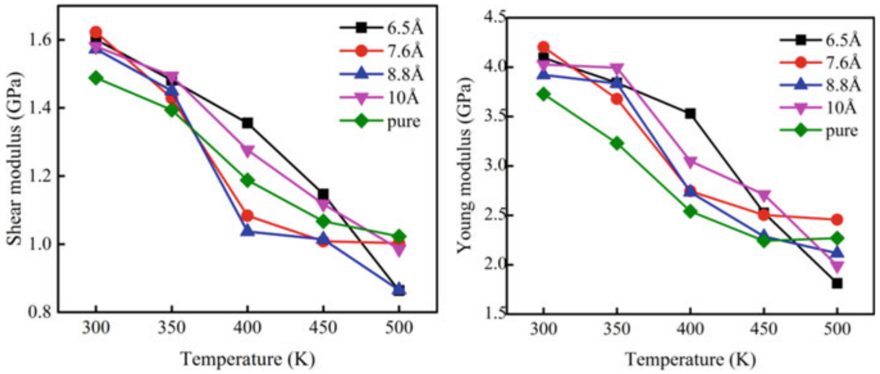

Fig. 7 Modulus of elasticity at different temperatures for each system with 67% crosslinking degree

However, when $T \leq 400$ K, the mechanical modulus value of the system with filler is generally higher than that of the pure epoxy system. Furthermore, every mechanical modulus value of the 6.5 Å system were consistently maintained within a high level. In accordance with the actual working condition, the insulation material is generally no longer used after undergoing glass transformation. For this reason, researching on the modulus value and heat resistance for each system before the temperature reaches T_g is of more engineering significance. On the whole, it can be concluded that the 6.5 and 10 Å system possess the best heat resistance.

1.2 Study About the Influence of SiO_2 Morphology and Content on the Structure and Properties of Its Epoxy Composites

In this section, three morphological Nano-SiO_2 filler models are constructed, and EP/SiO_2 cross-linking models with different morphologies and filling amounts were taken as the research objects, and the cross-linking models were simulated by MD.

Nano-SiO_2 is a familiar inorganic filler in EP composites, and its model construction can be divided into in three steps as described below.

(1) Firstly, import SiO_2 crystal structure as shown in Fig. 1.

(2) Secondly, construct filler particles with different morphologies. SiO_2 unit cells can be shaped into Nano-SiO_2 particle models with different shapes by using the Build Nanostructure function of MS software. This paper selects Nano-SiO_2 models with three shapes of sphere, tetrahedron and cube to simulate fillers with different morphologies [1]. To ensure the comparability of the calculation results, the packing model is constructed based on the principle of consistent number of Si atoms, with the packing for all three morphologies possessing 47 Si atoms.

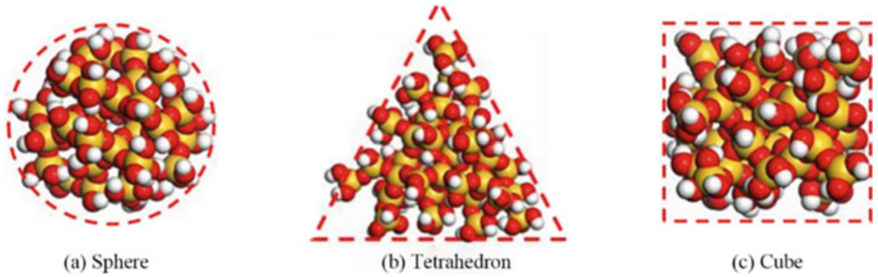

Fig. 8 Nano-SiO_2 models with different morphologies

(3) Thirdly, handle the oxidation on filler surface. In the formation of SiO_2 from the cell structure to filler particles, the Si–O bond on its surface is partially broken, which is a surface defect easily oxidized by air. Therefore, in this paper, hydroxyl groups are attached to the unsaturated Si atoms on the surface of the Nano-SiO_2 model to simulate the actual oxidation process. Figure 8 presents the model of Nano-SiO_2 filler after geometric optimization. Due to the various morphologies, the surface and dimensional parameters of the packing models are different. Additionally, the specific parameters are given in Table 2.

The effects of filler morphology and filling amount on the microstructure and thermodynamic properties of EP nanocomposites are taken as the research target. In this section, EP/Nano-SiO_2 composites with filling mass fraction of 10 wt% containing three filler shapes, namely sphere, tetrahedron and cube, and composite models with 5 wt%, 10 wt% and 15 wt% filled spherical fillers are modeled respectively. In order to simulate the idealized dispersion state of the filler, each model contained a Nano-SiO_2 filler, adjusting the filler mass fraction by changing the amount of the substrate. The detailed components of the model are listed in Table 3.

Subsequently, the interfacial binding energy, FFV, MSD and thermomechanical properties of the EP/Nano-SiO_2 model are calculated.

(1) Interfacial binding energy

The process of doping and compatibility of fillers into the substrate is completed relying on the physical interaction between substances. From this, the compatibility

Table 2 Dimensional parameters and atomic number of nano-SiO_2 with different morphologies

Filler profile	Dimensional parameters	Number of Si atoms	Number of O atoms	Surface light base
Sphere	Diameter 15 Å	47	126	64
Tetrahedron	Side length 23 Å	47	133	76
Cube	Side length 12 Å	47	129	67

Table 3 Component composition of different EP/nano-SiO_2 models

Models	Filler profile	Filling mass fraction (%)	Number of molecules		
			Nano-SiO_2	DGEBA	MTHPA
EP/5 wt% spherical SiO_2	Spherical	5	1	96	192
EP/10 wt% spherical SiO_2		10		45	90
EP/15 wt% spherical SiO_2		15		29	58
EP/10 wt% cubic SiO_2	Cube	10		47	94
EP/10 wt% tetrahedral SiO_2	Tetrahedron	10		47	94

between filler and substrate will directly affect whether the filler can be successfully doped into the substrate. Furthermore, the inorganic–organic bonding interface is established after the crosslinking of the composite system, and the strength of the interfacial binding effect will impact the modification effect of nano-doping. Binding energy between filler and substrate is the energy required to separate substrate and filler to "infinity", which is an essential parameter to evaluate the tightness of the bonding between composite substrate and filler. The binding energy can be calculated by the following equation [2]:

$$E_{Binding} = E_{EP} + E_{\mathrm{SiO_2}} - E_{Total} \tag{1}$$

where $E_{Binding}$ is the binding energy of SiO_2 filler and EP substrate in composite model. E_{Total} is the total intermolecular interaction energy of the composite model. E_{EP} is the interaction energy between the substrate molecules and $E_{\mathrm{SiO_2}}$ is the interaction energy of the filler.

In this section, the binding energy of SiO_2 filler and EP substrate in the composite model without crosslinking is calculated. The binding energy of filler-substrate in different models is summarized in Table 4. It can be noticed that it is the van der Waals force (VDW) that plays a dominant role in the model proposed in this paper, which is consistent with the conclusion of the literature [3]. The interfacial binding energy of SiO_2 filler with DGEBA molecules given in the literature [2] is close to 0. Consequently, the positive binding energy of SiO_2 filler with EP substrate (DGEBA/MTHPA) is mainly caused by the anhydride curing agent, which indicates that SiO_2 is suitable for the filler of DGEBA/MTHPA system in terms of compatibility. According to Table 4, the binding energy of SiO_2 to the substrate exhibits little change as the mass fraction of filler increases. While compared with the three shapes of filler, spherical SiO_2 offers the strongest binding energy and the greatest compatibility with the substrate. For this reason, the spherical SiO_2 is chosen for the analysis of the effect of filler amount on the structural and thermodynamic properties of the composites.

Table 4 Binding energy of filler-substrate for different models

Models	Combination of energy	Van der Waals interaction components	Static energy fraction
EP/5 wt% spherical SiO	1706.83	1829.18	−122.35
EP/10 wt% spherical SiO_2	1822.09	1943.49	−121.39
EP/15 wt% spherical SiO_2	1817.00	1918.54	−101.53
EP/10 wt% cubic SiO_2	1433.10	1542.97	−109.87
EP/10 wt% tetrahedral SiO_2	1537.89	1666.10	−128.21

(2) FFV analysis

The introduction of nanofillers will induce the variation of free volume in the materials. Accordingly, in this section, FFV is also used to characterize the free volume characteristics of the composite model, the influence of Nano-SiO_2 filler on the free volume characteristics of the composite model at room temperature is analyzed. The FFV calculations of EP/Nano-SiO_2 models for different systems are presented in Fig. 9.

There are multifaceted impact mechanisms by which fillers affect the free volume properties of polymer composites. For one thing, doping filler will introduce inorganic–organic interface layer, in which the filler and substrate are bonded together primarily by VDW interaction. And the presence of "pores" leads to an enlargement of free volume. For another, the filler will occupy a certain amount of free volume space and increase the total volume of the composite. Thus, the variation trend of FFV depends on the dominant force of the two factors. As revealed in Fig. 9, Nano-SiO_2 filler can reduce the FFV of EP composites, and both the morphology

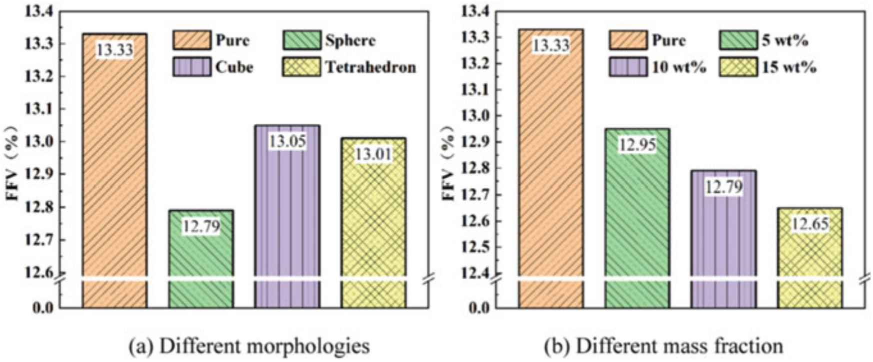

(a) Different morphologies (b) Different mass fraction

Fig. 9 FFV of EP/nano-SiO_2 models for different systems and addition amount of filler will affect the free volume properties of the composites. Compared with the fillers of different morphologies, the FFV of the composite models with three types of fillers decreased to some extent, and the spherical SiO_2 shows the greatest influence on the FFV of material. Specifically, the model FFV of the three fillers are ranked as sphere < tetrahedron < cube. This sorting has an opposite magnitude relationship with the model filler-substrate binding energy and also confirms the conclusion that there is more free volume in the interface region. Including that the mass fractions of the three fillers are the same and their capacity to occupy the free volume is equivalent, while the lower the binding energy, the weaker the binding effect. As a result, the interfacial layer is relatively loose and the free volume is larger. Besides, the FFV of the model gradually decreases with increasing mass fraction of filler. The same pattern can be also observed in the nano-SiO_2 and PVA/PVP blending system [4] together with micron SiO_2/EP composites [5, 6]. It can be summarized that the occupying effect of Nano-SiO_2 filler is greater than the introducing effect of interfacial layer. Therefore, the free volume fraction gradually declines with the increasing filling amount.

(3) MSD analysis

In order to characterize the Nano-SiO_2 filler on the chain segment motion properties of the composite model, the MSD values of all atoms in the model at room temperature are calculated by MD simulation in this section. The calculated MSD results for EP/Nano-SiO_2 models of different systems are shown in Fig. 10. It can be found that nano-SiO_2 filler doping can significantly reduce the MSD of molecular chain segments and limit the chain segment motion of material molecules. In addition, the model MSD of the three fillers are ordered as sphere < cube < tetrahedron and the MSD decrease gradually as the filler mass fraction increase.

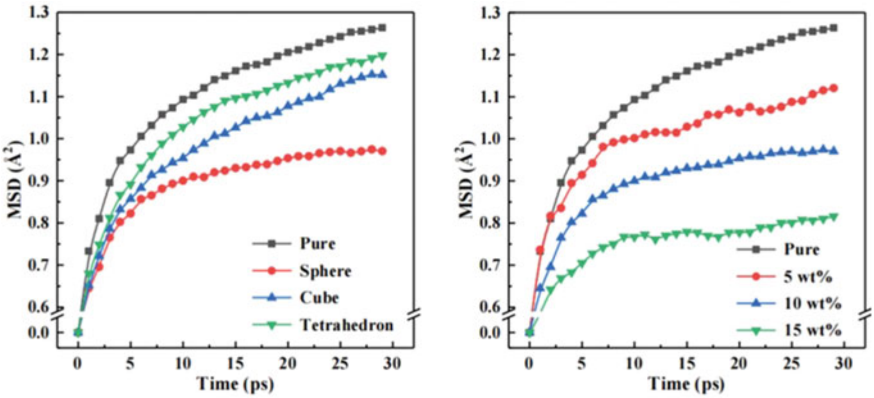

(a) Different morphologies (b) Different filling amount

Fig. 10 MSD of EP/nano-SiO_2 models for different systems

The free volume can provide space for the molecular chain segments of the material to move [7]. Therefore, for homogeneous materials, the free volume of the material is the primary factor that affects the motion characteristics of the chain segments. According to Fig. 10, the FFV of the material decreased obviously with the increase of filler mass fraction. Furthermore, the FFV and MSD of the doped spherical SiO_2 model are both evidently less than those of the other two systems. Nevertheless, the MSD of the model doped with tetrahedral SiO_2 is larger than that of the cube system, suggesting that there are other factors influencing the chain segment motion of molecules inside the material.

(4) Analysis of glass transition temperature

By linear fitting of the density-temperature curves during the annealing process of the model, the glass transition temperature of EP/Nano-SiO_2 composites with different filler morphologies and filling amounts can be obtained. And the results are displayed in Fig. 11. As can be seen from Fig. 11a, the SiO_2 filler doping can increase the T_g of epoxy by more than 20 K (the T_g of pure epoxy substrate is 400.46 K). The lifting effects of the three fillers were equivalent, and in comparison, the spherical SiO_2 filler had the most remarkable effect. According to Fig. 11b, the T_g of epoxy composites increased gradually with the rising mass fraction of filler. When the mass fraction of SiO_2 is 15 wt%, the T_g of the material reached 430.35 K, indicating that the filling amount has a much higher degree of influence on the T_g of material compared to the morphology of filler.

The effect of Nano-SiO_2 filler on the T_g of EP composites is a macroscopic manifestation of the change in its internal microstructure. It is generally believed that the process of glass transition occurs with some kind of chain segment movement within the material. As shown in Figs. 10 and 11, the MSD of the material presented a consistent variation pattern with T_g, because the T_g of material is strongly influenced by the movement of molecular chain segments within the material. A reduction in MSD indicates that the molecular motion of material is restricted. Moreover, with

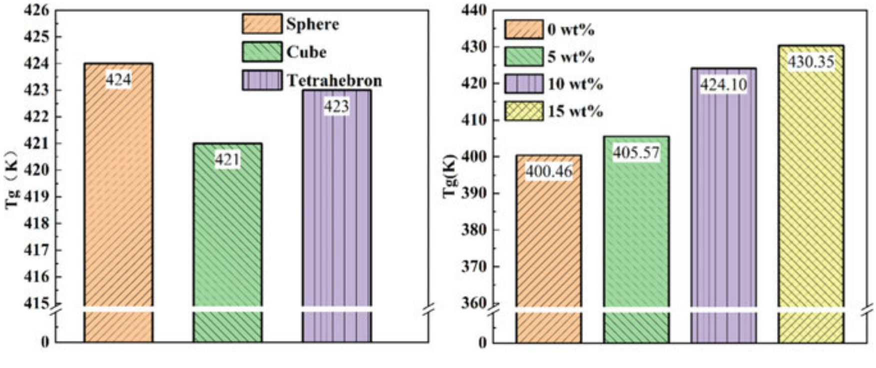

(a) Different morphologies (b) Different filling amounts

Fig. 11 T_g of EP/nano-SiO_2 models for different systems the increasing temperature, the degree of molecular motion is small and the glass transition is unlikely to occur, leading to a higher T_g.

(5) CTE analysis

The calculated results for CTE of EP/Nano-SiO_2 composites with different filler morphologies and filling amounts are exhibited in Figs. 12 and 13. According to Fig. 12, the thermal expansion characteristics of EP composites in glassy state and rubbery state remain remarkable are distinct. Additionally, the CTE of glassy state is smaller than that of rubbery state, which is consistent with the findings for the epoxy substrate. Compared with the pure epoxy substrate, the Nano-SiO_2 filler doping has a certain enhancement on the thermal expansion characteristics of the composites, but the gap of the filler modification effect among the three morphologies is obvious. For glassy epoxy materials, spherical SiO_2 doping works best, reducing the material CTE by about 19%. For epoxy materials in rubbery state, cubic SiO_2 doping has the best effect, reducing the material CTE by approximately 18%. However, the improvement effect of tetrahedral filler is not obvious in either glassy or rubbery state.

The filling amount of SiO_2 has considerable influence on the CTE of epoxy composites. As revealed in Fig. 13, the CTE of the material reduced gradually as the mass fraction of SiO_2 in the composite system raised. Additionally, the calculated results suggested that the CTE was close to a linear relationship with the mass fraction of SiO_2. This is attributed to the fact that the SiO_2 filler doped into the substrate and occupied part of the free volume, reducing the contribution of the free volume to the CTE by thermal expansion. Also, the CTE of the filler itself is far less than that of the organic substrate. Compared to the substrate with the equivalent volume, the CTE of composites is degraded by the reduction of organic molecules in composites. As the filler mass fraction raised, more free volume of the system was occupied and less organic matter content was contained. For this reason, the CTE of composites brought down with the increasing mass fraction of SiO_2 filler.

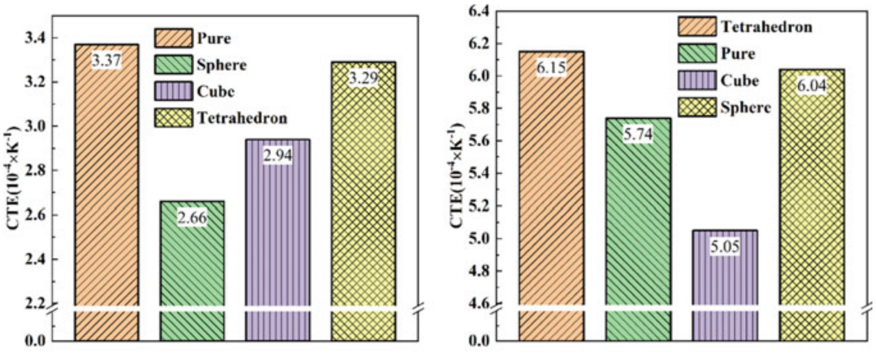

(a) Glassy state (b) Rubbery state

Fig. 12 CTE of EP/nano-SiO_2 composites with different filler morphologies

Fig. 13 CTE of composites with different nano-SiO_2 mass fractions

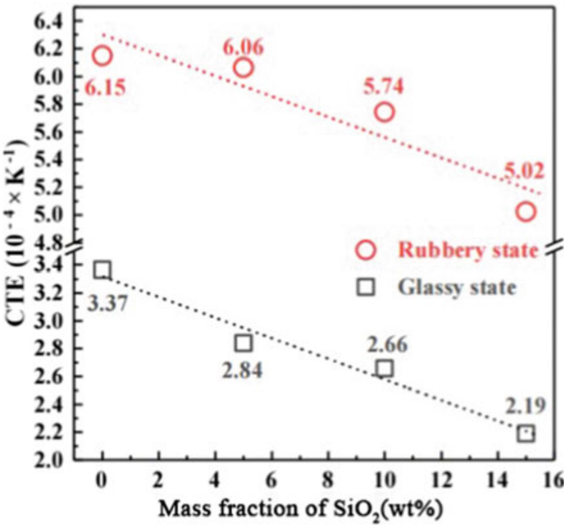

(6) Mechanical property analysis

The Young's modulus, shear modulus and bulk modulus of EP/Nano-SiO_2 composites with different filler morphologies (all with 10 wt% mass fraction) and filling amounts (spherical) at room temperature (300 K) are calculated by the static constant strain method. And the results are illustrated in Figs. 14 and 15. It can be noted that the three shapes of fillers improved the elastic modulus of materials to varying degrees. In order to compare the modification effects of fillers with different morphologies more accurately, the lifting rates for three elastic moduli of the material after doping are calculated. From Fig. 14, it can be concluded that the Young's modulus of the material was dramatically boosted by the three fillers. Nonetheless, the three fillers had unstable enhancing effects on the shear modulus and bulk modulus of the material. In contrast, the spherical SiO_2 enhanced all three moduli by over 10%, which is superior to the cubic and tetrahedral fillers.

According to Fig. 15, the three elastic moduli of epoxy composites presented an approximate linear enlargement within a certain range as the mass fraction of filler raised. When the mass fraction of filler reached 15 wt%, the Young's modulus, shear modulus and bulk modulus of composites improved by 24.56%, 32.45% and 23.24%, respectively, compared with the pure epoxy substrate. It can be seen that doping nanofillers into EP substrate is a proven effective measure to improve the mechanical properties of materials. And the reasons mainly lie in two aspects. As an inorganic material, SiO_2 has excellent mechanical properties of its own and high hardness properties. When filled into the epoxy substrate as a filler, SiO_2 can play an excellent supporting role in the material, making it less susceptible to be deformed by external force [8]. Besides, the SiO_2 filler occupies a certain free volume space in the substrate, which falls the movement of chain segments in model and likewise

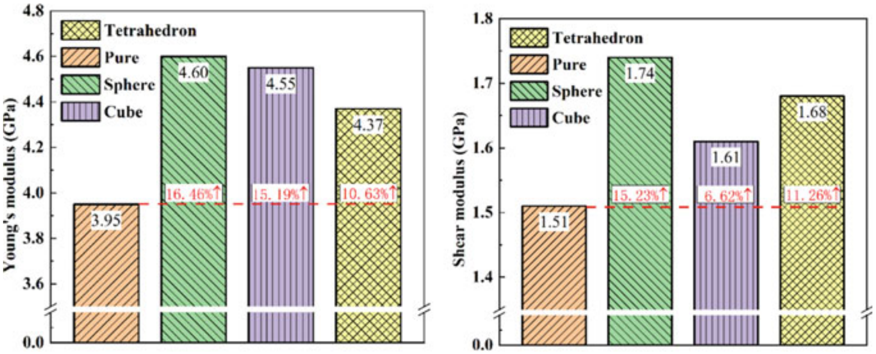

(a) Young's modulus (b) Shear modulus

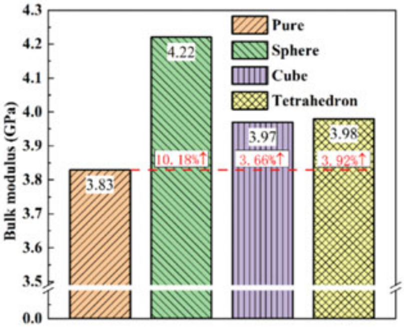

(c) Bulk modulus

Fig. 14 Mechanical properties of composites with different filler morphologies

Fig. 15 Variation of mechanical properties of EP/Nano-SiO_2 model with SiO_2 mass fraction

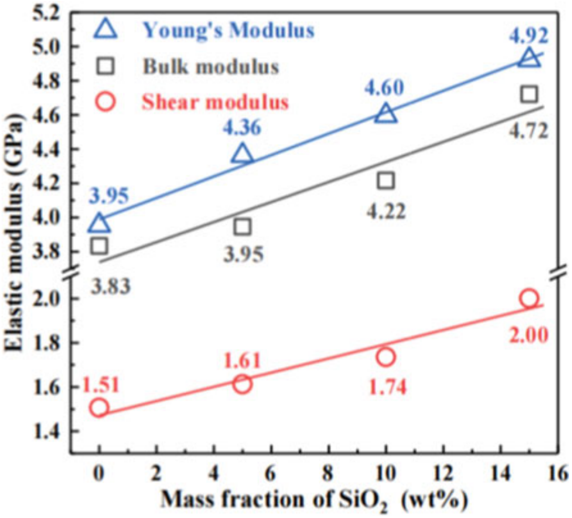

makes the molecular deformation of material difficult. Accordingly, doping SiO_2 filler can improve the mechanical properties of material obviously.

Nevertheless, some experimental studies have demonstrated that although SiO_2 fillers can significantly strengthen the composites, when the mass fraction of SiO_2 is above 3%, the mechanical properties of epoxy composites will boost slower or even degrade with the gain of nanofiller addition [9]. While from the results of this paper, the modulus values are still increasing when the mass fraction of SiO_2 reached 15 wt%. The main reason for this contradictory result lay in the dispersity of filler. When the mass fraction of filler is relatively low, the filler can be well dispersed in the substrate. At this moment, the mechanical properties of composites enhance as the mass fraction rise, indicating that the SiO_2 filler has excellent reinforcement effect. However, in the present experimental study, when the filler mass fraction rises to a certain level, agglomeration phenomenon appears, deteriorating its dispersity to cause a reduction in performance [10]. In this paper, the dispersion effect is idealized in the simulation process without agglomeration of filler, which can better reveal the potential of SiO_2 filler on the reinforcement effect of composites. Besides, the results of literature [11] demonstrate that the Young's modulus of composites still grows when the filling amount of SiO_2 filler reaches up to 14vol% with guaranteed dispersity. This also implies that the dispersion problem of nanofillers is an essential factor limiting the effectiveness of their modification.

1.3 Study on the Effect of SiO_2 Surface Modification on the Structure and Properties of Its Epoxy Composites

Nano-SiO_2 is extremely prone to agglomeration during the doping process since it has great surface energy and high surface activity [12], resulting in an enlargement of the filler particle size and loss of numerous properties as a nanomaterial, which leads to poor modification [13, 14]. Additionally, the surface of inorganic nanofillers is easily oxidized with a huge number of hydrophilic hydroxyl groups, contributing to a poor affinity between the filler and EP substrate. These problems restrict the filling amount and modification effect of nanofillers in EP composites. Studies have revealed that the dispersity of filler in the substrate can be improved by grafting the SiO_2 filler surface with silane coupling agent. However, current experimental methods pay more attention to the compatibility amelioration of filler with substrate by grafting on the surface of the coupling agent. While the influence of coupling agent itself on the microstructure and properties of material has rarely been reported. Furthermore, selecting the appropriate coupling agent for a particular composite system could be a lengthy and highly cost exploration process. To this end, three silane coupling agents are selected to graft Nano-SiO_2 filler in this section, with a Nano-SiO_2 surface modification model being constructed. The effects of various silane coupling agents and grafting rates on the microstructure and thermodynamic properties of EP composites are compared and analyzed based on MD simulations.

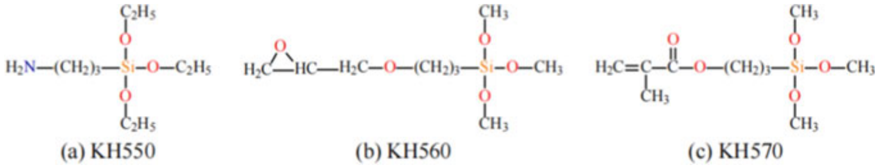

Fig. 16 Molecular structure formula of 3 common silane coupling agents

It is expected to provide some guidance for the selection of silane coupling agents in the production of Nano-SiO_2/EP composites.

Silane coupling agent is an organic substance with silyl groups, which is commonly used for surface treatment of micro and nano inorganic fillers. The commonly used coupling agent is generally trisilyl-based, and its molecular structure formula can be expressed as R_1–$Si(OR_2)_3$, where –R_1 is an organic group and –$Si(OR_2)_3$ is a silyl group. In this chapter, we select three silane coupling agents, 3-aminopropyltriethoxysilane (APTES, KH550), 3-glycidyl ether propyltrimethoxysilane (GOTMS, KH560), and 3-methylpropyltrimethoxysilane (MPTS, KH570) to simulate the surface modification of Nano-SiO_2 with a particle size of 15 Å. The structural formula is shown in Fig. 16.

After the hydrolysis of silane coupling agent, the formation of –OH groups on the Si atomic surface are required for grafting onto the SiO_2 surface. The mechanism of hydrolysis is that –H of water molecule replaces –R_2 in the coupling agent molecule, forming –OH group [15]. As shown in Fig. 17, the hydrolysis of a silane coupling agent results in the formation of three –OH groups on Si atoms.

In this section we used three coupling agents which have different functional groups, KH550 with an amino group, KH560 with an epoxy group, and KH570 with a methacrylate oxide group. The amino group will be involved in the crosslinking reaction of the epoxy resin, which needs to be pretreated in order to simplify the model crosslinking mechanism. For the amino groups of KH550, a DGEBA molecule is attached to each amino group by referring to the reaction mechanism of amino groups with epoxy groups in the literature [16]. In some conditions, the coupling agent can undergo a shrinkage reaction with the SiO_2 surface, forming covalent bonds and thus grafting the coupling agent onto the SiO_2 surface [17]. Figure 18 shows the reaction mechanism. Ideally, all the three –OH groups on the Si atom of the silane coupling agent will participate in the reaction. A total of five surface modification models of

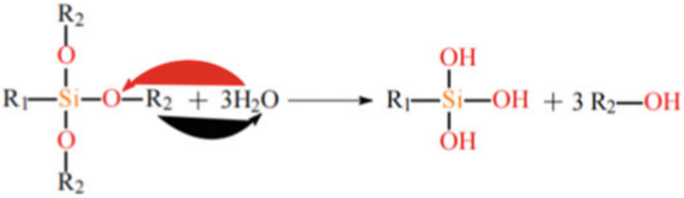

Fig. 17 Hydrolysis flux of silane coupling agent

Fig. 18 Reaction equation for grafting of silane coupling agent on SiO_2 surface

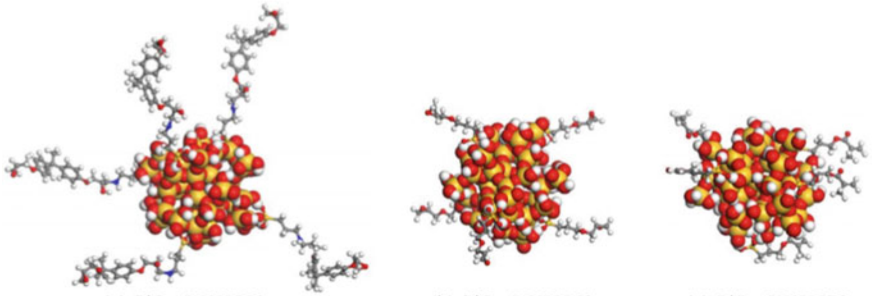

(a) SiO_2-5-KH550 (b) SiO_2-5-KH560 (c) SiO_2-5-KH570

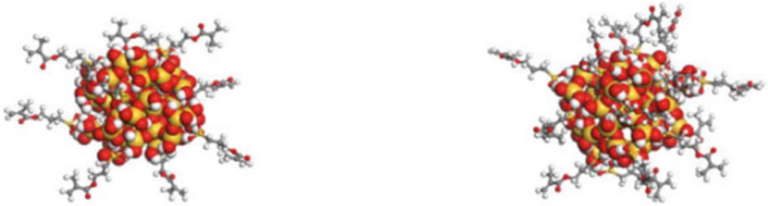

(d) SiO_2-10-KH570 (e) SiO_2-15-KH570

Fig. 19 Surface modification model of nano-SiO_2

Nano-SiO_2 are constructed in this section, as shown in Fig. 19. The naming rule is "SiO_2—number of graft—type of coupling agent", and the surface modification model of Nano-SiO_2 can be divided into two categories:

(1) Different coupling agent types: five treated KH550, KH560 and KH570 molecules are grafted onto the surface of spherical SiO_2 with a particle size of 15 Å, respectively, as shown in Fig. 19a, b, c; (2) Different grafting rates: 10 and 15 KH570 molecules are grafted on the surface of spherical SiO_2 with a particle size of 15 Å, respectively. According to Table 3, there are 64 –OH groups on the surface of spherical SiO_2 with a particle size of 15 Å. The grafting rates of the models shown in Fig. 19c, d, and e can respectively be calculated as 23%, 47%, and 70%.

After constructing the surface modification model, the EP/modified Nano-SiO_2 models with different coupling agents and different grafting rates are constructed using the Amorphous Cell module of MS software. The interfacial binding energy, diffusion coefficient, FFV, MSD and thermomechanical properties are calculated and analyzed, respectively.

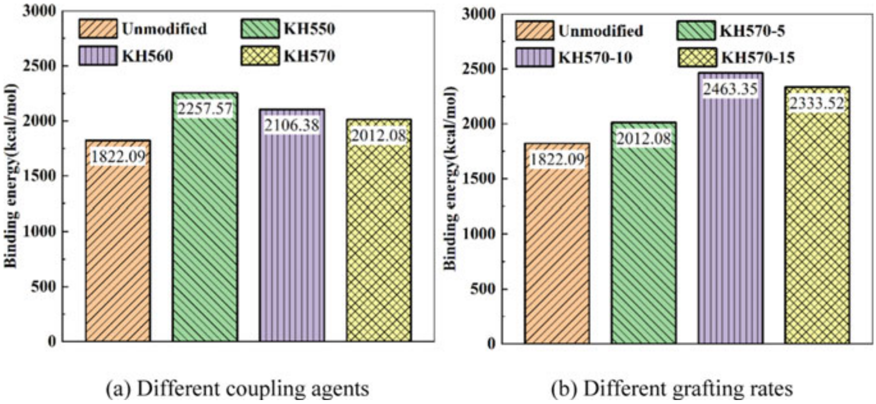

(a) Different coupling agents (b) Different grafting rates

Fig. 20 Bonding performance of modified SiO_2 with epoxy resin substrates

(1) Interface binding energy

In order to characterize the effect of Nano-SiO_2 surface coupling agent modification on the compatibility of filler and substrate, we calculate the binding energy between modified Nano-SiO_2 and epoxy resin substrate in this section, as shown in Fig. 20. It can be seen that the modification of SiO_2 surface by silane coupling agent can significantly improve the binding energy of SiO_2 filler and epoxy resin substrate. Among the three coupling agents, KH550 coupling agent modified system has the highest binding energy and KH570 coupling agent is relatively the lowest. The improvement of the bonding energy between filler and substrate indicates that the coupling agent improves the interfacial compatibility of filler and substrate. It enhances the bonding performance of both [18]. The reasons for this are twofold: one is that the coupling agent can reduce the hydrophilic hydroxyl groups distributed on the SiO_2 surface, thus weakening the hydrophilicity of the filler surface. The second is that the silane coupling agent is a lipophilic organic substance, and its grafting on the surface of the filler can improve the lipophilicity of the filler.

According to Fig. 20b, the binding energy of the filler to the substrate increases and then decreases as the amount of coupling agent increases. It indicates that there is an optimal amount of silane coupling agent to enhance the dispersion of filler, and too much amount will lead to a decrease in binding energy. We also found from the literature [19] that excessive amounts of coupling agents reduce the affinity of the filler with the organics. The reason for this may be that too much coupling agent wrapped around the filler surface increases the distance between the filler and the substrate, and it result in weaker Van der Waals interactions and lower binding energy [20].

(2) Diffusion characteristics analysis

To further analyze the compatibility of the modified Nano-SiO_2 filler with the substrate, in this section we analyzed the diffusion characteristics of the modified filler in the epoxy resin. The diffusion coefficient D of the filler is the most direct parameter reflecting the diffusion characteristics of the filler in the substrate, and D can be obtained by Einstein's equation:

$$D = \frac{1}{6N} \lim_{t \to \infty} \frac{\left\langle |R(t) - R(0)|^2 \right\rangle}{6t} = \frac{1}{6N} \lim_{t \to \infty} \frac{MSD}{6t} \tag{2}$$

In the formula, N refers to the particle number of the packing, $R(t)$ and $R(0)$ denote the displacements of the packing in the system at time t and the initial moment, respectively, MSD refers to the mean square displacement of the packing. It can be seen that if the MD simulation time is long enough, the slope of the MSD against time t can approximately characterize the diffusion properties of the filler and the larger the slope of the MSD, the larger the value of the diffusion coefficient.

The MSD of Nano-SiO_2 filler in EP/SiO_2 in composites before and after modification is shown in Fig. 21. The coupling agent can significantly enhance the diffusion behavior of the filler in the substrate. Compared to the three coupling agents, the diffusion behavior of the modified fillers was KH550 > KH570 > KH560 in order of strength to weakness. As the grafting rate of coupling agent increases, the diffusion coefficient of filler first increases and then decreases.

(3) FFV analysis

We gave the FFV of the EP/modified SiO_2 composite model in Fig. 22. All three silane coupling agents resulted in an increase in FFV values of the composites by about 1%, and the type of coupling agent have little effect on the free volume properties. The FFV of the composites tends to increase slightly with the increase of the coupling agent grafting rate. It shows that the coupling agent increases the free volume fraction of the composites.

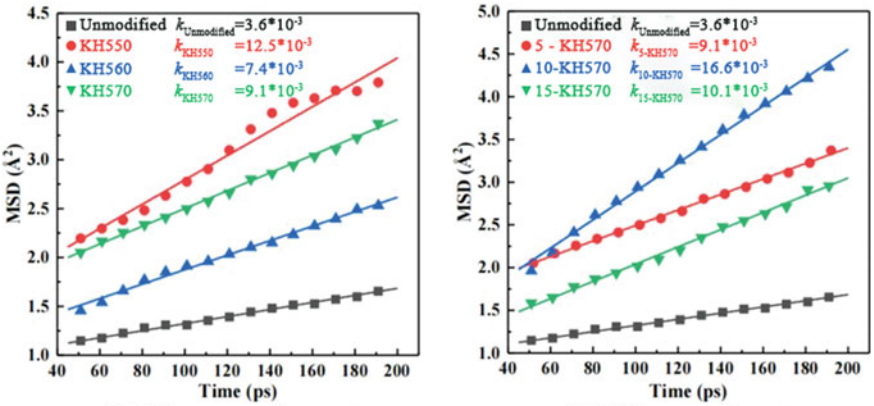

(a) Different coupling agents (b) Different grafting rates

Fig. 21 MSD versus time for nano-SiO_2 filler

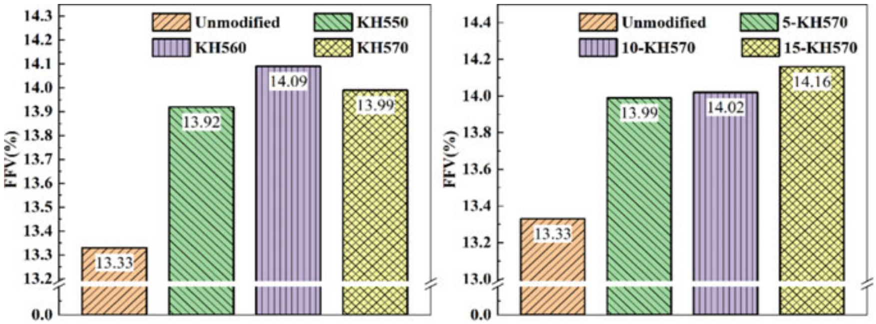

(a) Different coupling agents (b) Different grafting rates

Fig. 22 The FFV of EP/modified SiO_2 composite model

(4) MSD analysis

At normal temperature, Fig. 23 show the results of the all-atom MSD calculations for different system modification models. It can be seen that the MSD of the EP/modified SiO_2 composite model is greater than that of the unmodified system. The MSD magnitudes of the three coupling agent-modified composite models are in the order of KH550 < KH560 < KH570. With the increase of coupling agent grafting rate, the MSD gradually increases. In other words, the coupling agent leads to enhanced chain segment motion in the composite system. In our analysis, the increase in MSD leads to a larger space of motion of the molecules in the model due to the increase in the free volume of the system by the coupling agent. On the other hand, according to Fig. 21, the coupling agent enhances the diffusion characteristics of the filler, resulting in an increase in the MSD of the filler. So the MSD of the composite system rises (Fig. 23).

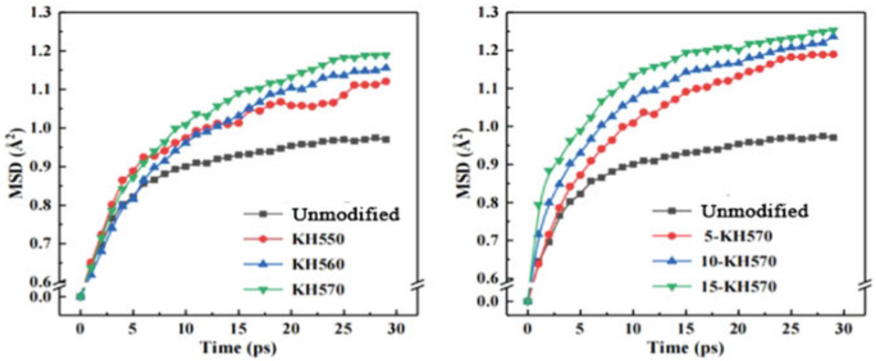

(a) Different coupling agents (b) Different grafting rates

Fig. 23 The MSD of EP/modified SiO_2 composite model

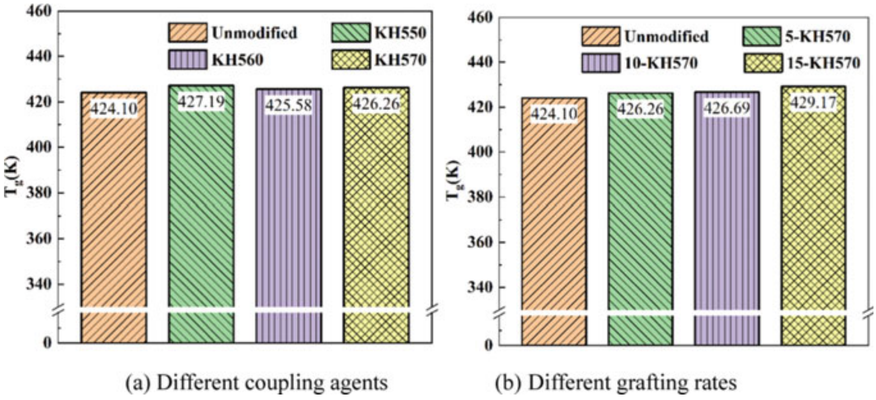

(a) Different coupling agents (b) Different grafting rates

Fig. 24 The T_g of EP/modified SiO_2 composite model

(5) Glass transition temperature

By linear fitting of the density-temperature curves during model annealing, we can obtain the T_g of EP/modified Nano-SiO_2 composites with different coupling agent types and grafting rates as shown in Fig. 25. When the filler is in the ideal dispersion state, the surface modification of SiO_2 filler by silane coupling agent can improve the T_g of the composite to some extent. Compared to the three coupling agents, the KH550 modified model is the most effective, with an increase in T_g of 3.09 K. The T_g of the composite increased with the increase in the amount of coupling agent grafted. When the grafting amount of KH570 coupling agent reached 15, the T_g increased by 5.07 K. However, when the grafting amount is 15, the grafting rate on the surface of SiO_2 filler has reached 70%, but the T_g is only elevated by 1.2%. It can be seen that the silane coupling agent has limited ability to enhance the T_g of the composite with good dispersion of the filler.

(6) CTE analysis

As shown in Fig. 25, different silane coupling agents have different effects on the thermal expansion characteristics of the composites. KH550, KH560 coupling agents lead to a slight increase in the CTE of the composites, while KH570 reduces the CTE of the composites by 7.14%. However, with the increase of KH570 grafting amount, the CTE of the material gradually increased. When the grafting amount reached 15, the CTE increased by 9.02%. It can be seen that the selection of suitable coupling agent modified SiO_2 filler can reduce the CTE of EP/Nano-SiO_2, but too much coupling agent will increase the CTE and lead to the deterioration of thermal expansion characteristics.

(7) Mechanical property analysis

In this section, we calculate the Young's modulus, shear modulus and bulk modulus of the EP/modified Nano-SiO_2 system with different coupling agents at 300 K to

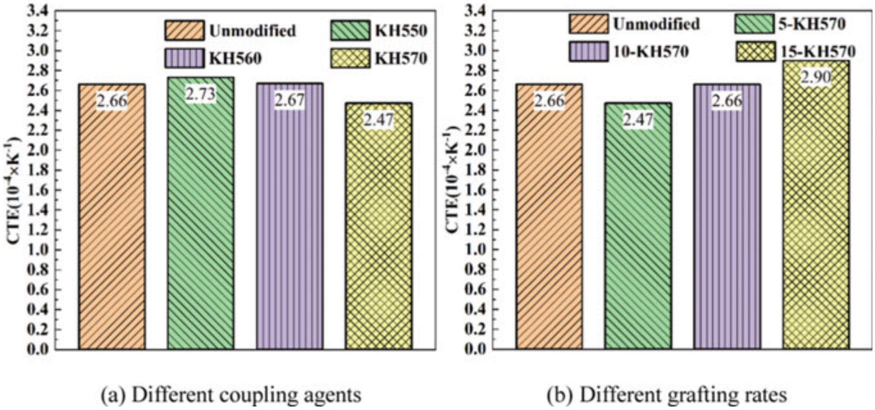

(a) Different coupling agents

(b) Different grafting rates

Fig. 25 The CTE of EP/modified SiO_2 composite model

characterize the mechanical properties of the composites. The results are shown in Fig. 26.

Compared with the unmodified composite model, all three moduli of the KH550 modified models show a significant decrease and the mechanical properties deteriorated. Both coupling agents KH560 and KH570 affect the mechanical properties of the composites to a comparable extent, but this effect is also slightly lower than that of the unmodified system. In Fig. 27 we give the effect of the amount of coupling agent on the mechanical properties of EP/modified SiO_2 composites. With the increase of coupling agent, the Young's modulus, shear modulus and bulk modulus of the composite show an overall fluctuating downward trend. When the grafting amount reached 15, the three modulus reduction rates are 6.74%, 13.22%, and 9.72%, respectively.

2 Model Construction and Performance Study of POSS/Epoxy Resin Composites

2.1 Study on the Effect of Nano-filler POSS Doping on the Properties of Epoxy Composites

Nanomodification of insulating materials is a new way to enhance the performance of epoxy nanocomposites. The doping of nanofillers can combine the excellent properties of fillers such as high toughness and high thermal conductivity with epoxy resin. The doping of nano-fillers can also enhance the thermal, electrical and mechanical properties of epoxy composites. In this section, two kinds of nano-POSS filler models were constructed, and two kinds of nano-POSS fillers with different mass fractions were doped into the epoxy resin substrate. According to MD simulation,

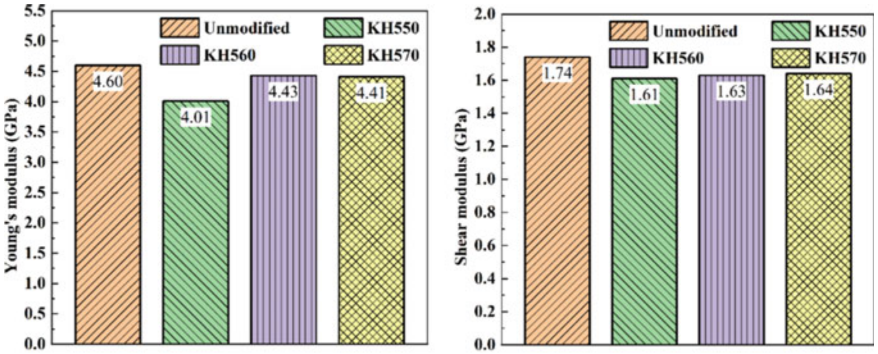

(a) Young's modulus (b) Shear modulus

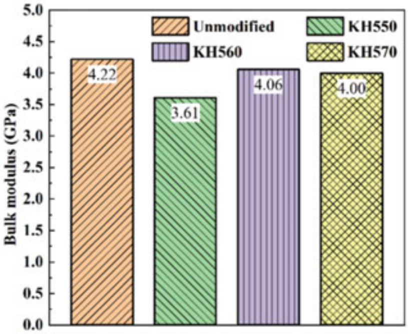

(c) Bulk modulus

Fig. 26 Mechanical properties of EP/modified SiO_2 composite model

we analyze the effects of the type and filling amount of nanofiller on the microstructure and thermal and mechanical properties of the double crosslinked epoxy resin composites.

Polyhedral oligomeric silsesquioxane (POSS) is an organic–inorganic hybrid material with the molecular formula $(RSiO_{1.5})_8$. The structure is shown in Fig. 28. It is connected by Si–O bonds to form a unique cage-like skeleton. Different organic groups R/X attach outside the backbone, such as methyl, phenyl, hydroxyl, etc. The particle size of POSS ranges from 1 to 3 nm and seven R organic groups are generally not active. The presence of seven R organic groups improves the compatibility of the POSS nano-structure with the polymer matrix. The X-active group can be chemically bonded to the polymer molecule, acting as a “rivet”. Because of its low dielectric constant, good thermal stability and high mechanical strength, nano-POSS has great value in the field of thermosetting resin modification.

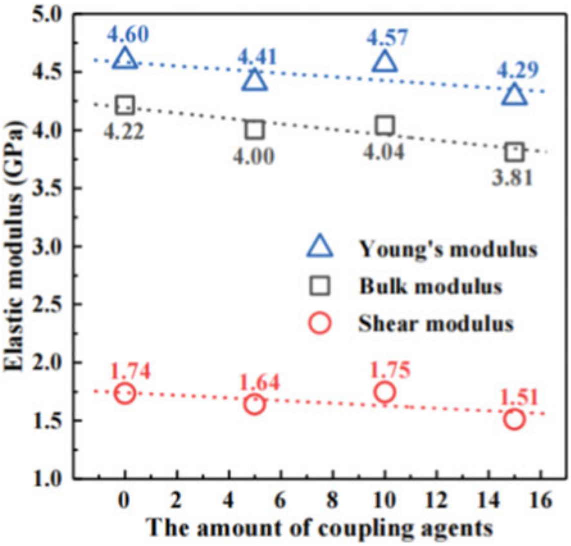

Fig. 27 Variation of model mechanical properties of EP/modified SiO_2 composites with the amount of coupling agent

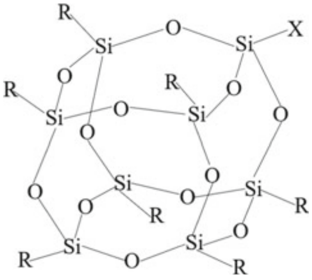

Fig. 28 Molecular structure formula of POSS

According to the molecular structure formula of POSS, two different nanofiller models are constructed in MS software: heptamethyl caged sesquisiloxane (methyl-POSS) and heptaphenyl caged sesquisiloxane (phenyl-POSS). And we optimize the structure, as shown in Fig. 29.

Based on the composite model construction method above, we constructed EP/POSS composites with filler (methyl-POSS) mass fractions of 5.1%, 9.6%, 15.1%, and 19.9% and filler (phenyl-POSS) of 6%, 11.4%, 16.2%, and 20.4%, respectively, as shown in Fig. 30.

Subsequently, this article analyze the FFV, MSD, radial distribution (RDF) and thermomechanical properties of the EP/POSS composite model.

(1) FFV analysis

As shown in Fig. 31, the nano-POSS filler can reduce the FFV of the epoxy composite system, and both the type and content of the filler affect the free volume percentage of the material. With the increase of nanofiller POSS content, the FFV of the system

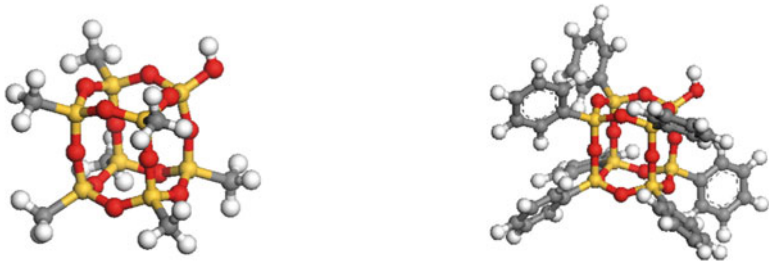

R=-CH_3, X=-OH

R=-C_6H_5, X=-OH

(a) Molecular model of methyl-POSS

(b) Molecular model of phenyl-POSS

Fig. 29 Molecular model of POSS

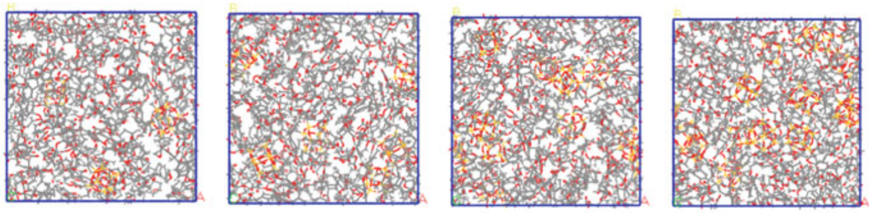

EP/methyl-POSS-5.1 EP/methyl-POSS-9.6 EP/methyl-POSS-15.1 EP/methyl-POSS-19.9

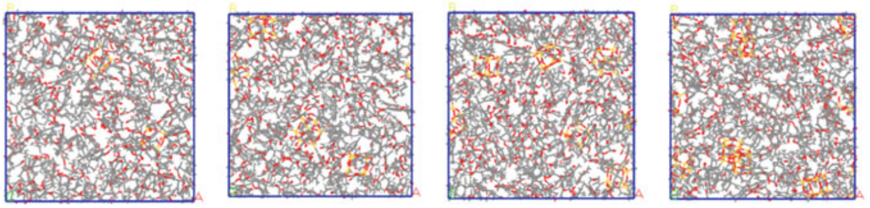

EP/phenyl-POSS-6 EP/phenyl-POSS-11.4 EP/phenyl-POSS-16.2 EP/phenyl-POSS-20.4

Fig. 30 Molecular modeling of nano-composite epoxy materials

show a law of first decreasing and then increasing. The magnitude of FFV at a filler mass fraction of 20% is approximately equal to the FFV of the double crosslinked epoxy system. It can be seen that the bonding interaction between POSS and epoxy molecular chain segments is greater than its own filling effect, when the content of POSS filler is around 0–10%. While the content of POSS filler is around 10–20%, the filling effect of nano-POSS itself is greater than its bonding with epoxy molecular chain segments. Meanwhile, the FFV of EP/phenyl-POSS system is smaller than that of EP/methyl-POSS system, which may be due to the better compatibility of the phenyl group of nano phenyl-POSS with the epoxy substrate.

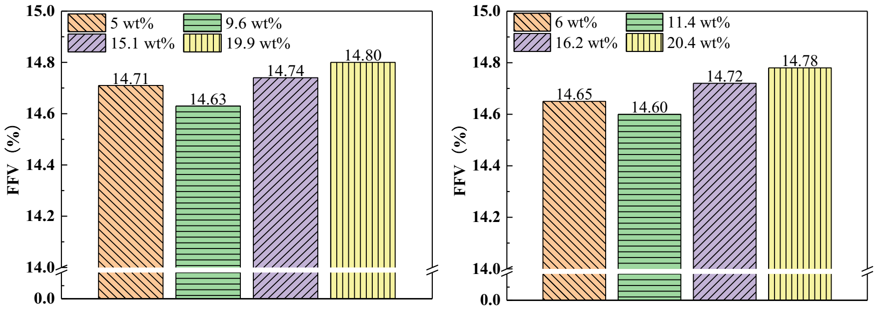

(a) FFV of EP/methyl-POSS system (b) FFV of EP/phenyl-POSS system

Fig. 31 FFV for different EP/POSS systems

(2) MSD analysis

As seen in Fig. 32, nano-POSS filler doping can restrict the motion of epoxy molecular chain segments, thus reducing the MSD of the epoxy system. With the increase of the nanofiller POSS content, the MSD value of the system show a pattern of decreasing first and then becoming larger. This trend is positively correlated with the results of the free volume share in the previous section. Therefore, for different EP/POSS systems, the free volume of the material is the main factor affecting the ability of the molecular chain segments to move.

(3) Radial distribution function (RDF) analysis

Radial Distribution Function (RDF) can reflect the characteristics of the material microstructure [21], whose value $g(r)$ reflects the magnitude of the relative probability of finding another atom or group of atoms at a distance r to the reference particle. The equation is:

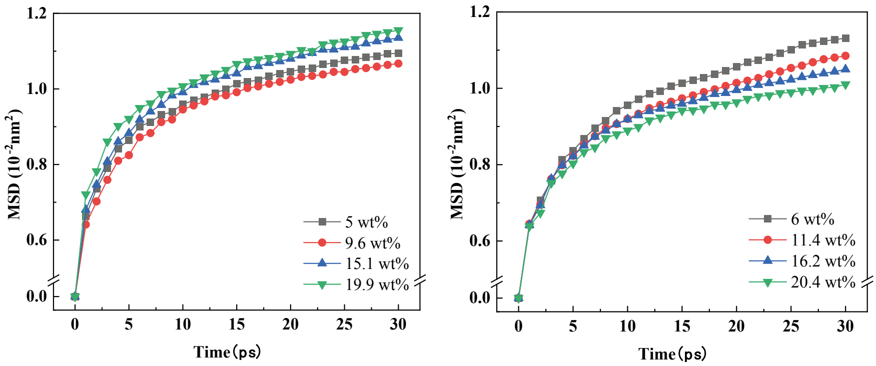

(a) MSD of EP/methyl-POSS system (b) MSD of EP/phenyl-POSS system

Fig. 32 MSD for different EP/POSS systems

Fig. 33 Schematic diagram of RDF

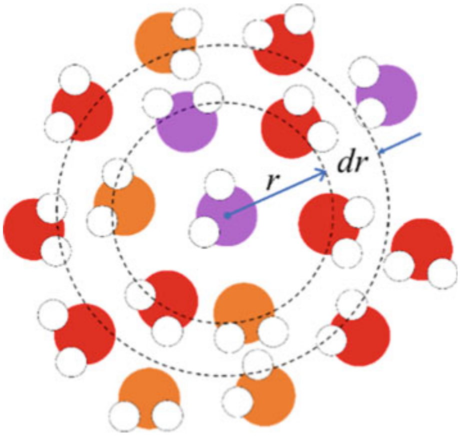

$$g_{\mathrm{A-B}}(r) = \frac{n_B \cdot V}{4\pi r^2 dr \cdot N_B} \tag{3}$$

In the above equation: n_B is the number of B atoms at a distance r around the A atom. N_B is the total number of B atoms. V is the volume of the whole system. The schematic diagram is shown in Fig. 33.

By analyzing the radial distribution function of nanofillers in the epoxy system, we can obtain the influence of POSS on the stacking of epoxy molecular segments. Figure 34 shows the images of the radial distribution function obtained based on the nano-POSS in the epoxy system. In terms of the general trend, the RDF images of the different epoxy systems varied almost equally, achieving significant peaks at $r = 1.1$, 1.35, and 1.65 Å, respectively. The absence of any spikes and the gradual convergence of $g(r)$ to 1 at $r > 8$ Å are considered as evidence of the amorphous character of the epoxy system. As the POSS mass fraction increases, the peak $g(r)$ becomes progressively smaller. This suggests that the presence of nano-POSS reduces the probability of finding another particle within the same distance range. This indicates an increase in the distance between the chain segments of the epoxy molecule. This may be due to two reasons: first, the cage structure of nano-POSS plays a supporting role for the epoxy molecular chain segments, which increases the distance between molecular chain segments and is not conducive to the tight bonding of the crosslinked network. Second, when the mass fraction of nano-POSS gradually increases, it is easy to form agglomerates due to its own surface properties, which further increases the distance between epoxy molecular chain segments. This effect becomes stronger as the POSS mass fraction continues to increase.

(4) Glass transition temperature

In this section, we used the density-temperature fitting method for the study of T_g of EP/POSS system. The calculation results of T_g of different EP/POSS systems are

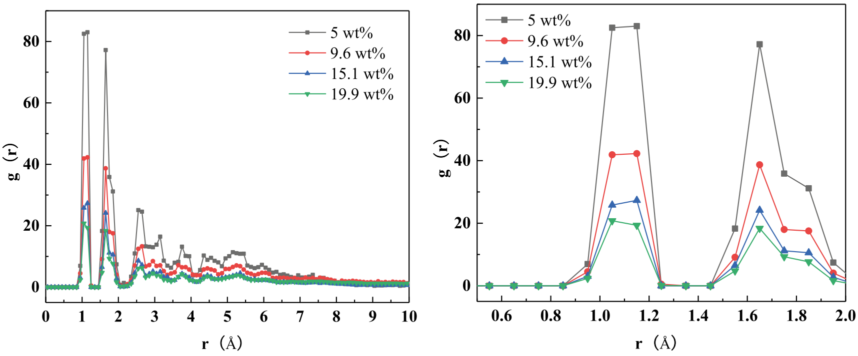

(a) RDF based on nano-methyl-POSS

(b) Partial enlarged view of (a)

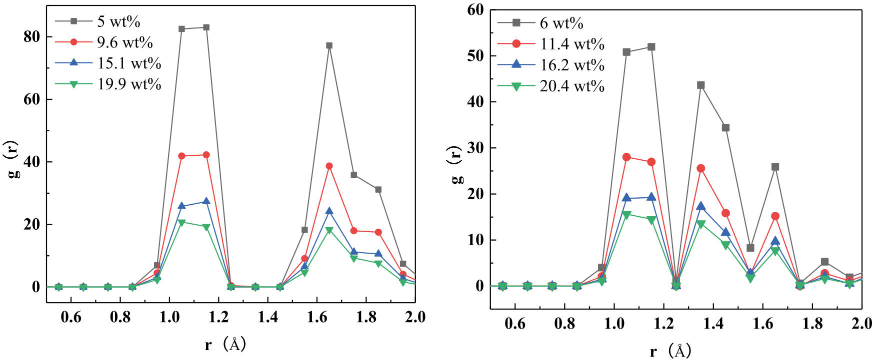

(c) RDF based on nano-phenyl-POSS

(d) Partial enlarged view of (c)

Fig. 34 RDF images of different EP/POSS systems

shown in Fig. 35. The calculation results show that: when the mass fraction of nano-POSS is low (about 0–10 wt%), it is uniformly distributed in the epoxy system. And it connected to the molecular chain segments in the form of chemical bonds. This connection acts as a strong mechanical interlocking effect limiting the movement of molecular chain segments and increasing the rigidity of molecular chain segments. At the same time, the addition of a small amount of nano-POSS has little effect on the build-up of the crosslinked network of the epoxy system. And the intermolecular chain segment forces are not significantly changed. As a result, the glass transition temperature of the epoxy system increases. When the POSS content continues to increase (about more than 10 wt%), it tends to agglomerate in the epoxy system. This leads to an increase in the distance between the epoxy molecular chain segments, the structure becomes loose and it reduce the forces between the molecular chain segments. At the same time, the bonding between nano-POSS and epoxy molecular chain segments is weakened, and the molecular chain segment motility is enhanced.

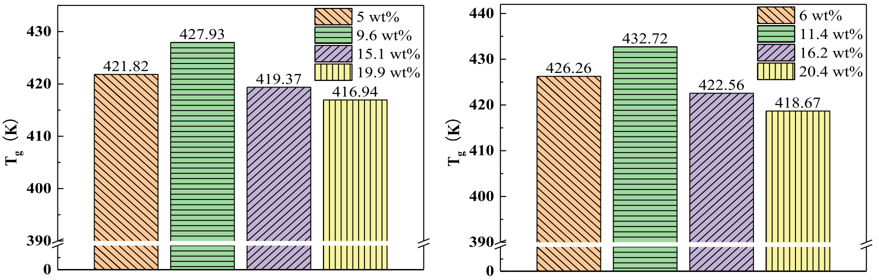

(a) T_g of EP/methyl-POSS system (b) T_g of EP/phenyl-POSS system

Fig. 35 T_g for different EP/POSS systems

In this moment the chain segment flexibility becomes better. As a result, the glass transition temperature of the epoxy system decreases.

(5) CTE analysis

This section calculated the CTE for different EP/POSS systems. Since the rubbery state epoxy composite does not have its mechanical properties as an insulating support, this section only focuses on the CTE of the epoxy material in the glassy state, as shown in Fig. 36. The calculation results show that different contents of POSS fillers have different effects on the thermal expansion characteristics of the epoxy system. As the POSS content of the system increases, the CTE of the epoxy system first decreases and then increases. This is because the CTE of the POSS filler itself is much smaller than that of the epoxy substrate. The introduction of a small amount of filler reduces the contribution of volume expansion by heat to the CTE. And as the mass fraction of filler increases, it hinders the accumulation of epoxy molecular chain segments. The crosslinked network structure becomes loose, which leads to poor thermal expansion characteristics. It can be seen that the selection of appropriate amount of nano-filler POSS can reduce the CTE of epoxy system.

(6) MSD analysis

The mechanical property parameters such as Young's modulus, shear modulus and bulk modulus of EP/POSS composites with different filler contents at room temperature (300 K) were calculated by the static normal strain method. The results are shown in Fig. 37.

From the figure, it can be seen that the mechanical properties of the system containing nanofillers are significantly better than those of the double crosslinked epoxy resin. And the performance enhancement effect is more significant when the nano-POSS content is 10%. Among them, Young's modulus increased by 4.20%, shear modulus increased by 6.02% and bulk modulus increased by 16.83%. On the one hand, the nano-POSS itself has excellent mechanical properties and a large elastic modulus. When it is introduced into the epoxy base material in appropriate amount as filler, it can play a good supporting role in the material, so that it is not

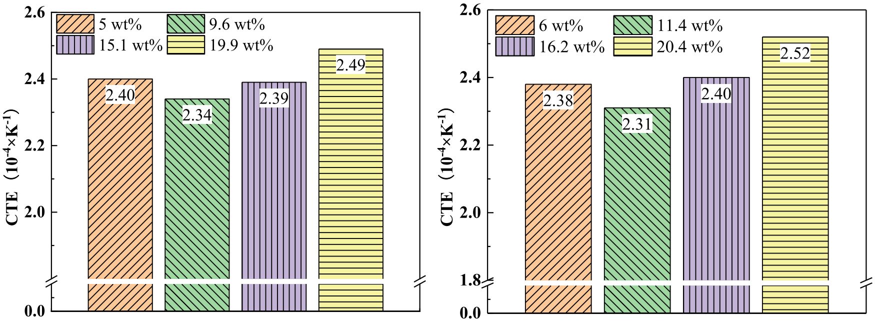

(a) Glassy CTE for EP/methyl-POSS system (b) Glassy CTE for EP/phenyl-POSS system

Fig. 36 Glass state CTE for different EP/POSS systems

easy to deformation due to external force. On the other hand, as the nano-POSS content continues to increase, its own emergence of agglomeration will affect the distance between epoxy molecular chain segments to a certain extent. This agglomeration enhances the motion of the molecular chain segments, which can lead to easy deformation of the material. Therefore, the epoxy system doped with appropriate amount of POSS nanoparticles presented better mechanical properties. Meanwhile, the mechanical properties of the EP/phenyl-POSS system are better than those of the EP/methyl-POSS system, which may be due to the greater rigidity of the R group (phenyl) of the nano phenyl-POSS.

2.2 Study on the Effect of POSS Surface Modification on the Performance of Epoxy Composites

In this section, we select three different functional groups to functionalize the X reactive group of heptaphenyl caged sesquisiloxane. These are phenol-functionalized heptaphenyl caged sesquisiloxane (P-phenyl-POSS), amine-functionalized heptaphenyl caged sesquisiloxane (A-phenyl-POSS) and fluorinated heptaphenyl caged sesquisiloxane (F-phenyl-POSS), respectively, as shown in Fig. 38.

Based on the above composite model construction method, three groups of EP/PPOSS composites with 10% filler mass fraction are constructed as EP/P-phenyl-POSS, EP/A-phenyl-POSS and EP/F-phenyl-POSS.

For the above model, we calculated and analyzed the FFV, MSD and thermomechanical properties respectively.

(1) Free volume characteristics

In order to determine the impacts of different surface modification methods on the free volume of EP/POSS systems, we calculate the FFV of different EP/POSS systems at

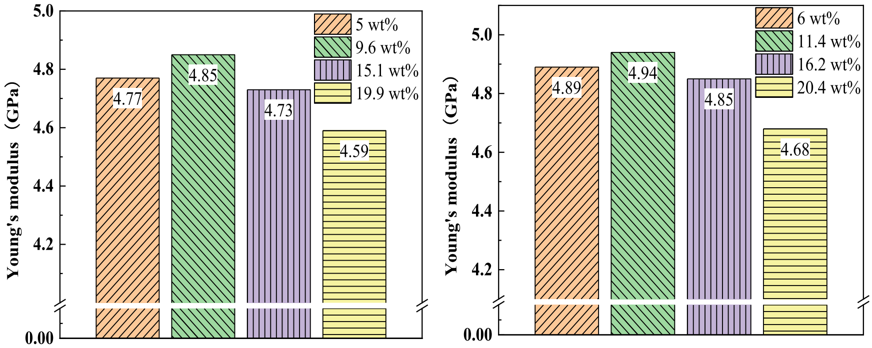

(a) Young’s modulus of EP/methyl-POSS system (b) Young’s modulus of EP/phenyl-POSS system

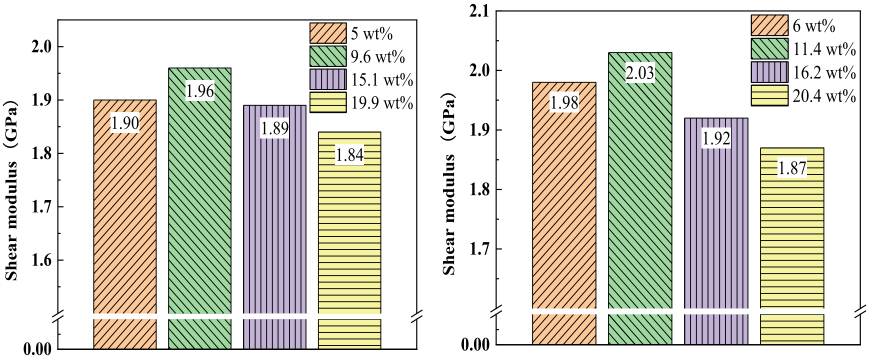

(c) Shear modulus of EP/methyl-POSS system (d) Shear modulus of EP/phenyl-POSS system

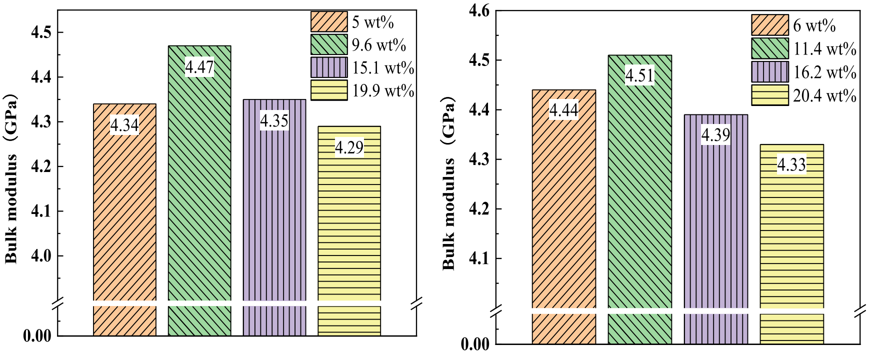

(e) Bulk modulus of EP/methyl-POSS system (f) Bulk modulus of EP/phenyl-POSS system

Fig. 37 Mechanical properties of different EP/POSS systems

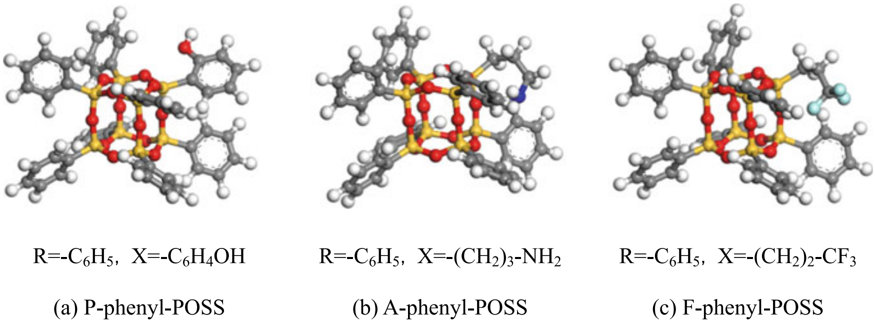

Fig. 38 Molecular model of modified POSS

room temperature (300 K), and the results are depicted in Fig. 39. The three surface modifications have a small effect on the free volume percentage of the epoxy system. Compared to the EP/phenyl-POSS system, the FFV of EP/P-phenyl-POSS system and EP/A-phenyl-POSS is slightly reduced and the FFV of EP/F-phenyl-POSS was slightly enlarged. It can be attributed that the nano P-phenyl-POSS and A-phenyl-POSS connect the epoxy molecular chain segments in a chemically bonded manner, while their compatibility with the epoxy substrate is better, consequently reducing the free volume. In contrast, nano F-phenyl-POSS mainly depends on van der Waals forces to bond with the epoxy substrate, and the interaction forces are weaker, thus increasing the free volume.

(2) Molecular chain segment motility

In order to characterize the effect of various surface modification techniques on the molecular chain segment motion properties of the EP/POSS system, we utilize molecular dynamics simulations to calculate the MSD values of different systems at room temperature (300 K). The results are shown in Fig. 40. It can be seen that the MSD

Fig. 39 FFV for different EP/modified POSS systems

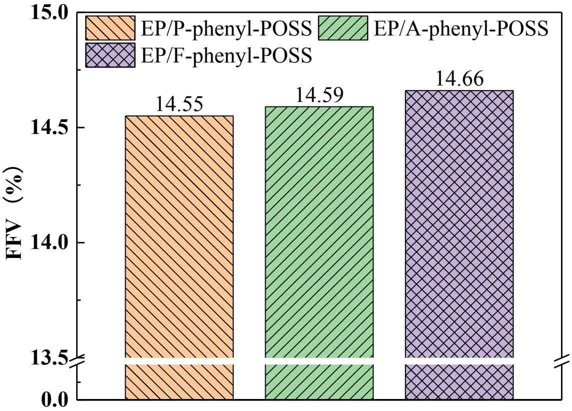

Fig. 40 The MSD for different EP/modified POSS systems

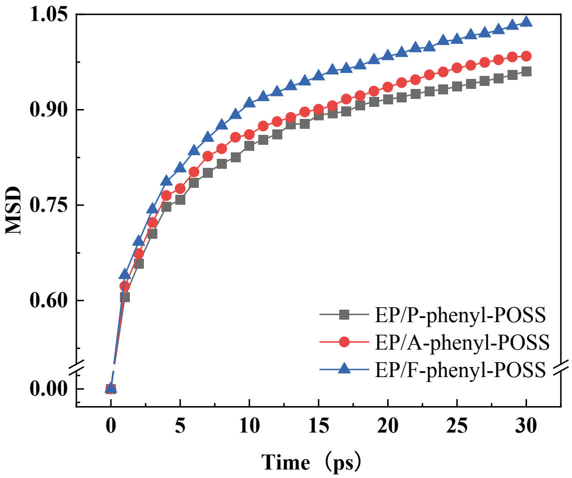

sort of the three surface-modified EP/PPOSS systems are ranked as EP/P-phenyl-POSS < EP/A-phenyl-POSS < EP/F-phenyl-POSS, which indicates that nano-filler surface modification can reduce the MSD of epoxy molecular chain segments and restrict the chain segment movement of the material molecules. Meanwhile, these findings are in accordance with the previous analysis of the free volume. It is once more demonstrated that there is a positive correlation between the molecular chain segment motility and the free volume of the epoxy system.

(3) Glass transition temperature

We can obtain the T_g of the EP/modified POSS system with different surface modification methods via linear fitting of the density-temperature curves during the annealing of the epoxy system. The result is shown in Fig. 41. It can be seen that when the mass fraction of filler is about 9%, the functionalized modification of nano POSS filler surface functional groups can improve the T_g of the composites to a certain extent. Compared with the three different surface modifications, the EP/P-phenyl-POSS system exhibits the greatest modification effect, resulting in a 6.4 K increases in T_g. This is because the nano P-phenyl-POSS reacts with the epoxy molecular chain segment to form a chemical bond connection. The interfacial interaction force is larger, which makes the cross-linked network structure tightly bound and confines the movement of molecular chain segments and thus the T_g of the epoxy system is correspondingly higher. However, the POSS surface modification has limited ability to enhance the T_g of the epoxy system under the doping with appropriate amount of nanofillers.

(4) Coefficient of thermal expansion

In this section, we calculate the glassy CTE of the EP/modified POSS system and the results are shown in Fig. 42. It can be concluded that different surface modifications have different impacts on the thermal expansion properties of the EP/modified

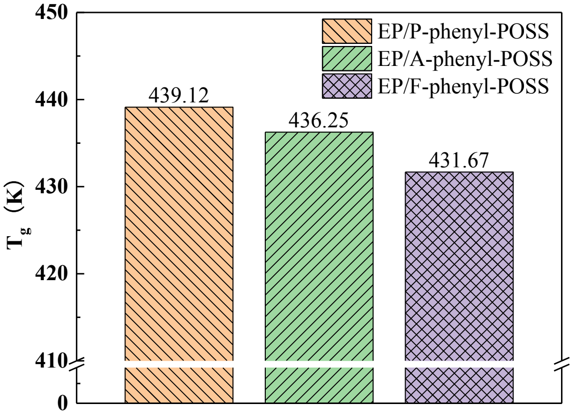

Fig. 41 The T_g for different EP/modified POSS systems

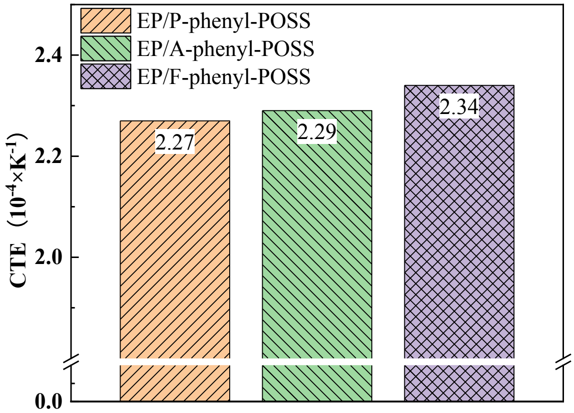

Fig. 42 The CTE for different EP/modified POSS systems

POSS system. In comparison to the EP/phenyl-POSS system, the CTE of EP/P-phenyl-POSS system and EP/A-phenyl-POSS is slightly reduced and the CTE of EP/F-phenyl-POSS is slightly enlarged. This could be attributed to the small thermal expansion coefficient of nano phenyl-POSS itself and the strong interaction between P-phenyl-POSS, A-phenyl-POSS and epoxy molecular chain segments.

(5) Static mechanical properties

In this section, we calculate the Young's modulus, shear modulus and bulk modulus of different EP/modified POSS systems at 300 K to characterize the mechanical properties of the composites, and the results are as follow in Fig. 43. Compared with the unmodified composite system, the mechanical properties of EP/P-phenyl-POSS system and EP/A-phenyl-POSS show somewhat enhancement, while the mechanical properties of EP/F-phenyl-POSS system are not significantly improved. This is due to there are strong interaction between nano P-phenyl-POSS and A-phenyl-POSS and epoxy substrate at high cross-linking degree. Furthermore, the EP/P-phenyl-POSS system exhibits a greater force, while the van der Waals interaction between the nano-F-phenyl-POSS and the epoxy matrix is weaker. Consequently, the system does not exhibit a remarkable resistance to deformation, and no significant improved in mechanical properties.

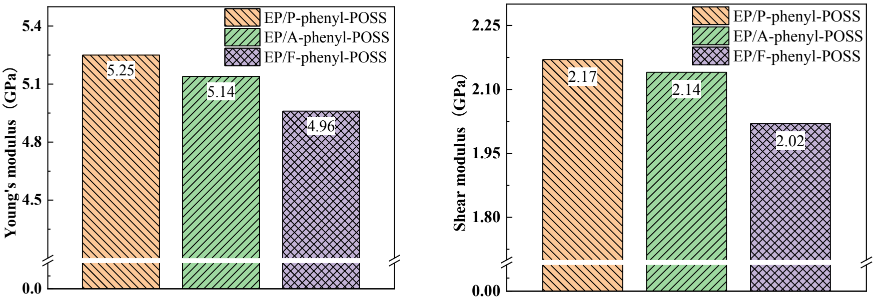

(a) Young’s modulus (b) Shear modulus

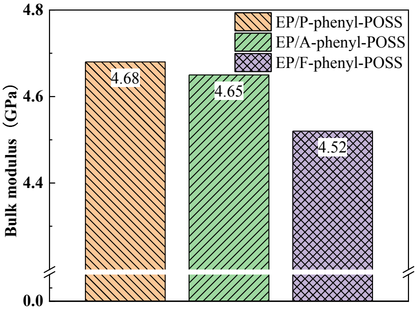

(c) Bulk modulus

Fig. 43 Mechanical properties of different EP/modified POSS systems

3 Model Construction and Performance Study of Graphene/Epoxy Composites

3.1 Research on the Effect of Graphene Doping on the Structure and Performance of Fluorine Resin Composites

The rapid growth of ultra-high voltage technology is driving the demand for higher performance of high-voltage epoxy insulation material for electrical equipment. The physicochemical properties of graphene are excellent and its derivatives can effectively be used as fillers to prepare better performance composites. This chapter takes BPAF/DGEBA fluorine resin as the fluorine epoxy matrix, and respectively chooses graphene (GR), graphene oxide (GO), and fluorinated graphene oxide (GF) as the fillers of the composites to construct models of various graphene/epoxy cross-linked network. Through molecular dynamics (MD) simulation, this research explores the influence law of modification method and doping amount of the graphene on microstructure and macro-performance of the fluorine epoxy resin.

Graphene is a two-dimensional carbon nanomaterial consisting of carbon atoms connected by sp2 hybrid orbitals, and it is a common inorganic filler in epoxy resin composites. There are 3 steps to construct the models of graphene with different modification methods.

(1) Import the crystal structure of graphene. Import the unit cell structure of graphite from the crystal base of Materials Studio, the coordination number of carbon atoms in the graphene model is 3 and the included angle of the carbon–carbon bond is 120°, as shown in Fig. 44.

(2) Construct the monomer model of graphene. After selecting the unit cell, we use the "Symmetry" of the Build module in the MS software and select Supercell in the menu bar to further construct a single-layer graphene supercell. This

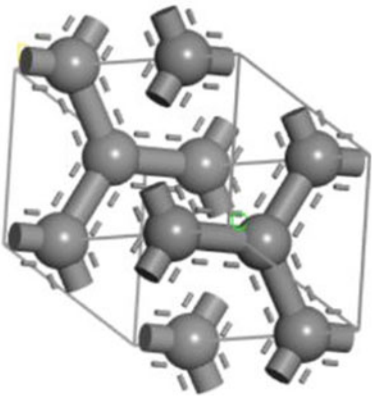

Fig. 44 Molecular model of graphite unit cell

method conducts geometry optimization of graphene monomer molecule and optimize the molecular configuration of it to the lowest energy configuration. The monomer molecular model of graphene constructed is shown in Fig. 46a.

(3) Construct the monomer model of modified graphene. Based on the "Lerf-Klinowski" theory, we construct the monomer molecular model of GO, and the simplest molecular formula of GO is $C_{10}O_1(OH)_1(COOH)_{0.5}$. The epoxy group and carboxyl group of GO model are randomly attached to the surface, while the carboxyl group is distributed at the edge of graphene oxide sheets. In this paper, we construct a GO sheet containing 82 carbon atoms and 22 oxygen atoms in order to represent the graphene oxide layer, and add hydrogen atoms to prevent the generation of unsaturated edge. The model of GO is shown in Fig. 45b. We further create fluorination modification of graphene oxide, and fluorine atoms are added to the edge of the graphene oxide according to a certain proportion of the total number of atoms to construct the model of modified graphene filler with a fluorinated surface. The model of GF is shown in Fig. 45c, and Fig. 45d–f shows different functional groups on the modified graphene surface.

The model of the GO/EP cross-linked network based on the method of constructing a composites model is shown in Fig. 46. Table 5 shows the compositions of each model. The subsequent articles calculate and analyze the interface binding energy, FFV, MSD, and thermomechanical properties of each model.

(1) The interface binding energy

Table 6 shows the binding energy of four different composites. The results indicate that the filler of the GF/F-EP system has maximum binding energy with the epoxy

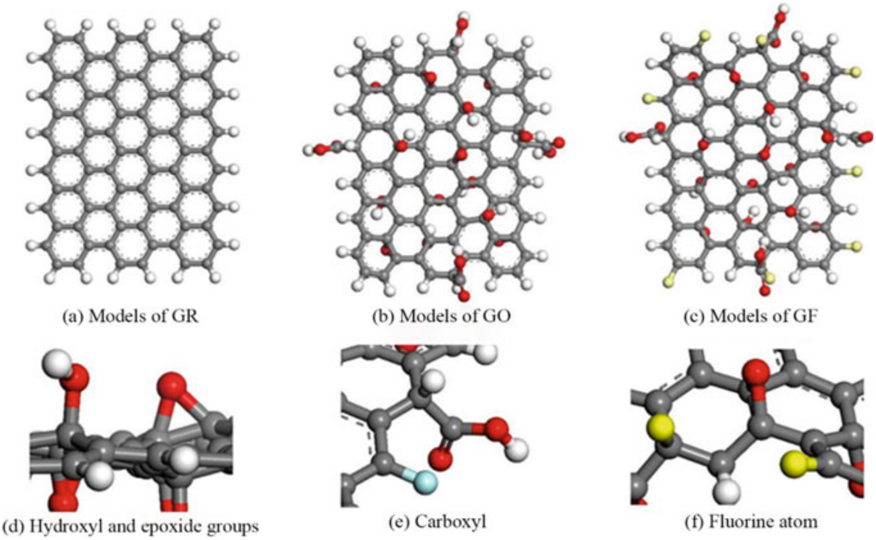
(a) Models of GR (b) Models of GO (c) Models of GF

(d) Hydroxyl and epoxide groups (e) Carboxyl (f) Fluorine atom

Fig. 45 Models of different modified graphene monomer molecules

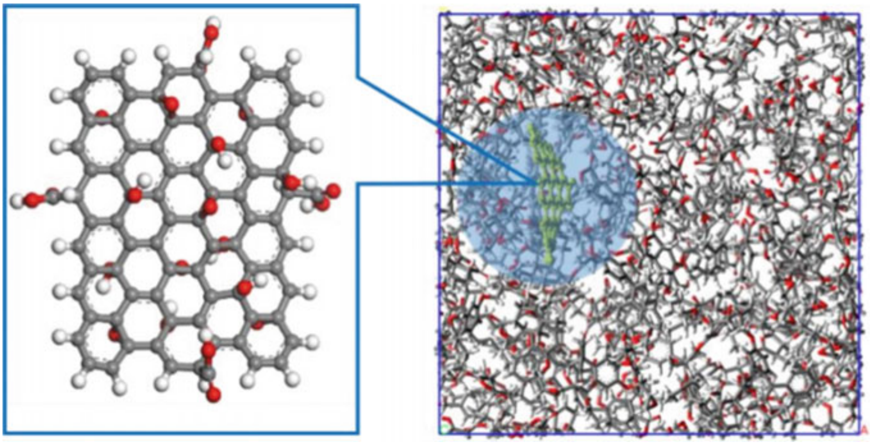

Fig. 46 Model of GO/EP cross-linked network

Table 5 Compositions of GO/EP epoxy nanocomposite system

Systems	Mass fraction of filler (wt%)	Number of molecules (number of articles)			
		Fillers	DGEBA	MTHPA	BPAF
GR/EP	2.8	1	50	100	0
GO/EP	3.9	1	50	100	0
GO/F-EP	3.2	1	50	100	25
GF/F-EP	3.5	1	50	100	25
GF/F-EP	6.7	2	50	100	25
GF/F-EP	9.8	3	50	100	25
GF/F-EP	12.6	4	50	100	25

matrix, while that of the GR/EP system is comparatively low, among the four epoxy composites systems. Our analysis demonstrates that modified graphene possesses various functional groups, such as the carboxyl group and hydroxyl group, which can react with the epoxy group to generate strong bonding effects, thus reinforce the combination between filler and epoxy matrix and improve the binding energy of nanofiller and epoxy matrix significantly. It also explicates that the surface modification of filler improves the interfacial compatibility between filler and base material and thus improve the interaction energy between the two.

(2) The FFV and MSD

Figure 47 shows the calculation results of FFV and MSD. The results indicate that nanofiller can notably reduce the free volume of the epoxy composite system and limit the motion ability of molecular chain segments effectively simultaneously. And a positive correlation appears between the FFV and MSD of the epoxy system.

Table 6 Binding energy of different epoxy composites

System	E_{resin}	E_{fiber}	E_{total}	$E_{interface}$
GR/EP	−1962	−2795	−3876	881
GO/EP	−1962	−769	−1467	1263
Cube	−4761	−769	−4157	1373
GF/F-EP	−4761	−805	−3766	1799

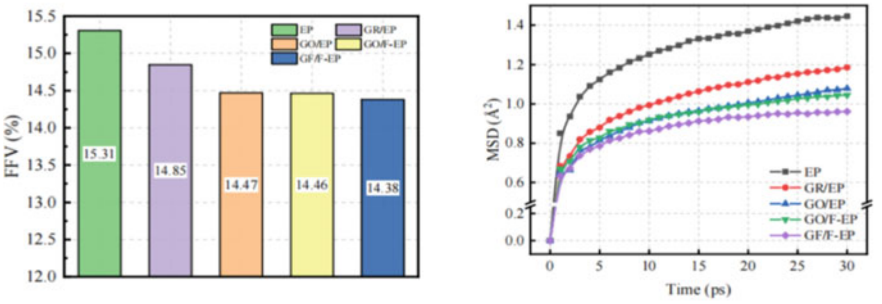

（a） FFV （b） MSD

Fig. 47 The FFV and MSD of different composites systems

Compared with the microscopic parameter of the cross-linked network of different systems, we can find that both FFV and MSD of GF/F-EP Epoxy composites system are the best.

The introduction of modified graphene will cause alterations in the free volume of the materials. On the one hand, the oxidation functional groups on the surface of the modified graphene can participate in the cross-linking and curing reaction with the epoxy system. They will generate bonding interaction with the epoxy group and create an inorganic–organic interface layer between the nanofiller and the epoxy molecules and then give rise to a strong mechanical interlocked effect and limit the movement of molecular chain segments, thus reducing the FFV of composites. On the other hand, part of the space volume of the epoxy system is occupied by the nanofiller, leading to an increase in the distance between molecular chain segments and impeding the stacking of molecular chain segments. This consequently promotes the free volume. Consequently, the leading factors of the above two elements determine the changing trend of the free volume of the epoxy system. Fluorinated graphene oxide has more functional groups when the mass fraction of filler is the same and has more sites for reacting with epoxy matrix. Moreover, higher levels of fluorine will generate hydrogen bonding, which enhances the intermolecular force in the system and effectively constrains the movement of molecular chain segments. GF at a low

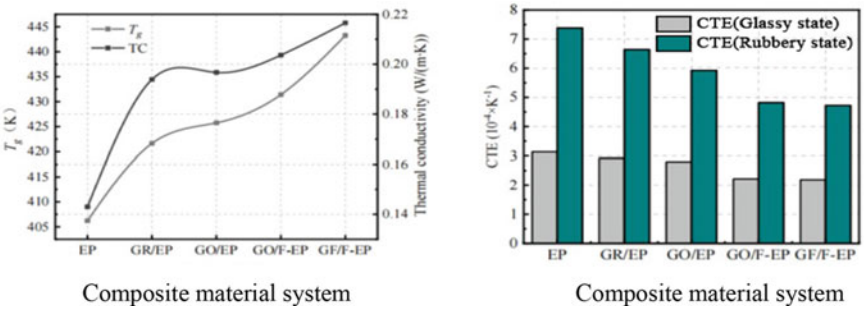

Fig. 48 The thermal properties of different composites systems

mass fraction can also fill the free volume of the cross-linked network better, thus reducing the FFV and MSD of composites.

(3) Analysis of the thermal properties

This section calculates the T_g, CTE, and thermal conductivity of different epoxy composites. And the results of the calculation are shown in Fig. 48.

The results demonstrate that the GF/F-EP system has the most ideal comprehensive thermal properties. Its T_g is 443 K, the thermal conductivity is 0.217 W/(m K), and its coefficient of thermal expansion is also improved considerably. For the glass transition temperature and coefficient of thermal expansion of the composites after doping modified graphene, both thermal properties of the composites are enhanced remarkably, compared with the DGEBA/MTHPA epoxy system. This suggests that doping modified graphene can boost the heat resistance of epoxy system.

The analysis concludes that graphene and modified graphene have better heat resistance than epoxy molecules, so the heat resistance of composites after doping modified graphene is noticeable increased. Following modification of graphene, a variety of functional groups on the surface of the modified graphene filler can react with the epoxy matrix, making a better dispersion and interfacial compatibility of GF in the epoxy resin. Combined with the calculation of FFV and MSD, we can find that a relatively dense cross-linked network and low molecular chain segments motion ability can promote the heat resistance of system effectively. Therefore, the T_g of the GF/F-EP fluorine resin system is relatively high and its thermal expansion performance is better.

It can be found that the epoxy composites doped with GF exhibit the highest thermal conductivity, compared with other different systems. It is likely that doping graphene or modified graphene can enhance the performance of the epoxy system effectively due to its impressive characteristics, such as ultrahigh carrier mobility of 15,000 $cm^2/(V\ s)$, excellent thermal conductivity of 5300 W/(m K) and large specific surface area. While the free volume ratio of the fluorinated modified graphene oxide/fluorine resin system is relatively small, and the cross-linked network is denser. The composites have better micro continuity because of the effective filling of the free volume and it is more conducive to increasing the efficiency of the heat conduction channels. Meanwhile, the smaller MSD parameter indicates that the interaction of the modified graphene with the epoxy matrix can considerably increase the binding forces on the atoms in the system, thus reducing the movement ability of the molecular chains and weakening the atomic vibration. Both the mean free path of the molecule and the thermal conductivity of the system are enhanced.

(4) Analysis of the mechanical properties

This section calculates the Young's modulus, shear modulus, and bulk modulus of different modified graphene doped composites at 300 K, and the results are shown in Fig. 49.

As illustrated in Fig. 49 that the mechanical properties of the modified graphene doped system are far more superior compared to that of the undoped epoxy resin system, and the mechanical properties improvement of the GF doped fluorine resin

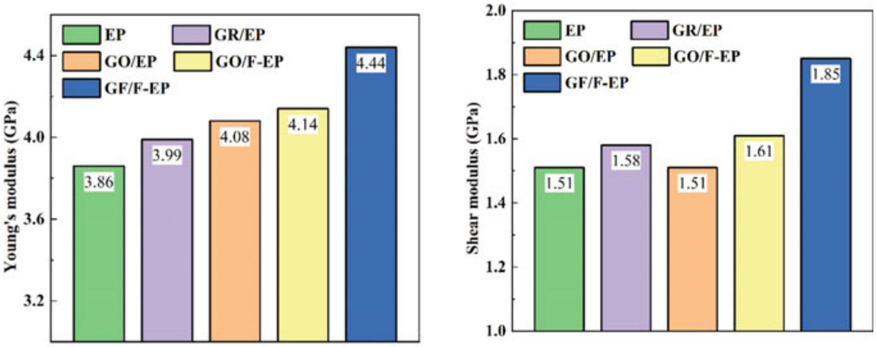

(a) Young's modulus (b) Shear modulus

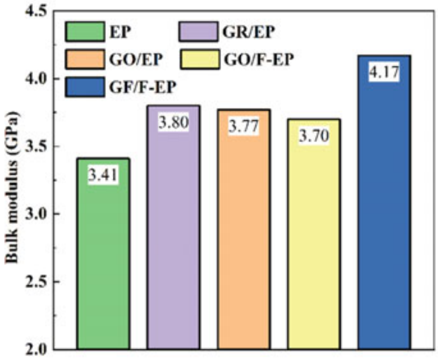

(c) Bulk modulus

Fig. 49 The elastic modulus of different composites systems is more significant. The GF/F-EP system has a 15.03%, 22.52% and 22.29% increase in Young's modulus, shear modulus and bulk modulus respectively, compared with the DGEBA/MTHPA system.

The analysis concluded that the modified graphene itself has excellent mechanical properties and a large elastic modulus. After introducing into the epoxy base material as a reinforcing filler, the modified graphene can support the material and fill the free volume space of the system. Therefore, it can form a dense cross-linked network and make the composites difficult to deform due to external force. Nevertheless, the molecules of GF have functional groups which can provide reaction sites. The interaction forces (encompassing Van der Waals force and hydrogen bonding) between modified graphene and the molecular chains of the epoxy matrix have been upgraded substantially by bonding the modified graphene and the epoxy group. And this also makes the combination between the epoxy matrix and the graphene closer. When the system has been exposed to external forces, this type of strong intermolecular force can meaningfully transfer the stress to the modified graphene filler, and further improve the mechanical properties of the composites. For this reason, doping modified graphene can enhance the mechanical properties of epoxy composites well.

3.2 Research on the Effect of Orderly Filling of Modified Graphene on the Structure and Performance of Fluorine Resin Composites

Because of the special molecular configuration, it is easy to generate a strong intermolecular interaction force between the different layers of graphene, which eventually leads to agglomeration in the composites and severely limits the application of graphene in high-voltage epoxy composites. This chapter chooses fluorinated graphene oxide/fluorine resin composites as the object. And we guide the ordered distribution of the internal structure of the epoxy composites by regulating the distribution state and dispersity of GF in the epoxy composites. Based on the BPAF/DGEBA fluorine epoxy base material, we add the GF filler with a mass fraction of 9wt% and then construct four epoxy composites models with fluorinating graphene oxide sheets spacing are 3 Å, 6 Å, 9 Å and 12 Å respectively and orderly filling by four fillers. And the influence law of the distribution state of modified graphene on the microstructure and thermal properties of the epoxy composites is studied.

In this section, we construct four models of the ordered GF molecules with sheets spacing of 3 Å, 6 Å, 9 Å, 12 Å and one disorderly distributed GF model respectively based on the "Construction" function of the "Amorphous Cell Calculation" module in the MS. And we fix the position coordinates of the GF molecules in the model. The fillers models are shown in Fig. 50.

The molecular models of the orderly distributed GF/F-EP composites are also constructed in this section, using the DGEBA/MTHPA as epoxy base materials. The mass fraction of the BPAF is 20 wt% and the mass fraction of the modified graphene

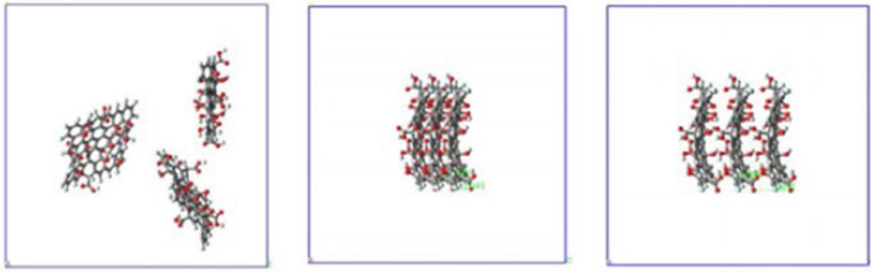

(a) Disorderly distributed (b) 3Å (c) 6Å

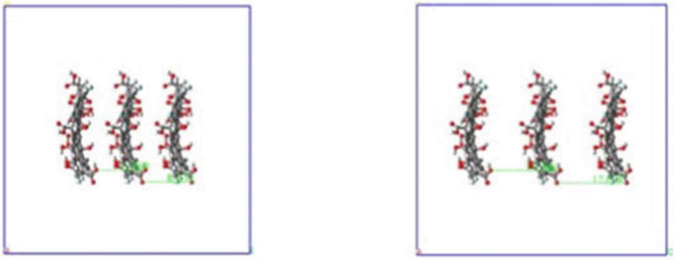

(d) 9Å (e) 12Å

Fig. 50 The models of GF molecules with different distribution state

is about 9 wt%. The specific components of each system are shown in Table 7, and the composite material model is shown in Fig. 51.

An analysis of density distribution, FFV, MSD, and thermomechanical properties of the composites model have been conducted in subsequent articles.

(1) Density distribution

In this section, we studied the effects of the distribution state of graphene on the distribution of matrix molecules in the composites by calculating the relative concentration distribution curves of the modified graphene/epoxy composites models in the z direction (the direction perpendicular to the surface of graphene). By observing the

Table 7 The compositions of the EP/modified GF orderly filled systems

System	Sheets spacing of GF (Å)	Number of molecular (strip)			
		GF	DCEBA	MTHPA	BPAF
0-GF/F-EP	Random	3	50	100	25
3-GF/F-EP	3	3	50	100	25
6-GF/F-EP	6	3	50	100	25
9-GF/F-EP	9	3	50	100	25
12-GF/F-EP	12	3	50	100	25

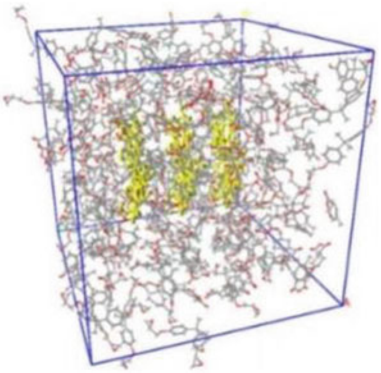

Fig. 51 The model of orderly filled GF/F-EP cross-linked network

density change of the composites, we can investigate the effect of the ordered distribution of modified graphene on the configuration of epoxy molecules. The epoxy matrix along the z-axis is divided into several small areas to calculate the density distribution. The results are shown in Fig. 52. Figure 52a shows the concentration distribution of the system of the GF disorderly distributed epoxy composites. It can be seen from the figure that the density distribution is uneven and has large fluctuations for the modified graphene disorderly filled epoxy composites.

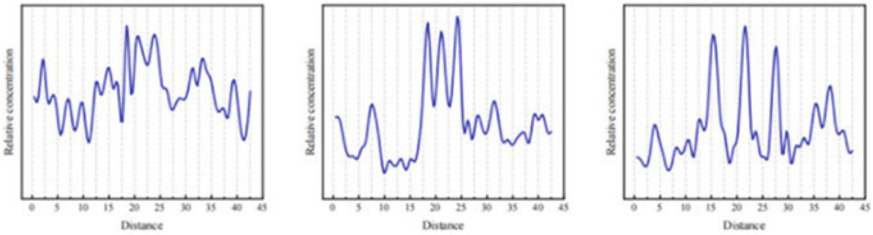

(a) Disorderly distributed (b) 3Å (c) 6Å

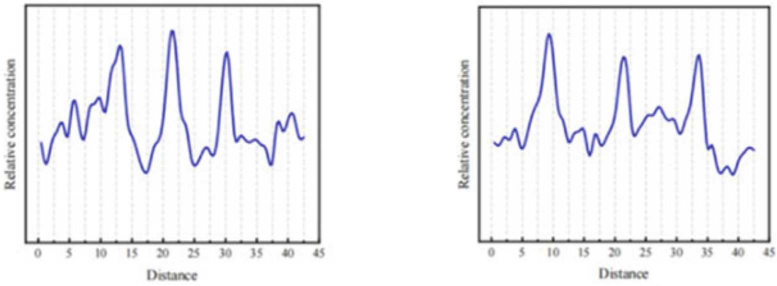

(d) 9Å (e) 12Å

Fig. 52 The density distribution of composites with different GF distribution

Figure 52b–e shows the concentration distribution of the GF ordered distributed epoxy composites system, indicating that the concentration distribution curves of the GF/epoxy composites systems with different sheet spacing all appear with three peak values, and the peak positions are the z-direction coordinates corresponding to the three graphene insert layers in the system. The density of the system near the GF/epoxy interface is relatively high, and the density value sharply decreases along both sides of the interface, which illustrates that the ordered distribution of the fillers exerts a marked impact on the internal structural distribution of the composites system. The analysis suggested that after orderly filling the modified graphene, the graphene intercalated will cause a considerable amount of epoxy resin to accumulate on both sides of the sheets, leading to the adsorption zone in the composites. The epoxy matrix near the filler-epoxy matrix interface presents the distribution of "adsorption type". This also reveals that the layers spacing control proposed in this paper can acquire the epoxy composites with ordered structure. The formation of the adsorption interface layer is attributed to the strong interaction between the modified graphene and the epoxy resin where near the GF surface, which causes the graphene surface to adsorb more epoxy resin polymers, and consequently presents a peak in the density distribution curve at this location. Furthermore, the bonding interaction generated among the active groups such as carboxyl and hydroxyl groups will further enhance the interaction between the filler and the epoxy matrix, resulting in a remarkable surge in the adsorption capacity of the modified graphene to the epoxy resin, and a directional stacking of specific chain segments. These can more efficiently guide the ordered distribution of the GF/epoxy composite structure.

Following further comparison of the density distribution in the z-direction of the four GF/epoxy composites models with varying layer spacings, we can notice that the peak value of the composites adsorption layer gradually decreases with the increase of the layer spacing, and the decreasing in the density curve on both sides of the adsorption layer tends to be smooth. And the curve values become more uniform. The analysis concluded that with the increase of the distance between the GF sheets, the adsorption strength of the modified graphene on the matrix molecules diminishes steadily, and the interaction between the sheets is also weakened, thereby resulting in a decrease in the peak value of the adsorption layer gradually. Whereas the multilayer modified graphene enables the matrix molecules in the system to form multiple adsorption layers. When the GF layer spacing is too small, the graphene piles up and the dispersion is poor. Only the matrix molecules surrounding the graphene are able to occur "absorption", while the epoxy matrix molecules over a farther range from the graphene surface are largely unaffected by the adsorption of the graphene. Currently, the internal structural distribution of the composites is not uniform enough. As the dispersion of the graphene increases, the contact surface between the GF and the epoxy matrix broadens further, thus extending the area within the composites that are affected by adsorption. When the graphene in the composites is completely dispersed, the "adsorption" area within the composite is the maximized, and at this moment the orderly filling of the modified graphene has the pronounced effect on the structural distribution of the epoxy composites. However, excessive layer spacing will weaken the interaction forces between the modified graphene sheets, but diminish the adsorption of the GF in the matrix material.

To conclude, the orderly filling of the modified graphene will lead to the matrix molecules forming "adsorption" on both sides of the graphene, thus resulting in a more uniform distribution of the structure of the matrix material. An appropriate layer spacing will maximize the influence of ordered fillers on the adsorption force and adsorption range of the epoxy system. Therefore, it can be inferred that the orderly filling of the fillers can well guide the structural distribution of the epoxy system and can significantly contribute to the controllable interface of the base material.

(1) Analysis of the FFV

In this section, we calculate the free volume proportion of the GF/F-EP system with different layer spacing, and the results are shown in Fig. 53. As the layer spacing of the GF filler increases, the FFV of the composites system tends to decline before rising. Compared to the GF/F-EP system with randomly distributed fillers, the FFV of the composites is substantially reduced when the layer spacing of the modified graphene sheets is in the range of 3–9 Å. When the layer spacing is further increased, the FFV of the system increases slightly.

The analysis revealed that the randomly distributed modified graphene is not homogeneously distributed throughout the system and shows a tendency to form agglomeration. Due to the strong interaction forces, the adsorption occurs between the modified graphene sheets, which causes agglomeration, increases the free volume of the system and has a larger FFV. While the modified graphene with appropriate layer spacing will fill the epoxy system uniformly and introduce an inorganic–organic interface layer, with adsorption occurring on both sides of the GF sheets. In the interface layer, the filler and base material are mainly combined through Van der Waals interaction. The regularly distributed modified graphene layer will effectively direct the organized disposition of epoxy molecules and supplement the free volume better, thus reducing the proportion of the free volume of the system. When the layer spacing is excessively wide, the molecular distribution inside the model of

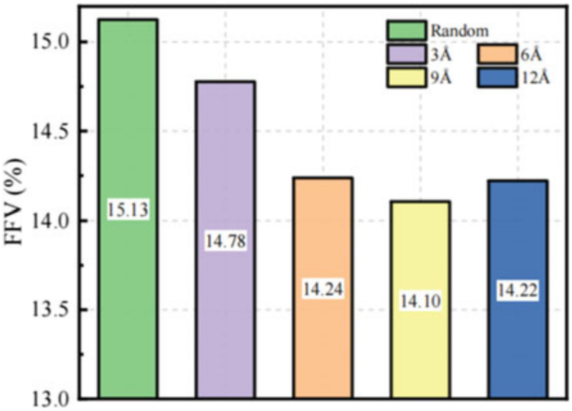

Fig. 53 The FFV of the composites with different GF distribution state

the modified graphene filled composites is too loose and the intermolecular force is relatively weak. More holes are generated, thus increasing the FFV.

(2) Analysis of the MSD

We calculate the MSD of the GF/F-EP systems with different filler distribution states at 300 K and the results are shown in Fig. 54. The MSD size of the fluorine epoxy composite systems with different GF distribution states is 9 Å < 6 Å < 12 Å < 3 Å < Random. This result appears in line with the calculation results of the FFV of the systems.

The analysis suggested that the adsorption layer can be formed in the system via the interaction force after orderly filling by the modified graphene. The oxygen-containing functional groups modified on the GF layer can bond with the epoxy matrix and further direct the distribution of the matrix chain segments, thus limiting the movement ability of the molecular chain segments usefully. A reasonable regulation of layer spacing can limit the segment motion of the material molecules effectively and reduce the MSD of the epoxy molecular chain segments.

(3) Analysis of the thermal properties

The influence law of the distribution state of the modified graphene on the T_g, CTE and thermal conductivity of the orderly filled GF/F-EP composites is shown in Fig. 55.

Comparing the T_g and CTE of the GF/F-EP systems with different filler distribution states, we can find that when the layer spacing of the GF is below 6 Å and above 9 Å, the orderly filling of the GF will lead to a certain degradation of the thermal properties of the GF/F-EP composites system. When regulating the layer spacing of the GF in the range of 6–9 Å, the orderly filling of the GF will increase the glass transition temperature of the fluorine epoxy composites significantly and decrease the CTE of the system.

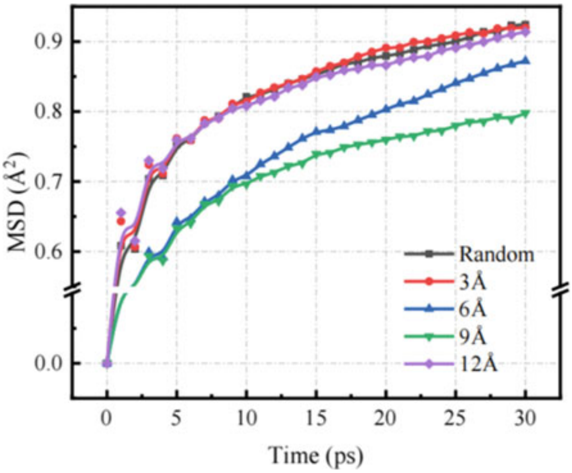

Fig. 54 The MSD of the composites with different GF distribution state

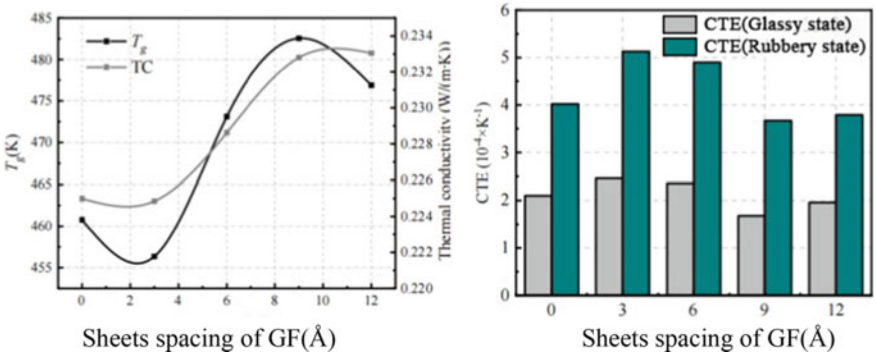

Fig. 55 The thermal properties of the composites with different GF distribution state

Analysis results suggested that when the layer spacing is too close, the modified graphene is not uniformly dispersed in the epoxy composites, thus occurring agglomeration and accumulation. However, excessive layer spacing will weaken the interaction forces between the graphene and between the graphene and matrix. In both cases, the advantages of structure regulation cannot be fully realized, resulting in the reduction of thermal properties.

A comparison of the Thermal Conductivity (TC) data of the composites system with different GF distribution states shows that the orderly filled modified graphene can significantly promote the thermal conductivity of the fluorine epoxy system. When the GF layer spacing is set to 9 Å, the TC of the system is increased by 3.47% in comparison to that of the disorderly distributed composites. The analysis shows that the graphene itself has typical anisotropic thermal conductivity. For the filler with anisotropic thermal conductivity, the common blending method only leads to a random distribution of the thermal conductive fillers within the matrix, making it difficult to take full use of their advantage of high thermal conductivity, and subsequently resulting in relatively low thermal conductivity values of the composites. After orderly filling the modified graphene, the uniformly dispersed oriented graphene sheet builds a bridging role for the BPAF/DGEBA composites on both sides of the sheets. This will make a significant reduction of the interface thermal resistance during heat conduction, forming an effective thermal conductive network. At the same time, the interconnected network structure between the graphene and matrix will be generated relying on strong interaction forces and thus generates a uniformly distributed adsorption layer. As the temperature rises, the heat flow is dispersed more rapidly along the uniform “adsorption” network structure, thus significantly improving the thermal conductivity of the epoxy composites. Nevertheless, if the layer spacing of the modified graphene is too close, the adsorption layer will be concentrated in the middle of the matrix and cannot form a uniformly dispersed heat conduction channel. While if the layer spacing is too large, the bridging effect will be invalidated, the interaction force in the system will be weakened, the structure of

Fig. 56 The mechanical properties of the composites with different GF distribution state

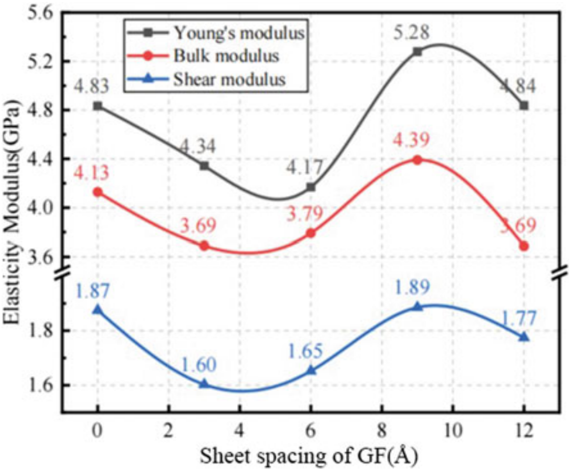

the system will not be dense enough, and the thermal conductivity of the system will be remarkably weakened.

In conclusion, after reasonably controlling the layer spacing of the modified graphene, the orderly filling of the nanofillers can effectively promote the homogeneity of the epoxy composites structure, and substantially improve the thermal properties of the GF/F-EP composites.

(4) Analysis of the mechanical properties

The Young's modulus, shear modulus and bulk modulus of the GF/F-EP system are shown in Fig. 56. In comparison to the GF randomly distributed composites system, there is a significant enhancement of the mechanical properties in the GF/F-EP system with a layer spacing of 6–9 Å.

The analysis concluded that when the layer spacing is small, the distribution of the composite structures is uneven, and the characteristics of the high elasticity modulus of the modified graphene cannot be fully utilized. When the layer spacing is too large, the Van der Waals interaction force between the GF and epoxy matrix is weak, resulting in the weak resistance to deformation of the system and the decline of its mechanical properties. After regulating to a suitable layer spacing, the modified graphene can fully contact with the matrix material and form a uniformly dispersed adsorption layer. The external stresses imposed on the matrix material can be effectively buffered in the adsorption layer and transferred to the modified graphene sheets with excellent mechanical properties. The interaction force between the GF filler and the epoxy matrix also restricts the movement of the molecular chains within the system, resulting in a denser cross-linked network. The functional groups adhered to the modified graphene surface allow the epoxy molecular chains to be well anchored to the reinforcing filler, which also disperses the stress on the epoxy matrix. Therefore, the orderly distributed GF/epoxy structure will improve the mechanical properties of the composites.

References

1. Tang, C., Zhang, S., Li, X., et al.: Molecular dynamics simulations of the effect of shape and size of SiO_2 nanoparticle dopants on insulation paper cellulose. AIP Adv. **6**(12), 125106 (2016)
2. Li, F., Lu, Z., Yang, Z., et al.: Surface interaction energy simulation of ceramic materials with epoxy resin. Polimery **60**(07/08), 468–471 (2015)
3. Xiaoxing, Z., Xiaoyu, C., Song, X., et al.: Molecular dynamics simulation of thermal-mechanical properties of modified SiO_2 reinforced epoxy resin. High Volt. Eng. **44**(3), 740–749 (2018)
4. Wei, Q., Zhang, Y., Wang, Y., et al.: A molecular dynamic simulation method to elucidate the interaction mechanism of nano-SiO_2 in polymer blends. J. Mater. Sci. **52**(21), 12889–12901 (2017)
5. Marzocca, A.J., Somoza, A., Goyanes, S.N., et al.: Characterization of free volume in particulate-filled epoxy resin by means of dynamic mechanical analysis and positron annihilation lifetime spectroscopy. Polym. Int. **51**(11), 1277–1284 (2002)
6. Yaping, Z., Rongchang, N.: The study on structure characters and properties of PHMS/VAC/NMA composite emulsion. Polym. Mater. Sci. Eng. **05**, 148–150 (2002)
7. Liu, L., Xie, Q., Liang, S., et al.: Molecular dynamics simulation of the influence of molecular number on the properties of cross-linked epoxy resin system. High Volt. Appar. **54**(05), 80–86 (2018)
8. Nikje, M.M.A., Garmarudi, A.B., Tehrani, Z.M., et al.: Thermal and mechanical evaluation of epoxy resin composites by synthesis of amine-based coupling agent-nano silica complex. Polym.-Plast. Technol. Eng. **50**(6), 646–650 (2011)
9. Xueqing, L., Jiyan, L., Huyi, Z., et al.: Study of mechanical properties of rice husk silica/epoxy resin nanocomposites. China Plast. Ind. **11**, 18–20 (2009)
10. Wu, Z., Wang, M., Wang, Z.: The gas phase SiO_2/epoxy nanocomposites with enhanced mechanical and thermal properties. High Perform. Polym. **27**(4), 469–475 (2014)
11. Johnsen, B.B., Kinloch, A.J., Mohammed, R.D., et al.: Toughening mechanisms of nanoparticle-modified epoxy polymers. Polymer **48**(2), 530–541 (2007)
12. Kashfipour, M.A., Mehra, N., Zhu, J.: A review on the role of interface in mechanical, thermal, and electrical properties of polymer composites. Adv. Compos. Hybrid Mater. **1**(3), 415–439 (2018)
13. Li, H., Wang, C., Li, L., et al.: Effects of silane coupling agent treatment on properties of SiO_2/epoxy nanocomposites. Insul. Mater. (02), 1–8 (2017)
14. Xu, M., Cao, X., Yu, B.: Study on properties of nano-SiO_2/epoxy resin composite—electrical and mechanical properties. Polym. Mater. Sci. Eng. (01), 153–155 (2005)
15. Gao, Z., Jiang, X., Guo, K.: Study of the hydrolysis of 3-aminopropyltriethoxysilane (KH550) and the surface modification of silica. J. Beijing Univ. Chem. Technol. (Nat. Sci.) (02), 7–12 (2012)
16. Han, Z., Zou, L., Xin, Z., et al.: Molecular dynamics simulation of vital physical properties of epoxy/carbon nanotube composite coatings on DC GIL insulators. Trans. China Electrotech. Soc. (20), 4692–4703 (2018)
17. Xie, Q., Liang, S., Liu, B., et al.: Structure, microparameters and properties of crosslinked DGEBA/MTHPA: a molecular dynamics simulation. AIP Adv. **8**(7), 75332 (2018)
18. Yang, Q., Chen, X., Lan, F., et al.: Molecular dynamics study of the interfacial properties of polyethylene and ethylene-vinyl acetate copolymer composites. High Volt. Eng. (11), 3626–3633 (2016)
19. Li, J., Wang, B.: Study on the surface modification process of quartz sand with silane coupling agent KH570. Non-Metall. Mines (02), 26–29 (2013)
20. Zhao, Y., Qi, X., Ma, J., et al.: Interface of polyimide-silica grafted with different silane coupling agents: molecular dynamic simulation. J. Appl. Polym. Sci. **135**(4), 45725 (2018)
21. Liu, W., Wang, J., Miao, R., et al.: Molecular dynamics simulations of the cross-linked epoxy resin TGDDM/DDS. Polym. Mater. Sci. Eng. **32**(5), 109–114 (2016)

Modulation of Surface Properties of Epoxy Resin by Plasma Modification

Jiyuan Yan, Qing Xie, Yanze Song, and Yixiao Zhang

1 Introduction

The formation and development of surface flashover of insulating materials has the interwovenness connection with the surface conductivity and surface charge movement characteristics. And these electrical parameters are associated with the surface morphology and chemical composition of the insulating materials [1]. If a method can be found to selectively modulate the physicochemical and electrical properties of insulating materials, it is expected to further enhance the surface flashover performance of insulating materials and help reveal the enhancement mechanism. Studies have shown that plasma modification methods can change the surface properties of insulating materials and improve surface flashover performance [2, 3]. Moreover, the method is easy to operate, diverse in methods, and easy to control experimental parameters, providing an experimental instrument for the modulation of epoxy resin surface properties.

Plasma modification technology refers to the use of multiple effects generated when high-energy plasma comes in contact with the material surface to achieve changes in the physical and chemical properties of surface. With the characteristics of high efficiency, simple operation and low equipment cost, it has become a popular modification technology for insulating materials [4, 5]. In addition, the premise of plasma modification technology is how to generate plasma. According to whether the heavy particles and electrons in the plasma are in thermodynamic equilibrium or not, the plasma is divided into thermal plasma and non-thermal plasma. Since the former has almost the same temperature of heavy particles and electrons, the overall temperature reaching nearly 20,000 K, while the latter has much higher electron temperature than that of the heavy particles and also has the characteristics of high

---

J. Yan · Q. Xie (✉) · Y. Song · Y. Zhang
Department of Electrical Engineering, North China Electric Power University, Baoding, China
e-mail: xq_ncepu@126.com

Q. Xie (ed.), *Electrical Materials*, Engineering Materials,
https://doi.org/10.1007/978-981-99-9050-4_3

energy and high activity. Therefore, non-thermal plasma is often used to achieve surface modification of materials [6, 7].

Plasma can be generated in the form of gas discharge [8, 9] because it is composed of positive and negative ions in gas. Currently, the main plasma discharge methods involving in the modification of insulating materials are Dielectric Barrier Discharge (DBD) and Atmospheric-Pressure Plasma Jet (APPJ). DBD refers to the insertion of quartz glass, polytetrafluoroethylene (PTFE) and other insulating materials between discharge electrodes. In this way, the infinite growth of inter-electrode currents can be effectively inhibited, avoiding the discharge transitioning to arc discharge [10]. APPJ refers to introducting working gas into the tubular electrode at a certain rate. When the gas is discharged, the plasma generated is blown out of the discharge region, thereby separating the discharge area from modified area [11].

The selection of precursors in plasma modification determines which effect is used to modify the material surface. The precursors refer to the substances involved in plasma discharge. Due to the extremely high energy generated during the plasma discharge, the chemical bonds of the precursors are broken and rearranged. According to the properties of precursors and the effects on the material, the effects of plasma on the material surface can be divided into plasma etching, plasma grafting and plasma polymerization [12]. For plasma modification of insulating materials, the plasma discharge form and precursors are usually selected appropriately. And plasma etching, grafting and polymerization are used to regulate the surface physicochemical properties of insulating materials, thus improving the electrical performance.

Plasma etching effect refers to the breaking and reorganizing of the chemical bonds on the surface of the material under non-reactive atmosphere conditions (such as inert gas Ar or He) by high-energy plasmas, resulting in changes in the original morphology of material surface [13]. Since the plasma acts on the material at a depth of only a few hundred nanometers, plasma etching effect can change the microstructure of material surface without damaging the internal physicochemical structure of the material [14]. Studies demonstrate that the surface morphology of insulating materials can affect their electrical properties. Therefore, many scholars take advantage of the plasma etching effect to improve the surface flashover performance of insulating materials. With the help of a radio-frequency plasma jet device, Luan et al. used an inert gas Ar as carrier gas and mixed it with a certain proportion of oxygen as precursor, thereby completing the surface etching of polystyrene, PMMA and polyvinyl alcohol, and the relationship between oxygen concentration and etching depth was investigated [15]. Dai et al. developed a set of separated maskless etching devices based on the atmospheric pressure He/O_2 plasma jets and micro-electro-mechanical system nozzles. By regulating the distance between nozzles and insulating materials, oxygen concentration and etching time, this device can etch different micropore characteristics in the insulating materials [16]. Seok et al. adopted DBD method to complete plasma etching of SiC and modulated the etching depth of SiC surface by varying the proportion of NF_3 gas in He and altering the power supply parameters [17]. Shao Tao's team, at the Institute of Electrical Engineering of the Chinese Academy of Sciences, used microsecond pulsed power to perform APPJ etching on PMMA and investigated the mechanism of plasma interaction with

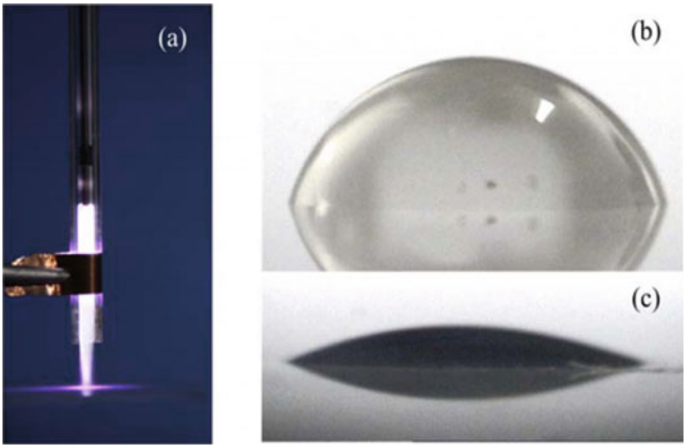

Fig. 1 Effect of plasma modification on surface hydrophilicity of insulating materials [18]

PMMA surface. It was found that APPJ etching can not only change the surface roughness of PMMA, but also enhance the hydrophilicity of PMMA in the plasma, which in turn improves the surface flashing performance of PMMA in vacuum [18]. The team used a similar approach to perform plasma etching on epoxy resin, finding that increasing the surface roughness of epoxy resin can effectively improve their surface flash performance. In addition, the surface chemical components of epoxy resin are also changed during plasma etching, which affects the trap energy level distribution and surface charge dissipation rate [19] (Fig. 1).

Studies above show that the adoption of plasma etching not only changes the surface micromorphology of insulating materials, but also introduces other groups with the participation of non-inert gases. Therefore, the plasma modification technology tends to utilize multiple plasma effects, and determine which effect dominates through the selection of plasma discharge form and precursor. The plasma grafting effect refers to the precursor contains functional groups or elements that need to be introduced onto the material surface. And the energy generated during plasma discharge used to break the chemical bonds between the precursor and the material surface at the same time. In this way, the functional groups in the precursor become free and a large number of reactive sites appear on the surface of material, and they will re-bond when coming into contact [20]. From the perspective of chemical composition, functional groups or elements in the precursors are grafted onto the surface of material. In the introduction of method for regulating the surface properties of epoxy resin, scholars propose the surface fluorination technique based on fluorine-nitrogen gas mixture, which introduces fluorine, the most electronegative element, into the material surface. However, fluorine gas itself is a highly toxic gas and has the drawbacks of low reaction effect and expensive equipment. Therefore, the plasma fluorination of insulating materials by using the plasma grafting effect has become a new direction of fluorination research.

Zhang Guanjun's team from Xi'an Jiaotong University used inert gas He mixed with non-toxic CF_4 as the precursor. They successfully implemented the surface fluorination of epoxy resin via APPJ method and found the chemical bond was formed on the surface of epoxy resin through chemical composition characterization. It was proved that the fluorine element was successfully grafted onto the surface of epoxy resin by plasma modification technology and plasma fluorination improved the vacuum surface flashover performance of epoxy resin [21]. Zhang Cheng et al. completed the plasma fluorination of PMMA using the DBD method and found that plasma fluorination have both etching and grafting effects, that is, the plasma fluorination increased the surface roughness of PMMA. And the surface of PMMA was grafted with CF_x groups additionally, which significantly improve the hydrophobicity of PMMA [22]. Zhan Zhenyu et al. studied the surface flashover performance of epoxy resin in C_4F_7N/CO_2 gas mixture by employing plasma fluorination method. They found that plasma fluorination increased the surface roughness of epoxy resin, leading to an increase in the creepage distance between electrodes. The presence of fluorine-containing groups accelerates the dissipation rate of negative charge, which ultimately enhances the surface flashover performance of epoxy resin [23]. Wan Fangchao et al. used Ar/CF_4 plasma fluorination to change the microscopic surface morphology of cross-linked polystyrene. The surface conductivity and surface charge capture ability of material were improved, finally enhancing the surface flashover performance [24, 25]. Xie Qing's team from North China Electric Power University investigated the timeliness of physicochemical properties of epoxy resin surface after plasma fluorination. They found that the epoxy resin after plasma fluorination had a tendency to return to its pre-modification physicochemical properties after a period of placement [26]. In addition, many scholars have compared the conventional surface fluorination technology with plasma technology. Peyroux et al. studied the effect of both surface fluorination and plasma etching on the hydrophobicity of insulating materials [27]. Zhang Cheng et al. thoroughly investigated the different effects of surface fluorination and plasma etching on the surface properties of epoxy resin/alumina basin insulators. It was found that the surface charge dissipation rate of the plasma etched sample will change considerably after a period of time, which suggested that plasma etching has a certain timeliness, while that of surface fluorination is not obvious [28, 29] (Fig. 2).

Plasma fluorination can not only modify the insulation surface, but also change the surface structure of micro-nano fillers, thus enhancing the mechanical and electrical properties of substrate. Matsubara et al. improved the hydrophobic properties of polystyrene powder by plasma fluorination [30]. Duan Qijun et al. carried out plasma fluorination on BTO nanofibers and incorporated the fillers into epoxy resin before and after modification respectively. Plasma fluorination of the filler was found to further enhance the surface flashover performance of epoxy resin composites [31]. Ruan Haoou et al. fluorinated Al_2O_3 and TiO_2 nanofillers respectively to study the effect of fluorination on the surface charge dissipation rate and surface flashover performance of epoxy resin matrix [32, 33]. Zhan Zhenyu et al. similarly improved the surface flashover performance of epoxy resin matrix by plasma fluorination of micron AlN [34], studied mixed the plasma fluorinated SiC nanofillers with epoxy

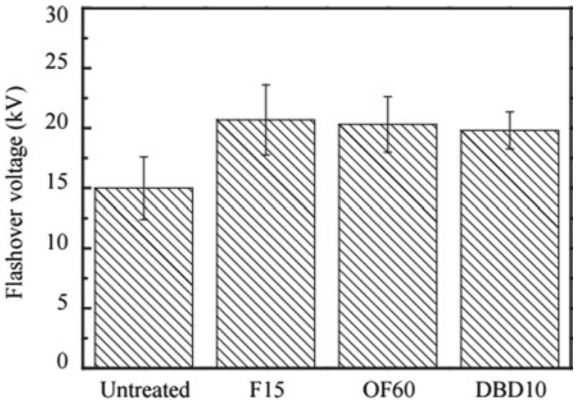

Fig. 2 Comparison of plasma modification and surface fluorination on surface flashover voltage [29]

resin to form a new coating and the effect of the coating on the physicochemical and electrical properties of epoxy resin surface [35].

The plasma breaks the chemical bonds of both the material surface and precursor, and recombines the free groups in the precursor with the active sites on the material surface. So is it possible to use plasma to directly break and recombine precursors to generate new substances and deposit them on the material surface? Many scholars have conducted in-depth research on this and concluded that the method takes advantage of the polymerization effect of plasma. Plasma polymerization usually refers to the method of forming coatings by polymerizing monomers in plasma environment. In the research of insulating materials, the plasma polymerization effect is usually used to cover the film on the surface of the material, directly changing the physicochemical properties of gas–solid interface, which in turn modulates the surface electrical properties of insulating materials [6]. Armenise et al. successfully deposited films containing carboxylic acid groups on polyurethane using APPJ with helium, acrylic acid and ethylene as precursors [36]. Kakiuchi et al. similarly used APPJ to successfully prepare SiOC films at atmospheric pressure with hexamethyldisilane and oxygen as precursors [37]. Using $(CH_3CH_2O)_3SiCH_2CH_2(CF_2)_7CF_3$, $(CH_3O)_3SiCH_2CH_2CF_3$ and $F_5ArSi(OCH_2CH_3)_3$ as precursors, Yim et al. deposited hydrophobic layers on the surface of ultrahigh molecular weight polyethylene (UHMWPE) by plasma polymerization [38]. The team of Xie Qing at North China Electric Power University used tetraethyl orthosilicate (TEOS) as precursor. SiO_x films were deposited on the epoxy resin surface using APPJ, and it was found that the SiO_x films covered the original defects on the epoxy resin surface. And a large number of shallow traps were introduced, which greatly increased the surface charge dissipation rate. This inhibits the accumulation of charge on the epoxy resin surface, which in turn enhances the surface flashover performance [39–41]. Additionally, the team successfully deposited ZrO_2 films on the epoxy resin surface taking zirconium nitrate as precursor, effectively improving the surface charge dissipation rate and surface flashover performance of epoxy resin [42]. Shao Tao's team at the Institute of Electrical Engineering, Chinese Academy of Sciences, has conducted extensive

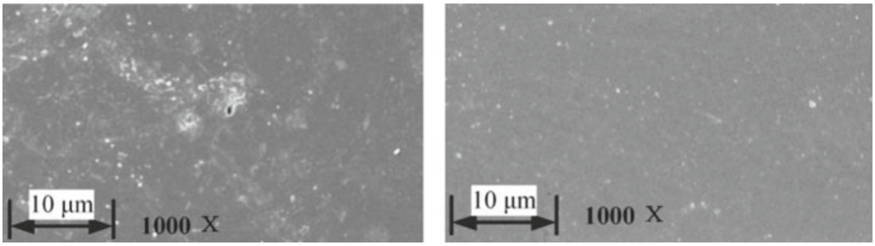

Fig. 3 Surface micro morphology of epoxy resin before and after plasma SiO_x deposition [39]

researches on the use of plasma polymerization. Different effects of plasma discharge electrode structures [1, 43, 44], precursor types [45, 46] and concentrations [47, 48] on the surface physicochemical and electrical properties of various modified substances [49–52] were deeply studied, providing substantial theories and experience for the development of plasma modification (Fig. 3).

The above mentioned studies fully illustrate that plasma modification can effectively alter the physicochemical and electrical properties of insulating materials, as well as engineer their surface characteristics by modifying process parameters. Nonetheless, most experts merely compare the comparison of surface properties between modified and unmodified plasma samples. Little attention has been paid to the different modulation mechanisms on surface properties of insulating materials by different plasma modification techniques [53–55], leading to restricted modulation range on the surface properties of those materials. This chapter will introduce sub-atmospheric pressure glow discharge modification, plasma fluorination modification and plasma SiO_x deposition modification methods. The modulation effects and mechanisms of various modification methods on the surface micromorphology, chemical components and electrical properties of epoxy resin are thoroughly illustrated. Subsequent to this, a comparison between the advantages and disadvantages of various means will be provided to present theoretical and experimental basis for the plasma modification technology of insulating materials.

2 Plasma Modification Platform for Epoxy Resins

Although plasma modification can regulate the surface micromorphology and chemical composition of epoxy resins, thus contributing to the surface charge distribution and polydisperse properties and ultimately improving the flashing performance along the surface. Different plasma modification methods use different modification mechanisms and have different modification effects, so it is necessary to build specific modification platform for each of them, and unify the measurement so as to compare the effects of effects of the different modification methods on the surface micromorphology, chemical composition and electrical properties of epoxy resins.

This section outlines the construction methods of the three modification platforms, namely sub-atmospheric glow discharge, plasma dielectric barrier discharge and atmospheric pressure plasma jet, respectively. It then describes the specific steps and experimental parameters of the three methods, namely sub-atmospheric glow, plasma fluorination and plasma SiO_x deposition. The measurement methods for surface micromorphology, chemical components and electrical properties were evaluated using methods previously outlined and will not be repeated here.

2.1 Plasma Modification Platform for Epoxy Resins

2.1.1 Sub-atmospheric Glow Discharge Modified Platform

The group deployed a sub-atmospheric pressure glow discharge low temperature plasma surface treatment system (HPD-280) from Nanjing Suman Plasma Technology Limited for material modification of epoxy resins (as Fig. 4). The system is capable of performing various surface modification such as surface polymerization, surface limb joining, surface catalysis, metal nitriding and insulating material modification. The driving power source for the system is a high frequency high voltage power supply embedded into the cavity. During the experiments, the material modification can be regulated in a stepwise fashion by adjusting parameters such as discharge time, discharge power, discharge spacing, gas atmosphere and discharge air pressure.

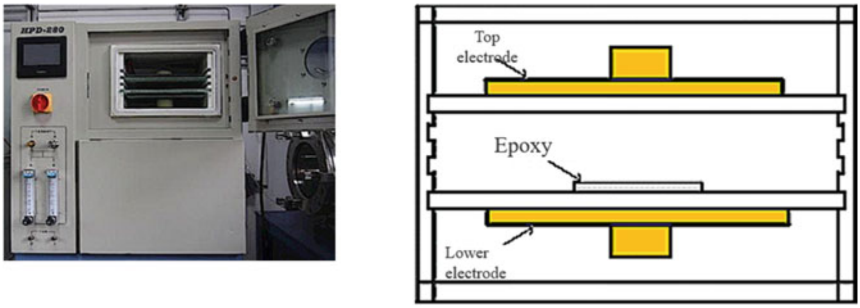

(a) Physical view of the glow discharge modified cavity

(b) Schematic diagram of the glow discharge modified cavity

Fig. 4 Glow discharge modified cavity and parameter setting interface

2.1.2 Plasma Dielectric Barrier Discharge Modification Platform

The group constructed a plasma dielectric barrier discharge platform, featuring both a circuit part and a gas circuit part. The circuit part comprises a plasma power supply, a dielectric barrier discharge reactor, a grounding capacitor, an oscilloscope and a voltage probe. The gas circuit section consists of gas cylinders, mass flow meters, precursors and their supporting devices. Each piece of equipment is discussed in details below.

(a) Circuit:

Nanjing Suman Plasma Technology Co., Ltd. offers Model CTP-2000K, as seen in Fig. 5. Plasma is formed by applying a high-energy excitation to a gaseous substance, thereby inducing ionization of the internal molecules of the gas, resulting in the presence of both positive and negative ions and neutral substances, forming an overall externally electrically neutral plasma. The group employs a high-frequency, high-voltage power supply to excite the gas for plasma generation. The power supply has a center frequency of 50 kHz and a maximum voltage of 30 kV, it also displays its output voltage and current for output power estimation, and has an internal power supply detection port for monitoring the output voltage waveform with an oscilloscope and voltage probe.

Dielectric barrier discharge reactor: The reactor, also manufactured by Nanjing Suman Plasma Technology Co., Ltd., consists of a metal flat plate electrode, an adjustable support, a quartz reactor and a quartz glass cover sheet, as illustrated in Fig. 6. The flat metal electrodes have a diameter of 100 mm and are held in a fixed distance between the two electrodes. During the operation, the upper electrode is connected to the high-frequency high-voltage power supply and the lower electrode is grounded via a grounding capacitor. The quartz reactor has an outer diameter of 200 mm, a thickness of 10 mm and a circular recess of 100 mm in diameter and 8 mm in thickness for the epoxy resin sample; There are a concentric cylinder on the left and right sides, with the cylindrical axes coinciding which serves as a pathway for

Fig. 5 Actual photograph of high frequency high voltage power supply

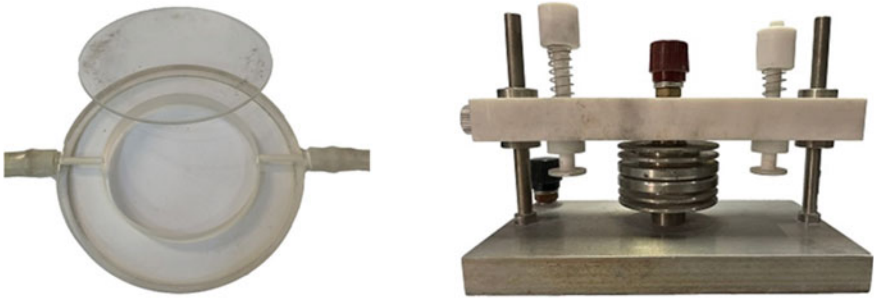

(a) Quartz reactor and glass sheet (b) DBD reactor

Fig. 6 Actual photograph of DBD reactor

various gas circuits. The quartz glass, 120 mm in diameter and 2 mm thick, is sealed on the quartz reactor to form a confined reaction space in the internal recesses.

Grounding capacitance: by connecting a 0.1 μF grounding capacitor to the flat electrode on the grounding side, the plasma discharge power can be calculated by monitoring the voltage waveforms on both sides of the capacitor during the plasma discharge and by combining this with the voltage waveform of the power supply using the Lissajous graph method. The method is based on the following principle: let the ground capacitor be C_1, the voltage across the capacitor during discharge be U_1, the corresponding supply voltage be U_2, and let the discharge current be I, the corresponding charge be Q, and the time of one discharge cycle be T. Then we have [23]:

$$I = \mathrm{d}Q/\mathrm{d}t = \mathrm{d}(C_1U_1)/\mathrm{d}t = C_1\mathrm{d}U_1/\mathrm{d}t \tag{1}$$

The discharge power P is:

$$P = \frac{1}{T}\int_0^T U_2I\mathrm{d}t = \frac{C_1}{T}\int_0^T U_2\frac{\mathrm{d}U_1}{\mathrm{d}t}\mathrm{d}t = fC_1\oint U_2\mathrm{d}U_1 \tag{2}$$

As evidenced above, the discharge power can be can be determined by ascertaining the discharge frequency, the value of the earth capacitance, the supply voltage and the earth capacitance voltage waveform.

The oscilloscope and voltage probe: oscilloscope model Tektronix DPO 2002B. For the purpose of computing the discharge power with the Lissajous graph method, an essential step is to deduce the integration of the supply voltage and ground capacitance voltage. As depicted in Fig. 7, when the supply voltage value serves as the horizontal coordinate and the ground capacitance voltage as the vertical coordinate at the identical point in time, the points thereafter in a fixed interval of time form a typical Lissajous diagram. The data thus derived is imported into Origin data

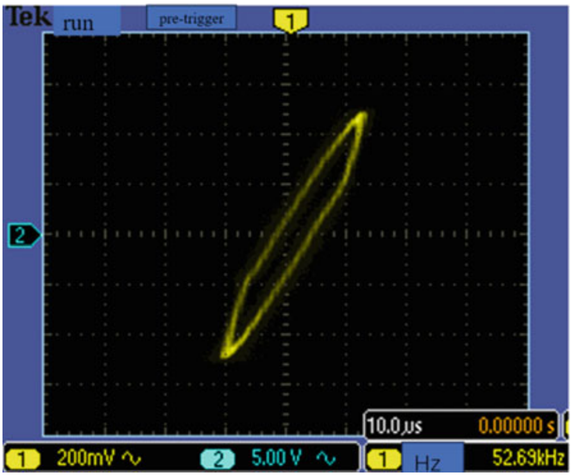

Fig. 7 Typical Lissajous diagram of plasma discharge

processing software, and the discharge power can be computed by the formula $P = f \times C_1 \times A$. The graph displays a supply frequency of f = 53 kHz and a ground capacitance of 0.1 μF, which gives a approximately discharge power of 35 W.

(b) Air circuit:

Gas cylinders: argon (Ar) and carbon tetrafluoride gas (CF_4), both with a purity of 99.99%. Despite the fact that a wide range of gases such as air can be used as a plasma source, they introduce a large number of functional groups such as hydroxyl groups when used to treat materials, which can impede the treatment outcome. Hence, the group used argon as the plasma source because it is an inert gas, generating plasma with minimal impurities and with comparatively little energy input. It can be used independently to etch the surface of the material or in tandem with the precursor as a carrier gas. Since direct plasma discharge with CF_4 is difficult to achieve and the discharge phenomenon is quite unbalanced and intensive, the group opted CF_4/Ar as the plasma source to achieve plasma fluorination of epoxy resin. On the one hand, Ar is easy to generate plasma discharge and can catalyse the ionisation of CF_4, on the other hand, Ar is an inert gas and does not react with CF_4 after ionisation and does not leave other impurities on the material surface.

Mass flow meter: it composed of a mass flow controller and a flow indicator, its physical diagram is shown in Fig. 8. The mass flow controller models D07-26C and D07-19B, and the flow indicator model D08-2F, both from Beijing Seven Star Huachuang Flowmeter Co., Ltd. The mass flow meter can be used to precisely regulate the flow rate and ratio of each gas, while maintaining accuracy. Estimating the type of gas and the approximate flow rate required for the experiment enables the selection of the necessary scope of mass flow controller, thus necessitating a dedicated mass flow meter for each way of gas. Specifically, the D07-26C mass flow controller designed to manage the Ar flow rate, with a standard range of 4 standard liters per minute (slm), and the D07-19B mass flow controller for CF_4 display with a

(a) Mass flow controller (b) Flow indicator

Fig. 8 Actual photograph of mass flowmeter

standard range of 400 sccm. The flow indicator simultaneously shows the flow rate of the two gases, enabling precise control in aspect of each gas ratio.

Precursors and their supporting devices: Precursors are substances containing the functional groups or elements necessary for the modified material in plasma modification. They are often used in conjunction with a carrier gas, such as ethyl orthosilicate (TEOS) which is used in the study to achieve plasma SiO_x deposition on the surface of epoxy resin using Argon (Ar). TEOS, which has a molecular formula of $Si(OC_2H_5)n(OH)_{4-n}$, is a colorless liquid at room temperature and is difficult to mix directly with gas. In order to tackle this issue, the group the group designed a supporting device, depicted in Fig. 9, which allowed for the TEOS to be conveniently mixed with Ar. The system was composed of a gas flask with a double-hole stopper and two glass tubes, one short and one long, inserted into each of the holes. The long tube submerged in the TEOS at one end and connected to the Ar gas line via a mass flow meter at the other end. Meanwhile, the short tube not submerged in the liquid and connected to the reactor at the other end. In order to make the TEOS more volatile, the bottom of the flask was outfitted with a water bath heater, which was heated to 70 °C during the experiment.

The plasma dielectric barrier discharge modification platform is shown in Fig. 10. Its circuit section is connected as follows: the high frequency high voltage power supply is connected to the high voltage terminal of the reactor, the low voltage side of the reactor is coupled to the oscilloscope's Channel 1 through a grounding capacitor, while the power monitoring port of the high frequency high voltage power supply is connected straight to the oscilloscope's Channel 2. As for the gas section, Ar and CF_4 are supplied to one end of the reactor via a mass flow meter, Ar, in turn, is fed to the long tube of the gas wash bottle through its mass flow meter the short tube of the gas wash bottle is connected to the reactor, the other end act as a gas collection device for the exhaust gas released post-experiment.

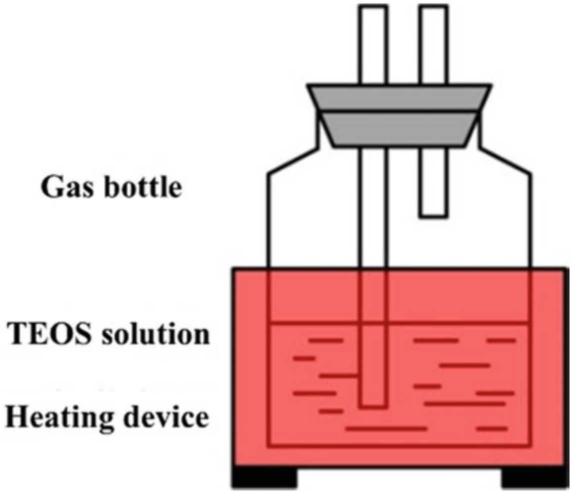

Fig. 9 Schematic diagram of precursors and supporting devices

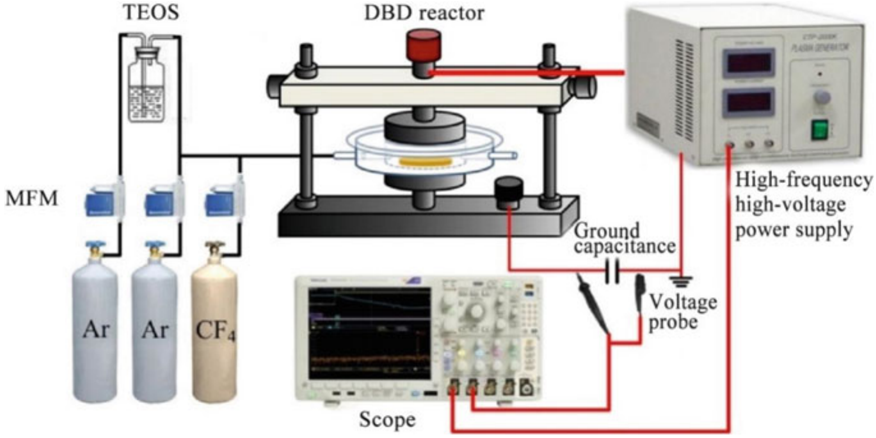

Fig. 10 Schematic diagram of DBD modification platform

2.1.3 Atmospheric Pressure Plasma Jet Modification Platform

As with the plasma dielectric barrier discharge (DBD) platform, the atmospheric pressure plasma jet platform is also composed of an electrical section and a gas section, with the exception of the discharge electrodes, the rest of the equipment is identical. The main difference between the two platforms is the structure of the discharge electrodes. While the discharge area and the treatment area coincide in the DBD platform, with the epoxy resin sample placed between the two flat electrodes and the quartz glass as a barrier medium, for the jet platform the separation of the

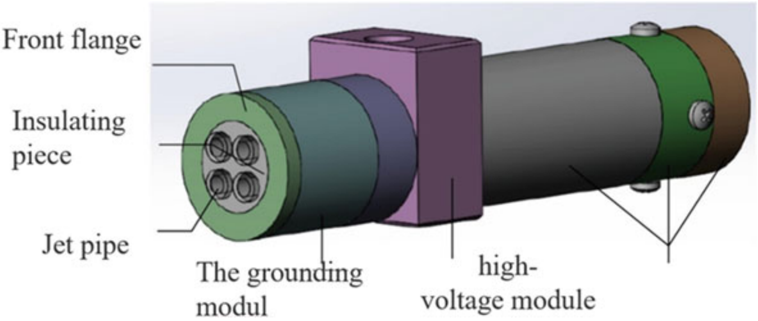

Fig. 11 Structure diagram of jet electrode

discharge area and the treatment area requires, a redesign of the discharge electrodes. The plasma jet electrode used by the group is still made by Nanjing Suman Plasma Co., Ltd. and can be seen schematically in Fig. 11, with the following structure.

The jet electrode consists of a circuit module, a gas circuit module and insulation and fixing components. The circuit module comprises two metal cylinders electrodes with a diameter of 40 mm and a thickness of 20 mm as arranged in parallel with a distance of 50 mm, the upper electrode is connected to the high-frequency high-voltage power supply and the lower electrode is grounded via a grounding capacitor. Both electrodes have four small 2 × 2 holes with a diameter of 8 mm for the quartz glass tube. The gas path module consists of four quartz glass tubes with an external diameter of 8 mm, an internal diameter of 4 mm and a length of 180 mm. One end is connected to the gas path of the plasma jet platform and the other end passes through the two cylindrical electrodes via a small hole. The rest of the jet electrode is filled with PTFE to act as an insulating support for the entire electrode.

The atmospheric pressure plasma jet modification platform is depicted in Fig. 12. The circuit section is connected as follows: the high frequency high voltage power supply is wired to the high voltage side of the jet electrode, the low voltage side of the jet electrode is linked through a grounding capacitor, both sides of the grounding capacitor are attached to channel 1 of the oscilloscope through a voltage probe, and the power monitoring port of the high frequency high voltage power supply is directly coupled to channel 2 of the oscilloscope. The gas section is connected as follows: one way Ar and one way CF_4 are connected to one end of the jet tube via a mass flow meter, the other way Ar is linked to the long tube of the gas wash bottle via a mass flow meter, and the short tube of the gas wash bottle is connected to the jet tube. As the small cross-sectional area of the plasma plume produced by a single jet tube is relatively small, it is difficult to cover the entire sample area. In order to improve the uniformity of the plasma jet treatment, the group added a lifting platform and a rotating platform, on which the epoxy resin sample placed. The rotating platform is situated on the lifting platform, with the centre of the lifting platform on the axis of the jet electrode. In this way, the epoxy resin sample is completely exposed to the plasma plume, while the contact area between the plasma plume and the epoxy resin

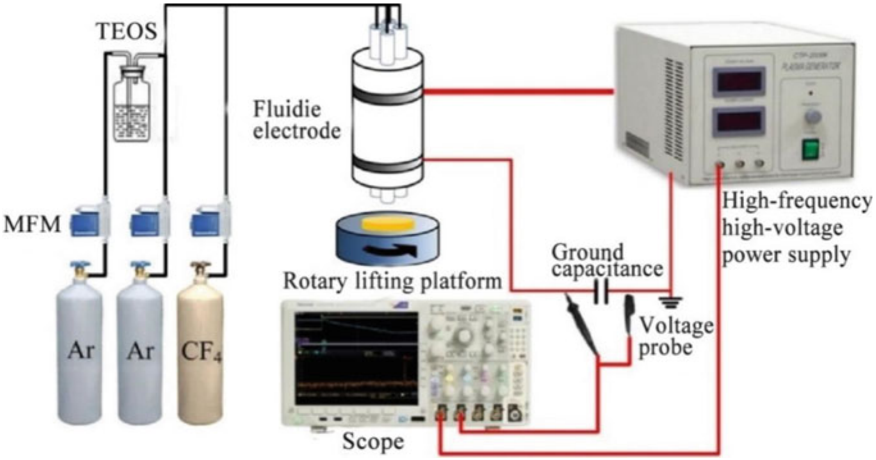

Fig. 12 Schematic diagram of APPJ modification platform

sample is constantly changed by the rotational rotation, thereby leading to a more even plasma jet treatment from an overall perspective.

2.2 Plasma Modification Methods

2.2.1 Sub-atmospheric Glow Discharge Modification

The concrete steps for the modification of epoxy resins by sub-atmospheric pressure glow discharge are:

(1) The pre-prepared epoxy resin samples are subjected to an ultrasonic cleaner and ultrasonically cleaned with anhydrous ethanol and deionized water for 10 min respectively, and then put into a vacuum oven to air dry for 24 h.
(2) Place the epoxy resin into the sub-atmospheric pressure glow discharge low temperature plasma surface treatment system, adjust the parameters of discharge spacing, discharge power and discharge time in the operation interface, ensuring the vacuum level within the range of 2000 Pa.
(3) After the selection of the working mode, the evacuation process is initiated and once the vacuum chamber reaches within the specified discharge vacuum, the vacuum pump is switched off and the discharge is taken place.
(4) A stable glow discharge is obtained at a voltage of 2.8 kV and a current amplitude of 7 A without significant current pulses. In addition, the discharge was stable and uniform over the entire surface of the electrode. The discharge emitted a lavender glow without any discernible discharge filaments.
(5) Following the end of the discharge, the pressure relief process is triggered and the modified sample is removed.

2.2.2 Plasma Fluorination

A plasma DBD platform is employed to realize the plasma fluorination modification of epoxy resin. The experimental steps are as follows:

(1) Put the prepared epoxy resin sample into the ultrasonic cleaning machine, undergoing cleaning increments with absolute ethanol and deionized water for 10 min respectively. Then put it into the vacuum oven to air dry for 24 h.
(2) Take out the dried sample and place it in the center of the glass reactor encompassed with quartz glass. And adjust the discharge electrode be intimately adhered to the upper side of the quartz glass sheet and the lower side of the glass reactor, with the electrode spacing at 10 mm.
(3) Open the pneumatic valves of Ar and CF_4, with the mass flowmeter setting of 5 slm for Ar and 0.5slm for CF_4, giving the total flow rate a Ar:CF_4 = 10:1 ratio [55]. Pass the mixed gas into the reactor for 1 min to achieve a complete depletion of air.
(4) Turn on the oscilloscope and set it to X–Y display mode, turn on the high-frequency high-voltage power supply and set the supply voltage to 5 kV, continuously adjust the supply frequency and monitor the current value on the power supply display. When the current value rises sharply and a large amount of orange filamentary discharge occurs in the reactor, these indicate that Ar/CF_4 has been ionized. At this time, the supply frequency is observed to be about 53 kHz through the oscilloscope. Simultaneously commence recording treatment time at the same time.
(5) Set the plasma fluorination treatment time of each sample to 1 min, 2 min, 3 min, 4 min, 5 min, and lable them as DBD-F1, DBD-F2, DBD-F3, DBD-F4, DBD-F5 respectively. After the treatment was completed, the power supply voltage was gradually reduced to 0, and it is found that the discharge then gradually disappears. Since the former plasma discharge produced such a high temperature in the reactor and sample, a short period of a mixed-gas ventilation is demanded for cooling. After the reactor is cooled down, lift the flat electric board and take out the sample, and the plasma DBD fluorination experiment is completed.

The plasma fluorination modification of epoxy resin can also be carried out by using the APPJ modification platform, albeit with quite different experimental steps. The specific steps are as follows:

(1) Following the cleaning and drying steps of epoxy resin sample, similar to that of plasma DBD modification experiment.
(2) Take out the dried sample and place it in the center of the rotating platform. Adjust the lifting platform so that the sample is 40 mm away from the bottom of the jet pipe to ensure that the sample will not contact the plasma plume at the beginning of the generation of the plasma plume.
(3) Open the pneumatic valves of Ar and CF_4, use the mass flowmeter to set the flow rate of Ar to 6 slm and CF_4 to 0.5 slm. At this time, with the sound of mixed gas discernible when ejecting from the jet pipe.

(4) Turn on the oscilloscope and set it to X–Y display mode, and activate the high-frequency high-voltage power supply, adjusting the supply voltage to 5 kV. Monitor the current value displayed on the power supply adjust the supply frequency. When the current value rises sharply and orange plasma plume continuously ejected from the jet pipe, this indicate that Ar/CF_4 has been ionized. At this time, turn on the rotating platform to make the sample rotate at a uniform speed, and lift the sample to 15 mm away from the bottom of the jet pipe. Ensuring that it's adequately exposed to plasma plume, while avoiding instability or the disappearance of plasma plume due to close proximity to the jet pipe. When the sample reaches the specified position, and the supply frequency is observed to be about 53 kHz through the oscilloscope, start recording treatment time.

(5) Set the plasma fluorination treatment time of each sample to 1 min, 2 min, 3 min, 4 min, 5 min, and lable them as APPJ-F1, APPJ-F2, APPJ-F3, APPJ-F4, APPJ-F5 respectively. After the treatment was completed, the power supply voltage was gradually reduced to 0, and it is found that the plasma plume then gradually disappears. At this time, the temperature of the sample is too high due to the plasma discharge, and it needs to be cooled before being taken out from the rotating platform. The APPJ fluorination experiment is completed.

2.2.3 Plasma SiO_x Deposition Modification

Because the precursor of plasma SiO_x deposition is different from plasma fluorination, the corresponding experimental steps are also different. Achieve the plasma SiO_x deposition of epoxy resin by using plasma DBD. The specific steps are as follows:

(1) Following the cleaning and drying steps of epoxy resin sample, similar to those of plasma fluorination experiment, which will not be repeated here.

(2) The method of placing the sample into the reactor is the same as that of plasma fluorination experiment, which will not be repeated here.

(3) Set the temperature of water bath to 70 °C. After heating for 5 min, open the two-way Ar, and set mass flowmeter to 5 standard liters per minute (slm) of Ar going directly into the reactor and 0.5 slm Ar going into the gas-washing bottle containing TEOS, yielding an Ar:Ar/TEOS ratio of 10:1. When there is a small amount of bubbles in the gas-washing bottle, this indicates gas mixed with TEOS and Ar has been blown out of the gas-washing bottle. Allow the mixed gas to continue flowing into the reactor for 1 min to deaerate the reactor.

(4) Also turn on the oscilloscope set it to X–Y display mode and turn on the high-frequency high-voltage power supply. Unlike plasma fluorination, the existence of CF_4 will increase the threshold of plasma discharge, but TEOS has little effect on plasma discharge. Therefore, set the supply voltage to only 4.5 kV during the plasma SiO_x deposition, and continuously adjust the supply frequency and monitor the current value on the power supply display. When lilac filamentary discharge occurs in the reactor, it indicates that Ar/TEOS has been ionized.

Oscilloscope readings show that the frequency is around 52 kHz at this point. Start recording treatment time.

(5) Additionally, set the plasma SiO_x deposition treatment time of each sample to 1 min, 2 min, 3 min, 4 min, 5 min, and lable them as DBD-Si1, DBD-Si2, DBD-Si3, DBD-Si4, DBD-Si5 respectively. Follow the same sample cooling step utilized for the plasma fluorination experiment. The plasma DBD SiO_x deposition experiment is completed.

The plasma SiO_x deposition modification of epoxy resin can also be achieved by the APPJ modification platform, but the experimental steps are quite different. The specific steps are as follows:

(1) Following the cleaning and drying steps of epoxy resin sample, similar to those of plasma fluorination experiment.
(2) Same as in a plasma fluorination experiment, the sample is placed in its designated position.
(3) Set the temperature of water bath to 70 °C. After have heating for 5 min, open the two-way Ar, and set the flow rate of the Ar directly flowing into the reactor to 6slm through the mass flowmeter, and the flow rate of the Ar connected to the gas-washing bottle containing TEOS to 0.6 slm. When a small amount of bubbles is visible in the gas-washing bottle, it indicates that the gas mixed with TEOS and Ar has been blown out of the gas-washing bottle. At this time, the sound of mixed gas ejecting from the jet pipe can be heard.
(4) Also turn on the oscilloscope and set it to X–Y display mode, turn on the high-frequency high-voltage power supply, set the supply voltage to 4.5 kV, continuously adjust the supply frequency and monitor the current value on the power supply display. When the current value rises sharply and lilac plasma plume continuously ejected from the jet pipe, it indicate that Ar/TEOS has been ionized. At this time, start the rotating platform to move at an even speed, and lift the sample to 15 mm away from the bottom of the jet pipe. This measure allows the epoxy resin sample to be fully contacted with the plasma plume in order to achieve modification without bringing it too close to the jet pipe, which will result in instability or even disappearance of the plasma plume. Upon reaching the desired position, the supply frequency is observed to be about 52 kHz through the oscilloscope, and begin recording treatment time.
(5) Set the plasma SiO_x deposition treatment time of each sample to 1 min, 2 min, 3 min, 4 min, 5 min, and lable them as APPJ-Si1, APPJ-Si2, APPJ-Si3, APPJ-Si4, APPJ-Si5 respectively. Subsequently, the voltage was gradually decreased to 0, resulting in a gradual weakening of the plasma plume. As the temperature of the samples had raised significantly due to the plasma discharge, they needs to be cooled down before being taken out from the rotating platform. The plasma SiO_x deposition experiment is completed.

3 Modulation of Plasma Modification on Epoxy Resin Surface Micromorphology

Studies have shown that altering the surface morphology of insulating material on micro and nano scales has an substantial effect on electrical properties of material. However, most existing studies only focus one kind of plasma modification technique. Even when accounting for factors such as processing time, concentration of precursors and other parameters, it is difficult to control surface morphology at multiple scales, and there is inadequate research on the varying effects of varying effects of different plasma modification devices on insulating material surface morphology. Hence, there is a lack of clarity regarding how surface morphology affects the electrical properties of insulating materials. To address this gap, other plasma-modification techniques must be explored and incorporated.

This chapter investigates how sub-atmospheric glow discharge, plasma fluorination and plasma SiO_x deposition modify the micromorphology of epoxy resin surface. Furthermore, it explores the effect rules of plasma treatment under different conditions on epoxy resin micromorphology.

3.1 Modulation of Sub-atmospheric Glow Discharge on Epoxy Resin Surface Micromorphology

The surface of epoxy resin was subjected to modification for 1, 2, 3, 5 and 10 min at the power of 320 W and the distance of 30 cm. Figure 13 exhibits an optical 3-D microscope image of the material surface magnified 500x, as presented below. Figure 13a shows the surface of epoxy resin without glow discharge, which can be observed that the smoothness of material surface is excellent before modification. A few scratches and some large particles are randomly distributed on the surface. This condition provided a strong reference of the resin's intrinsic refractive index. Figure 13b, c and d depict the surface morphology of epoxy resin after glow discharging for 1, 3 and 5 min. After modification, it uniformly distributed granular matter forms on the surface of epoxy resin, and as the time increases, the distribution of granular matter become more uniform. The 3-D ultra-depth field microscope was used for a deep synthesis study of the height information at the same position on the surface. As shown in Fig. 14, with increasing treatment time, the original irregularly particles gradually increased in size, and small particles merged to form large bumps. The distribution of bumps possesses a comparably regular pattern. Meanwhile, the corresponding height difference increases with the prolongation of the treatment.

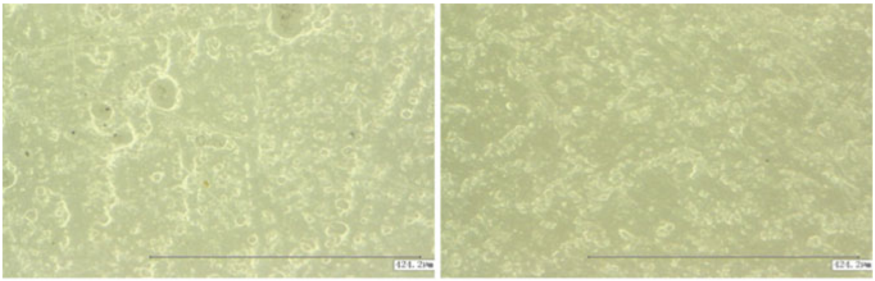

(a) untreated (b) 1 min

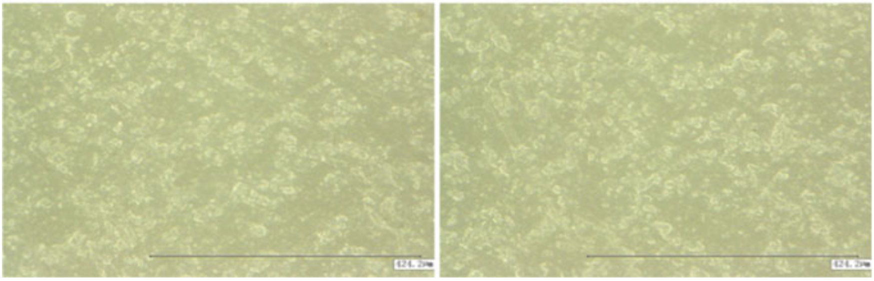

(c) 3 min (d) 5 min

Fig. 13 Surface morphology at different modification time

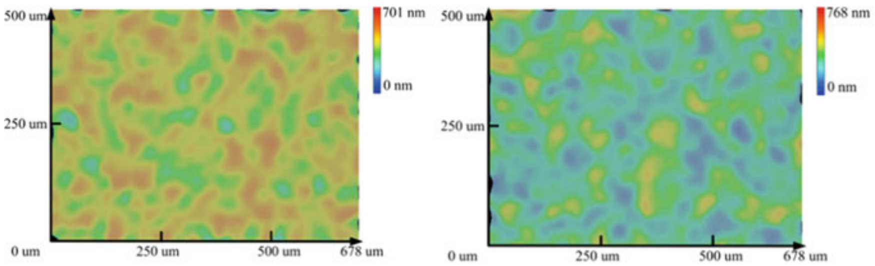

(a) untreated (b) 1 min

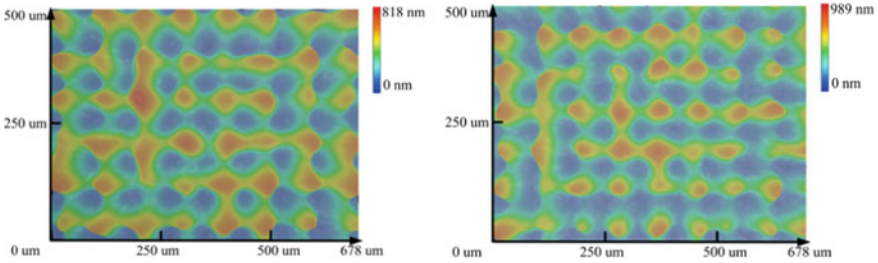

(c) 3 min (d) 5 min

Fig. 14 Surface 3-D height maps at different modification times

3.2 Modulation of Plasma Fluorination on Epoxy Resin Surface Micromorphology

Under the same plasma modification means and different treatment time, the surface morphology of epoxy resin has little difference. Therefore, sample treated for 3 min is treated as representation for all various plasma modification. Figure 15 shows the unprocessed, DBD fluorinated, APPJ fluorinated epoxy resin. Visually, the surface of unprocessed epoxy resin sample is light gray. Besides, though the surface appears to be flat, tiny depressions and bumps can be found by careful observation. Surface of samples after DBD fluorination and APPJ fluorination has little difference with unprocessed sample, making it difficult to validate the success of plasma fluorination. Thus, microscopic characterization is essential for further study.

Scanning electron microscopy (SEM) was used to investigate the surface micromorphology of unprocessed, DBD fluorinated and APPJ fluorinated epoxy resin at a magnification of 100 μm (Fig. 16). The untreated epoxy resin sample as relatively flat with a small amount of particles distributing on itself. In contrast, a large amount of bumps and depressions exist on the surface of epoxy resin after DBD fluorination, rendering the overall sample is significantly rough in appearance. This result shows that DBD fluorination can etch epoxy resin surface. The surface of epoxy resin after APPJ fluorination also has a mass of bumps and depressions, and the sample surface is also quite rough, though the sample is less rough than the DBD fluorinated one, demonstrating a comparatively weaker etching effect of APPJ fluorination than that of DBD fluorination.

However, SEM observation of surface morphology before and after plasma fluorination is not considered to be an accurate enough metric. A surface profilometer is needed to quantitatively measure the micromorphology before and after modification. The surface micro profile measurement results of each sample are shown in Fig. 17. As indicated by the figure, darker red colors represent areas of greater relative height and darker blue colors represent areas of lower relative height. The more pronounced the color change in figure, the more significant the surface undulation of sample, which means a rougher sample. In addition, the extreme values of

(a) Untreated (b) DBD fluorination (c) APPJ fluorination

Fig. 15 Actual photograph of epoxy resin samples before and after plasma fluorination

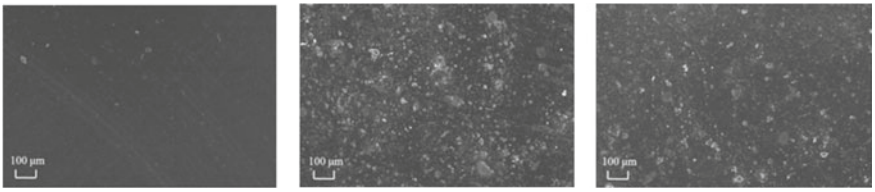

(a) Untreated (b) DBD fluorination (c) APPJ fluorination

Fig. 16 SEM figure of epoxy resin before and after plasma fluorination

relative height of each sample are given on the right side of the figure, allowing a direct comparison of the roughness of different samples in color. It is observed that a large number of particles distributed across its surface and a few large bumps and depressions. The number of particles on epoxy resin surface after DBD fluorination is larger and the bumps become rougher. Compared to the untreated epoxy resin, the overall height difference of sample is bigger, indicating the sample's surface has roughened due to DBD fluorination. More particles on the surface of the bumps indicates that DBD fluorination can etch epoxy resin and preferentially etch the elevated area. The surface of epoxy resin after APPJ fluorination is similar to that of DBD fluorinated sample, retaining rougher bumps. But the overall height difference of epoxy resin after APPJ fluorination is between the DBD fluorinated and untreated samples, which proves that APPJ fluorination can also etch epoxy resin though with a lesser effect than that of DBD fluorination.

Internationally, the arithmetic mean of the absolute value of the surface profile deviation is commonly used to quantitatively characterize the surface roughness of material. It is named as contour arithmetic mean deviation and denoted as "Ra" wherein higher values correspond to rougher surfaces [56]. In order to calculate the effect of plasma fluorination modification on epoxy resin surface morphology at different discharge electrodes and treatment time, the surface roughness value before and after plasma fluorination can be worked out by the surface micro profile shown in Fig. 17. The calculation result is shown in Fig. 18. It is observed that the result is in line with the SEM pictures and surface micro profile pictures. As the surface roughness value (Ra) increase after plasma fluorination, and Ra has a positive correlation to the treatment time. Besides, the improvement of surface roughness modified by DBD fluorination is greater than that via APPJ fluorination. The untreated epoxy resin had a Ra value of 426 nm. which is remarkably increased to 1055 nm via DBD-F5, the maximum value among all the plasma modification of all plasma modification, while Ra of APPJ fluorination reaches only achieved 889 nm at most.

Based on the experimental results and analysis above, it is evident that plasma fluorination can etch the surface of epoxy resin and then increase the surface roughness of it. The discharge power of DBD electrode is higher than that of APPJ electrode, making its fluorination yield better results in terms of etching performance and a greater variance in the surface roughness value. Furthermore, it is possible to adjust

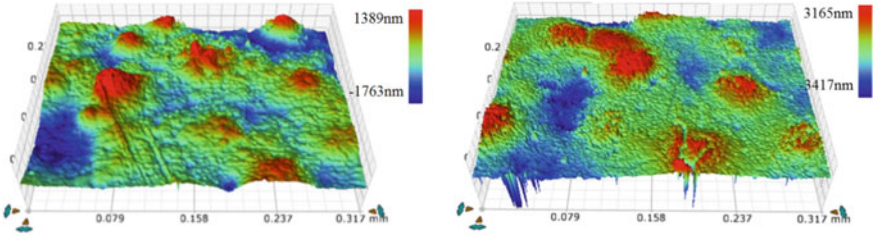

(a) Untreated (b) DBD fluorination

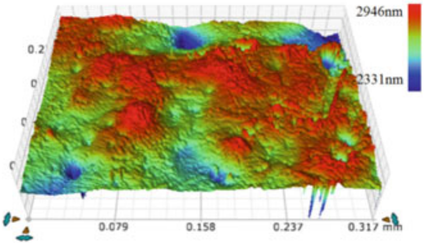

(c) APPJ fluorination

Fig. 17 Surface micro profile of epoxy resin before and after plasma fluorination

Fig. 18 Surface roughness of epoxy resin before and after plasma fluorination

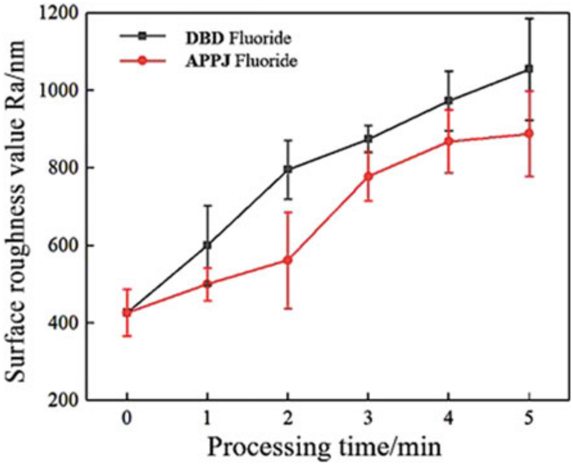

the surface roughness value Ra of epoxy resin to a range of 400–1000 nm. By varying the structure of plasma discharge electrode and treatment time.

3.3 Modulation of Plasma SiO_x Deposition on Epoxy Resin Surface Micromorphology

The same research concept regarding modulation of plasma SiO_x deposition on epoxy resin surface micromorphology has been implemented, and the sample treated by plasma SiO_x deposition for 3 min is used as a representative. Untreated, DBD-SiO_x deposited and APPJ-SiO_x deposited epoxy resin is shown in Fig. 19. Unlike plasma fluorination, upon irradiation by natural light at a specific angle, on the surface of plasma SiO_x deposited epoxy resin will reflect light waves of multiple colors. This phenomenon is called film interference. The phenomenon occurs due to the existence of thin films, close to visible light wavelengths, on the surface of plasma SiO_x deposited epoxy resin. Thereby, when the light passes through such thin film, light waves will be reflected respectively from its upper and lower surfaces, subsequently leading to their interference, and formation of a new light wave. Consequently, some hues in natural light are intensified, while the intensity of other hues is reduced, and finally, multiple hues of light waves can be perceived by the human eyes. In essence, this distinguishing effect of film interference indicates that plasma SiO_x deposition deposits nanoscale films on epoxy resin surface. Moreover, it was also found that the film deposited by DBD-SiO_x is irregular in shape, while the film deposited by APPJ-SiO_x is approximately circular. Then wiping the film with absolute alcohol resulted in no disappearance or deformation, which indicates that the formed film is dense and solid.

The surface micromorphology of epoxy resin after plasma SiO_x deposition is further investigated and the SEM figure of samples is shown in Fig. 20. It was found that particles on surface of epoxy resin were obviously covered by film after plasma SiO_x deposition, but bright or dark spots are observed on the surface of epoxy resin after DBD-SiO_x deposition. The thickness of film deposited on surface is not uniform, which leads to the difference of intensity of reflected light. So different bright and dark areas will show in SEM picture. In comparison, the color distribution of SEM picture of APPJ-SiO_x deposition is more uniform than that of DBD-SiO_x deposition, which indicates the film formed by APPJ-SiO_x deposition is more homogeneous.

(a) Untreated (b) DBD SiO_x deposition (c) APPJ SiO_x deposition

Fig. 19 Actual photograph of epoxy resin samples before and after plasma SiO_x deposition

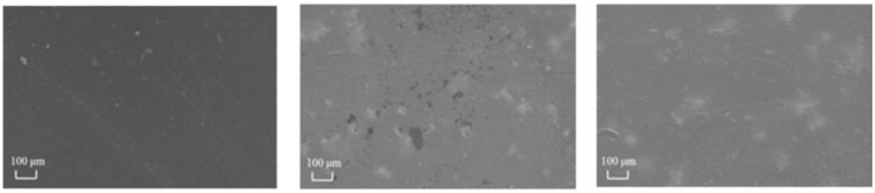

(a) Untreated (b) DBD SiO_x deposition (c) APPJ SiO_x deposition

Fig. 20 SEM figure of epoxy resin before and after plasma SiO_x deposition

The measurement scale of SEM is extended to 1 µm and 200 nm, and the obtained SEM figure of plasma SiO_x deposition is shown in Fig. 21. Upon inspection of the SEM image on 1 µm magnification, numerous particles can be observed to have deposited on the surface of epoxy resin after plasma SiO_x deposition. However, it is evident that the particle distribution of APPJ-SiO_x deposition yields a more uniform coverage, signifying a more homogenous film formation. Analyzing SEM picture at 200 nm magnification, reveals that the film generated by plasma SiO_x deposition is coralloid, which is aggregated by a large number of nanoscale particles.

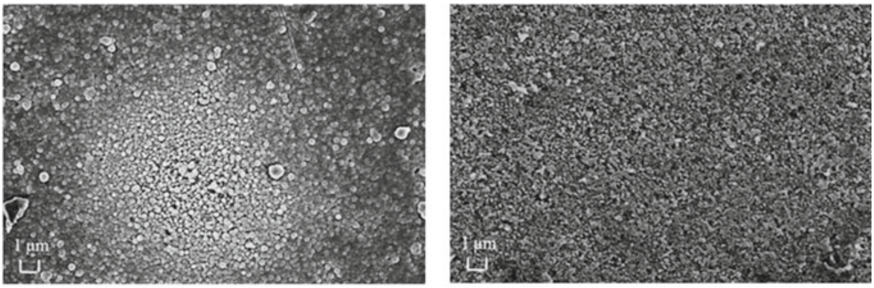

(a) DBD-SiO_x deposition at 1µm (b) APPJ-SiO_x deposition at 1µm

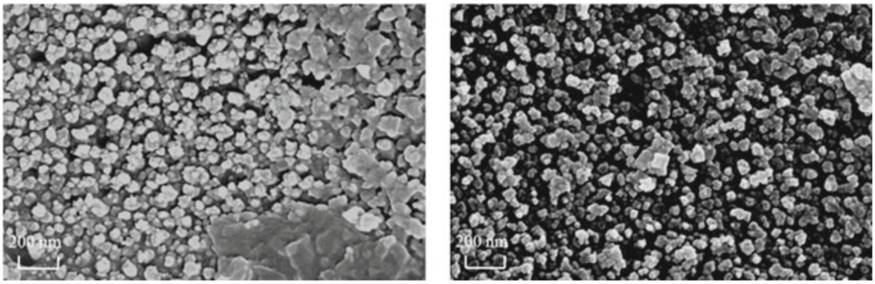

(c) DBD-SiO_x deposition at 200nm (d) APPJ-SiO_x deposition at 200nm

Fig. 21 SEM images of SiO_x deposition samples with high magnification

It evident from both visual inspection and SEM imaging that the plasma SiO_x deposition method can deposit film on surface of epoxy resin. But it is difficult to discern whether the surface of epoxy resin become rougher after modification. Therefore, surface micro profile of epoxy resin after plasma SiO_x deposition is needed to be measured, as shown in Fig. 22. The figure shows that plasma SiO_x deposition can notably decrease the overall relative height difference of epoxy resin surface. It implies that film generated by plasma SiO_x deposition covers the original defects of untreated epoxy resin surface, thus diminishing its roughness to a certain extent. Nevertheless, many large bumps appear on the surface of epoxy resin after DBD-SiO_x deposition, indicating that the film generated by DBD-SiO_x deposition has an uneven thickness. To the contrary, the surface of epoxy resin after APPJ-SiO_x deposition exhibited more flatness, hinting that APPJ-SiO_x yields films with a more uniform thickness.

To quantify characterize variation of epoxy resin surface roughness before and after plasma SiO_x deposition, surface roughness value (Ra) of epoxy resin before and after modification by plasma SiO_x deposition at different electrodes and treatment time was also calculated. The results are shown in Fig. 23. Like that of untreated sample, the Ra of epoxy resin after DBD-SiO_x deposition fluctuates varied between 375 and 579 nm with increasing treatment time. Ra of sample after APPJ-SiO_x deposition decrease monotonically with the increasing treatment time, and it is obviously smaller than that of untreated epoxy resin. Of these samples, Ra of APPJ-Si5 reaches 171 nm, which is the smallest value of plasma modified sample. These analysis above

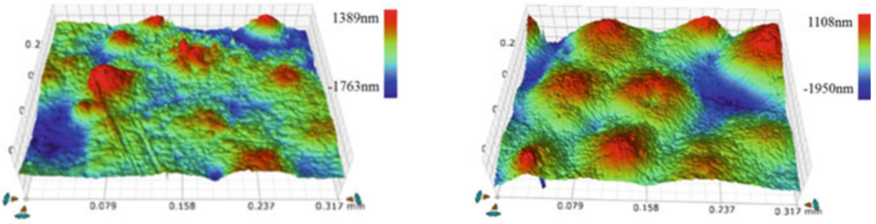

(a) Untreated (b) DBD SiO_x deposition

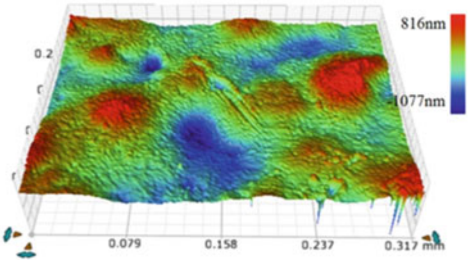

(c) APPJ SiO_x deposition

Fig. 22 Surface micro profile of epoxy resin before and after plasma SiO_x deposition

Fig. 23 Surface roughness of epoxy resin before and after plasma SiO_x deposition

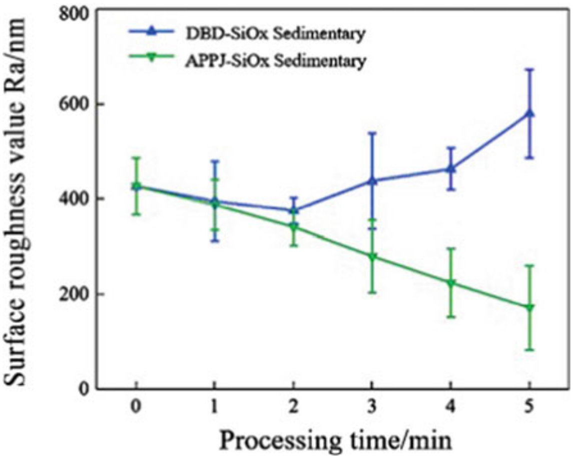

imply that APPJ-SiO_x deposition method effectively decrease surface roughness of epoxy resin by depositing uniform film to cover original defects of epoxy resin. For DBD-SiO_x deposited samples, the inconstancy of the surface roughness of epoxy resin results from the irregular thickness of film.

By combining the experimental results and analysis above, it can be concluded that plasma SiO_x deposition can decrease surface roughness by depositing film on the surface of epoxy resin, though the amount of reduction depends on whether uniformity of the film thickness. Specifically, the fixed structure of DBD electrodes yields an unevenly deposited film. Making it unsuitable for regulating micromorphology of epoxy resin. The APPJ electrode is flexible and can be combined with a rotating platform to make the thickness of generated film more even. The surface roughness value (Ra) of epoxy resin can be adjusted between 100 and 400 nm by varying the treatment time of APPJ-SiO_x deposition.

4 Plasma Modification on the Modulation of Surface Chemical Components of Epoxy Resin

Studies have revealed noteworthy differences in the distribution of main chemical elements on the surface of insulating materials following the use of different precursors, thereby altering the electrical properties. Similarly, it has been determined that changes to the surface functional groups, and thus electrical properties, are attainable when the same precursor is employed but with shifts in plasma discharge form and treatment times. Notably, these adjustments play a pivotal role in better understanding of the interplay between the chemical composition on the surface of insulating materials and electrical properties. In addition, studying the chemical composition and functional group changes of epoxy resin before and after plasma modification can clarify the reaction form between plasma and epoxy resin surface, reveal the mechanism of plasma's influence on the physicochemical properties of epoxy resin, and realize the regulation of the chemical composition of epoxy resin surface.

This section begins by presenting the discharge electrode form, treatment time, the control effects of subatmospheric pressure glow discharge, as well as plasma fluorination and plasma SiO_x deposition on the surface chemical composition of epoxy resin. It then analyzes the change pattern and reaction mechanism of the plasma treatment under different conditions on the chemical composition of the epoxy resin surface.

4.1 Modulation of Chemical Composition on the Surface of Epoxy Resin by Sub-atmospheric Glow Discharge

Attenuated total reflection-Fourier transform spectroscopy was employed to investigate the effect of glow discharge plasma on the surface composition of materials from both qualitative and quantitative aspects. Figure 24 reveals the typical molecular formula of epoxy resin. It is observable from the molecular formula that there are a large number of organic functional groups on the surface of the material: benzene ring, $–CH_x$, –CH(O)CH–, etc.

According to the composition of functional groups and chemical bonds of epoxy resin, Table 1 shows the typical infrared spectrum absorption peaks of epoxy resin. Together with the infrared spectrum, it is used to examine the influence of sub-atmospheric pressure glow discharge on the chemical structure of epoxy resin in combination.

The infrared spectra of epoxy resin before and after glow discharge modification are portrayed in Fig. 25. The FTIR spectrum of EP includes C–H absorption peaks at 3033–2871, 1180 and 827 cm^{-1}, CH_2 and CH_3 absorption peaks at 1460, C=O characteristic peaks at 1730 cm^{-1} and C=C absorption peaks at 1607 and 1506 cm^{-1}. Glow discharge modification did not change the surface absorption peak of epoxy resin.

To further analyze the effect of plasma modification on the chemical composition of the material surface, XPS technology was employed to determine the change of material elements and the composition ratio. Querying the XPS binding energy comparison table shows the binding energy of the chemical bond of each functional group is obtained, as depicted in Table 2.

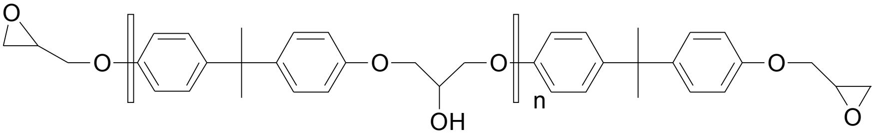

Fig. 24 Molecular formula of epoxy resin

Table 1 Typical infrared absorption peaks of epoxy resin

Absorption peak (cm^{-1})	Molecular structure
3033–2871	C–H
1730	C=O
1607	C=C
1506	C=C
1460	CH_2, CH_3
1180	C–H
827	C–H

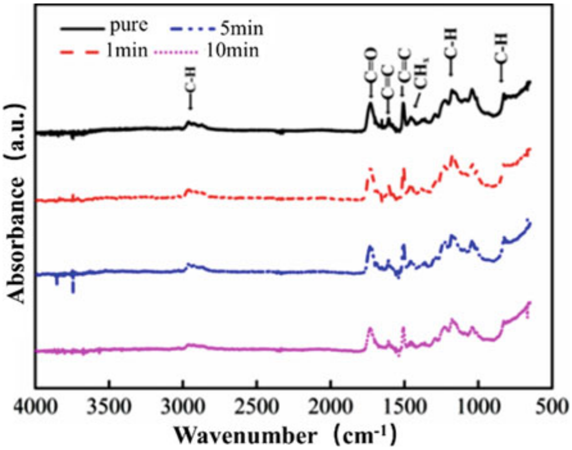

Fig. 25 FTIR spectral lines under different modification times

Table 2 Binding energy of chemical bonds of each functional group

Functional group chemical bond	Binding energy (eV)
C–C/C–H	284.7
C–O	286.3
C=O	288.8

Figure 26a and b are the XPS analysis spectra of the untreated and the samples treated for 3 min, respectively. It can be observed from the figure that the surface of untreated epoxy resin mainly contains an O 1s peak, C 1s peak, soft Si 2s peak, Si 2p peak and Al 2p peak. The appearance of the Al 2p peak is primarily attributed to the filler alumina in EP. the appearance of Si 2s and Si 2p is primarily attributed to the bisphenol A-based raw materials. After glow discharge treatment, the peak value of the O 1s peak increased significantly, and the peak value of the C 1s peak decreased slightly.

Figure 27 shows the C 1s peak spectrum on the epoxy resin surface before and after glow discharge treatment. As shown in Fig. 27a, C 1s of untreated EP can

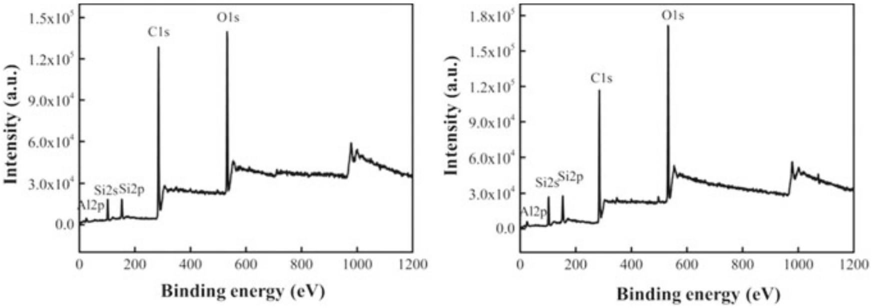

(a) Unprocessed

(b) Processing 3 min

Fig. 26 XPS spectra of material surface before and after modification

be decomposed into two peaks, C–C/C–H and C–O. After glow discharge treatment, the peak height and peak width of C 1s in the high binding energy part of EP were increased, indicating that glow discharge changed the composition and proportion of carbon-containing groups on the surface of epoxy resin. It can be seen that after glow discharge modification, the C–C/C–H content of the epoxy resin surface decreases, the C–O content increases, along with the integration C=O oxygen-containing groups.

The XPS PEAK software was used to analyze the percentages of the sample elements before and after treatment, as shown in Table 3. It was found that the content of carbon elements decreased from 63.41 to 50.07% after 3 min of treatment, while the oxygen increased from 24.41 to 40.41%.

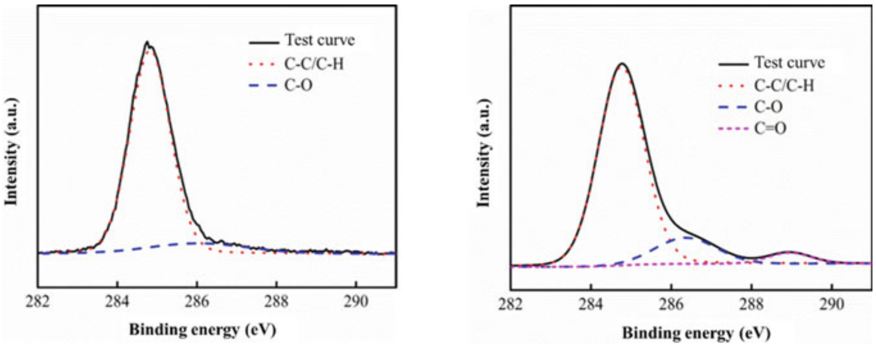

(a) Unprocessed C 1s split peak line

(b) C 1s split peak line after processing

Fig. 27 XPS peak splitting lines on the surface of epoxy resin before and after modification

Table 3 Change percentage of element content

Element content percentage (%)	C	O	Si
Unprocessed	63.41	24.41	8.36
Processing 3 min	50.07	40.41	9.14

4.2 Modulation of Surface Chemical Composition of Epoxy Resin by Plasma Fluorination

Figure 28 presents the XPS spectra of epoxy resin surfaces before and after fluorination of all DBD and APPJ. Observing the XPS spectrum, it was found that compared with the untreated epoxy resin sample, the C1s peak, O1s peak and F1s peak changed significantly after plasma fluorination, especially the F1s peak of DBD fluorination increased significantly. Based on the XPS spectrum, the relative content of the main elements can be calculated, as shown in Table 4. The epoxy resin sample is a three-dimensional network structure formed by carbon chain crosslinking filled with a considerable amount of micron alumina. This structure leads to the untreated epoxy resin sample being dominated by carbon elements and containing some oxygen elements and negligible fluorine elements. The content of fluorine element on the surface of the epoxy resin sample fluorinated by DBD increased obviously. It was observed that the fluorine content increased continuously with the increase of treatment time, up to 24.31%. The increase in fluorine content shows that plasma fluorination can increase fluorine elements' content on the epoxy resin surface and the treatment effect increases monotonically with the treatment time. Similarly, the fluorine elements' content on the epoxy resin's surface changed little after APPJ fluorination with the highest proportion of fluorine is only 5.14%, showing a negligible impact compared to carbon and oxygen. This can be attributed the contact area between the plasma plume and the epoxy resin is small during APPJ treatment and the discharge power of APPJ is smaller than that of DBD, Thus, resulting in the mediocre effect of APPJ fluorination.

It isn't straightforward to understand how plasma fluorination increases the fluorine content of epoxy resin only by comparing the relative content of chemical elements. In addition, the form in which fluorine element introduced on the surface of the epoxy resin remains unclear. Therefore, by further studying the XPS spectra and splitting the C1s peaks of untreated epoxy resin, DBD-F3 and APPJ-F3, the changes of carbon-containing functional groups before and after plasma fluorination can be obtained, as shown in Fig. 29. It was found that the C1s peak of untreated epoxy resin can be further subdivided into three peaks. In contrast, the C1s peak after plasma fluorination can be divided into more peaks, up to five peaks of DBD fluorination, and the peaks of each peak with distinct characteristics.

To quantitatively study the types and changes of carbon-containing functional groups before and after plasma fluorination, the peak values of each peak can be compared with the binding energy of specific functional groups in the XPS binding energy comparison table. At the same time, the ratio of the peak area of each spectrum

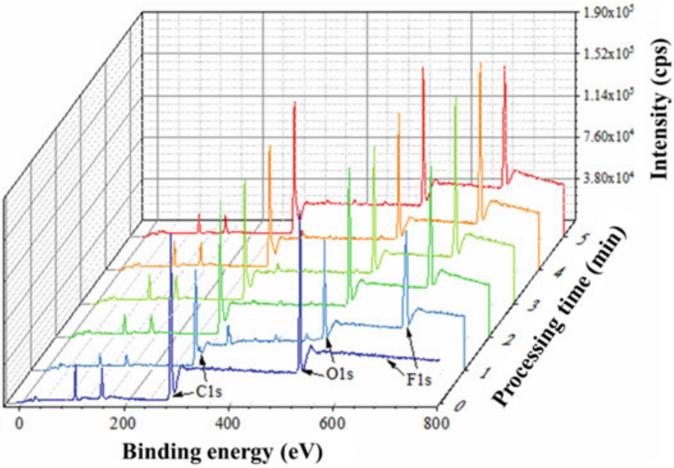

(a) DBD fluorination

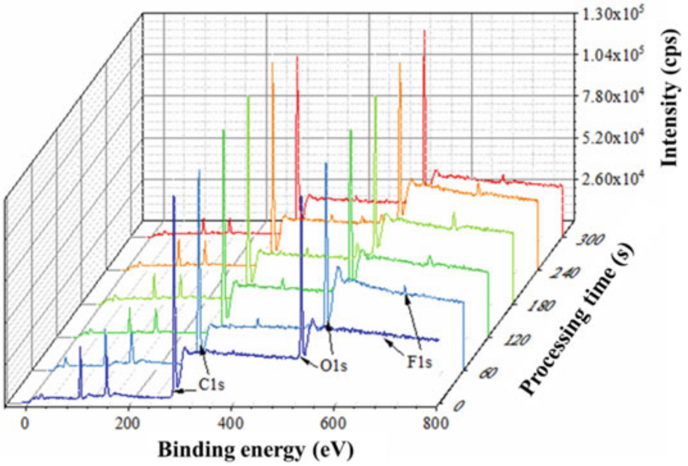

(b) APPJ fluorination

Fig. 28 XPS spectra of samples treated by plasma fluorination

to the total peak area is calculated and the summarized in Table 5. The analysis and summary results show that the carbon-containing functional groups on the surface of the untreated epoxy resin are mainly C–C bonds, together with some C–O bonds and O–C=O bonds. A large number of CF_x functional groups are added after plasma fluorination because the binding energy of the C–F bond (485 kJ/mol) and H–F bond (565 kJ/mol) is much higher than that of the F–F bond (153 kJ/mol) and C–H bonds (414 kJ/mol). When the high-energy plasma bombards the surface of the epoxy resin

Table 4 Relative element content of sample surface before and after plasma fluorination treatments

Relative element content/% (min)	C		O		F	
	DBD-F	APPJ-F	DBD-F	APPJ-F	DBD-F	APPJ-F
0	70.28		29.60		0.12	
1	60.33	61.29	26.58	37.43	13.09	1.28
2	57.89	70.85	26.17	26.43	15.94	2.72
3	57.69	68.89	26.29	25.97	16.02	5.14
4	51.82	69.84	26.24	25.36	21.93	4.80
5	54.43	69.78	21.26	26.37	24.31	3.86

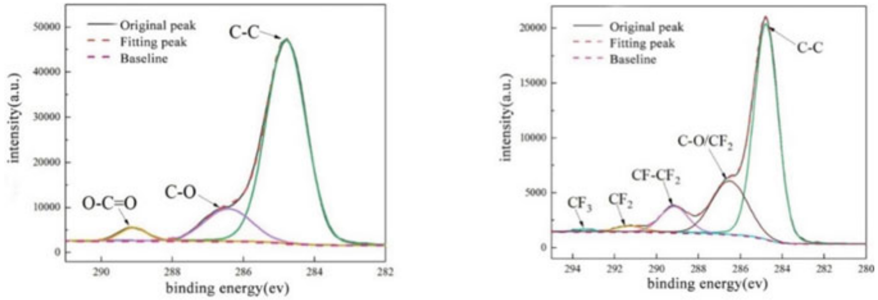

(a) Untreated (b) DBD fluorination

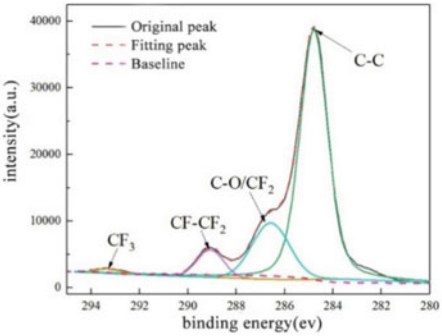

(c) APPJ fluorination

Fig. 29 C1s XPS spectra of samples before and after plasma fluorination

to break the carbon-containing chemical bond, this position will become a reactive site, thus allowing the amalgamation with the free fluorine element in the plasma to form a more stable C–F bond—a process known as plasma grafting.

Further analysis of the composition of each functional group after plasma fluorination revealed that both DBD and APPJ contained C–CF_2 (286.6 eV), CF–CF_2 (289.3 eV) and CF_3 (293.0 eV) functional groups after fluorination. However, the relative amount of each functional group is different. The amount of CF_2-containing

Table 5 Ratios of chemical bond content before and after plasma fluorination

Approach	Relative element content/%					
	C–C	C–O/C–CF_2	O–C=O/C–F	CF–CF_2	CF_2	CF_3
Unprocessed	81.50	15.01	3.49	–	–	–
DBD fluorination	61.25	24.73	–	11.36	1.98	0.68
APPJ fluorination	73.09	20.15	–	5.95	–	0.82

functional groups (C–CF_2 and CF–CF_2) after DBD fluorination was significantly higher than that of APPJ fluorination and additional CF_2 (291.0 eV) functional groups were added to the surface of epoxy resin after DBD fluorination. When taking into account the considerable the discharge power of DBD fluorination as well as the relative presence of F element, it is suggested that the DBD structure can provides a more comprehensive plasma fluorination.

In addition, the F 1s peak in the XPS spectrum after fluorination of DBD is subjected to peak splitting and the obtained spectrum is shown in Fig. 30. It can be found that the F1s peak is divided into two peaks, corresponding to the organometallic fluorine peak (685 eV) and the organic fluorine peak (688 eV). The organic fluorine peak refers to the CF_x functional group formed by the free fluorine element and the carbon element on the surface of the epoxy resin. The metal fluorine peak is attributable to the $AlOF_x$ functional group, as C–H bonds are broken, leading to the generation of free protons reacted with the free hydrogen elements to form HF. Moreover, there are a certain amount of micron alumina particles on the surface of the epoxy resin, and more alumina is exposed after plasma fluorination. The aluminum oxide will react with hydrogen fluoride to give rise to $AlOF_x$ functional groups. Besides, hydrogen fluoride is corrosive, further improving the etching effect of plasma fluorination [57].

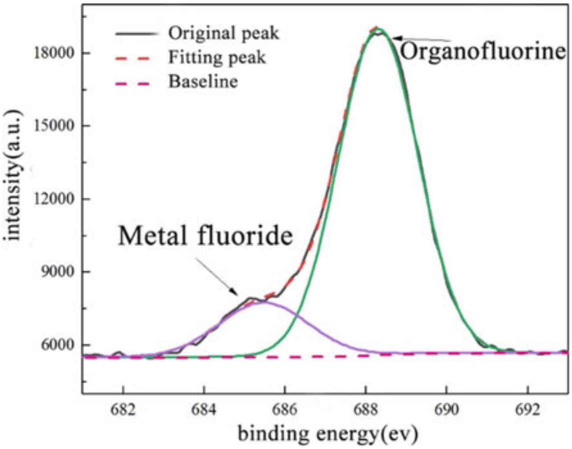

Fig. 30 F1s XPS spectrum of the epoxy resin after DBD fluorination

By studying the alterations in physical and chemical properties after plasma fluorination, the mechanism of the influence of plasma fluorination on the surface physical and chemical properties of epoxy resin can be obtained: The Ar/CF_4 mixed gas, up being excited by a high-frequency high-voltage power supply and transformed into a plasma state with tremendous energy, which internally ionizes many free fluorine elements. When the high-energy plasma bombards the surface of the epoxy resin, the high-energy plasma will break carbon-containing chemical bonds such as C–C bonds and C–H bonds and form reactive active sites. The reactive sites will combine with the free fluorine elements in the plasma to form strong C–F bonds. From the point of view of physical properties, the bond breaking and recombination of carbon chains lead to the destruction of the original surface morphology, and some alumina particles are exposed. Therefore, plasma fluorination can etch the surface of epoxy resin, the etching intensity strengthening with the extension of treatment time. From the perspective of chemical properties, plasma fluorination changes the original distribution of chemical elements on the surface of epoxy resin. A large amount of fluorine being grafted onto the surface of epoxy resin in the form of CF_x functional groups significantly increased the relative content of fluorine. In addition, hydrogen fluoride produced by C–H bond cleavage is corrosive. Hydrogen fluoride can react with alumina to generate $AlOF_x$ functional groups, further enhancing the plasma fluorination etching. From the above analysis we can conclude that the plasma fluorination method can regulate epoxy resin's surface element distribution, especially the fluorine elements' relative content. The reaction mechanism of plasma fluorination on the surface of epoxy resin is shown in formula (3). In addition, due to the higher discharge power of the DBD electrode, the plasma fluorination reaction can be more sufficient and the etching effect is more pronounced. Therefore, the surface of the epoxy resin is rougher after DBD fluorination, and more fluorine is grafted. Compared with APPJ, DBD modification can improve the effect of plasma fluorination.

$$\begin{cases} \text{R-H} \rightarrow \text{R}\cdot + \text{H}\cdot \\ \text{CF}_4 \rightarrow \text{CF}_3\cdot + \text{F}\cdot \\ \text{CF}_3\cdot \rightarrow \cdot\text{CF}_2\cdot + \text{F}\cdot \\ \cdot\text{CF}_2\cdot \rightarrow \cdot\text{CF}\cdot + \text{F}\cdot \\ \text{R}\cdot + \text{F}\cdot \rightarrow \text{RF} \\ \text{H}\cdot + \text{F}\cdot \rightarrow \text{HF} \\ \text{HF} + \text{Al}_2\text{O}_3 \rightarrow \text{AlOF}_x + \text{H}_2\text{O} \end{cases} \tag{3}$$

4.3 Modulation of Chemical Composition on the Surface of Epoxy Resin by Plasma SiO_x Deposition

Similar to the research steps of plasma fluorination, the XPS spectra of epoxy resin before and after plasma SiO_x deposition is shown in Fig. 31. It was found that the C1s peak, O1s peak and Si 2p peak changed after plasma SiO_x deposition. The peak value of C1s decreased with the extended plasma SiO_x deposition time, while the O1s peak and Si 2p peak increased with the increase of modification time. The relative content of main elements before and after plasma SiO_x deposition was also computed based on XPS spectra, as shown in Table 6. It was found that the untreated epoxy resin sample is still mainly composed of C element, but there is about 12% Si element. This is because a certain amount of silicon-containing coupling agent will be added to the micro-alumina filler during production, which can reduce the degree of agglomeration between the fillers and enhance the dispersion of the filler in the matrix, though a certain amount of Si element will be introduced. Unlike plasma fluorination, the relative content of C element decreased significantly after plasma SiO_x deposition. Instead, the content of Si element has increased, and the content of O element increased sharply. Especially after APPJ-SiO_x deposition, the content of O element accounts for 56% at most, which indicates that plasma SiO_x deposition not merely augmented the prevalence of Si element on the epoxy resin surface, but boosted the O element portion as well. The improvement effect changes slightly with the deposition time of plasma SiO_x. Furthermore, despite the DBD electrode encouraging the reaction, the content of O and Si elements in APPJ-SiO_x deposition is still higher than those in DBD-SiO_x deposition, which is contrary to the conclusion of plasma fluorination. This is because DBD-SiO_x deposition is carried out in the reactor, with the reaction atmosphere consisting of argon, while the reaction environment of APPJ-SiO_x deposition is air. Consequently, the plasma plume is exposed to the air and interacts with the epoxy resin sample, resulting in the surrounding oxygen participating in the reaction. Some studies have confirmed that by incorporating a appropriate amount of oxygen during plasma SiO_x deposition can promote the formation of thin films [47]. Therefore, the APPJ-SiO_x deployment can complete the reaction more efficiently.

Currently, it has been verified that plasma SiO_x deposition does indeed create a film on the surface of epoxy resin. In order to study the chemical composition of the film, the Si 2p in the XPS spectrum after plasma SiO_x deposition is processed by peak separation, and the new spectra is shown in Fig. 32. It can be found that the Si 2p peak before and after procedure can be divided into three peaks with the same peak value, but the peak areas of the three peaks corresponding to different methods are significantly different.

In order to ascertain the composition of the film on the surface of epoxy resin after plasma SiO_x deposition, each peak value was compared with the binding energy of typical functional groups in the XPS binding energy comparison table, and calculate the proportion of each peak area to the total peak area in each spectrum. The summarized results are shown in Table 7. It is found that the silicon-containing functional

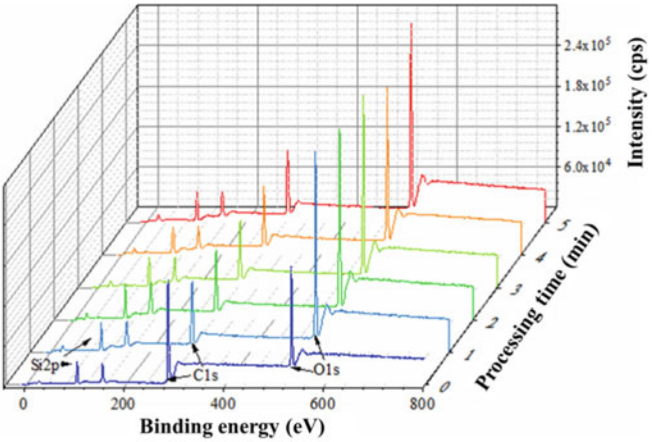

(a) DBD SiO_x deposition

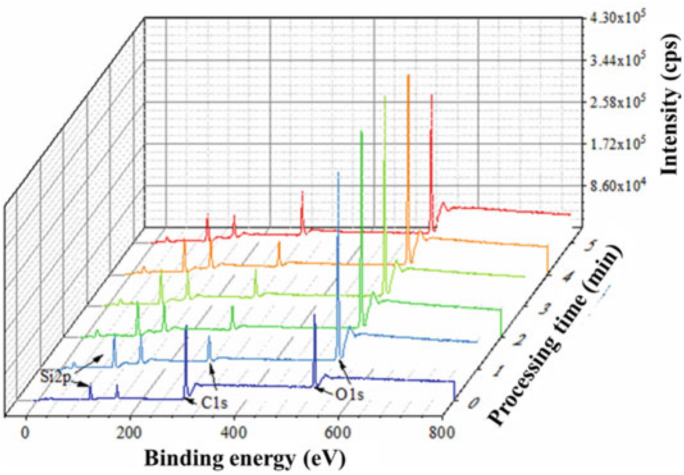

(b) APPJ SiO_x deposition

Fig. 31 XPS spectra of samples treated by plasma SiO_x deposition

groups before and after plasma SiO_x deposition are Si $(-O_2)$ (102.2 eV), Si$(-O_3)$ (102.8 eV) and Si$(-O_4)$ (103.4 eV). The relative content of Si$(-O_2)$ in untreated epoxy resin is up to 88%, while the relative content of Si$(-O_3)$ and Si$(-O_4)$ after plasma SiO_x deposition is significantly increased, especially in APPJ-SiO_x deposition, the relative content of Si$(-O_4)$ is up to 92%, while Si $(-O_2)$ is only 5%. This is consistent with the significant increase of O element content after plasma SiO_x deposition, and the increase of the proportion of Si$(-O_4)$ attests to a higher degree of reaction completeness in plasma SiO_x deposition.

Table 6 Relative element content of sample surface before and after plasma SiO_x deposition

Relative element content/% (min)	C		O		Si	
	DBD-Si	APPJ-Si	DBD-Si	APPJ-Si	DBD-Si	APPJ-Si
0	64.37		23.41		12.22	
1	41.63	24.81	41.37	52.97	17	22.22
2	39.47	19.75	41.7	56.43	18.83	23.81
3	40.01	22.25	39.24	53.34	20.75	24.41
4	43.78	20.85	38.49	54.66	17.73	24.48
5	43.09	35.61	39.44	43.18	17.48	21.2

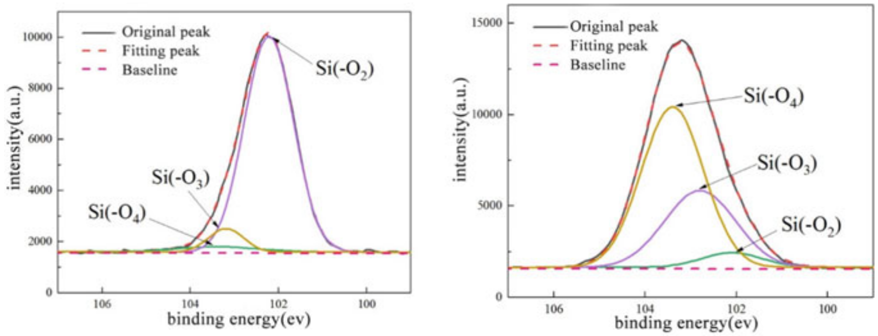

(a) Untreated

(b) DBD SiO_x deposition

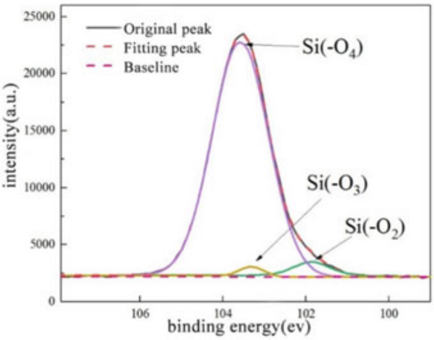

(c) APPJ SiO_x deposition

Fig. 32 Si 2p XPS spectra of samples before and after plasma SiO_x deposition

Table 7 Ratios of chemical bond content before and after plasma SiO_x deposition

Treatment method	Relative element content/%		
	Si(–O_2)	Si(–O_3)	Si(–O_4)
Untreated	88.79	7.19	4.01
DBD-SiO_x deposition	5.43	33.41	61.15
APPJ-SiO_x deposition	5.39	1.67	92.93

By comprehensive analysing the changes of physical and chemical properties after plasma SiO_x deposition, it can be concluded that the influence mechanism of plasma SiO_x deposition on the physicochemical properties of epoxy resin surface is as follows: one way of argon will blow TEOS out of the gas-washing bottle and mix with the other way of argon to form Ar/TEOS mixed gas. The mixed gas will be converted into plasma state under the excitation of high-frequency high-voltage power supply. The high energy plasma will decompose TEOS to generate reactive $Si(OH)_x$ compounds. These substances interact with Si–OH existing functional groups in the plasma and generate numerous of Si–O–Si functional groups. Finally, SiO_x film is formed and deposited on the surface of epoxy resin.

From the perspective of physical properties, plasma SiO_x deposition will generate a large number of nanoparticles on the surface of epoxy resin, and these particles aggregate to form a coralloid film. The film can cover the original defects on the surface of epoxy resin, ultimately reducing the surface roughness and thereby resulting in a more even surface. And the film coverage will continue to increase with the extension of treatment time. From the perspective of chemical properties, plasma SiO_x deposition also changed the original chemical element distribution on the surface of epoxy resin by introducing silica functional groups on the surface of epoxy resin in the deposited form, significantly improving the relative content of silicon and oxygen elements. The analysis above shows that the surface element distribution of epoxy resin can be modulated by plasma SiO_x deposition, especially the relative content of silicon element, and the reaction mechanism of plasma SiO_x deposition on the surface of epoxy resin can be obtained as shown in Formula (4) and Formula (5). In addition, because the reaction environment of APPJ-SiO_x deposition is air, the presence of ambient oxygen will accelerates the reaction process, so the APPJ electrode makes the reaction more sufficient; Because the APPJ electrode is more flexible, there are corresponding devices to ensure the uniformity of treatment, so the film produced by APPJ-SiO_x deposition is more even in comparison to DBD-SiO_x deposition.

$$\mathrm{Si(OC_2H_5)}_n\mathrm{(OH)}_{4-n} + e \rightarrow \mathrm{Si(OC_2H_5)}_{n-1}\mathrm{(OH)}_{4-n+1} + \mathrm{C_2H_4} + e \quad (4)$$

$$\mathrm{Si{-}OH} + \mathrm{Si{-}OH} \rightarrow \mathrm{Si{-}O{-}Si} + \mathrm{H_2O} \quad (5)$$

5 Modulation of Electrical Properties of Epoxy Resin Surfaces by Plasma Modification

It has been established that the surface physicochemical properties of insulating material are correlated to its electrical properties. Previous research has demonstrated that the physicochemical properties of the epoxy resin can be mortified by changing the experimental parameters. Therefore, it is necessary to further investigate into the effects of plasma modification methods on the electrical properties of epoxy resins, as well as the mechanism of electrical property changes.

This section presents the effect of different means on the flashover performance of epoxy resin surface, and analyze the influence of different methods on electrical parameters such as surface conductivity and surface charge aggregation characteristics. Additionally, the enhancement mechanism of various modification methods on the surface flashover performance will be explored, thereby establishing the correlation between plasma modification, physical and chemical properties of epoxy resin and electrical properties of epoxy resin. This enables the plasma modification to modulate the surface conductivity and surface charge dissipation rate of epoxy resin, as well as to enhance the surface flashover e performance.

5.1 Modulation of Surface Conductivity of Epoxy Resin by Plasma Modification

For the sub-atmospheric glow discharge treatment, the trend of surface conductivity with treatment time was illustrated in Fig. 33. It can be seen that the surface conductivity increase from 8×10^{-15} to 4×10^{-14} S/m when the treatment time is 1 min. The surface conductivity increased by a factor of 5. The surface conductivity continue to increase with the extension of the treatment time, but the increase in surface conductivity maintained a gradual yet slow rate. When the treatment time reaches 10 min, the surface conductivity of the sample is rose by a 10x. However, the bulk conductivity increase slightly after the modification, but the magnitude is much smaller than the surface conductivity increase. In summary, the glow discharge showed great efficacy in boosting the material surface conductivity by 10x.

Figure 34 shows the surface conductivity results of all samples before and after plasma fluorination and SiO_x deposition. The surface conductivity of the untreated epoxy resin samples is 3.11×10^{-18} S/m, and the surface conductivity is enhanced after various treatments. In general, the surface conductivity of the samples is monotonically increasing with the treatment time. In addition, the surface conductivity of the sample after plasma SiO_x deposition is higher than that of plasma fluorination. DBD-SiO_x deposition has the best effect in enhancing the electrical conductivity of epoxy resin surface up to 1.87×10^{-14} S/m. And the sample with the highest surface conductivity in plasma fluorination is DBD-F5, which is only 6.89×10^{-16} S/m. This result also shows that the surface conductivity of the epoxy resin can be

Fig. 33 Surface conductivity at different times of sub-atmospheric glow discharge

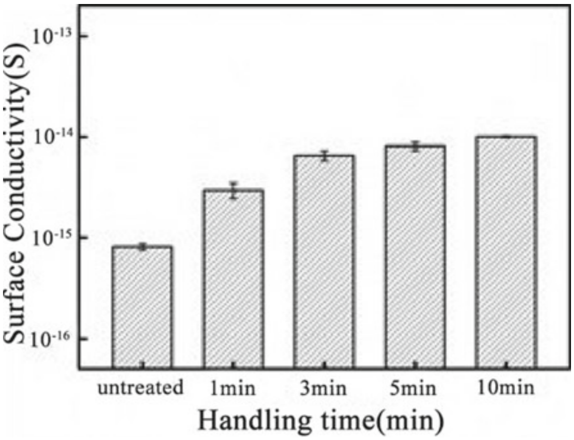

regulated between 10^{-18} and 10^{-16} S/m orders of magnitude using the plasma fluorination method described herein. However, plasma SiO_x deposition can modulate the surface conductivity of the epoxy resin between 10^{-17} and 10^{-14} S/m orders of magnitude.

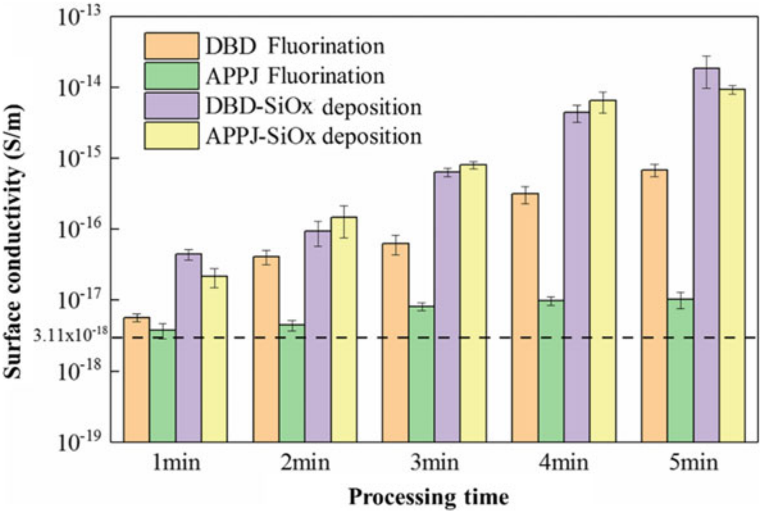

Fig. 34 Surface conductivity of epoxy resin before and after plasma modification

5.2 Modulation of Charge Dissipation Rate on Epoxy Resin Surface by Plasma Modification

Studies have shown that the surface flashover performance of an insulating material is influenced by the dissipation of the surface charge. And this rate can be approximated by the decay of surface potential [58]. With respect to the sub-atmospheric glow discharge, the Fig. 34 shows the sample surface potential decay curves at different modification times. It can be seen that These curves exhibit a double exponential decay form over the passage of time. In the initial moment of dissipation, an accelerated decline is observed on the surface potential, and the decay curve becomes slow and smooth as the dissipation time increases. Both the initial potential amplitude and the dissipated 600 s potential amplitude of the surface of the modified samples are lower than those of the untreated samples. It is also seen that the rate of decrease of surface potential rises with the increase of modification time from 0.5 to 3 min process. However, when the modification time continued to increase to 10 min, a saturation trend in the drop of surface potential was registered without any major variation in response to the prolonged modification duration.

For plasma fluorination and SiO_x deposition, the Fig. 35 shows the normalized surface potential decay from 0 to 30 min. The black dotted line in the figure denotes surface potential decay of the untreated epoxy resin. It can be found that the surface potential decay curves of most of the samples are below the black curve, indicating that the surface potential decay rate of these samples is faster than that of the untreated samples. In other words, the surface charge dissipation rate of these samples is faster than that of the untreated epoxy. From the perspective of processing time, the surface potential decay rates of all plasma-treated samples are positively correlated with the processing time. It is suggested that extending the processing time of plasma modification can accelerate the dissipation of charge on the surface of epoxy resin. From the perspective of the processing method, it is obvious for the decay of the epoxy resin surface potential after plasma SiO_x deposition. In particular, the surface potential of the APPJ-Si5 sample after 30 min is only 10% of the initial surface potential. And the degree of potential change of epoxy resin surface after plasma fluorination is not as good as plasma SiO_x deposition, especially APPJ fluorination. The surface potential of the APPJ-F5 sample with the highest decay is 83% of the initial surface potential at 30 min. Even the surface potential of the APPJ-F1 and APPJ-F2 samples decayed more slowly than that of the untreated samples. It indicates that both plasma fluorination and SiO_x deposition can accelerate the rate of charge dissipation on the epoxy resin surface. However, plasma SiO_x deposition is significantly more effective in dissipating the surface charge than plasma fluorination. From the perspective of plasma discharge electrodes, DBD fluorination is more competent in the decay of epoxy resin surface potential than APPJ fluorination. But APPJ-SiO_x deposition promotes the decay of epoxy resin surface potential better than DBD-SiO_x deposition. It indicates that the use of DBD electrode structure can enhance the dissipation rate of plasma fluorination on the surface charge of epoxy

Fig. 35 Decay curve of surface potential under different modification time

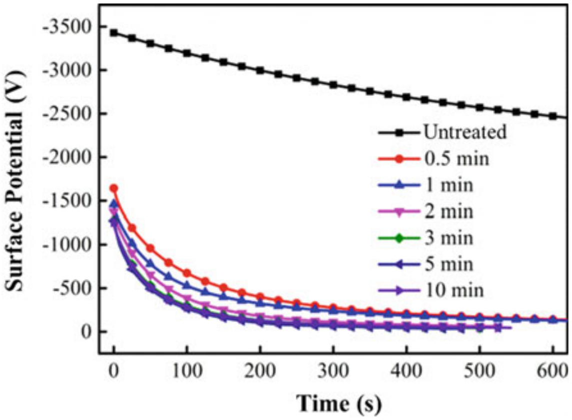

resin, while the use of APPJ electrode structure can boosts the dissipation rate of plasma SiO_x deposition on the surface charge of epoxy resin.

According to the solid state energy band theory [59, 60], the ordered stacking of atoms in crystals creates an overlapping array of atomic orbitals, forming quasi-continuous molecular orbital energy levels. This results in multiple energy bands and an energy gap between them. In general, the highest energy band in which electrons can survive and exist stably in a crystal determines the properties of the crystal, and this energy band is called the valence band. Since the electron distribution follows the principle of lowest energy, the energy band, which is lower in energy than the valence band, has been filled with electrons and cannot conduct electricity. The energy band, which is higher in energy than the valence band, is only partially occupied by electrons, allowing for the free movement of electrons here and they can conduct electricity. This energy band is called the conduction band. One criterion in solid state physics to distinguish a crystal as a metal, semiconductor or insulator is the size of the energy gap between the valence band and the conduction band. With no gap present, a material is a metal, a gap greater than 4 eV makes it an insulator, and between 0 and 4 eV causing a semiconductor. The region between the valence band and the conduction band is called forbidden band, since it's where electrons cannot exist stably.

But in fact, the atomic arrangement of most insulators is disordered, especially the epoxy resin is a three-dimensional network structure formed by countless carbon chains cross-linked and intertwined, which is a typical amorphous, plus the intrinsic defects of the material or the role of additives, will form a localized state whose energy level is in the forbidden band, where the electrons will transition and be bound. This localized state is called a carrier trap. On the one hand, the carrier trap will restrict the movement of carriers and promote the accumulation of a large number of charges. On the other hand, the carrier trap will reduce the energy of electronic transition, but will promote the migration of carriers. Whether carrier traps bind or promote carrier migration depends on the energy level of the traps. Therefore, studying the depth and distribution of trap energy levels on the surface of epoxy resin before and after plasma modification can reveal mechanism of the effect of plasma modification on the charge dissipation rate on the surface of epoxy resin.

According to the Isothermal Surface Potential Decay (ISPD) theory [61], the surface potential decay of an insulating material satisfies a certain function with its trap energy level depth and trap density. Therefore, it is necessary to describe the surface charge decay curve by a functional relationship. Studies show that the double exponential function fit the surface potential decay curve of epoxy resin. The fitting formula is shown in Eq. (6):

$$\varphi_{\mathrm{s}}(t) = Ae^{-\frac{t}{m}} + Be^{-\frac{t}{n}} \tag{6}$$

where $\varphi_{\mathrm{s}}(t)$ is the surface potential, t is a moment of the surface potential decay curve, and A, B, m, and n are the fitting coefficients. Therefore, the trap energy level E_{T} and trap density Q_{s} of this sample are calculated as shown in Eqs. (7) and (8):

$$E_{\mathrm{T}} = k_{\mathrm{B}}T\ln(vt) \tag{7}$$

$$Q_{\mathrm{s}} = t\frac{\varepsilon_0\varepsilon_r}{eL}\cdot\frac{\mathrm{d}\varphi_{\mathrm{s}}(t)}{\mathrm{d}t} \tag{8}$$

where k_{B} is the Boltzmann constant of 1.380649×10^{-23} J/K; T is the absolute temperature. The surface charge dissipation experiments of the group were conducted at a temperature of 26 °C. So the absolute temperature is taken as 299 K; v is the electron attempt escape frequency, taken as 4.17×10^{13} s^{-1}. e is the meta-charge, which is 1.6×10^{-19} C; L is the thickness of the sample, the epoxy resin samples prepared by the group are 3 mm thick, so the thickness of the sample is taken as 3 mm. ε_0 is the vacuum dielectric constant, which is 8.85×10^{-12} F/m; ε_{r} is the relative dielectric constant of the sample, and the study shows that the modification of the epoxy resin surface has less effect on its dielectric constant. Then the relative dielectric constant is taken as 4.5, which is the relative dielectric constant of the untreated epoxy resin.

For the sub-atmospheric glow discharge, Fig. 37 shows the surface charge trap energy level distribution curves of the specimens at varying modification times. It can be seen that the surface charge trap distribution curve of the untreated sample shows 2 characteristic peaks, corresponding to 2 different trap energy level depths and different peaks. After plasma treatment, the trap energy depths of the 2 characteristic peaks of the epoxy resin were gradually decreased. The second characteristic peak gradually disappears as the modification time increases. By further increasing the modification time, the depth of the trap energy level corresponding to the characteristic peak no longer decreases. The surface potential drop curves in Fig. 34 all show a double exponential drop pattern, implying that there are two trap mechanisms inside the epoxy resin. Corresponding to the pattern shown in the curves of Fig. 36, the peaks corresponding to the lower trap energy level depths in the figure represent shallow traps, while the peaks corresponding to higher trap energy level depths are associated with deep traps. It corresponds to 2 processes of rapid decrease of the specimen surface potential at the initial moment and slow decrease at the later stage [62]. With the extension of the modification time, the two trap energy levels become progressively shallower in depth, and the deep traps gradually decrease or even disappear. However, further increasing the modification time did not significantly change the trap energy depth. This was in line with the pattern reflected in Fig. 34, it can be seen that the trap energy level depth and peak of the surface charge trap energy level distribution curve can reflect the rate of surface potential drop.

For plasma fluorination and SiO_x deposition, Fig. 37 shows the trap energy level distribution curves for all samples. The trap energy level distribution curve of the epoxy resin was found to consist of a single peak or a double peak, and the depth of the trap energy level corresponding to the peak of the curve is the depth of the trap energy level mainly distributed in the sample. The trap energy level curve of the untreated epoxy is a single peak with a peak corresponding to a trap energy level depth of 1.08 eV. It indicates that the surface of untreated epoxy resin is mainly distributed with traps of energy level depth of 1.08 eV. This trap is deeper and is

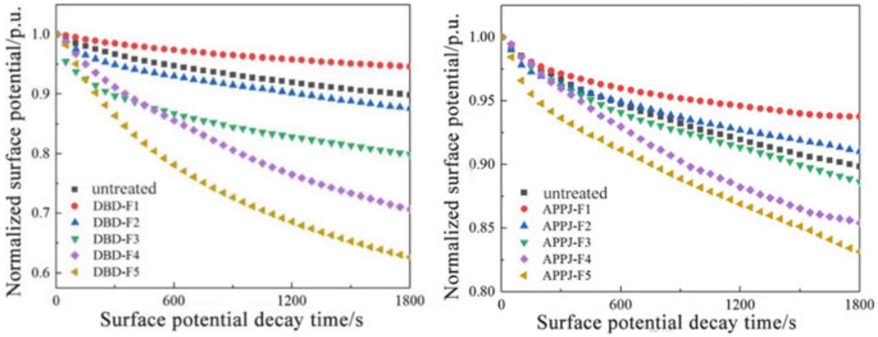

(a) DBD fluorination (b) APPJ fluorination

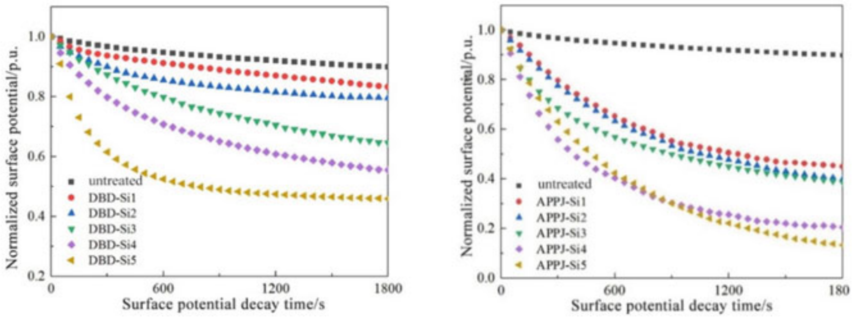

(c) DBD SiOx deposition (d) APPJ SiOx deposition

Fig. 36 Surface potential decay curve of epoxy resin before and after plasma modification

Fig. 37 Energy level distribution of surface traps under different modification times

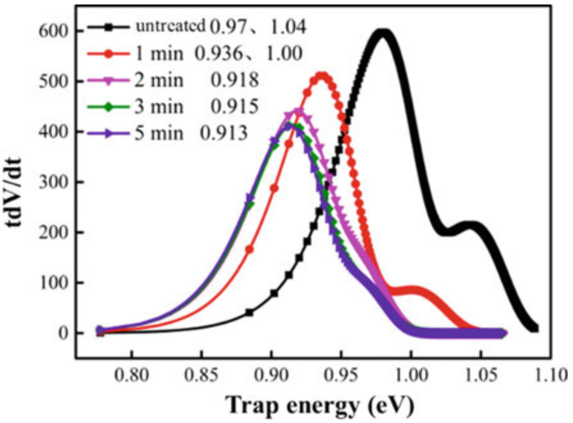

generally referred to as a deep trap. By analogy, the trap energy level distribution curve of APPJ-Si1 sample shows not only a deep trap peak of 1.06 eV, but also a peak with a trap energy level depth of only 0.98 eV. This trap depth is generally referred to as a shallow trap, indicating that there is already a partial distribution of shallow traps on the surface of the APPJ-Si sample (Fig. 38).

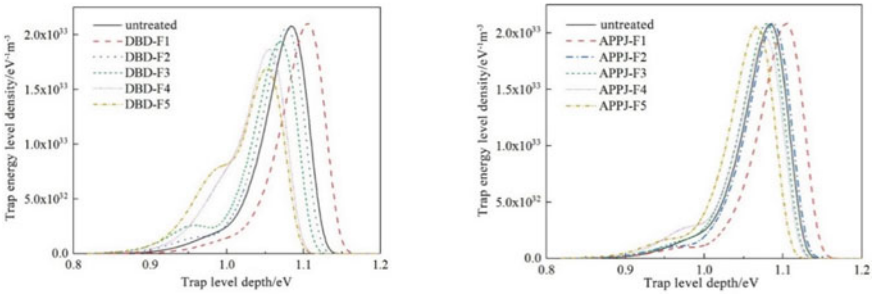

(a) DBD fluorination (b) APPJ fluorination

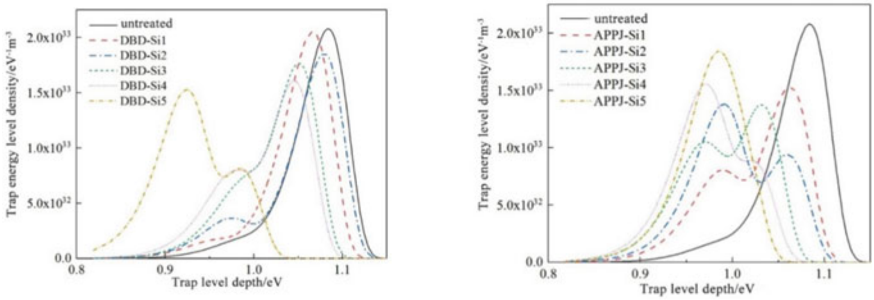

(c) DBD SiO_x deposition (d) APPJ SiO_x deposition

Fig. 38 Charge trap variation curve of epoxy resin before and after plasma modification

Further analysis of the trap energy level distribution curves on the surface of epoxy resin before and after plasma modification showed that most of the plasma-modified epoxy resin trap energy level depths are smaller than those of the untreated epoxy resin, and some samples exhibit shallow trap peaks. Increasing the plasma treatment time leads to progressive reduction of traps depths. This confirms that treating for longer periods would yield shallow the epoxy resin surface trap energy level depth. From the modification method, the depth of deep trap energy level of most DBD fluorinated epoxy resin becomes shallower, and then shallow traps appear. Of particular note, the shallow trap energy level depth of DBD-F3 sample reached 0.95 eV, but the epoxy resin after DBD fluorination still has deep trap as the main trap distribution. It indicates that DBD fluorination can lighten the epoxy resin surface trap energy level depth to some extent. However, the energy depth of deep traps in epoxy resin after APPJ fluorination is almost unchanged, and even if there are shallow traps, their proportion is much smaller than that of deep traps. It indicates that the effect of APPJ fluorination on the energy level distribution of epoxy traps is not significant. Plasma SiO_x deposition not only makes the depth of the deep trap energy level in the trap energy level distribution curve of the epoxy resin surface smaller, but also increases the area of the shallow trap peak. For example, the shallow trap peak height of DBD-Si5 and APPJ-Si5 samples has exceeded the deep trap. It shows that plasma SiO_x deposition can not only shallow the deep traps of epoxy resin, but also introduce more shallow traps, resulting in significant changes in the trap energy level distribution on the surface of epoxy resin.

Finally, through a comparison of the surface charge dissipation and trap energy level distribution of epoxy resin before and after plasma modification, it can be found that the epoxy resin samples with higher deep trap density have a notably slower rate of surface charge dissipation rate. This can be attributed to the fact that the deep trap binds the free charge which require significant energy to get out of the trap thus inhibiting the charge dissipation. The shallow trap with small trap energy level depth can easily trap the free charge, and the free charge can easily absorb enough energy to get out of the trap, thus accelerating the charge migration process, resulting in an acceleration of the charge dissipation.

5.3 Mechanistic Analysis of Plasma Modification to Enhance the Flash Performance of Epoxy Resin Along the Surface

For the sub-atmospheric glow discharge, the magnitude of the negative DC voltage resistance before and after the modification was tested at an atmospheric ambient electrode distance of 5 cm, as shown in Fig. 39. After a certain time of glow discharge, the increase in surface conductivity accelerates the original surface charge collection and slows down the effect of surface charge on electric field distortion. This leads to an increase in the DC flashover voltage. When the modification time is increased to 5 min, the increase in conductivity of the material surface reaches saturation, thus

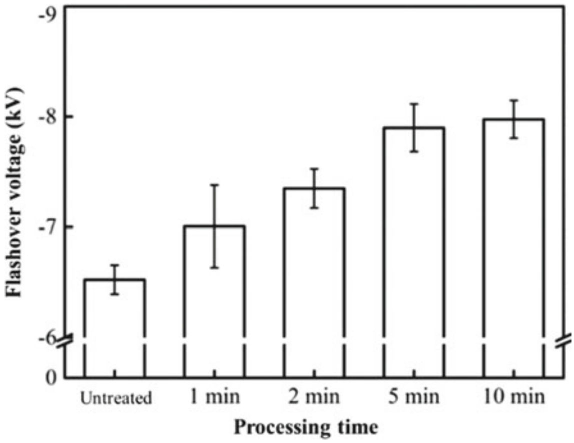

Fig. 39 Flashover voltage under different modification time

causing a cessation in surface charge dissipation rate growth and inhibiting further enhancement of flashover voltage. Therefore, with the extension of modification time, the flashover voltage sharply initially and then more slowly and the surface flashover voltage increased from −6.6 to −7.8 kV without treatment, with a maximum increase of about 17%.

For plasma fluorination and SiO_x deposition, the surface flashover voltages of all epoxies before and after modification are shown in Fig. 40. Since we use a negative polarity DC power supply to test the surface flash performance of all the samples, we take all the along-surface flash voltage values as absolute values for the sake of comparison. It can be discovered the surface flashover voltage of the untreated epoxy samples is 9.45 kV, and the along-surface flashover voltage of all the plasma-modified epoxies has increased. The DBD fluorinated epoxy resin has the best increase in flashover voltage up to 11.45 kV, which is 21.2% higher than the untreated sample. We observed the effect of various plasma modification methods on the surface flashover voltage with respect to the length of treatment time. We found that all plasma modification means caused a decrease in the flashover voltage at long modification time. Among them, the flashover voltage of APPJ-SiO_x deposition decreased severely after 3 min of modification, with the highest decrease from 11.28 kV at 3 min to 10.03 kV, which is a decrease of 11%. The plasma treatment time of 3 min and less was considered as short time treatment, and the enhancement effect of each plasma modification method on the epoxy resin along the surface flash in this interval was ranked as follows: DBD fluorination > APPJ-SiO_x deposition > DBD-SiO_x deposition > APPJ fluorination. Taking the plasma treatment time of 3 min and above as the long time treatment, the enhancement effect of each plasma modification method on epoxy resin along the surface flash in this interval was ranked as follows: DBD fluorination > DBD-SiO_x deposition > APPJ fluorination > APPJ-SiO_x deposition.

Based on a range of the experimental studies and analyses, we uncovered the correlation between the plasma modification method, physical and chemical properties of

Fig. 40 Surface flashover voltage of epoxy resin before and after plasma modification

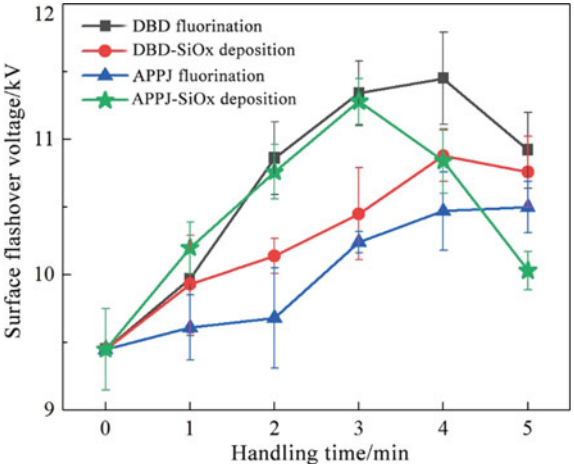

epoxy resin, and electrical properties of epoxy resin, and analyzed the mechanism of plasma modification to enhance the surface flash performance of epoxy resin.

To explain the process of flashing along the surface of the epoxy resin: when the negative polarity DC high-voltage power supply is continuously boosted, a large amount of surface charge is generated at the junction of the needle-pin electrode, the epoxy resin surface and the air. These charges migrate to the opposite electrode aided by the action of the external electric field. When the surface charge continuously migrates and forms a conductive channel through, the two electrodes conduct and flashover occurs along the surface. If surface charges accumulate in a large amount at the triple bonding point, these charges will seriously distort the external electric field, which will further promote the occurrence of flashover along the surface. Therefore, the flashover performance of epoxy resin mainly depends on the dissipation rate of surface charges. The surface conductivity of the untreated epoxy sample is only 10^{-18} orders of magnitude and the deep trap density is too high, which makes it difficult for surface charges to migrate across the surface. This leads to the gathering of substantial amount of charges at the triple bonding point, thereby distorting the external electric field and triggering surface flashover. The results of the surface flashover experiments further confirm that the untreated epoxy resin has the lowest surface flashover voltage.

Sub-atmospheric pressure glow discharge, on the one hand, the modification improves the surface conductivity of the material, and promotes the surface charge dissipation process along the surface. On the other hand, the surface trap level depth of the modified sample is lower than before, and the number of deep traps is significantly reduced, which accelerates the charge detrapping process. The improvement of surface conductivity and the shallowing of trap energy levels jointly promote the rapid dissipation of surface charges, thereby slowing down the effect of surface charges on electric field distortion and inhibiting the occurrence of discharge along the surface.

As for plasma fluorination and SiO_x deposition, we compared the surface flashover voltage of all modified epoxy resins, and APPJ fluorination has the smallest increase in the surface flashover voltage of epoxy resins. It was also found that APPJ fluorination improved the surface roughness of epoxy resin. However, only a small amount of fluorine was grafted on the surface of the epoxy resin, and the surface conductivity and surface charge dissipation rate were slightly improved, with surface trap energy level distribution changing little. It can be known from the literature [18] that an appropriate amount of surface roughness of insulating materials can increase the probability of surface charges being recaptured during surface migration, thereby increasing the rate of surface charge dissipation. Therefore, it can be concluded that the improvement mechanism of APPJ fluorination on the surface flashover performance of epoxy resin: Due to the lower discharge power and small treatment area of APPJ fluorination. Only a small amount of fluorine is grafted onto the surface of the epoxy resin, which has little effect on the chemical composition of the surface of the epoxy resin. Therefore, the surface roughness of the epoxy resin is mainly increased by the etching effect of the plasma, which increases the chances of the surface charge being recaptured when it migrates on the surface of the epoxy resin. At the same time, APPJ fluorination also slightly increased the surface conductivity of the epoxy resin. Thereby, the dissipation of the surface charge is accelerated, suppressing the distortion effect caused by the accumulation of the surface charge. So compared with untreated epoxy resin, APPJ fluorination can slightly improve the flashover performance along the surface.

This paper experimentally demonstrates that DBD fluorination of epoxy resin vastly supersedes APPJ fluorination in terms of improving the surface flashover voltage of epoxy resin. It is revealed that DBD fluorination produces a rough surface texture with a high concentration of fluorine atoms and groups, both of which enhance surface conductivity and charge dissipation rate. In addition, the deep traps on the surface of epoxy resin were shallowed and a small number of shallow traps appeared. These combined changes hold profound implications on the surface flashover performance of epoxy resin—that DBD fluorination improves the surface flashover performance of epoxy resin: due to the high discharge power and large treatment area of DBD fluorination, a large number of fluorine elements and fluorine-containing groups are grafted onto the surface of epoxy resin. And the etching effect of the high-energy plasma is used to greatly improve the surface roughness of the epoxy resin. On the one hand, the presence of fluorine-containing groups changes the original chemical composition of the epoxy resin surface. This leads to changes in the distribution of surface trap energy levels, that is, the depth of deep trap energy levels becomes shallower and a small number of shallow traps are introduced, thereby promoting the migration of surface charges on the surface of epoxy resin; On the other hand, a rougher surface will also increase the probability of surface charges being captured during surface migration, and the increase in surface conductivity will also accelerate surface charge migration. DBD fluorination guarantees greater charge dissipation compared to APPJ fluorination. It makes the surface charge more difficult to accumulate, so the effect of DBD fluorination on the surface flashover performance of epoxy resin is better than that of APPJ fluoridation.

The above analysis suggests that increasing the charge dissipation rate can improve the surface flashover performance. However, experiments show that the surface charge of APPJ-SiO_x deposited on the surface of epoxy resin dissipates the fastest, and its surface flashover voltage has an obvious downward trend when the treatment time is greater than 3 min. In addition, the lowest creeping flashover voltage is even close to that of untreated epoxy resin, and the surface charge dissipation rate of the DBD fluorinated 5 min sample is greater than that of other DBD fluorinated samples. However, the phenomenon of flashover voltage drop along the surface also appeared. These observations indicate that further explorations are required to understand the mechanism of flashover lifting along the surface. Further studying the changes in physicochemical properties and electrical properties of epoxy resin after APPJ-SiO_x deposition, we found that APPJ-SiO_x deposition enables TEOS to go through a condensation reaction, resulting in the formation and deposition of dense nanoscale SiO_x films over the epoxy resin surface. Through doing this, the existing material defects in the epoxy resin are covered up, thus flattening its surface. In addition, the deposited SiO_x films introduce an abundance of silicon-oxygen groups, which change the original chemical composition of the epoxy resin surface. The wax film is filled with a multitude of shallow traps, which also changes the trap energy level distribution on the epoxy resin surface and increases the surface conductivity of the epoxy resin by nearly four orders of magnitude. Even though the reduction in surface roughness decreases the rate of surface charge dissipation, the presence of a large number of shallow traps, on the contrary, greatly promotes the migration of surface charge. Therefore, the surface charge dissipation of the epoxy resin after APPJ-SiO_x deposition is the most rapid. However, due to excessive charge migrating to the opposite electrode, flashover may take place along the face. If the surface charge of epoxy resin is dissipated at a rapid speed, although the surface charge is not easy to accumulate in large quantities and distort the external electric field, it will provide seed charge for the development of flashover along the surface and promote the formation of penetrating conductive channels. This will make the surface flash performance of epoxy resin decline.

Reviewing the flashover voltage and surface charge dissipation along the surface of DBD fluorination and APPJ-SiO_x deposition, we found that the surface charge of epoxy resin dissipated too fast at 5 min of DBD fluorination and greater than 3 min of APPJ-SiO_x deposition. These findings indicated flashover voltage decrease along the surface. Therefore, it can be summarized that the mechanism of APPJ-SiO_x deposition to improve the flash performance of epoxy resin along the surface: APPJ-SiO_x deposition, through the polymerization effect of high-energy plasma, causes TEOS condensation reaction to generate SiO_x film and deposit on the surface of epoxy resin, covering the original defects of epoxy resin and reducing the surface roughness. At the same time the presence of SiO_x films introduces a large number of silicone oxygen groups on the epoxy resin surface, which significantly increases the surface conductivity while making the surface trap energy level distribution dominated by shallow traps. This greatly accelerates the dissipation of surface charge. Therefore, the short time of APPJ-SiO_x deposition also inhibits the accumulation of surface charges and improves the performance of flashover along the surface. However, prolonged

APPJ-SiO_x deposition causes too rapid dissipation of surface charge, which inhibits surface charge accumulation but significantly accelerates charge migration between electrodes and promotes the formation of penetrating conductive channels, which instead reduces the flashover performance along the surface.

The changes in the physicochemical properties and electrical properties of the epoxy resin surface after DBD-SiO_x deposition are basically the same as those of APPJ-SiO_x deposition, so the enhancement mechanism of DBD-SiO_x deposition on the flashing properties of the epoxy resin along the surface is similar to that of APPJ-SiO_x deposition. However, the effect of DBD-SiO_x deposition on the flashover voltage along the surface of epoxy resin is generally more limited due to the fixed the relative position of the DBD electrode, which makes it difficult to control the uniformity of the SiO_x film. This affects the effect of improving the electrical properties of the epoxy resin. The APPJ electrode structure is more flexible, and other devices can be configured to improve the uniformity of the deposited film. Moreover, the deposition of APPJ-SiO_x is carried out in the air, with oxygen further promoting the decomposition of TEOS and thus allowing for a better effect than DBD-SiO_x deposition.

Finally, a summary of the correlation between the plasma modification conditions, the physical and chemical properties of the epoxy resin surface, and the electrical properties of the epoxy resin surface can be made: the reaction precursor determines which plasma effect is used to modify the epoxy resin surface. Using CF_4 as a precursor facilitates both plasma etching and grafting effects to increase the surface roughness of the epoxy resin and graft fluorine-containing groups on the surface of the epoxy resin, thereby increasing the surface conductivity and reducing the depth of the original trap level. Ultimately, the surface charge dissipation rate is increased. Using TEOS as a precursor can make use of the plasma polymerization effect to cause TEOS to become polymerized and form a SiO_x film and deposit it on the surface of epoxy resin. This leads to reduction of the surface roughness of the epoxy resin and introduction of a large number of siloxane groups, thereby greatly improving the surface conductivity and significantly reducing the depth of the original trap level and forming an array of shallow traps—thus greatly increasing the surface charge dissipation rate.

The duration and the discharge electrode employed are significant factors that affect the efficacy the plasma modification. Prolonging the treatment time allows the plasma to modify the epoxy resin, and strengthen the effects of plasma etching, grafting and polymerization. This magnifies the advantages and disadvantages of plasma modification. The DBD electrode has a greater discharged power and a larger treated area, which enable more sufficient; but the structure of the DBD electrode is fixed, which leads to an uneven treatment effect, so it is not suitable for plasma SiO_x deposition. The APPJ electrode structure is flexible, and can be combined with appropriate apparatus to boost the evenness of modification, and the reaction can be carried out in the air. Therefore, when combined with the plasma SiO_x deposition method, the SiO_x film formed is uniform and dense; but the discharge power of the APPJ electrode is low, and the treatment area is small, which leads to poor effect of plasma fluorination.

6 Conclusion

This chapter systematically presents three plasma modification methods of epoxy resin, including sub-atmospheric glow discharge, plasma fluorination, and plasma SiO_x deposition. In addition, this chapter makes a comprehensive comparison of the effects of three methods on the surface properties of epoxy resins. Experiments attest to the effect of three plasma modification methods on the surface micro-morphology, chemical composition, surface conductivity and surface charge dissipation rate of epoxy resin. The relationship among the plasma modification method, the physical and chemical properties of the epoxy resin surface and the electrical properties of the epoxy resin surface was established. The mechanism of plasma modification to improve the surface flashover performance of epoxy resin is also elucidated. The main work and conclusions are as follows:

(1) Sub-atmospheric pressure glow discharge and plasma fluorination modification utilize the etching effect and grafting effect of high-energy plasma. The subatmospheric pressure glow discharge increased the oxygen content of the epoxy resin. In addition, the plasma fluorination enhanced the surface roughness and the relative content of fluorine-containing groups of the epoxy resin. Plasma SiO_x deposition modification utilizes the polymerization effect of high-energy plasma. Plasma SiO_x deposition modification reduces the surface roughness and increases the content of siloxane groups by depositing SiO_x film on the surface of epoxy resin.

(2) Increasing the surface roughness of epoxy resin will accelerate the dissipation rate of its surface charge. Introducing oxygen-containing and siloxy groups on the surface of epoxy resin will reduce the depth of trap energy levels and present many shallow traps, through which the charge can rapidly transit, leading to significantly improvement in the surface charge dissipation rate.

(3) Improving the surface charge dissipation rate is conducive to evacuating surface charges, thereby restraining the electric field distortion effect caused by a large amount of charge accumulation. Therefore, increasing the surface charge dissipation rate is beneficial to improving the surface flashover performance of epoxy resin. Nevertheless, the rapid dissipation of surface charge will promote the formation of penetrative conducting channels between electrodes, thus diminishing the surface flashover performance. To sum up, the surface charge dissipation rate needs should be appropriately regulated within a certain range.

References

1. Shao, T., Kong, F., Lin, H.F., et al.: Correlation between surface charge and DC surface flashover of plasma treated epoxy resin. IEEE Trans. Dielectr. Electr. Insul. **25**(4), 1267–1274 (2018)
2. Lu, X.P., Yan, P., Ren, C.S., et al.: Review on atmospheric pressure pulsed DC discharge. Sci. Sinica Phys. Mech. Astron. **41**(07), 801–815 (2011)

3. Wang, F., Fang, Z., Qiu, Y.C.: Study of charge accumulation on insulator surface in HVDC gas-insulated switchgear. J. Chin. Electr. Eng. Sci. **03**, 107–111 (2005)
4. Dai, D., Ning, W.J., Shao, T.: A review on the state of art and future trends of atmospheric pressure low temperature plasmas. Trans. China Electrotech. Soc. **32**(20), 1–9 (2017)
5. Xie, Q., Wang, Y., Liu, X., et al.: Characteristics of microsecond-pulse surface flashover on epoxy resin surfaces in SF6. IEEE Trans. Dielectr. Electr. Insul. **23**(4), 2328–2336 (2016)
6. Zhang, H.B., Chen, Q.: Recent progress of non-thermal plasma material surface treatment and functionalization. Phys. Sci. J. **70**(9), 22–38 (2021)
7. Zhang, C., Gu, J.W., Shao, T., et al.: Discharge mode in the repetitive nanosecond-pulsedischarge in atmospheric pressure air. High Power Laser Part. Beams **26**(4), 203–209 (2014)
8. Shen, Y., Wang, R.X., Zhang, C., et al.: Characterization of atmospheric pressure helium plasma jet driven by microsecond pulse. High Power Laser Part. Beams **28**(5), 112–118 (2016)
9. Ma, Y.F., Zhang, C., Li, C.Y., et al.: Experimental study of accelerating surface charge dissipation on polymer treated by repetitively pulsed discharge plasmas. J. Chin. Electr. Eng. Sci. **36**(6), 1731–1738 (2016)
10. Ishikawa, S., Yukimura, K., Matsunaga, K., et al.: Surface modification of poly (tetrafluoroethylene) film using dielectric barrier discharge of intermittent pulse voltage. Jpn. J. Appl. Phys. **39**(9R), 5223 (2000)
11. Sarani, A., Nikiforov, A.Y., Leys, C.: Atmospheric pressure plasma jet in Ar and Ar/H_2O mixtures: optical emission spectroscopy and temperature measurements. Phys. Plasmas **17**(6), 063504 (2010)
12. Shao, T., Wang, R.X., Zhang, C., et al.: Atmospheric-pressure pulsed discharges and plasmas: mechanism, characteristics and applications. High Volt. **3**(1), 14–20 (2018)
13. Mei, D.H., Fang, Z., Shao, T.: Recent progress on characteristics and applications of atmospheric pressure low temperature plasmas. J. Chin. Electr. Eng. Sci. **40**(4), 1339–1358+1425 (2020)
14. Liu, W.Z., Chai, M.L., Hu, W.L., et al.: Generation of atmospheric pressure diffuse dielectric barrier discharge based on multiple potentials in air. Plasma Sci. Technol. **21**(7), 074004 (2019)
15. Luan, P., Knoll, A., Wang, H., et al.: Model polymer etching and surface modification by a time modulated RF plasma jet: role of atomic oxygen and water vapor. J. Phys. D: Appl. Phys. **50**(3), 03LT02 (2016)
16. Dai, Y.C., Zhang, M., Li, Q., et al.: Separated type atmospheric pressure plasma microjets array for maskless microscale etching. Micromachines **8**(6), 173 (2017)
17. Seok, D.C., Yoo, S.R., Lee, K.I., et al.: Relation between etching profile and voltage–current shape of sintered SiC etching by atmospheric pressure plasma. Plasma Sci. Technol. **21**(4), 045504 (2019)
18. Shao, T., Zhou, Y.X., Zhang, C., et al.: Surface modification of polymethyl-methacrylate using atmospheric pressure argon plasma jets to improve surface flashover performance in vacuum. IEEE Trans. Dielectr. Electr. Insul. **22**(3), 1747–1754 (2015)
19. Shao, T., Liu, F., Hai, B., et al.: Surface modification of epoxy using an atmospheric pressure dielectric barrier discharge to accelerate surface charge dissipation. IEEE Trans. Dielectr. Electr. Insul. **24**(3), 1557–1565 (2017)
20. Shao, T., Zhang, C., Wang, R.X., et al.: Atmospheric-pressure pulsed gas discharge and pulsed plasma application. High Volt. Eng. **42**(3), 685–705 (2016)
21. Chen, S.L., Wang, S., Wang, Y.B., et al.: Surface modification of epoxy resin using He/CF_4 atmospheric pressure plasma jet for flashover withstanding characteristics improvement in vacuum. Appl. Surf. Sci. **414**, 107–113 (2017)
22. Zhang, C., Zhou, Y., Shao, T., et al.: Hydrophobic treatment on polymethylmethacrylate surface by nanosecond-pulse DBDs in CF_4 at atmospheric pressure. Appl. Surf. Sci. **311**, 468–477 (2014)
23. Zhan, Z.Y., Ruan, H.O., Lv, F.C., et al.: Plasma fluorinated epoxy resin and its insulation properties in C_4F_7N/CO_2 mixed gas. Trans. China Electrotech. Soc. **35**(8), 1787–1798 (2020)

24. Wan, F.C.: The Surface fluorination of Crosslinked Polystyrene and Its Vacuum Surface Flashover Performance Research. Wuhan University of Technology (2017)
25. Wan, F.C., Xu, F.F., Wei, W., et al.: Surface modification of cross-linked polystyrene by CF_4 plasma and its vacuum surface flashover performance. High Volt. Eng. **44**(12), 3857–3864 (2018)
26. Kang, Y.C., Yan, J.Y., Peng, C.K., et al.: Plasma dielectric barrier discharge fluorination modified epoxy resin and its ageing behavior. High Power Laser Part. Beams **33**(6), 161–171 (2021)
27. Peyroux, J., Dubois, M., Tomasella, E., et al.: Enhancement of surface properties on commercial polymer packaging films using various surface treatment processes (fluorination and plasma). Appl. Surf. Sci. **315**, 426–431 (2014)
28. Zhang, C., Ma, Y.Y., Kong, F., et al.: Atmospheric pressure plasmas and direct fluorination treatment of Al_2O_3-filled epoxy resin: a comparison of surface charge dissipation. Surf. Coat. Technol. **362**, 1–11 (2019)
29. Kong, F., Chang, C., Ma, Y.Y., et al.: Surface modifications of polystyrene and their stability: a comparison of DBD plasma deposition and direct fluorination. Appl. Surf. Sci. **459**, 300–308 (2018)
30. Matsubara, K., Danno, M., Inoue, M., et al.: Surface fluorination of polystyrene particles via CF_4 plasma irradiation using a barrel-plasma-treatment system. Surf. Coat. Technol. **236**, 269–273 (2013)
31. Xie, Q., Duan, Q.J., Shao, S., et al.: Effect of barium titanate nanofibers and plasma fluorination on surface insulation properties of epoxy resin composites. J. Chin. Electr. Eng. Sci. **40**(12), 4051–4063 (2020)
32. Ruan, H.O.: The Effect of Nano-Al_2O_3 and Nano-TiO_2 and Their Fluorination on the Surface Insulation Properties of Epoxy Resin. North China Electric Power University, Baoding (2019)
33. Ruan, H.O., Xie, Q., Lü, F.C., et al.: Filler fluorination of nanoTiO_2/ER composites and their surface insulation properties: a comparison of dielectric barrier discharge and chemical solution fluorination. J. Phys. D Appl. Phys. **53**(14), 145204 (2020)
34. Lv, F.C., Zhan, Z.Y., Zhang, L.G., et al.: Effect of plasma fluorinated modified micro-AlN filler epoxy resin on the insulation properties. Trans. China Electrotech. Soc. **34**(16), 3522–3531 (2019)
35. Lv, F.C., Liu, C.B., Zhan, Z.Y., et al.: Effect of plasma fluorinated nano-SiC/epoxy composite coating on the flashover characteristics. High Volt. Eng. **46**(7), 2444–2452 (2020)
36. Armenise, V., Milella, A., Fracassi, F., et al.: Deposition of thin films containing carboxylic acid groups on polyurethane foams by atmospheric pressure non-equilibrium plasma jet. Surf. Coat. Technol. **379**, 125017 (2019)
37. Kakiuchi, H., Higashida, K., Shibata, T., et al.: High-rate HMDSO-based coatings in open air using atmospheric-pressure plasma jet. J. Non-Cryst. Solids **358**(17), 2462–2465 (2012)
38. Yim, J.H., Rodriguez-Santiago, V., Williams, A.A., et al.: Atmospheric pressure plasma enhanced chemical vapor deposition of hydrophobic coatings using fluorine-based liquid precursors. Surf. Coat. Technol. **234**, 21–32 (2013)
39. Xie, Q., Lin, H.F., Zhang, S., et al.: Deposition of SiCxHyOz thin film on epoxy resin by nanosecond pulsed APPJ for improving the surface insulating performance. Plasma Sci. Technol. **20**(2), 025504 (2017)
40. Lin, H.F., Wang, R.X., Xie, Q., et al.: Rapid surface modification by plasma jet to promote surface charge decaying. Trans. China Electrotech. Soc. **32**(16), 256–264 (2017)
41. Lin, H.F.: Study of Effect of Film Deposition by Low Temperature Plasma on Surface Electrical Properties of Epoxy Resin. North China Electric Power University, Baoding (2018)
42. Lian, H.L., Yan, J.Y., Xie, J., et al.: Enhancement of surface insulation properties of alumina/epoxy composites through ZrO_2 film sprayed by plasma atomization. Polym. Compos. **41**(10), 4020–4030 (2020)
43. Ma, Y.Y., Zhang, C., Kong, F., et al.: Effect of plasma jet array assisted film deposition on epoxy resin surface electrical characteristics. High Volt. Eng. **44**(9), 3089–3096 (2018)

44. Zhou, Y.X., Shao, T., Zhang, C., et al.: Atmospheric pressure plasma jet array in helium driven by microsecond pulses. High Power Laser Part. Beams **26**(4), 68–72 (2014)
45. Wang, R.X., Li, W.Y., Zhang, C., et al.: Thin insulating film deposition on copper by atmospheric-pressure plasmas. Plasma Process. Polym. **14**(7), 1600248 (2017)
46. Zhang, C., Lin, H.F., Zhang, S., et al.: Plasma surface treatment to improve surface charge accumulation and dissipation of epoxy resin exposed to DC and nanosecond-pulse voltages. J. Phys. D Appl. Phys. **50**(40), 405203 (2017)
47. Wang, T.T., Zhang, C., Zhang, F.Z., et al.: Effect of oxygen concentration on improvement of surface pressure resistance of epoxy resin by atmospheric pressure plasma deposition. High Volt. Eng. **46**(10), 3708–3714 (2020)
48. Zhang, P.H., Zhang, S., Kong, F., et al.: Atmospheric-pressure plasma jet deposition of bumpy coating improves polypropylene surface flashover performance in vacuum. Surf. Coat. Technol. **387**, 125511 (2020)
49. Cui, C.C.: Study on the Inhibition of Micro Discharge by Surface Treatment of Atmospheric Pressure Plasma. Zhengzhou University (2018)
50. Cui, C.C., Zhang, C., Ren, H.Y., et al.: Surface modification of Cu by atmospheric pressure plasma jet for micro discharge inhibition. J. Chin. Electr. Eng. Sci. **38**(5), 1553–1561 (2018)
51. Hai, B., Zhang, C., Wang, R.X., et al.: Plasma depositing SiO_2-like film to suppress surface charge accumulation on epoxy resin. High Volt. Eng. **43**(2), 375–384 (2017)
52. Hu, D., Ren, C.Y., Zhang, C., et al.: Effect of deposited film on the surface insulation characteristics of FEP material by atmospheric pressure plasma jet. J. Chin. Electr. Eng. Sci. **39**(15), 4633–4641 (2019)
53. Kostov, K.G., Nishime, T.M.C., Castro, A.H.R., et al.: Surface modification of polymeric materials by cold atmospheric plasma jet. Appl. Surf. Sci. **314**, 367–375 (2014)
54. Zhang, C.Q.: The Surface Plasma Treatment and Its Study on Electrical Properties of Epoxy Resin. North China Electric Power University, Baoding (2020)
55. Yan, J.Y., Liang, G.S., Lian, H.L., et al.: Improving the surface flashover performance of epoxy resin by plasma treatment: a comparison of fluorination and silicon deposition under different modes. Plasma Sci. Technol. **23**(11), 115501 (2021)
56. Xue, J.Y., Wang, H., Chen, J.H., et al.: Effects of surface roughness on surface charge accumulation characteristics and surface flashover performance of alumina-filled epoxy resin spacers. J. Appl. Phys. **124**(8), 083302 (2018)
57. Riello, D., Zetterström, C., Parr, C., et al.: AlF_3 reaction mechanism and its influence on α-Al_2O_3 mineralization. Ceram. Int. **42**(8), 9804–9814 (2016)
58. Gao, Y., Wang, X.F., Li, N., et al.: Characterization method for carrier trap and the effect on insulation breakdown within polymer insulating materials: a review. High Volt. Eng. **45**(7), 2219–2230 (2019)
59. Lei, Q.Q., Liu, G.Y.: How to understand the two basic physical processes of polarization and conductance in engineering dielectrics and scientific principles and methods of their measurement. J. Chin. Electr. Eng. Sci. **38**(23), 6769–6789+7113 (2018)
60. Lei, Q.Q., Liu, G.Y.: Basic physical knowledge of engineering dielectrics and learning thinking method. J. Chin. Electr. Eng. Sci. **38**(16), 4898–4917+4995 (2018)
61. Simmons, J.G., Tam, M.C.: Theory of isothermal currents and the direct determination of trap parameters in semiconductors and insulators containing arbitrary trap distributions. Phys. Rev. B **7**(8), 3706 (1973)
62. Que, L.K., An, Z.L., Ma, Y., et al.: Improved DC flashover performance of epoxy insulators in SF6 gas by direct fluorination. IEEE Trans. Dielectr. Electr. Insul. **24**(2), 1153–1161 (2017)

Regulation Method and Mechanism of Functionalized Modified Nano Filler on Electrical Properties of Epoxy Resin

Haoou Ruan, Qing Xie, Qijun Duan, and Jun Xie

1 Introduction

Epoxy resin is a kind of insulating material with excellent electrical, thermal and mechanical properties. It is widely used in GIS, GIL, dry-type transformers, IGBT and other electrical equipment in high-voltage transmission [1, 2]. However, epoxy insulation components not only face higher requirements such as power resistance and heat resistance, but also have to endure extreme conditions and withstand long-term use. This high demand is intensified with the increasing construction of UHV transmission grids, extended transmission range, and complex operational environment. The insulation strength of general epoxy resin base material is far from sufficient to withstand the demand of high voltage or even ultra-high voltage power transmission. Therefore, the modification of epoxy curd materials has become a hotspot. Filler doping is an important modification method to improve the comprehensive properties of epoxy resin [3, 4]. The epoxy casting composite insulators in high voltage transmission engineering promote the overall withstand level, thermal and mechanical properties of the materials by doping with a large number of inorganic fillers. Epoxy composite insulating materials can synthesize insulating components with excellent electrical properties by making use of epoxy resin matrix as continuous phases and inorganic filler particles such as alumina and silicon oxide as dispersed phases (Figs. 1 and 2).

Nano-doping modification is a technology that uniformly fills nanoscale inorganic filler particles into the polymer or other matrix materials to synthesize composite materials with excellent properties. Originated in the early 1980s, nanocomposites are the composites material with the size of dispersed phase material at least within 100 nm in a one-dimensional direction. The common synthesis methods of polymeric

H. Ruan · Q. Xie (✉) · Q. Duan · J. Xie
Department of Electrical Engineering, North China Electric Power University, Baoding, China
e-mail: xq_ncepu@126.com

Q. Xie (ed.), *Electrical Materials*, Engineering Materials,
https://doi.org/10.1007/978-981-99-9050-4_4

Fig. 1 Gas-insulated switch

Fig. 2 Epoxy resin composite insulation

nanocomposites include the sol–gel method, blending method, in-situ polymerization method, and intercalation and polymerization method, etc. [5, 6]. Since the introduction of "nanocomposite dielectric" by Lewis in 1994, a lot of research in electrical composite materials has suggested that the unique high specific surface area and size effect of nano-inorganic fillers can effectively modify the insulating properties of composite materials. Furthermore, the characteristics of nano inorganic fillers render the electrical composite materials excellent properties such as dielectric response, bulk breakdown strength, corona resistance and electric trace resistance. All of this makes nanocomposites a necessary functional material in the field of high-voltage insulation [7]. Moreover, many scholars have provided molecular explanations and theoretical models with regard to nanocomposites' macroscopic effect and charge behavior. Lewis proposed an interface model to divide the association region between nano particles and epoxy resin into shielding and dispersion regions [7].

In 2005, Tanaka put forward a multi-core model which separated the filler interface from bonded, bound and loose layers [8]. The multi-core model further divides the interface between filler and matrix and also comprehensively describes the differences in charge behavior between different layers in the interface region (Figs. 3 and 4).

Although the introduction of nano filler has dramatically promoted the overall performance of epoxy resin systems, there remain two major practical issues. Firstly, the surface activity of nano filler is very high, which leads to the agglomeration in the process of resin curing. This phenomenon significantly affects the dispersion

Fig. 3 Interface model

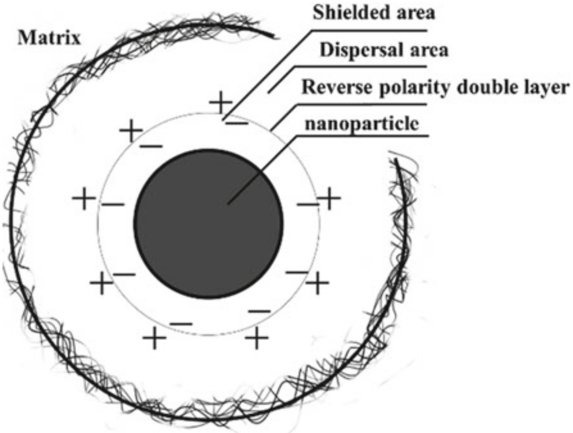

Fig. 4 Multicore model

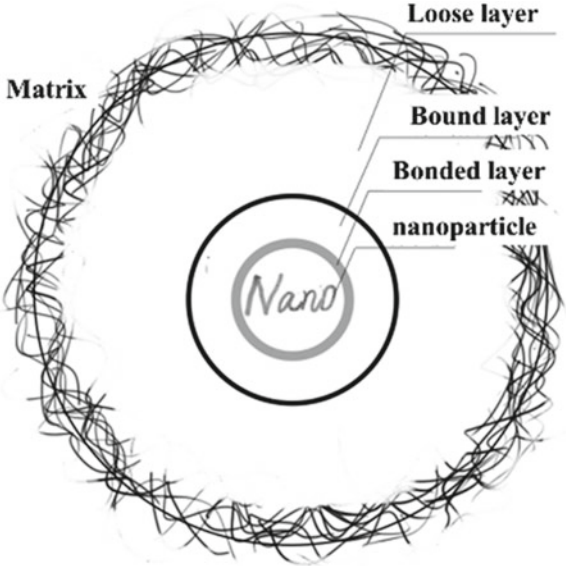

properties of epoxy resin system, consequently diminishing the nano-modification effect. Secondly, the surface of inorganic nanofillers often lack groups that can form durable bonds with the resin, resulting in poor compatibility between fillers and epoxy resin. To sum up, these two problems seriously restrict the modification of nano filler on the performance of epoxy resin composites, and have become the principal impediment to nano filler modification research. Therefore, modifying nano fillers has become a prevalent approach in the advancement of nano dielectrics. The modification methods can be categorized as physical morphology modification, surface functional modification, element or defect doping modification, etc. In these modification methods, the surface functional modification of nano fillers can optimize the dispersion and compatibility of filler in the matrix, as well as regulate the interface properties of the filler-matrix simultaneously. In addition, due to the relatively simple operation and diverse treatment methods, surface functional modification has become the highly regarded technique in the field of nano-modification.

The functionalization of the filler-matrix surface can introduce various functional groups into the filler-matrix interface layer. These functional groups have changed many electrical properties of the composites. For example, the nonpolar groups in the interface layer create an energy barrier for carrier transport between the matrix and the filler, resulting in the high interface resistance of charge transport. In addition, the grafted functional groups on the filler surface will cause many physical and chemical defects in the composite which will form charge traps of different energy levels and become the critical factor affecting their charge transfer ability [7]. Currently, in the research of epoxy nanocomposites, the methods for functionalizing the surface of nano filler include coupling agent grafting modification, fluorination modification, amination modification, hydroxylation modification, dopamine modification, etc. The functional grafting on the filler surface has a significant effect on further improving the performance of epoxy composites. Wang et al. used two silane coupling agents, octamethylcyclotetrasiloxane and hexamethyl-disilazane, to graft nano-SiO_2 and dope it to prepare composite materials. Subsequent analysis showed that the surface charge accumulation of epoxy nanocomposites was mitigated in comparison to pure epoxy after surface grafting [9]. Luca Valentini et al. proposed to graft fluorinated groups on the surface of single-walled carbon nanotubes and further functionalized amino with the help of fluorinated groups [10] which improved the dispersion of the modified filler in the epoxy resin matrix and enhanced the electrical and mechanical properties of the composite. Li Licheng and his team applied dopamine to modify h-BN and alumina microspheres and co-doped the two fillers to modify epoxy resin. The team found that the grafting modification of filler can adjust the interface interaction between the particle group and EP matrix. This modification can not only alleviate the ablation of insulating materials caused by surface discharge, but also enhance the apparent activation energy of the EP pyrolysis process [11].

This chapter focuses on the surface functionalization modification technology of nano filler in the research of epoxy composites which introduces in detail the methods of coupling agent grafting, fluorination grafting, and amination grafting in the surface functionalization of nanofiller and their influence rule on the properties of epoxy composites. In addition, the chapter analysis the mechanism of functionalization of nano fillers and its effect on the performance of epoxy composites by combining the interface model, molecular dynamics simulation, and Density Functional Theory (DFT) calculation.

2 Functional Modification of Filler and Preparation and Characterization of Composite

2.1 Functional Modification of Nanofiller

Surface functional modification of nanofiller is referred to the treatment of filler that grafting organic functional groups or certain element onto the filler surface, with the purpose of conferring the filler with certain property. Surface functional modification is commonly achieved through hydrothermal method, self-assembly method, plasma treatment and so on. In these methods, groups with functional elements like F and N or biomolecules such as dopamine are grafted to the nanofiller surface, in order to make up for the filler defects and enhance comprehensive performance of composite. The functional modification of nanofiller surface can ameliorate the dispersibility and compatibility of filler in matrix while also regulating the interface between filler and matrix, and pointedly improve the electrical properties of epoxy composite. This section introduces an overview of the experimental platforms and preparation methods involved in coupling agent modification, fluorination modification and amino modification of nanofiller for epoxy nanocomposite.

2.1.1 Platform and Method of Coupling Agent Grafting Modification

Coupling agents are frequently used in conventional synthesis of epoxy composite to graft and modify doped fillers. Regular coupling agents feature an inorganic group at one end and organophilic group on the other. Coupling agent is also called the surface modifier due to the improvement of the dispersibility and compatibility of filler in a resin matrix. The most commonly used coupling agent in epoxy composite is silane coupling agent. Generally, the processability, insulating property and thermal property of composite can be effectively improved by coupling agent with 0.5–2% of filler mass fraction. The technology that using coupling agent to modify nanofiller is relatively mature and convenient, which can be achieved by basic material preparation platform. A brief introduction is as follows.

(1) Platform of coupling agent grafting modification for nanofiller

The coupling agent treatment platform mainly includes magnetic stirrer, ultrasonic disperser and vacuum drying oven.

Magnetic stirrer is mainly applied to stir liquid with low viscosity or solid–liquid mixture. Utilizing the fundamental principle of magnetic field that the same polarity will repel each other, the magnetic stirrer inside container is pushed to rotate by continuously transforming two polarities at the base of the vessel and then rotate the samples in container by stirrer to achieve the purpose of uniformly mixing samples. Typically, coupling agent treatment regards ultrapure water or ethyl alcohol as dispersant, and filler will be added to container to stir for completely reaction after the coupling agent and solvent are uniformly mixed (Fig. 5).

Ultrasonic cleaner, one of the physical dispersion methods, utilizes ultrasonic dispersion technology to reduce nanoparticle agglomeration. As shown in Fig. 6, with stainless still liner and mechanical control heating inside, ultrasonic cleaner can autonomously control environment temperature during dispersion process and improve the dispersion efficiency of nanoparticle. The frequency of ultrasonic vibration head inside is 40 kHz, and the device can adjust the ultrasonic time according to specific experimental requirement. The ultrasonic dispersion of the mixture of filler and coupling agent contributes to complete contact and reaction between filler and coupling agent molecules.

Vacuum drying oven can provide stable reaction temperature and steady high-temperature environment to dry nanofiller. The temperature fluctuation is constantly lower than 1 °C. When processing the coupling agent grafting reaction of filler over

Fig. 5 Thermal collecting homoiothermic magnetic stirrer

Fig. 6 Ultrasonic cleaner

Fig. 7 Vacuum drying oven

a long time, the temperature can be controlled invariable using a vacuum drying oven. Furthermore, under the vacuum, it can also rapidly evaporate solvent such as ultrapure water and ethyl alcohol after reaction (Fig. 7).

(2) Method of coupling agent grafting modification for nanofiller

Firstly, required quality of coupling agent was weighed and added to a beaker, and then proper absolute alcohol was also added to the beaker followed by placing the beaker on a magnetic mixer and stirring for 30 min at 30 °C in order to thoroughly mix coupling agent and absolute alcohol. Secondly, nanoparticle to be processed was added to the uniformly-stirred mixture of coupling agent and absolute alcohol. The mass ratio of nanoparticle to coupling agent is 100:5. After that, stirring the mixture for another 30 min at 30 °C in magnetic mixer, and then placing the mixture into a ultrasonic cleaner to disperse for 10 min to completely mix filler and coupling agent solution. Finally, the samples mixing uniformly were placed in a vacuum drying oven to sufficiently react for 20 h, and the solvent was completely evaporated. The dried nanoparticle, presenting as lumpy and realizing coupling agent surface grafted, can be preserved to reserve after grinding in mortar.

2.1.2 Platform and Method of Fluorination Modification

Filler fluorination, one of the filler functionalization, can effectively improve the dispersibility of filler in matrix by grafting strongly electronegative fluorine-containing groups on the surface of the nanofiller. Simultaneously, the unique atomic structure of fluorine entrusts nanofiller fortissimo charge binding ability, which can improve the insulating property of composite significantly [12]. At present, the grafting methods of filler fluorination mainly include hydrothermal fluorination, fluorine-containing coupling agent grafting, direct process with fluorine gas, plasma fluorination, etc. This paper focuses on the hydrothermal fluorination.

(1) Platform of fluorinated grafting modification for nanofiller

As shown in Fig. 8, platform of hydrothermal fluorination mainly consists of high-temperature hydrothermal reactor, suction flask and vacuum pump. High-temperature hydrothermal reactor can provide a stable, high-temperature and high-pressure environment during hydrothermal fluorination. Suction flask and vacuum pump are used to obtain fluorinated nanofiller by suction filtration following hydrothermal reaction.

(2) Method of fluorinated grafting modification for nanofiller

Firstly, To begin with, 0.04 g/ml Sodium hydrogen fluoride ($NaHF_2$) solution was prepared by stirring $NaHF_2$ particle of 98% purity in deionized water for 30 min at 60 °C. Subsequently, nanofiller was weighed and added to the solution above to continuously stir for 10 min. The mixed solution was then added to the polytetrafluoroethylene liner of a high-temperature hydrothermal reactor. After that, the liner was hermetically sealed with a stainless steel high pressure reactor and placed into a vacuum drying oven to heat to 90 °C for full reaction for 24 h. After the reactor was cooled down to room temperature, it was removed from the drying oven and suction filtrated under vacuum. The resulting sample was cleaned by deionized water until the solution presents as neutral and was placed into the vacuum drying oven to dry thoroughly at 60 °C. Finally, the nanofiller after drying can be used in experiment after grinding by a mortar.

Fig. 8 Major equipment of hydrothermal fluorination

2.1.3 Platform and Method of Amination Modification

Amination modification of nanofiller is a new method to adjust the filler-matrix interface of epoxy composite insulation material. By grafting amino groups on the surface, filler can form cross-linked bonds with epoxy resin, which has a splendid effect on improving the compatibility of filler and matrix. Meanwhile, amino groups can accelerate the migration rate of composite space charge, which has a positive effect on inhibiting charge accumulation and field distortion effects in local insulating material.

(1) Platform of amination grafting modification for nanofiller

Taking the amino modification of BN nanosheet as an example, this paper introduces the platform of amino modification. The required experimental equipment includes planetary ball mill, suction filtration device, vacuum filtration pump, agate mortar, vacuum drying oven, etc. Planetary ball mill can co-ball mill the hexagonal boron nitride together with urea, and graft amino groups on the surface of boron nitride nanosheet during the ball milling stripping. Suction filtration device is used to clean and suction filter the modified filler in order to remove excess reagent. Drying oven and mortar can dry and grind the modified filler (Figs. 9 and 10).

(2) Method of amino grafting modification for nanofiller

The method to amination modification of Boron Nitride Nanosheets (BNNS) introduced in this book is a one-step fabrication method of urea co-ball milling [13].

Fig. 9 Planetary ball mill

Fig. 10 Stainless steel ball mill tank

Initially, 1 g hexagonal boron nitride powder and 4 g urea were weighted and 25 ml isopropyl alcohol solution was measured before being homogenously combined and stirred in an agate jar of a planetary ball mill. Whereafter, the agate jar was placed into the planetary ball mill and the rotate speed of mill was set to 300 r/min. After continuously operating for 48 h, take out the mixture and place it in a beaker to for 2 h static. Then the upper suspension was extracted into a suction flask with an injector, and was suction filtered through a filtration membrane with 0.22 μm aperture. The samples on the filtration membrane were placed into a vacuum drying oven to dry for 12 h at 80 °C. After cooling at room temperature, the blocky boron nitride nanosheet grafted with amino were obtained. Finally, the powder of boron nitride nanosheet grafted with amino groups were obtained by grinding the nanosheet in a mortar.

2.2 Platform and Method of Epoxy Nanocomposite Preparation

Epoxy composite have been extensively utilized in high voltage insulation field at present. In industry, micro filler is often applied to dope and modify epoxy resin. This process can be achieved by conventional material mixing and curing reaction, which is relatively simple and mature. Nevertheless, due to the large specific surface area and the small size effect of nanofiller, the doping amount of nanofiller is limited. What's more, the process also has problems with easy aggregation, bubble abundance, undermixing and others. It is worth noting that filler functionalization is an important means to alleviate these issues. Filler surface grafting modification can facilitate the interaction between filler and matrix, reduce the actual synthesis difficulty of epoxy nanocomposite, and improve the comprehensive properties of material. This chapter introduces the preparation platform and technology of epoxy nanocomposite commonly used in laboratory, which can be applied to the synthesis of most epoxy nanocomposite.

2.2.1 Preparation Platform of Epoxy Nanocomposite

The preparation of epoxy nanocomposite can be divided into the steps of blending, degassing, casting, curing and demolding. The required equipment mainly includes balance, stirring device, dispersion device, vacuum drying oven, vacuum pump and mold, etc.

Machine mixer is mainly used in mixing. A high power, high-speed mechanical mixer is necessary to intensively mix all raw materials due to the viscosity of epoxy resin at normal temperature is high and the difficulty in dispersing nanofiller into the epoxy matrix by surface energy effect. Stirring paddle and rotating rod are made of polytetrafluoroethylene, which is a kind of natural release agents that can effectively alleviate the adhesion between epoxy resin and equipment. The stirring device is equipped with temperature-regulated electric heating equipment that can heat the epoxy resin mixture and reduce its viscosity, thereby promoting that all kinds of raw materials are mixed more homogeneously. At the same time, with glass reactor as its complement, it allows one to observe the mixing state of blends at any moment.

Shear machine is used to decompose and diffuse the solid or liquid which is incompatible with liquid medium, and form an even distribution within the medium. The principle is generating a strong centrifugal force field through the high-speed rotation of the rotor, and forming a negative pressure zone inside the knife head. Nanoparticle to be processed will enter the dispersion knife head along the axial direction, then are removed from the slots that arranged on the stator and rotor by the internal force, radially disperse in all directions. The forces that effect nanoparticle are strong shear force and axial force generated by high acceleration process. In addition, shear gradient generated between stator and rotor will form strong turbulence, which makes agglomerate particle to disperse and mix under high-speed impact.

Vacuum drying oven and vacuum pump are necessary equipment to prepare epoxy composite, which are applied for vacuum degassing of mixed material and material casted into the mold. During the epoxy resin preparation, on the one hand, lots of bubbles will mix in the blend when stirring, on the other hand, a great deal of air will be introduced in the process of casting which will form a large amount of defect sites inside the epoxy composite material, and seriously degrade the mechanical and electrical properties of cured product. The material vacuum degassing through vacuum drying oven and vacuum pump can effectively eliminate bubbles mixed in material and improve the comprehensive properties of material.

Aiming at the practical application and testing requirements, epoxy composite needs to be casted to solidified samples with different shapes. Therefore, different kinds of molds need to be pointedly customized. Metal mold possess impressive heat resistance, solidity and durability. Moreover, it has excellent manufacturability and convenient to process which makes it the most prevalent casting mold in industry. However, metal mold is easy to bond with epoxy resin, so releasing agents are usually coated on the iron mold to release epoxy material after curing in industry (Fig. 11).

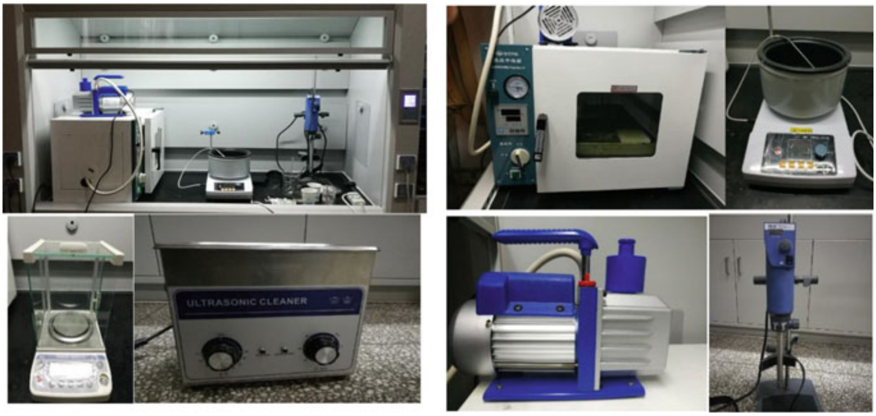

Fig. 11 Preparation platform and equipment of epoxy resin composites

2.2.2 Preparation Method of Modified Epoxy Composite

The preparation method of epoxy composite is shown in Fig. 12. Firstly, all raw materials were weighed in equal proportion according to established mass fraction and poured into a glass reactor. The heating temperature was 60 °C to reduce the viscosity of epoxy resin composite. About 5 min later, the height of agitating valve was adjusted to immerse the valve into the blend solution, and the rotate speed was 300 r/min, stirring at 60 °C. After about 10 min, the mixing could be considered uniform and the stirring could be stopped if the blend presents as faint yellow homogeneous liquid. Later, the blend after stir was placed into a vacuum drying oven at 60 °C and a vacuum pump was used to extract air until the oven is close to vacuum state. It could be observed through an inspection window that bubbles in blend continually rose and broke. About 30 min later, if there were no bubbles in the blend, the oven was returned to normal pressure and the blend was picked out to cast. The mold needed to be preheated before casting. Coated with mold release agents on the surface of metal mold and preheated the mold to 80 °C could prevent the huge temperature difference between mold and blend destroying properties of cured products during casting process. After preheating, the blend was slowly poured into the mold and degassed again. Subsequently, the mold was placed into the vacuum drying oven to heat to 80 °C and repumped to vacuum state until there were no bubbles in all the blend in mold. After degassing, the mold was placed into the drying oven, and the temperature in oven was adjusted to 120 °C for continuously curing for 2 h. During the process, the blend in mold would occur crosslinking reaction, eventually solidifying. The mold was removed from the vacuum drying oven after solidifying and left to cool to room temperature. Finally, the cured epoxy nanocomposite samples were obtained by releasing the mold after it was cooled to room temperature. The samples was placed into the vacuum drying oven at 120 °C to continuously solidify for 10 h, which can fully cross-link the epoxy resin and acid anhydride. This process

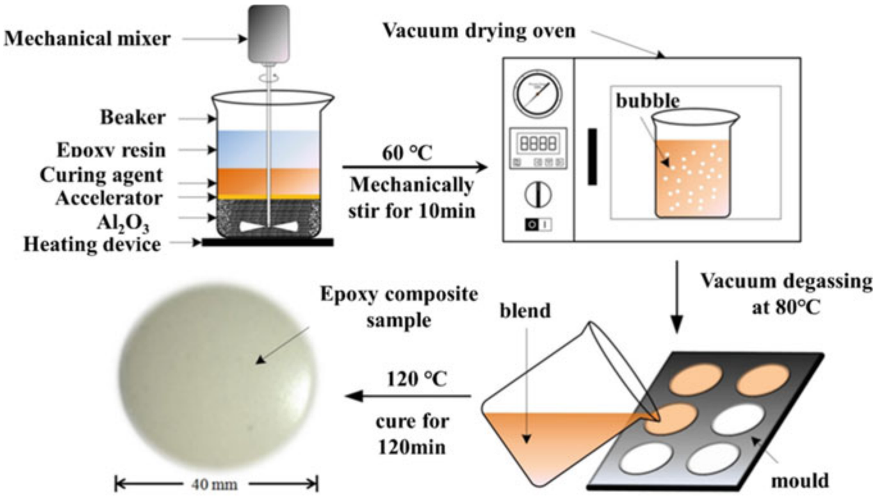

Fig. 12 Preparation process of epoxy resin composites samples

can guarantee that the largest crosslinking of epoxy composite condensate, and the uniform properties of different samples become more excellent.

2.3 *Characterization Method of Material*

Epoxy nanocomposite can optimize the properties of matrix materials with the help of nanofiller performance. The doping of inorganic filler on the macro-level effects insulation, mechanical property, heat resistance and other properties of material by adjusting the internal microstructure and chemical composition of composite. According to the interface model proposed by T. J. Lewis and the multicore model introduced by Tanaka, the independent properties and the action mechanism between interphases of composites at multiple scales should be focused depending on the characterization and joint analysis for components, morphology, structure and properties of material when analyzing the effect rule of nanofiller. Various characterization methods are available in current technology for experiment and research on epoxy composite materials. With the help of Scanning Electron Microscope (SEM), Atomic Force Microscope (AFM), Fourier Transform infrared spectroscopy (FTIR) and X-ray photoelectron spectroscopy (XPS), the comprehensive analysis of the micro-morphology and molecular organization of nanofiller and composite was conducted. In addition, various properties of material can be measured and characterized in accordance with different professional standards.

2.3.1 Characterization of Material Microstructure

(1) SEM

Currently the SEM primarily utilized to observe the surface micromorphology of opaque material. The fundamental principle of SEM is as below: Atoms on sample surface will escape electrons upon absorbing the energy of electron beam, and these free electrons are called secondary electrons, which are highly sensitive to the sample surface morphology. Any variation in the emission intensity of secondary electrons can be transformed to the brightness changes in the corresponding points on display through a series of processes. Among these the area to be scanned is point-to-point corresponding to the display. The SEM shown in this book is Sigma300, manufactured by The Zeiss in Germany. The characterization results showed below are the micromorphology of BFO nanoparticle and FBTO/EP composite section (Fig. 13).

(2) AFM

AFM can be used to study surface morphology, nanostructure and chain conformation of sample to obtain information on nanoparticle size, aperture, material surface roughness, material surface defects, etc. At the same time, it can also track the surface structure and morphology (vary with time, temperature and other conditions). The pictures below are stereograms and plans of surface morphology at flat of electrode edge characterized by AFM (Fig. 14).

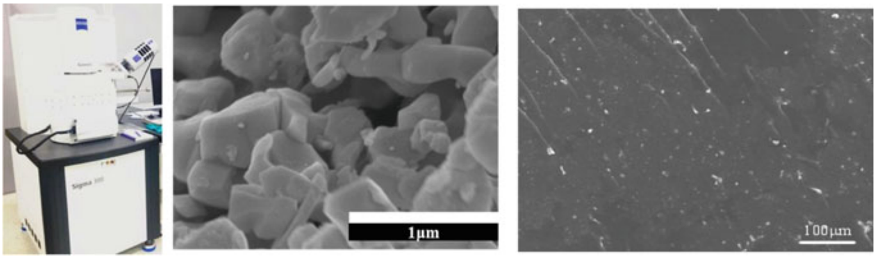

Fig. 13 SEM and characterization results

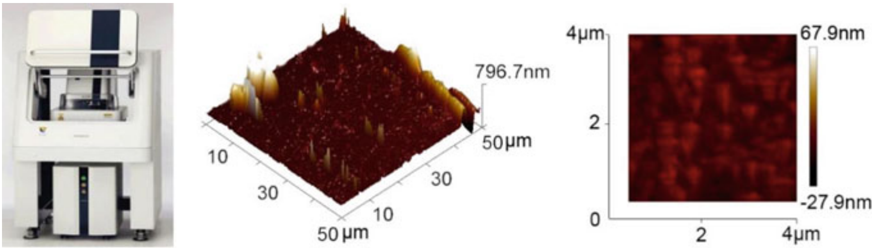

Fig. 14 AFM and characterization results

2.3.2 Characterization of Material Chemical Constituents

(1) XPS

At present, the content of chemical elements and functional groups on the material surface is usually measured by XPS. The principle is: When X-ray with certain energy is irradiated to sample surface, if the energy of X-ray is greater than the work function of sample surface, electrons in atoms at sample surface will break away from the nucleus and become photoelectrons. Now that the energy of X-ray is known, we can measure the kinetic energy of photoelectron, thereby obtaining the electron binding energy of the sample. Because the orbital electron binding energy of various atoms and molecules is constant, the elements composition in samples can be quantitatively known by measuring binding energy. The XPS shown below is Escalab250Xi by The Thermo Fisher Scientific, and the characterization results are XPS spectra of ZnO nanofiller before and after modification (Fig. 15).

(2) XRD

In order to characterize the crystal structure of sample and confirm information on physical phase, crystal structure and space groups of prepared materials, now X-ray diffraction (XRD) is frequently used. The fundamental is below: Crystals consist of lattice cells formed by regular arrangement of atoms. The interatomic distance arranged regularly has the same order of magnitude with the wavelength of incident X-ray. Consequently, when a beam of monochromatic X-ray is incident on crystal, the X-ray scattered by various atoms will interface with each other, resulting in strong diffraction in some special directions. The spatial distribution directions and intensity of diffracted ray is particularly related to the structure of crystal (Fig. 16).

(3) FTIR

There are many kinds of vibrations in molecule, and some of which can change the molecular dipole moment. When the frequency of these types of vibrations is same

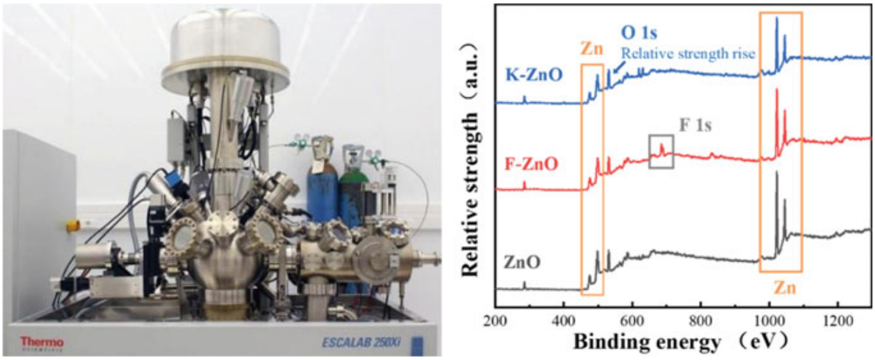

Fig. 15 XPS and characterization result spectra

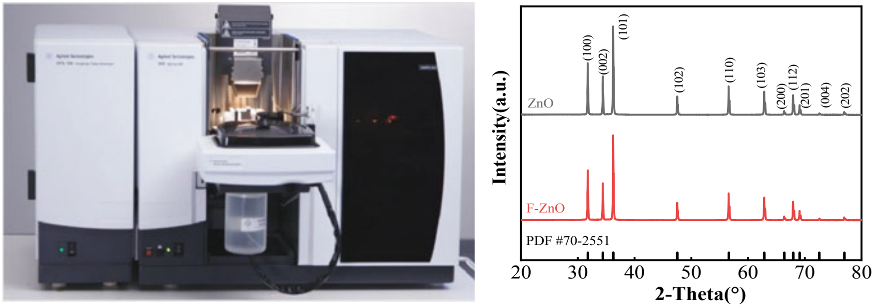

Fig. 16 XRD and characterization result spectra

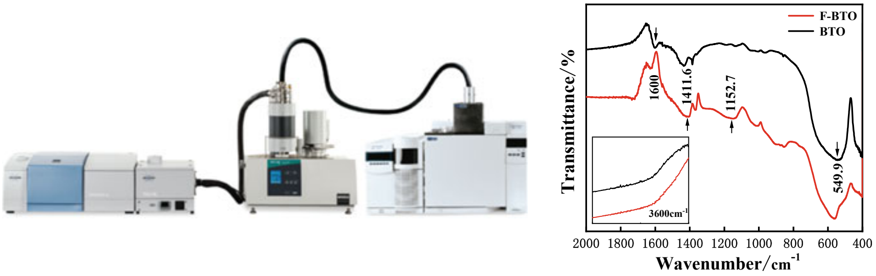

Fig. 17 FTIR and characterization result spectra

to that of infrared light, molecules can absorb the energy of infrared light to form infrared absorbing spectrum (IR). Different compounds have different characteristic peaks of infrared absorption spectrum due to their different molecular structures. FTIR analysis is a significant modern analytical method, which has been widely used for structure identification, quantitative analysis and study of chemical kinetic, etc. Its analysis can provide a large amount of information about functional groups. The position and intensity of infrared absorption peaks reflect characteristics of molecule structure, which can be applied to identify the unknown substance by structural composition or determine the chemical groups. The absorbance intensity of a band is related to the content of chemical groups, which can be used for quantitative analysis and confirming its purity. The below images are FTIR characterization results of BN before and after fluorination (Fig. 17).

2.3.3 Electrical Performance Test

(1) Dielectric

Relative permittivity is a physical parameter that characterizes the dielectric property or polarization property of dielectric materials. It is determined by the capacity ratio of the same size capacitors that are respectively made of predictive materials and vacuo as dielectric. And the value also reflects the characterization of material power storage. The picture showed below is impedance analyzer Agilent 4294A with a circle with radius of 5 mm effective measurement area and its frequency domain ranges from 40 Hz to 110 MHz (Fig. 18).

(2) Conductivity

The surface conductivity and volume conductivity can be measured by high precision ohmmeter. The device showed in picture below is Hioki SM-7100 ohmmeter. During measurement, samples are placed into a shielding box and three metal electrodes are built in electrode according to the three electrodes method. The ohmmeter can apply voltage to electrodes and detect trace leakage currents before and after application, thus it can calculate the surface conductivity and volume conductivity of samples to be measured (Fig. 19).

(3) Surface flashover voltage

The surface flashover test platform of epoxy resin includes high voltage DC power supply, metal cavity, experimental electrode, protection resistor, oscilloscope and

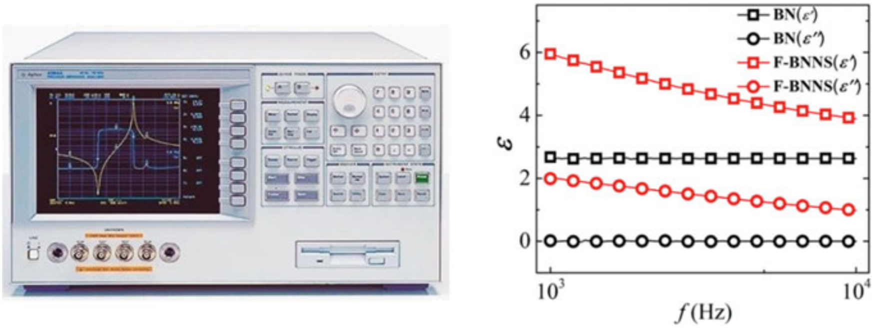

Fig. 18 Impedance analyzer and characterization results

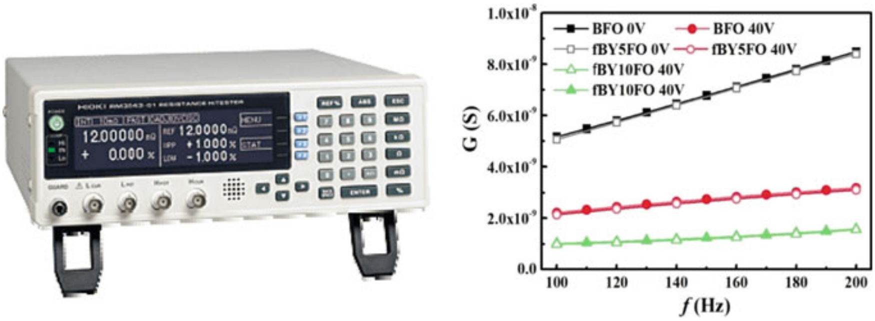

Fig. 19 Ohmmeter and characterization results

Fig. 20 Experimental platform of epoxy resin surface flashover

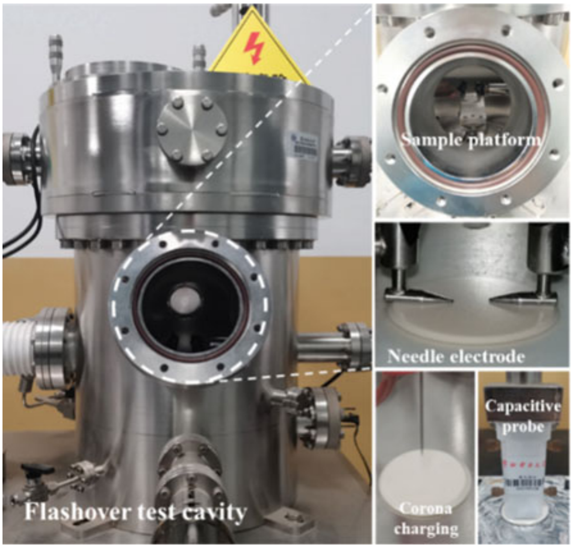

high voltage probe. The surface flashover test platform of epoxy resin is showed as Fig. 20. Via a protection resistor, the high voltage DC power supply is connected in series with a needle electrode connected to cavity high voltage terminal. And the needle electrode on ground side is directly grounded via the cavity ground terminal. The distance between two electrodes is 7 mm. One end of high voltage probe is propped on the protection resistor, and the other accesses channel 1 of oscilloscope through cable. The steps of epoxy resin surface flashover experiment are as follows:

(1) The experiment was conducted under an ambient temperature of 26 °C and a relative humidity of 30%.
(2) Opened the observing window and placed the epoxy resin samples on lift platform. After closing observing window, lifted those samples until their surface clings to the bottom of needle-needle electrode.
(3) The oscilloscope was turned on and set as rising edge trigger. The high voltage DC power supply was turned on and its voltage was increased at a uniform velocity of 0.5 kV/s, and then continuously observed the experimental phenomena in cavity.
(4) If the sample surface in cavity generated arcs along the needle-needle electrodes with discharge sound of "pop" and the oscilloscope detected rising edge waveform simultaneously, surface flashover was considered to have occurred in the sample. The source was turned off immediately this moment and the voltage value displayed on the oscilloscope was recorded. After 5 min, the sample was restored to insulation.
(5) After waiting, step (3) and (4) were repeated. 10 times was recorded on the voltage of the sample surface flashover, and the average was taken as the final surface flashover voltage of the sample.

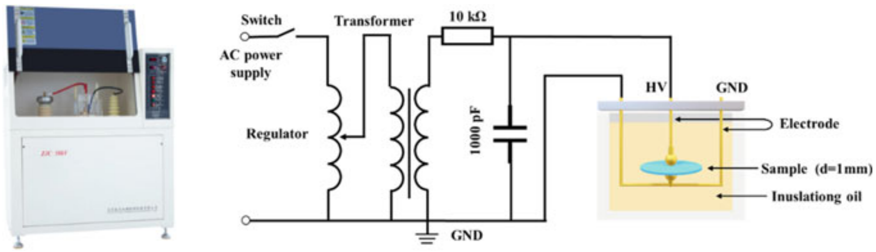

Fig. 21 Measurement of power frequency breakdown voltage

(6) After 10 flashovers, lifted the platform and separated the sample and electrode. Following this step, the observing window was opened to replace a new sample. And then step (2) was repeated.

(4) Breakdown strength measurement

Breakdown strength was measured according to the national standard GB/T 1408.1-2016 (sphere electrode). In order to prevent corona discharge from affecting the value of breakdown voltage, the whole electrode system was placed in transformer oil filtered clean and was polished by abrasive paper. Voltage booster was rotated to increase voltage with the speed of 2 kV/s until the sample was broke down, and recorded the voltage at breakdown. Breakdown strength is an important index that characterizes the materials insulating property which is defined as the ratio of voltage U to the thickness d of sample when the breakdown occurs. And the average breakdown field strength was represented by E. The computational formula is shown below in (1) (Fig. 21).

$$E = U/d \tag{1}$$

(5) Surface charge measurement

The experiment platform of interfacial charge aggregation and dissipation includes high voltage DC power supply, two-dimensional motion control device, charging pin, electrostatic probe, electrometer, data acquisition card and lift platform. The experiment platform of epoxy resin interfacial charge aggregation and dispersion is shown in Fig. 22. High voltage DC power supply is series connected to the charging pin. The charging pin and electrostatic probe are fixed to the X-axis of two-dimensional motion control device, respectively. Besides, stepping motors on X-axis and Y-axis are connected to the motion control device through data transmission line, and the motion control device is connected to computer by the same way. The outlet terminal of electrostatic probe accesses the electrometer, and the data transmission terminal of electrometer accesses computer by data acquisition card.

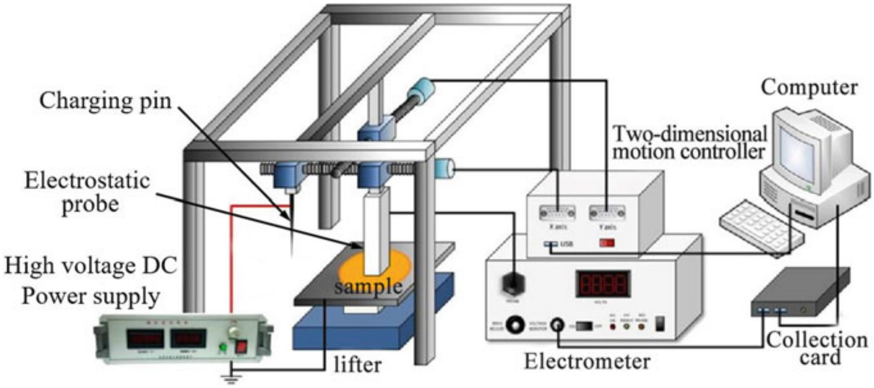

Fig. 22 Experiment platform of epoxy resin interface charge

The procedure of epoxy resin interfacial charge dissipation experiment are as follows:

(1) The experimental ambient temperature was at 26 °C, and the relative humidity was set as 30%. The motion control device and electrometer were turned on. Subsequently, the motion control software and data acquisition software were opened with the sampling frequency setting as 10 Hz.

(2) The sample to be processed was placed on the lift platform centre. After that, the charging pin was moved to 7 mm above the centre of sample by two-dimensional motion control device and lift platform.

(3) High voltage DC power supply was turned on and its voltage was uniformly increased to −7 kV with the speed of 0.5 kV/s. The voltage was kept constant for 60 s to charge the sample surface.

(4) The power was turned off and the charging pin was moved away after charging. Instead, the electrostatic probe was moved to 2 mm above the centre of sample by two-dimensional motion control device and lift platform. At the same time, electrostatic probe was switched to work by electrometer. Following preparation, the sample surface potential was measured rapidly with a sampling frequency of 10 Hz for 30 min.

(5) Upon the completion of the first interfacial charge dissipation experiment after sampling, the data acquisition card and electrostatic probe were turned off, and the sample was substituted by a new one to repeat step (2). To guarantee the accuracy of experiment, each sample was needed to be tested for 5 times. The average of 5 values at the same time was taken as the surface potential of sample at that time.

(6) In order to compare all samples directly, the data sampled completely were needed to be processed normalization, which means finding out surface potential with the largest absolute value and dividing all potential values by the maximum.

(6) Calculation of surface charge trap

According to the Isothermal Surface Potential Decay (ISPD) [14], surface potential decay of insulation material is a function of its trap level depth and trap density. As a consequence, a function equation can be used to describe the surface charge decay curves. Research shows that double exponential function can fit the epoxy resin surface potential decay curve. The fitting formula is as shown in Eq. (2):

$$\varphi_{\mathrm{s}}(t) = Ae^{-\frac{t}{m}} + Be^{-\frac{t}{n}} \tag{2}$$

In Eq. (2), where $\varphi_{\mathrm{s}}(t)$ is the surface potential, t is one moment of the surface potential decay curve. A, B, m, n are fitting coefficients. Therefore, the trap level E_{T} and trap density Q_{s} can be worked out by Eqs. (3) and (4) shown below:

$$E_{\mathrm{T}} = k_{\mathrm{B}}T\ln(vt) \tag{3}$$

$$Q_{\mathrm{s}} = t\frac{\varepsilon_0\varepsilon_r}{eL}\cdot\frac{\mathrm{d}\varphi_{\mathrm{s}}(t)}{\mathrm{d}t} \tag{4}$$

In the two equations, k_{B} is the Boltzmann constant that is 1.380649×10^{-23} J/K. T is the absolute temperature taken as 298 K for the reason that the interface charge dissipation experiment was conducted at 25 °C. Where v is the electron escape frequency taken as 4.17×10^{13} s^{-1}, e is the elementary charge quantity of 1.6×10^{-19} C. Besides, L is the thickness of samples of 3 mm since thickness of all the samples prepared in this paper is 3 mm. ε_0 is the vacuum permittivity of 8.85×10^{-12} F/m and ε_{r} is the relative permittivity of samples. According to the equations above, the samples trap level distribution curve can be worked out.

3 Regulation Electrical Properties of Epoxy Resin by Coupling Agent Modified Nano Filler

Coupling agent is an additive used to improve the organism and the filler interface performance during the preparation of composite materials. The coupling agents can be divided into four categories in terms of chemical composition: organic complexes, aluminate compound, titanates and silanes. Taking the silane coupling agent (KH550) treating nano-SiO_2 as an example, the reaction process is shown in Fig. 23.

The silane coupling agent can react with the hydroxyl groups on the surface of nano-SiO_2 after hydrolysis. The hydrophilic hydroxyl group is replaced by the lipophilic group, which makes the nano-SiO_2 particles change from hydrophilic to lipophilic, reducing the surface energy. This reaction enhances the compatibility of nano-particles in an organic environment, effectively decreasing the agglomeration of nano-particles and improving their dispersity in the matrix. In addition, one end of the coupling agent molecular chain is connected with the nano-SiO_2 surface and the

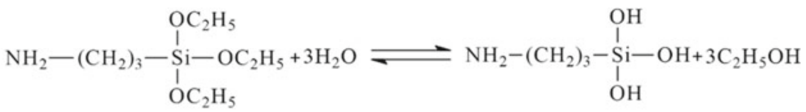

$$NH_2-(CH_2)_3-\overset{\displaystyle OC_2H_5}{\underset{\displaystyle OC_2H_5}{Si}}-OC_2H_5+3H_2O \rightleftharpoons NH_2-(CH_2)_3-\overset{\displaystyle OH}{\underset{\displaystyle OH}{Si}}-OH+3C_2H_5OH$$

(a) Hydrolysis of coupling agent

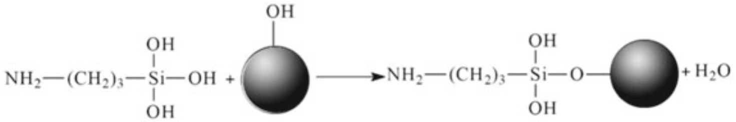

(b) Reaction of coupling agent with SiO_2

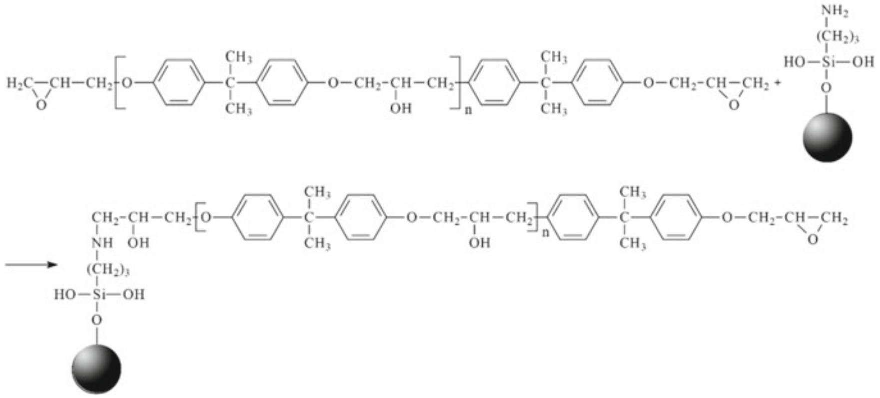

(c) Modified SiO_2 reacts with epoxy resin

Fig. 23 Action mechanism of silane coupling agent

other is associated with the matrix polymer chain, as shown in Fig. 23c. The nanoparticles are connected with the polymer chains through chemical bonds, improving the compatibility of the nanoparticles in the matrix. This chemical bond connection can also effectively avoid microphase separation inside the composite material under external factors such as electric, thermal, and force fields. In addition, it can also improve the stability of the composite material interface and increase the interaction between the two phases, so that the composite material can be used for a long time.

3.1 *Effect of Different Kinds of Nano Filler Coupling Agent Grafting on Electrical Properties of Epoxy Resin*

The coupling agent modified nano filler primarily regulates the interface area between the filler and the matrix, but there are different effects on different types of nano filler coupling agent. This paper provide an overview of the effect of silane coupling agents on the properties of composite materials by taking two insulating fillers of 100 nm SiO_2 and Al_2O_3 as examples.

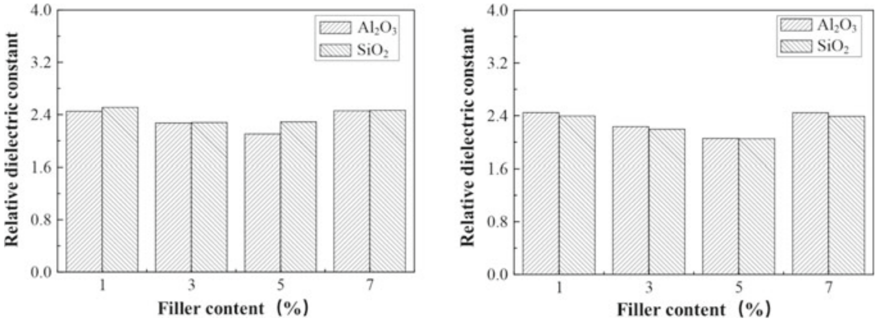

(a) Before coupling agent treatment (b) After coupling agent treatment

Fig. 24 Test results of composite materials dielectric constant

The agglomeration of nanoparticles will directly affect the interface effect between nanoparticles and the epoxy matrix. The more agglomeration phenomenon of particles, the wider the overlapping area of the interface. The overlapped interface layer loses its stable and compact structure, which impacts its dielectric constant, thus affecting the properties of the composite material. Simultaneously, particle agglomeration affects the interaction between the nano-particles and the epoxy resin matrix, reduces the resistance of the polar polymer chain segment or the side group turning at the interface. Consequently, particle agglomeration increases the dielectric constant of the composite.

After treatment with a coupling agent, the agglomeration of filler has been significantly improved and the overlapping range of the interface layer has been decreased. Moreover, the effect of coupling agent treatment on the interaction between nanoparticles and resin matrix is also reduced, resulting in a slight decrease in the dielectric constant. When the nano-particles are well dispersed, the composite can reflect the excellent performance of the filler itself (Fig. 24).

After being treated with coupling agent, the dispersion of nanoparticles in the epoxy resin composite system is significantly improved and the overlapping area of the interface layer is reduced. As a result, the charge high-conductivity channel is reduced, effectively improving the composite material insulation performance. At the same time, the trap energy level generated by the introduction of inorganic particles such as nano-SiO$_2$ and nano-Al$_2$O$_3$ will also limit the movement of space charges, thereby increasing the flashover voltage along the surface. It can be seen from the above that nano-doping will change the trap density as well as the energy level of the composite. However, under the same ratio, the number of nano-SiO$_2$ particles is larger than that of nano-Al$_2$O$_3$ at the same ratio, leading to the higher trap density of nano-SiO$_2$/epoxy resin composite compared to the nano-Al2O3/epoxy resin composite. At the same time, it also makes the charge carrier more easily trapped and has a more vital binding ability to charge. Therefore, the flashover voltage of modified nano-SiO$_2$/epoxy resin composite is higher than that of nano-Al$_2$O$_3$/epoxy resin composite (Fig. 25).

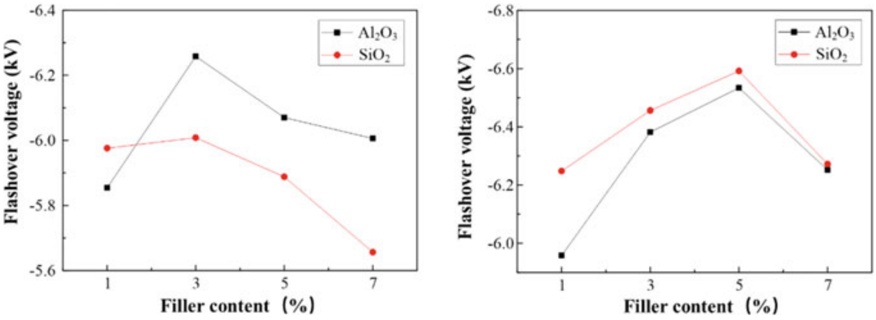

(a) Before coupling agent treatment (b) After coupling agent treatment

Fig. 25 Test results of composite materials flashover voltage

3.2 *Effect of Mass Fraction of Coupling Agent Modified Nano-filler on Electrical Properties of Epoxy Resin*

The mass fraction of filler doping is one of the key factors affecting its modification effect. It is difficult to dope a large quantity of nano fillers at present when conducting a study of nanofillers doping modification as the fillers surface energy and small size effect play a role. It is an essential issue for the ongoing research on nano-modification of epoxy composites to Seek the optimal doping concentration and obtain a higher modification effect with a lower filling cost. This book introduces the change rules of epoxy composites electrical properties with nano filler mass fractions of 1%, 3%, 5%, and 7% respectively and studies the nano content impact on the properties of composites. The test results demonstrate that the dielectric constant of the composite initially decreases and then increases with the increase of the content. This is attributed to the low dielectric constant of the interface layer between the nano-particles and epoxy resin, and the interface area has a larger volume relative to the material. The interface region plays a leading role in the macroscopic properties, making the composite have a small dielectric constant. With the gradual increase of nano fillers, more interface layers will be introduced, further reducing the dielectric constant. Moreover, with the increase of nano fillers, the interaction between nano-particles and resin matrix will be intensified, further hindering the turning of polymer chain segments or side groups. Consequently, the dielectric constant of the composite will decrease as the content of nanofillers increases.

In addition, the dielectric constant of the composite will not decrease limitlessly with the increasing content of nano fillers. Once the content of the nano filler reaches to a point, excess particles per unit volume will lead to an intensified agglomeration of nanofiller as well as a larger overlapping area of the interface layer. At the same time, the increasing number of nanoparticles enhances the overlapping probability of the interface layer and further increases the overlapping range of the interface layer. The overlapping interface layer destroys the previous stable structure and affects the original small dielectric constant of the interface layer. Furthermore, the interaction

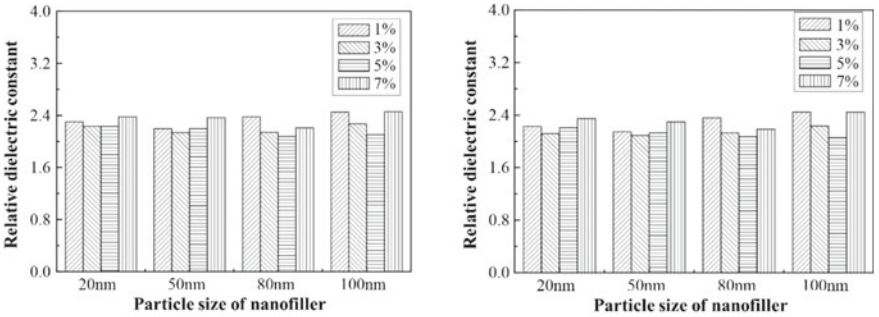

(a) Unmodified Al_2O_3 (b) Modified Al_2O_3

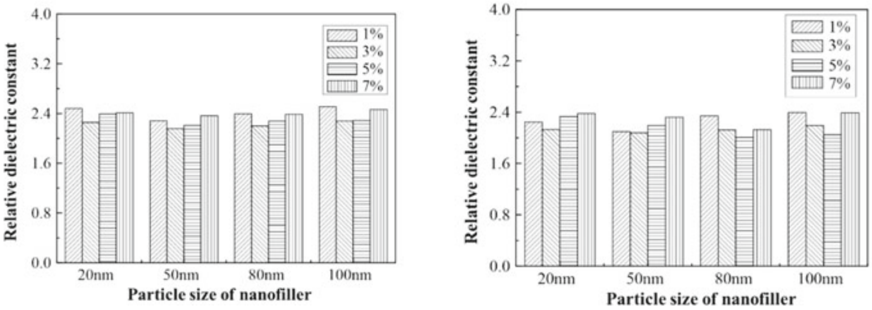

(c) Unmodified SiO_2 (d) Modified SiO_2

Fig. 26 Dielectric constant of composites with different nano content

between nano-particles and resin matrix has also changed, and the restriction on the polar polymer chain segment or side group turn in the interface area has weakened, therefore enhancing the dielectric constant of the composite. Consequently, the dielectric constant of the composite will increase with the increasing number of nano filler content when the nano filler content exceeds a specific limit (Fig. 26).

The results show that the trapped energy level will be generated after the ionization of the doped nano filler. Carriers flowing through the adjacent region will be attracted and bound within the interface region. At this time, the carriers are transported mainly by hopping conductivity and the primary process is trapped electrons—thermal excitation—conduction band electrons—reentry—trapped electrons. Due to the high trap energy level introduced by nano-particles, it is challenging for the trapped electrons to detrap through thermal excitation, thus severely restricting the charge transport between the dielectric body and the interface impeding the advancement of flashover. Therefore, creating conductive channels has been highly difficult, impeding the advancement of flashover. With the increase of nano content, more and more traps are introduced, which increases the trap density of composite materials and further decreases the mobility of carriers. At the same time, it lessens the concentration of free electrons participating in the conduction and further amplifies

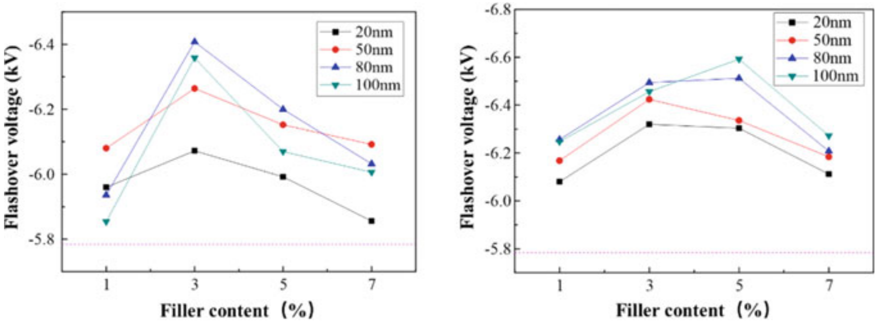

(a) Unmodified Al_2O_3 (b) Modified Al_2O_3

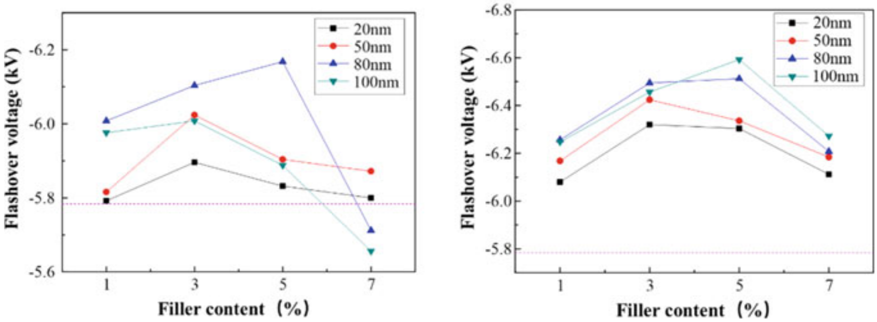

(c) Unmodified SiO_2 (d) Modified SiO_2

Fig. 27 Flashover voltage of composite materials with different nano content

the flashover voltage of the composite. As the concentration of nanoparticles per unit volume reaches a certain threshold, the agglomeration of nano-particles begins to occur. However, there are not many high conductivity channels generated as a result of the interface layers overlapping, the average mobility of carriers will not be improved significantly, thus having little effect the insulation performance of the composite. Concurrently, a slight increase in the conductivity leads to a rapid dissipation of the composite surface charge and mitigates the distortion of the space electric field, thus improving the flashover voltage of the composite further (Fig. 27).

3.3 Effect of Particle Size of Nano-filler Modified by Coupling Agent on Electrical Properties of Epoxy Resin

The particle size of nano filler will directly affect the interface effect between filler and matrix which further affects many macroscopic properties of the composite. In practical engineering applications, nanofillers with smaller sizes comes with greater preparation difficulty and higher production expense in practical engineering applications. Therefore, while utilizing the nano-size effect of fillers, it is also necessary to screen the particle size of fillers to obtain a cost-effective and high-performance epoxy nanocomposite preparation. In this paper, four types of nano fillers with particle sizes of 20, 50, 80 and 100 nm are used to analysis the effect of stuffing particle size on the performance of composite materials. In addition, the work also tests the dielectric constant and flashover voltage of composite materials.

The dielectric constant of the composite decreases first and then increases with the decrease of the filler particle size. With the filler particle size reduction, its specific surface area, reflecting the interfacial bonding degree between the nano-particles and the resin matrix and affecting its interfacial properties, gradually increases. The increase of specific surface area increases the interaction between nano-particles and epoxy resin and strengthens the restriction on the molecular chain movement of epoxy resin, and then makes it difficult for the main chain or side group to turn, thereby reducing the polarization inside the composite material and decreasing the dielectric constant with the decrease of the particle size of the filler.

When the particle size of nano filler is too small, although it provides a large specific surface area and reinforces the interfacial effect of epoxy resin, it also improves the adsorption of particles, leading to agglomerate more easily. The agglomeration of nano-particles impairs the interfacial bonding performance of nano-particles and epoxy resin and enhances the dielectric constant of the interface layer. In addition, agglomeration affects the interaction between nano-particles and resin matrix, leading to alleviation of the restrictions on the movement and direction of molecular chains in epoxy resin. At the meantime, the dielectric constant of the composite is improved in two ways. Therefore, when the particle size of the nano-particles is less than a certain value, the dielectric constant of the composite will increase with the diminution of the particle size (Fig. 28).

The flashover voltage of the composite increases first and then decreases with the decrease of the filler particle size. As the particle size of the filler continues to decline, its specific surface area and surface energy continues to increase which is easy to adsorb other particles and agglomerate. The aggregation of fillers makes the interface layer overlap between the adjacent nano-particles and the resin matrix, generating a high-conductivity charge channel, and thus promoting the carrier migration. However, the number of high-conductivity channels is small at this moment, and the mobility of carriers is not heightened, which does not affect the insulation performance of the composite. On the contrary, it can accelerate the surface charge dissipation of composite materials and reduce the space electric field distortion caused by charge accumulation. Thus, the surface flashover voltage of the composite is further optimized.

When the particle size of the filler decreases to a critical point, the agglomeration becomes serious. Owing to the interface layers overlapping, numerous high-conductivity channels of charge are established, leading to a remarkable augmentation in carrier mobility. The researches demonstrate that the small particle size of the filler curtails the formation of deep traps, and the smaller the particle size is, the stronger the inhibition ability will be. This phenomenon reduces the density

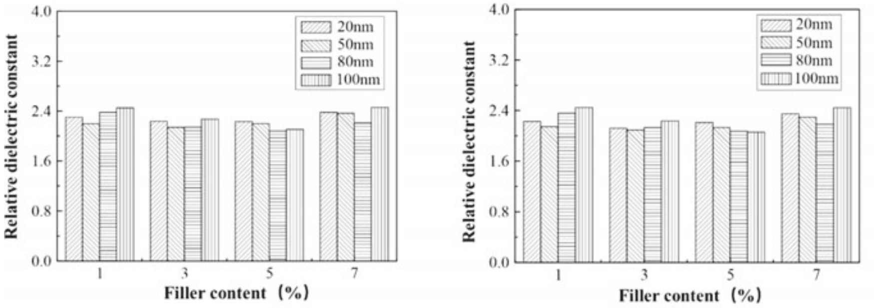

(a) Unmodified Al_2O_3 (b) Unmodified Al_2O_3

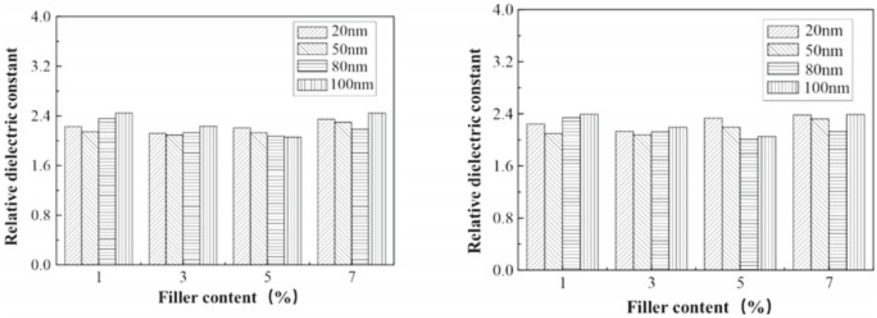

(c) Unmodified SiO_2 (d) Modified SiO_2

Fig. 28 Dielectric constants of composites with different nano-particle size

of deep traps and boosts the density of shallow traps. However, the lifetime of carriers in shallow traps is much shorter than that in deep traps. Therefore, carriers in shallow traps easily get stimulated and de-trapped, increasing carrier concentration. In summary, when the particle size of the filler is small to a certain degree, the flashover voltage of the composite decreases with the decrease in particle size of the filler (Fig. 29).

4 Regulation Electrical Properties of Epoxy Resin by Fluorinated Modified Nano-filler

Fluorination modification has proven to be a conducive approach to augmenting the insulation properties of epoxy composites. This method has been extensively acknowledged by industry experts as an area deserving of further exploration. Fluorine has extremely strong electronegativity, which can firmly bind valence electrons near its atomic nucleus and makes fluorine-containing groups have predictable inhibition ability to the development process of discharge [12]. The current research

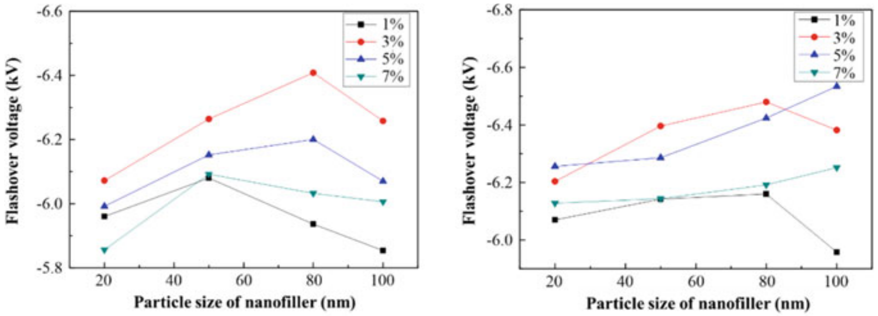

(a) Unmodified Al_2O_3 (b) Unmodified Al_2O_3

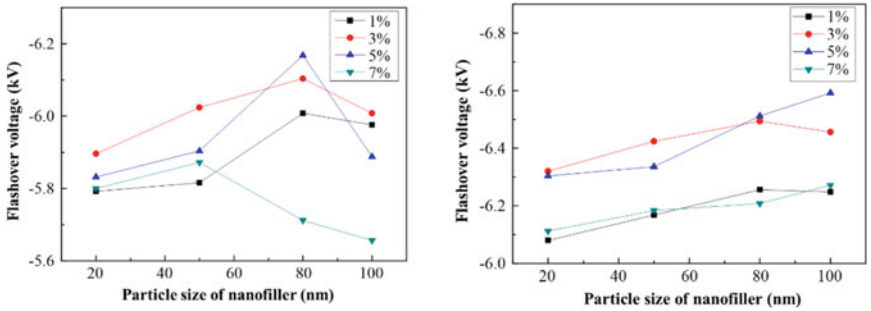

(c) Unmodified SiO_2 (d) Modified SiO_2

Fig. 29 Flashover voltage of composites with different nano-particles diameters

on fluorination modification primarily focus on surface fluorination. The fluorinated layer can inhibit the secondary electron emission and improve the trap distribution characteristics on the surface of epoxy composites, resulting in an improvement of the pressure resistance along the surface. Grafting fluorine-containing groups onto epoxy resin monomer can also effectively improve the insulation performance of cured epoxy. Fluorination of nano fillers is an innovation to introduce fluorine-containing groups into epoxy composites. The fluorine-containing group graft modification of nano filler functions as a coupling agent thereby enhancing the dispersion of filler in the polymer matrix and heightening the compatibility between the filler and matrix. Simultaneously, fluorine-containing groups are introduced at the interface between filler and matrix for grafting modification. This paper introduces the influence of fluorinated nano filler on the electrical properties of epoxy composites, taking BN nanofiller [15] and graphene nano filler [16] as examples.

4.1 Effect of BN Fluoride on Electrical Properties of Epoxy Resin

Figure 30a and b are the SEM images of BN and Fluorinated boron nitride nanosheets (F-BNNS), respectively. Untreated BN is a layered structure with a large transverse size (2–40 μm), stacked in disorder with each other. The transverse dimension of F-BNNS after fluorination stripping is a micron order, about 2 μm. As illustrated in the figure, the boron nitride, after fluorination stripping, presented a twisted dispersion with a thickness of several nm. It was related to the fluorination stripping of boron nitride. The F-ion first combined with the B element in BN, which changed the hybridization mode of the B element, and made the BN surface begin to twist. After that, NH_4^+ was inserted into the gap between the twisted layers, making F-BN fall into F-BNNS. The infrared spectrum analysis results could confirm the chemical combination of F-ion and B elements, as shown in Fig. 31. The BN before and after treatment displayed three same absorption peaks. The absorption peaks at 1372.8 cm^{-1} and 815.9 cm^{-1} respectively corresponded to the in-plane stretching vibration of the sp2 hybrid B-N bond and the out-of-plane bending vibration of the B-N-B bond. The broad absorption peak at 3431.8 cm^{-1} corresponded to the stretching vibration of the O–H bond between molecules demonstrating that water molecules were adsorbed on the surface of the filler (BN is easy to absorb moisture). In addition, the unique absorption peak of F-BNNS at 1594.7 cm^{-1} corresponded to the B-F covalent bond vibration, and the spectral intensity was changed. Therefore, it is believed BN after ammonium fluoride treatment has achieved exfoliation fluorination.

The law of surface charge dissipation of epoxy composites was explored by applying positive and negative corona to BN/EP and F-BNNS/EP composites. Normalized data were obtained by dividing all the measured potentials by the initial potential, as shown in Fig. 31. It was found that the trend of charge decay under positive and negative polarity is roughly similar. Over time, the total charge quantity revealed a decay law of initially fast and then slow, and the decay rate increases with filler concentration. Comparing the charge dissipation rate of the two materials, it

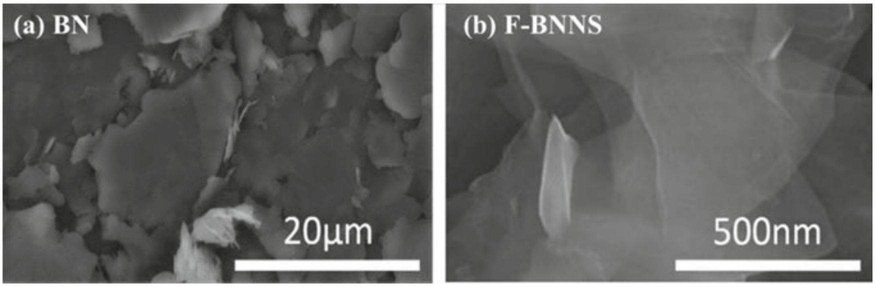

Fig. 30 Microstructure of BN nano fillers before and after fluorination

Fig. 31 FTIR spectra of BN nano fillers before and after fluorination

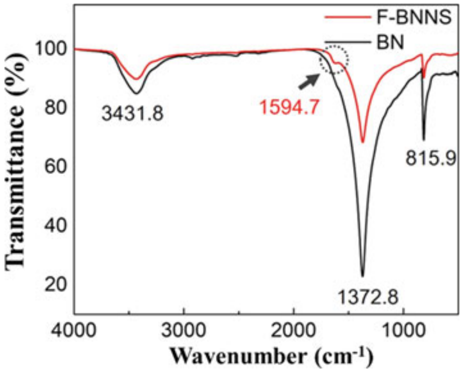

was observed that the charge dissipation rate of F-BNNS/EP nanocomposite was higher than that of BN/EP composite.

Material surface traps will trap corona charges. Upon removal of the charging pin, observed charge dissipation rate followed an arrangement of initially fast and then slow, which is closely related to the charge de-trapping. At the initial stage of corona charging, due to the large charge density on the material surface, many charges will de-trap under the excitation by its own electric field, and the charge will decay rapidly. Over time, the surface electric field of the sample decreases continuously due to the charge decay. Consequently, the rate of charge de-trapping also dwindles gradually (Fig. 32).

The flashover voltage of BN/EP and F-BNNS/EP composites increases with the filler mass fraction. There is a positive correlation between them, which is consistent with the charge dissipation rate. When the filler mass fraction is 8%, the flashover voltage of the BN/EP composite reaches the maximum value of 9.68 kV. Similarly, F-BNNS/EP nanocomposites have the highest flashover voltage of 10.5 kV when the mass fraction of filler is 8%. It is noteworthy that the flashover voltage of F-BNNS/EP nanocomposites has been substantially improved in comparison to the BN/EP composite.

The high flashover voltage of F-BNNS/EP nanocomposites can be attributed to the following reasons. First, by comparing the charge dissipation rate, it can be deduced that F-BNNS/EP nanocomposites with the same filler concentration possess a superior charge dissipation ability in comparison to BN/EP composites. This can be attributed to the fact that boron nitride fluoride can reduce its band gap width and make boron nitride change from insulator to the semiconductor. Therefore, compared with untreated BN/EP composites, F-BNNS filled with the same filler concentration accelerates the charge decay of the composites and alleviates the charges accumulation that induce surface flashover. In addition, the fluorine element on the surface of fluorinated boron nitride filler can react with epoxy groups with active chemical properties. Fluorinated nano-sheets with a high specific surface area have better adhesion with resin, which widens the charge dissipation channel inside the composite. Thus, the surface charge accumulation is further suppressed, and the flashover voltage is increased (Fig. 33).

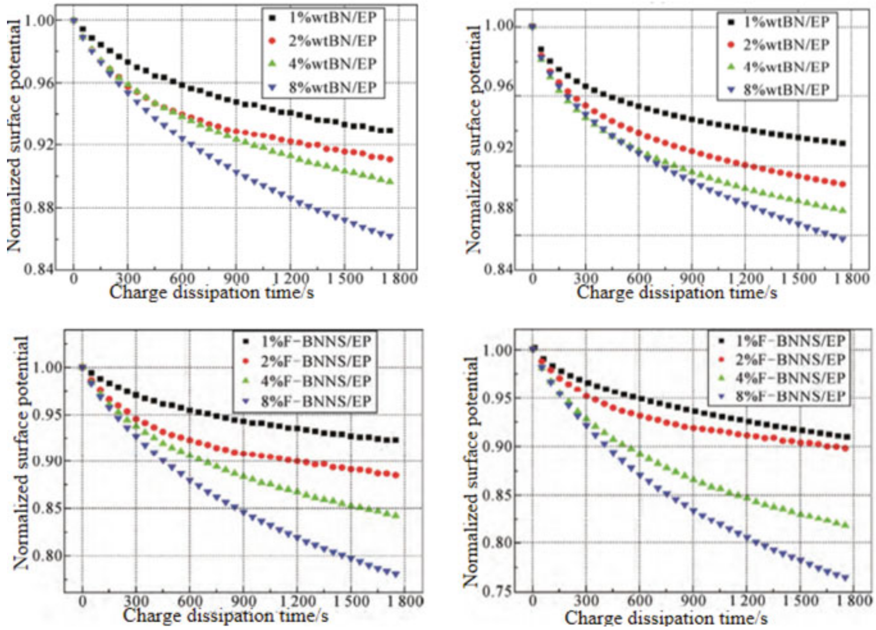

(a) Positive corona (b) Negative corona

Fig. 32 Charge dissipation rate

Fig. 33 Surface flashover voltage

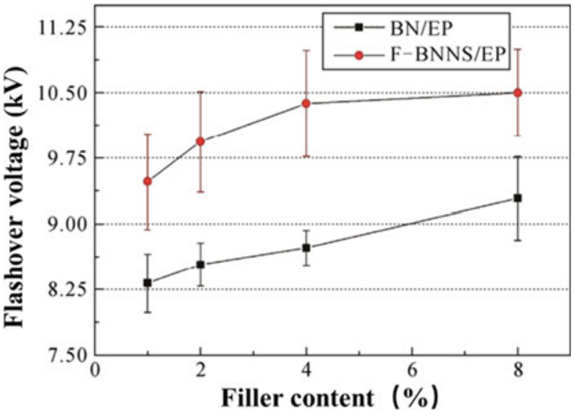

4.2 Effect of Fluorographene Nano-sheets on Electrical Properties of Epoxy Resin

Firstly, graphene nanosheets (GNs) were prepared by ball milling and fluorinated graphene nano-sheets (F-GNs) were prepared by grafting modification with fluorinated coupling agents. XPS characterization of graphene nano-sheets before and after modification was shown in Fig. 34. There were apparent F1s peaks at 689 eV in the GNs after fluorination treatment, belonging to the fluorine element grafted by surface treatment. Moreover, F-GNs had a Si 1 s peak at 835 eV, belonging to the silicon element in the fluorinated coupling agent. Further dividing the peaks of C 1 s shown a prominent peak corresponding to the C–F bond at 286.58 eV and a peak corresponding to –CF_3 at 291.98 eV. According to the FTIR examination results of GNs fillers before and after fluorination treatment, C–F peak and –CHF_2 peak appeared in F-GNs at about 803 cm^{-1} and 1265 cm^{-1}, respectively. The test demonstrates that the fluorinated group was successfully grafted on the GNs surface (Fig. 35).

Comparison with the surface micro-morphology of graphene nano-sheets before and after fluorination reveals that the thickness of GNs and F-GNs are 100 nm. The surface and edges of unmodified GNs appear to be relatively smooth. However, after the fluorination, slight protrusions can be observed on the surface and edge of F-GNs. It is believed that the fluorinated GNs are combined with the fluorinated coupling agent by bonding. Fluorine-containing long link branches construct a fluorine-containing coating on the surface of the filler, which increases the surface roughness of the material (Fig. 36).

The DC surface flashover voltage of EP composite with nanofiller was higher than that of pure EP through the DC surface flashover test of GNs before and after fluorination modification. With the increasing nanofiller doping, the flashover voltage of epoxy composites increased at first and then decreased. When the doping content

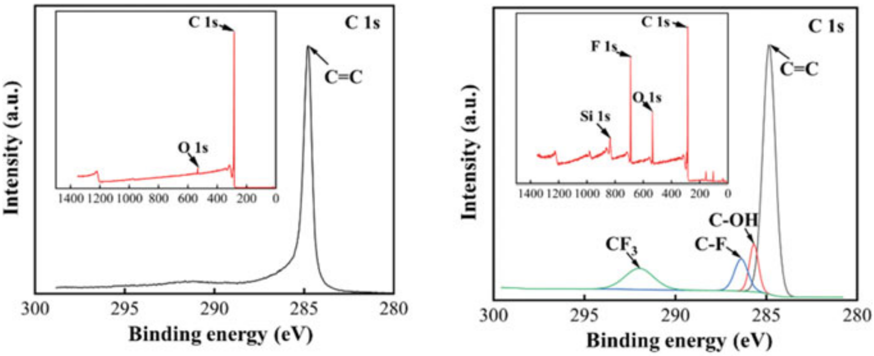

(a) GNs (b) F-GNs

Fig. 34 XPS spectra of **a** GNs and **b** F-GNs

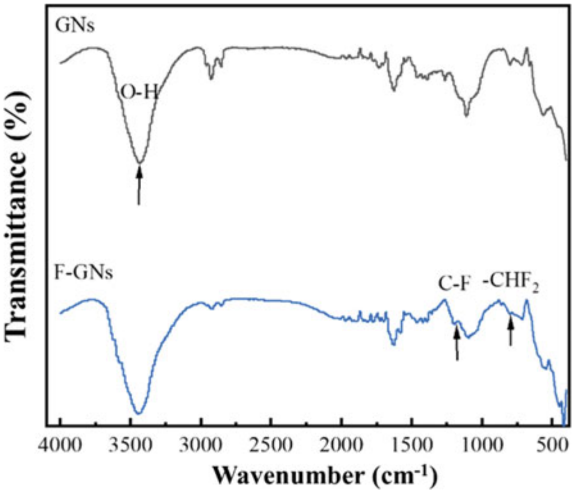

Fig. 35 FTIR spectrum of GNs before and after fluorination

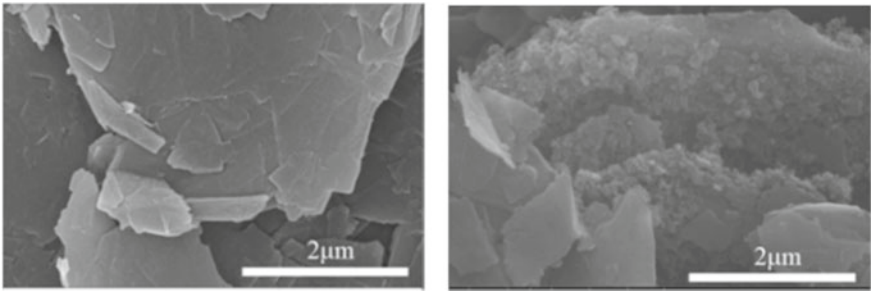

(a) GNs (b) F-GNs

Fig. 36 SEM spectrum of GNs before and after fluorination

of GNs/EP is 0.4%, the flashover voltage reaches the highest value of 9.77 kV. F-GNs/EP achieves its highest flashover voltage when doping concentration is 0.2%, which is up to 10.31 kV. It has been analyzed that there is a strong correlation with the formation of the fluorinated interface layer between the filler and the matrix and the percolation effect of the filler (Fig. 37).

By using the surface potential decay test and trap distribution calculation, the mechanism for the increase of the surface flashover voltage of fluorinated nano filled epoxy composites can be explored in depth. The charge curve revealed that GNs/EP surface potential decay rate dropped and then increased, while the decay rate of F-GNs/EP surface potential exhibited an upward trend with the increase of filler concentration. According to the calculation of charge traps on the surface of materials, the depth of surface traps of GNs/EP composites increased first and then decreased

Fig. 37 Surface flashover voltage of EP composite

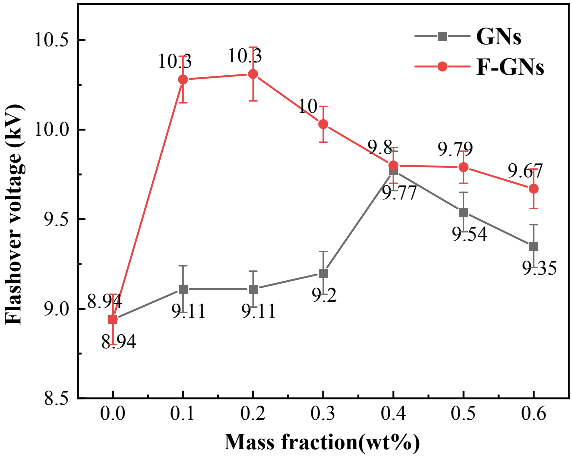

as the doping amount increase, however, the trap depth of the surface layer of the F-GNs/EP composite revealed a downward trend. When the filler concentration reached 0.6%, the trap depth of GNs/EP composites before and after fluorination decreased significantly. This phenomenon indicated that when the doping concentration of graphene nano-sheets is higher than 0.6%, the material has exceeded the percolation threshold. Due to the high conductivity of graphene nano-sheets, the electrical properties of epoxy composites have changed dramatically, and the surface charge dissipation rate has improved significantly (Fig. 38).

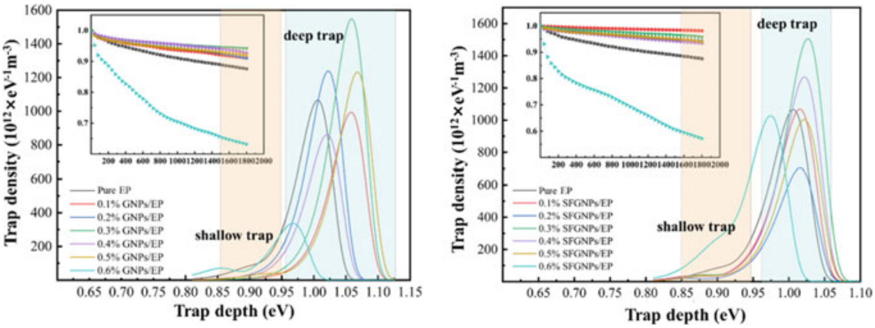

(a) GNs/EP (b) F-GNs/EP

Fig. 38 Surface charge dissipation characteristics and trap distribution curve

5 Regulation of Electrical Properties of Epoxy Resin by Amination Modified Nanofiller

In the study of improving the insulation properties of epoxy composites, a key problem is to explore and regulate the charge dispersion effect. Numerous researches have shown that inhibition of charge migration alone is ineffective in continuous improvement of the insulating materials performance, particularly in the case of surface insulation where the accumulation of charge will lead to electric field distortion and induce flashover discharge. Therefore, introducing an appropriate concentration of low-level traps into the material is an effective approach to control the charge accumulation effect. In the study of epoxy resin composites, it is possible to effectively regulate the trap properties of composites by grafting polar groups on the surface of nanofillers. The amino group not only processes a strong polarity, but also can bond with the epoxy resin matrix, which gives it distinct benefits. Amination modification of nanofillers can enhance the bonding with the matrix, make nanomaterials participate in the cross-linked network of EP, and alleviate the effect of nanofiller on EP cross-linked structure. At the same time, graft modification can adjust the bandgap characteristics and dielectric properties of nanofillers to a certain extent, and further affect the flashover performance of EP composites. In this chapter, we first grafted amino groups on BNNS and layered GNs [17], then we filled the amino-grafted two-dimensional nanofiller into EP to further enhance the electrical properties and investigate its flashover characteristics, charge dissipation, and trap characteristics.

5.1 Effect of Amino Modified BNNS on Electrical Properties of Epoxy Resin

This paper introduces a method for preparing amino-modified BN nanosheets [13], which uses the urea co-ball milling method. Figure 39 is the characterization results of the microstructure of BN nanosheets before and after modification. As illustrated in the figure, we can see that the BNNS possesses a thin sheet with the lateral size is 300–500 nm, a thickness of tens of nanometers, and a smooth, no-particles surface. The overall distribution is multi-layer stacked. Because aminodized boron nitride nanosheets (A-BNNS) is grafted with a large number of amino groups, there are many nano-scale particles attached to its surface and showed a layer of rough granular protrusions. Figure 39c, d are the cross-sectional morphologies of the composites after doping epoxy resin with the filler before and after modification. The unmodified BNNS in the figure displays a granular distribution in the epoxy matrix, and there is a marked agglomeration in partial areas, whereas the modified A-BNNS was well dispersed in the EP matrix, and the filler showed a dendritic distribution. Following analysis, we believe that this phenomenon may be caused by the bonding between the amino groups on the surface of BNNS and the EP matrix.

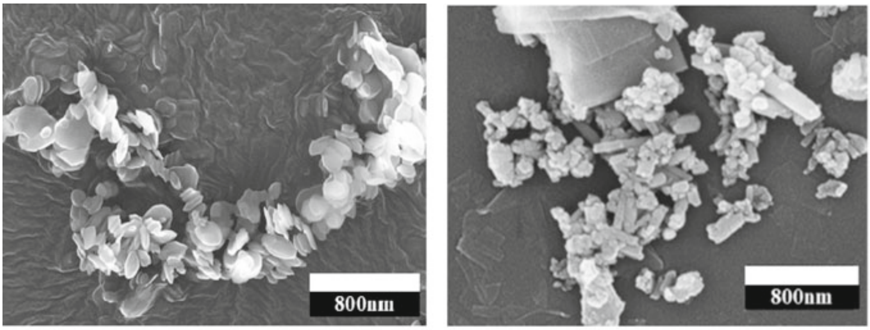

(a) BNNS (b) A-BNNS

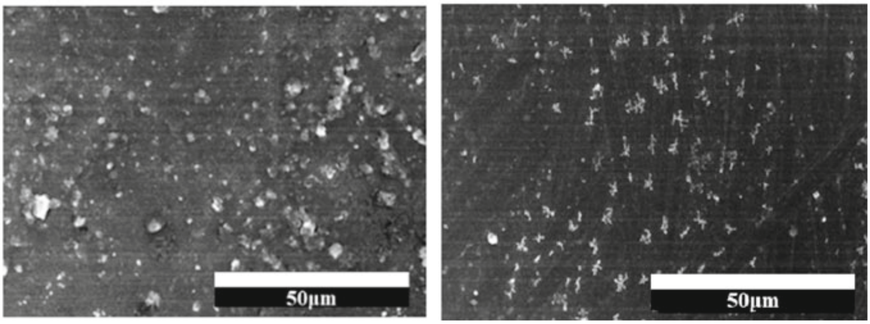

(c) BNNS/EP (d) A-BNNS/EP

Fig. 39 SEM images of BNNS and its epoxy composites

In Fig. 40, FTIR analysis of BN nanosheets before and after amination modification can characterize the change of surface groups of fillers. Before and after modification, B-N bending vibration peaks and stretching vibration peaks all appeared at 806 and 1380 cm^{-1} for both fillers. A-BNNS has N–H absorption peaks at 3100–3500 cm^{-1}, and there are obvious double peaks of $–NH_2$ at 3208 and 3433 cm^{-1}, but BNNS does not appear the absorption peaks of these groups. This shows that after amination modification, NH_2 groups were successfully grafted onto the surface of BN nanosheets.

We doped BN nanosheets with different mass fractions of modified epoxy resins both before and after amination modification. Figure 41 presents the test result of its DC flashover voltage. The enhancement of surface flashover characteristics of EP composites is generally more prominent than that of A-BNNS. With the increase of filler content, the flashover voltage of BNNS and A-BNNS doped EP composites experienced a fluctuating tendency initially increasing, then decreasing and finally rising again. And the highest increase is achieved when the filler mass fraction is 0.5%. A-BNNS/EP increased by 11.3% compared with pure EP, and BNNS/EP increased by 10.77%. Upon conducting the analysis, we believe that the excellent insulating properties of BN can improve the overall surface flashover characteristics

Fig. 40 FTIR of boron nitride nanosheets before and after amination modification

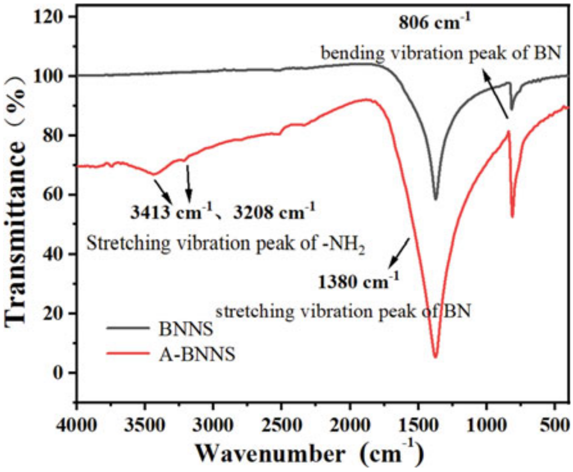

of EP composites, and at the same time, the interface region derived from nanofillers will also have a considerable impact on the surface pressure resistance of composites. There is less interfacial bonding between BNNS and the epoxy matrix, and its introduction will destroy a degree of the crosslinking network of the epoxy matrix. The filler-matrix interface layer formed by A-BNNS and EP through bonding has more polar groups, which can provide reliable charge dissipation channels.

The introduction of nano-fillers can regulate the charge dissipation and trap distribution characteristics of EP composites. The potential-time variation curve of EP composites is shown in Fig. 42. In the figure, we can see that the dissipation rate of the material surface charge presents a trend of climbing first and then sagging as the filler content increases. As a whole, the charge dissipation rate of the A-BNNS/EP composite demonstrates a higher value than the BNNS/EP composite. This is

Fig. 41 Flashover voltage of EP composite materials

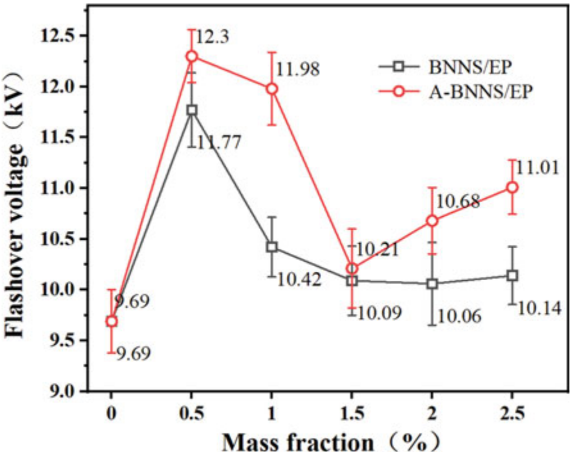

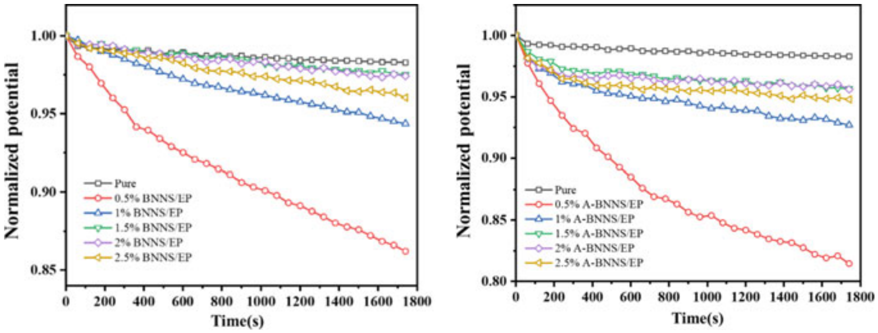

(a) BNNS/EP (b) A-BNNS/EP

Fig. 42 Surface potential decay characteristic curve of EP composite material

consistent with the change of the flashover voltage of the material, which shows that the accumulation effect of the surface charge of the EP composite material plays a major role in leading to the flashover. After A-BNNS was doped with modified EP, the interface layer between the filler and the matrix formed a charge transport network composed of dipoles, promoting the rate of space charge dissipation through the surface side and the solid side.

Figure 43 is the distribution characteristics of traps on the surface of EP composites. After adding nanofillers, the trap energy levels of EP composites can be shown that declining before rising. Moreover, the trap energy level of the A-BNNS/EP composite is lower than that of the BNNS/EP composite with the same filler mass fraction. As the EP matrix is a high polymer with a relatively high energy gap, approximately 8–10 eV, the introduction of BNNS into the EP matrix caused a formation of free-moving molecular segments in the interfacial region, which made defects in the formerly dense macromolecular network structure, thus introducing lower-energy traps. As the filler content increases, the interfacial regions begin to overlap and this effect is gradually weakened. At the same time, more BN with high energy gap is introduced into the matrix, which makes an upward trend in the trap energy level on the surface of the material. The surface of A-BNNS contains NH_2 groups, which upgrades the compatibility between the filler and the matrix and also introduces a more polar group which makes it easier for the EP composite to form polarized charges under the action of an electric field. Consequently, the trap energy level of the A-BNNS/EP composite is significantly lower than that of the BNNS/EP composite. The shallower trap energy level boosts the carrier mobility within the EP composite. Under the effect of an external electric field, the space charge injected into the material is hard to accumulate, which alleviates the electric field distortion in the local area. This makes it trouble for the initial electrons to be excited during the generation of the flashover discharge, and forming a large-scale electron avalanche is hard to do because of the inadequate of high-field-strength accelerated energy after the secondary electrons emission in the flashover development stage. Therefore, this

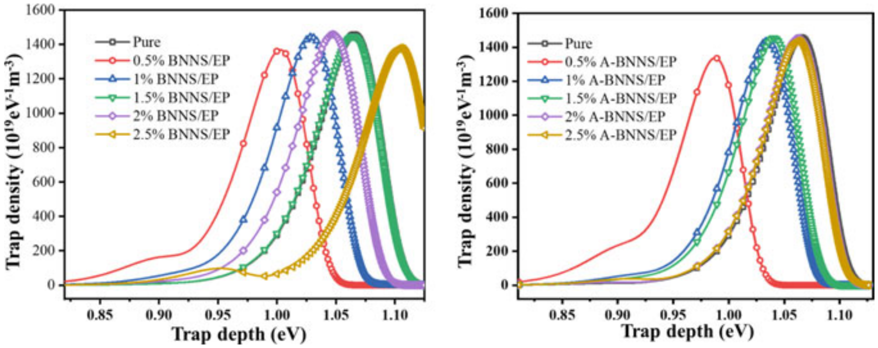

(a) BNNS/EP (b) A-BNNS/EP

Fig. 43 Energy level distribution of traps on the surface of EP composites

hinders the development of flashover discharge and is conducive to improving the surface flashover voltage of the material.

5.2 Effect of Amino Modified GNs on Electrical Properties of Epoxy Resin

The preparation process of GNs nanosheets and aminated GNs nanosheets is basically the same as that of BNNS, which is to obtain two-dimensional sheet materials by ball milling exfoliation. We used scanning electron microscopy to characterize the exfoliated nanosheets, and the result is shown in Fig. 44. Figure (a) depicts the microscopic morphology of GNs, which averages in size to around 500–800 nm and features a smooth nanosheet surface without any additional attached particles. The nanosheet thickness is estimated to be approximately 100 nm. Figure (b) shows the microscopic characterization of AGNs nanofillers. Its particle size is closely resembling that of GNs. Rough particles are attached to the surface of aminated GNs nanosheets, and amino groups are grafted on the surface of GNs through chemical bonds.

We filled EP with GNs before and after amination modification to prepare composite materials. Figure 45 displays the dispersion effect of fillers inside the matrix. Analysis of the characterization results reveals that the dispersion of GNs filled EP composites is relatively poor with many fillers experiencing serious agglomeration. The surface of AGNs is grafted with a large number of amino groups, which can participate in the curing crosslinking reaction of the epoxy resin/anhydride system, thus providing better compatibility with the matrix. Simultaneously, it is hard for a condensation reaction to proceed between two amino groups, resulting in minimal agglomeration of the filler particles. This makes it the optimal choice for dispersibility.

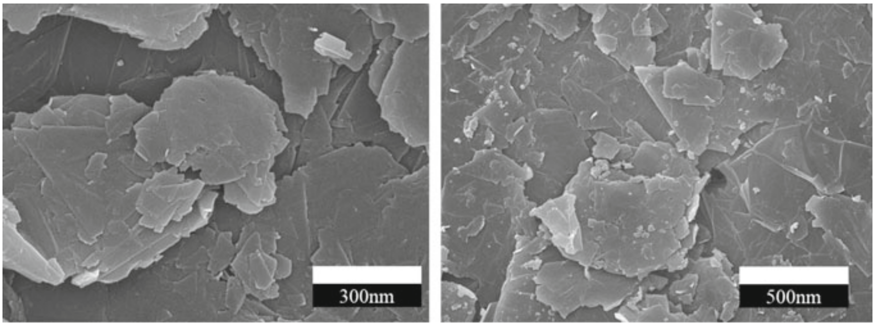

(a) Graphene Nanosheets (b) Aminated graphene

Fig. 44 Microscopic morphology of graphene and aminated graphene

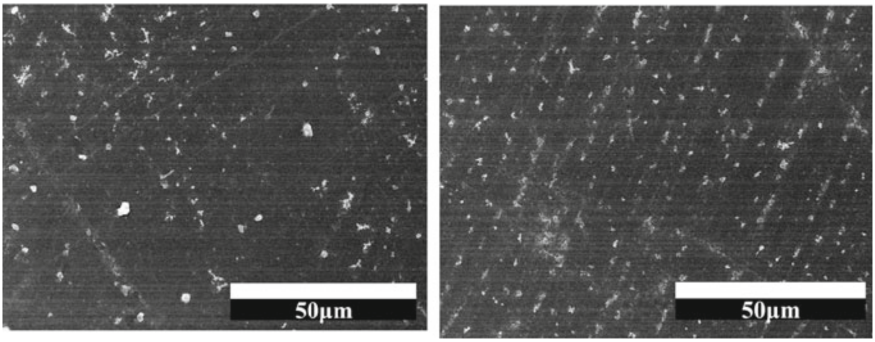

(a) GNs (c) AGNs

Fig. 45 Graphene nanofiller dispersion SEM

We performed FTIR and XPS analysis on graphene nanosheets before and after amination modification, using Nicolet Nexus 410 Fourier infrared spectrometer and ThermoFisher K-Alpha X-ray photoelectron spectrometer. Figure 46 is the analysis result. The FTIR spectrum of AGNs showed the characteristic peak of C–N bond at 1446 cm^{-1} and the characteristic peak of N–H bond representing amino group at 1592 cm^{-1}, which indicated a successful grafting of amino group. The scanning results of XPS displayed that the AGNs after amination modification exhibited N 1 s peak at 401.5 eV. By merging the results of the FTIR characterization, it can be concluded that the amination grafting modification effectively graft the amino groups onto the surface of GNs (Fig. 47).

Due to the high conductivity of graphene nanofillers, the mass fraction of fillers in EP composites needs to be controlled at a relatively low level in order to effectively promote the surface insulation performance. The flashover voltage of EP composite samples modified by graphene nanofillers was significantly higher than that of pure epoxy resin. The flashover voltage of the EP composite sample doped with GNs is

Fig. 46 FTIR of graphene and its modified filler

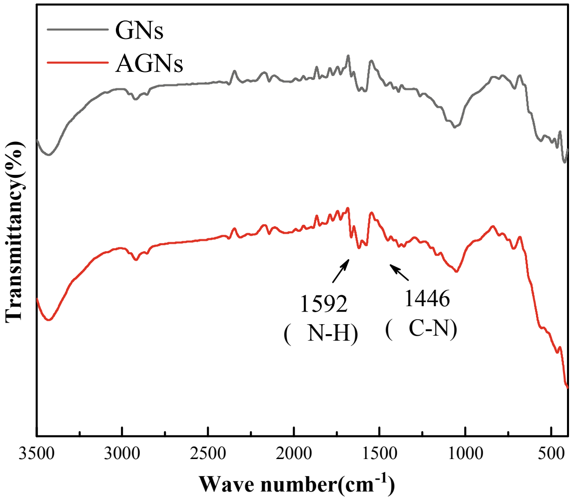

Fig. 47 Graphene and its modified filler XPS

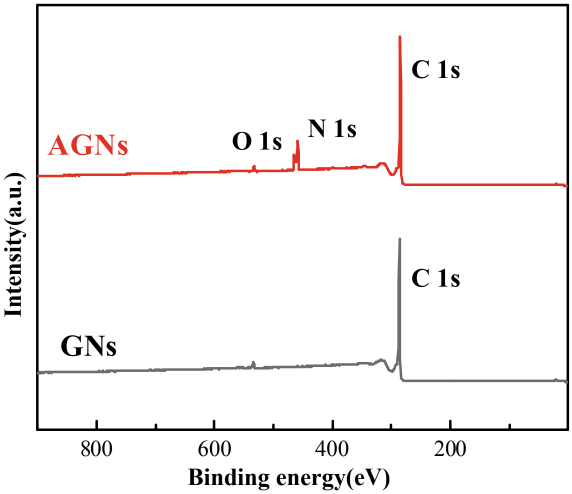

demonstrated by the black curve. When the doping amount is 0.2 wt%, compared with the pure epoxy resin, the flashover voltage of the sample increased by 20.26%, reaching 11.22 kV, which is an obvious improvement; but as the mass fraction of GNs advanced to 0.4 wt%, the flashover voltage dropped to 9.6 kV, and then the flashover voltage gradually increased with the mass fraction increasing. The amination grafting of GNs can effectively strengthen the compatibility between the filler and the EP matrix, and reduce the physical and chemical defects during the preparation process. The blue curve in Fig. 48 is the flashover voltage change curve of the AGNs system. When 0.2 wt% of AGNs is dropped, the flashover voltage of the sample increases to 11.26 kV, an increase of 20.68% compared to that of the pure EP. Upon further

Fig. 48 Flashover voltage of graphene material modified EP sample

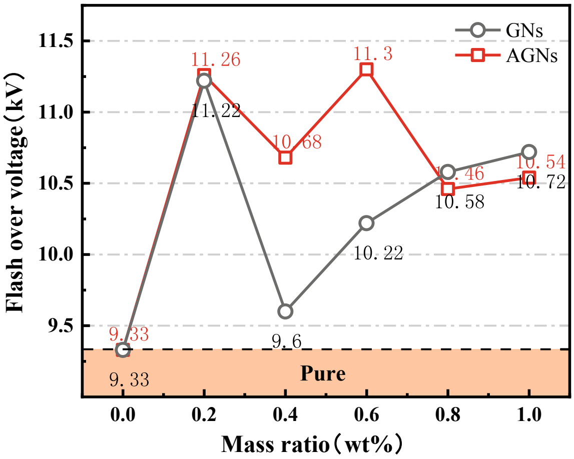

increasing the doping content of AGNs, the flashover voltage presents a "W"-shaped change pattern, exhibiting the optimal performance at 0.6 wt%, reaching 11.3 kV, 21.11% higher than that of pure EP. The contribution of AGNs to the improvement of flashover is primarily through accelerating charge dissipation, which is highly affected by the interface effect. The repetitive overlapping of multi-layer interface models results in the "N" type change law of the flashover voltage of the AGNs/EP system.

We can get the curve in Fig. 49 by testing the surface potential decay characteristics of the epoxy composite before and after modification. The charge dissipation rate generally presents a trend of first decreasing and then increasing as the doping concentration increases. After GNs are incorporated into the EP matrix, the compatibility with EP is poor, leading to difficulty in forming a stable chemical bond, which cause destroying the cross-linked structure of the EP matrix to a certain degree. The original conductive path is blocked and thus reduce the rate of charge dissipation. However, with the increasing doping amount of GNs nanofillers, the contact and overlap between the nanosheets are formed, and new conductive paths are generated. The GNs itself has a high carrier mobility, so the surface charge dissipation rate of GNs/EP composites continues to accelerate with the increase of doping amount. The AGNs can crosslink with the EP matrix due to the grafting of a considerable amount of amino groups on the surface. As the doping concentration rises, the superior dispersibility and matrix compatibility make AGNs nanosheets overlap with each other, adding a large number of new conductive paths, which makes a better charge dissipation rate of the system than that of GNs system at higher doping concentration.

Figure 50 shows the relationship between the trap concentration and energy level of epoxy composites before and after modification. Pure EP demonstrates a complete cross-linking structure and a lower concentration of shallow traps and thus there is a

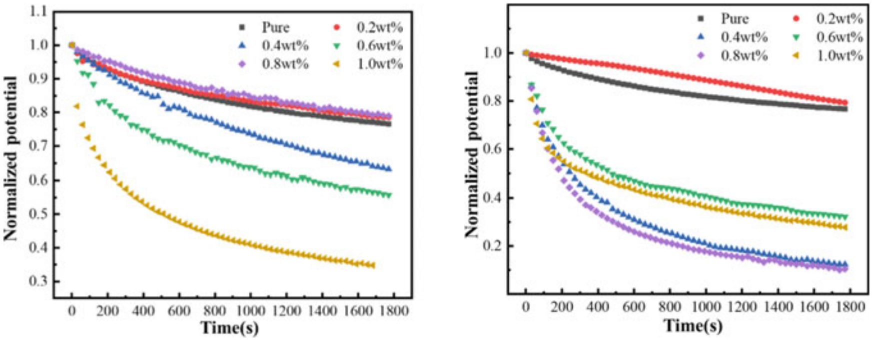

(a) The charge dissipation curve of GNs/EP composites

(b) The charge dissipation curve of graphene nanofiller doped EP

Fig. 49 Charge dissipation curve of graphene nanofiller doped EP

slow rate of charge dissipation. After doping GNs, with the increase of doping concentration, the concentration of shallow traps gradually increases, while the concentration of deep traps first climbing and then sagging. Following our analysis, we have determined that there exists a substantial number of charge traps within the interface region between the filler and the matrix, and the interface effect is closely related to the compatibility of materials and the width of the interface between particles. Once the doping concentration of nanofillers surpasses a specific value, overlap among the different layers of particles may be induced, which will further lead to changes in trap energy level and concentration. Moreover, upon reaching the percolation threshold of filler mass fraction, the high electrical conductivity of GNs would significantly accelerate the rate of charge transfer, which is also manifested as a shift in the trap energy level to a lower direction. As the doping concentration of the AGNs system increases, the trap distribution characteristics of the composite material develop in the direction of increasing the concentration of shallow traps and decreasing the concentration of deep traps. This is due to the fact that the amino groups grafted on the surface of the nanosheets can easily react with the EP matrix, the bonding between the filler and the matrix is stronger, and thus the promotion of GNs itself on trap shallowing can be better exerted.

6 The Regulation Mechanism of Filler Functional Modification on the Electrical Properties of Epoxy Resin

The modification of epoxy nanocomposites mainly is largely determined by the properties of filler particles and the interfacial phase formed by them. And the functionalization of nanofillers is primarily manifested in two aspects. On the one hand, it is to maximize the effect of nanoparticles within the composite material. On the other

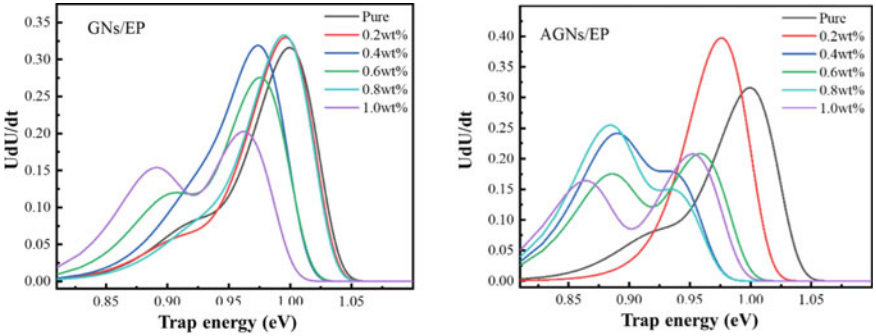

(a) Trap distribution of GNs/EP composites (b) Trap distribution of AGNs/EP composites

Fig. 50 Composite trap distribution characteristics

hand, regulate the interfacial interaction between the filler and the matrix in chemical methods. Tanaka proposed a multi-nuclear model in 2005 [8], which categorized the filler interface as a bond layer (the layer where the valence bond is formed), a bound layer (the layer where the high-energy trap is formed), a loose layer (the layer where the ion trap or low-energy trap is formed) and the electric double layer (the layer where the overlaps with the first three layers). The multi-nuclear model divides the filler-matrix interface more finely, and also adequately explains the difference in charge behavior between different layers in the interface region. With the deepening of the research and the continuous advancement of the current computer simulation technology, the researchers used simulation methods such as molecular dynamics, density functional theory to analyze the action principle of the filler-matrix interface region at the molecular scale. It provides a new theoretical reference for revealing the regulation mechanism of filler functional modification on the electrical properties of epoxy resin. This chapter illustrates the research results of the interaction law of the filler functional interface and its influence on the electrical properties of epoxy composites.

6.1 Interface Structure Between Filler and Matrix

The interfacial properties of nano-filler and matrix are closely related to the types of functional groups on the surface of the filler, the length of the bond segment, the bonding strength and other factors. The interface layer act as a conductive area, thus allowing the accumulation of electrons on the surface of the filler and between the bonding layer and the transition layer. An interface region is formed after doping with different fillers, which will alter the trap energy level and density inside the composite material. The carriers can only transition after gaining enough energy owing to the fact that there are potential barriers inside the bonding layer and the

Fig. 51 Polymer charge transport diagram

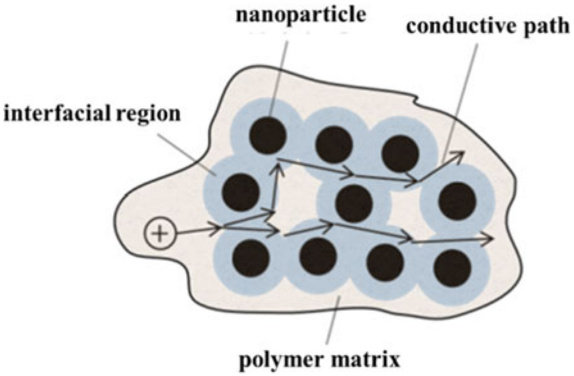

transition layer. Due to the width of the transition layer being shorter than the mean free path of the carriers, when the amount of doped filler is small, the filler particles are isolated in the EP matrix, and the carrier migration is limited by the transition layer. As the amount of filler doping increases and the filler percolation threshold is reached, the interface regions will overlap to form percolated conductance channels, that is, conduction paths. As shown in the figure, it shows that the binding effect on the carriers is weakened, and the carriers in the composite material are easily transported through the conductive path (Fig. 51).

This section takes the fluorinated interface as an example to illustrate the impact of the interface structure on the material properties. The multi-nuclear model reveals that that the interface layer mainly consists of the bond layer and the transition layer. The former is where the surface groups of the nanofillers interact with the epoxy matrix and generally has a narrow width. This layer is composed of fluorinated reagent molecular chains coated on the surface of the filler or grafted fluorine-containing groups, and has a small width. The transition layer is mainly composed of molecules of the polymer matrix, which has a low density and a large width. The hydrothermal fluorination treatment destroyed the molecular structure of the surface of the nanofiller and grafted fluorine-containing groups on the surface of the filler. These groups manifested strong oxidizing properties, allowing for a chemical reaction with the epoxy matrix to realize the chemical bond connection in the interface region. Another fluorination technique is to utilize fluorine-containing coupling agent to fluorinate the nanofiller. One end of the molecular structure of the fluorinated coupling agent reacts with the filler surface to graft a longer fluorine-containing segment on the surface, which is difficult to form a bond with the epoxy matrix.

After the nanofiller is directly doped with the epoxy matrix, forming a stable bond with the matrix is hindered because the surface of the filler lacks active groups, resulting in the narrowness of the bonding layer. The interface layer forms a potential barrier due to Coulomb blockade effect, and the negative charge injected at the electrode is not easy to de-trap after being trapped, forming a deep trap, and thus the charge is not easy to dissipate. Following hydrothermal fluorination, the filler can be combined with the EP matrix through a small amount of covalent bonds and ionic

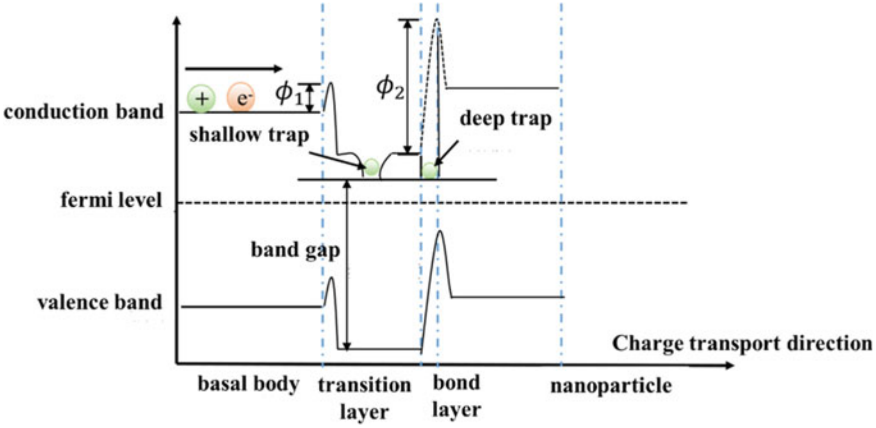

Fig. 52 The relationship between band gap characteristics and charge traps of materials

bonds, thus extending the breadth of the bonding layer to a slight degree. Electrons can fully participate in the charge transport through chemical bond migration, then the charge transport rate becomes faster, and the surface traps of the composite material converted to lower energy levels. As for the nanofiller modified by fluorine-containing coupling agent, its surface is grafted with fluorine-containing coupling agent molecules with longer chain segments, and the width of the bonding layer is larger. The filler and the matrix can only be connected through a longer fluorine-containing chain segment, which enhances the Helmholtz effect at the between the filler-matrix interface. The bound state charge centers of fluorine atoms seriously hinder the charges injected from the outside from transferring to the filler, causing a slowdown of the charge dissipation rate. Both the energy level and density of the traps showed an increasing trend (Fig. 52).

6.2 MD-Based Interfacial Interaction Mechanism Analysis

In the study of nano-modification of composite materials, the agglomeration effect of fillers is a crucial hindrance that affects the modification effect, especially in terms of insulation properties. Agglomeration will bring about uneven distribution of filler interface area and interface layer thickness, and the interaction between filler and matrix interface molecules will produce a special structure and properties, influencing multiple electrical properties of the material. Nanofillers, due to their relatively high surface energy, are often poorly compatible with organic matter, and tend to form agglomerates with mutual affinity within the polymer. The development of computer simulation technology has enabled researchers to explore the interaction between microscopic particles increasingly through methods such as molecular dynamics simulation. This can more effectively analyze the performance alteration mechanism of the material. Molecular dynamics simulation can be employed to construct nanofiller models with different surface functionalization, and analyze the interaction mechanism between functionalized filler particles and between filler and polymer matrix.

This paper presents a case of constructing a nano-interface model. We initiated the process by building an epoxy polymer matrix model. Based on the Materials Studio software, we constructed the monomer molecules of epoxy resin and acid anhydride, and put the two monomer molecules into the periodic box with the quantity of 80/40. After that, a geometric optimization process was conducted on the uncross-linked epoxy resin-anhydride system to guarantee that the molecular structure and segment distribution remained more reasonable. Then under the conditions of 298 K and 0.1 Mpa, the NPT and NVT optimization of 200 ps were carried out respectively to obtain the epoxy resin model. Then we imported the crystal structure of the inorganic filler, treated the unit cell with section method, and then construct the super cell. The following procedure was to utilize the build layer function to create the filler-epoxy resin interface model, and set a vacuum layer with a thickness of 30 Å above the model to eliminate the impact of periodicity. We then performed geometric optimization and 200 ps NVT optimization on the interface model with a 1 fs time step and a frame file being output every 1 ps. Subsequently, we calculated the interface binding energy of different models, selected the interface energy of the last 50 frames and took the average value as the final data. The interface interaction energy can be calculated by the following formula:

$$E_{interface} = E_{total} - (E_{Layer1} + E_{Layer2}) \tag{5}$$

As demonstrated in Fig. 53, the calculation result reveals that the interfacial interaction between fluorinated nanoparticles is significantly less than that of nanofillers with coupling agent modified and unmodified.

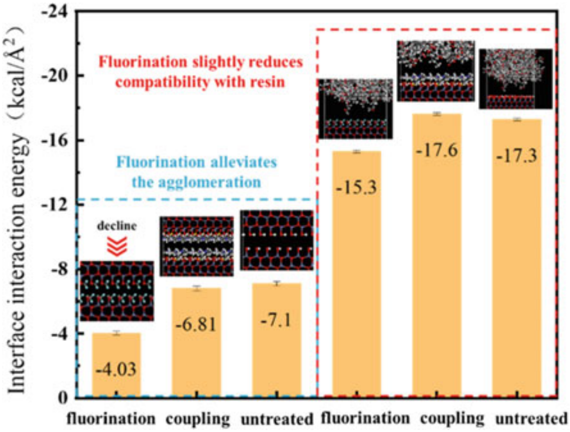

Fig. 53 Interface interaction energy

After analysis, we believe that fluorine-containing groups have been grafted onto the filler surface after fluorination treatment. The special structure of fluorine atoms makes it tightly bind the valence electrons near the nucleus, which endows it with extremely low surface energy. It enables the interaction energy between fluorine-containing groups much lower than that of general chemical groups. When two adjacent fluorinated fillers are in close proximity, the high surface energy and mismatching sites originally caused by the nano-size effect are covered by fluorine-containing groups. The nature between the filler particles transitions from affinity to mutual exclusiveness, leading to a significant enhancement in dispersion within the epoxy matrix. At the same time, we calculated the interaction energy between the three nanofillers and the uncross-linked epoxy resin to assess their compatibility with the epoxy matrix. It can be observed that the interaction energy between the fluorinated filler and the epoxy resin is slightly diminished, while the modification of the coupling agent can improve the affinity between filler and the epoxy matrix. This can be attributed to the introduction of fluorine-containing groups which reduce the affinity sites between the filler surface and epoxy, and the lower surface energy of fluorine-containing groups also weakens the interfacial interaction.

6.3 Influence Mechanism Analysis of Trap Characteristics Based on DFT

To further discover the influence mechanism of functional modification of fillers on the surface flashover characteristics of EP composites, three common treatment methods such as unmodified fillers, fluorinated fillers, and coupling agent grafted fillers were selected for study. And we took the molecular chain segment at the interface between the nanofiller and the epoxy matrix as the object, calculating the molecular orbital energy level of the interface chain segment by quantum chemical method. Then we used MS software to construct the models of the three interface molecular segments. Based on the Dmol3 module, we performed DFT calculations on it with the PBE as the exchange correlation functional and using the generalized gradient approximation. Taking into account the electronic polarization effect, the double numerical plus polarization (DNP) basis set was used for calculation and the optimal quality grid size was adopted as numerical integration [18]. In the calculation process, we firstly performed geometric optimization of the molecule, then engaged NVT optimization at 50 ps, and then analyzed the molecular orbital energy levels of the three chain segments. Figure 54 displays the calculation result. The orbital energy levels of molecular segments in the interface region include the lowest unoccupied orbital and the highest occupied orbital. The LUMO orbital acts as a trap site for capturing electrons inside the material, and the HOMO orbital acts as a trap site for electron holes. The midpoint of the two energy levels is the Fermi level. Electrons, after being excited, will have a transition from the HOMO orbital to the LUMO orbital to obtain conductivity, and the energy required for its transition is the energy

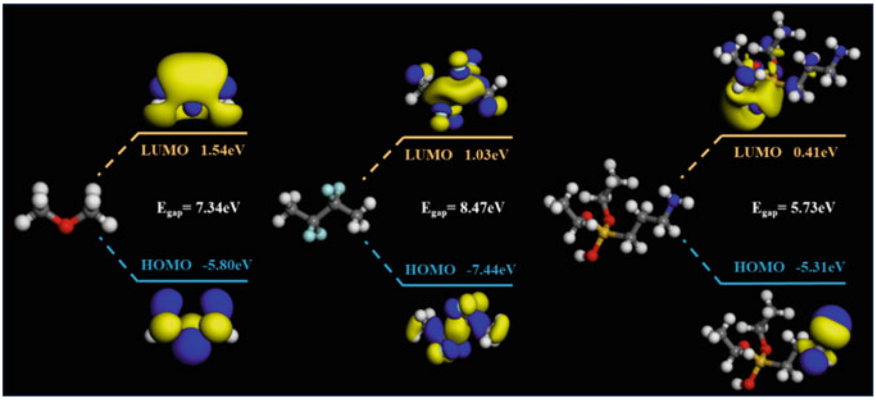

Fig. 54 DFT calculation results

gap. The energy gap between LUMO energy and HOMO energy can reflect the electronic transition ability. In the study of insulating materials, Egap is considered to be a form of trap existence [19]. The model frontier orbital level gap is:

$$E_{gap} = E_{LUMO} - E_{HOMO} \tag{6}$$

The calculation results indicate that the surface of the unmodified filler forms bonds with epoxy through a small amount of hydroxyl groups, and its energy gap is basically at 7.34 eV. Nevertheless, it is worth pointing out that the surface of the untreated filler contains only a tiny amount of hydroxyl groups and thus there are often more vacuum bands at its interface. This makes it tougher for carriers to migrate between the filler and the matrix. The filler treated with the coupling agent is linked to the epoxy via the coupling agent segment. Since there are more polar groups in the molecular chain segment, it can be easily to form polarized charges and transport carriers in the interface region. The energy gap of treated filler is much smaller than that of the untreated filler, leading in a significant increase in the density of shallow traps within the composite material. The fluorinated nanofiller is bonded to the epoxy matrix through the fluorine-containing chain segment, and the fluorine-containing group makes the energy gap of the chain segment significantly climbed. Thereby introducing a large number of deep traps at the interface. Meanwhile, the fluorine-containing chain segment also provides some bonding sites between the filler and the matrix, thus remaining a relatively stable density of the interface trap energy level, and the charge can still be transported through the chain segment. The energy required for carriers is still reduced compared to directly transitioning from the epoxy side to the filler side.

The functional modification of nanofillers has two main effects in ameliorating the surface pressure resistance of epoxy composites. On the one hand, it can improve the bonding state between the filler and the matrix, enhance the dispersibility and compatibility of the nanofiller in the resin matrix, thus better upgrading ability of the nanofiller itself in charge release and discharge suppression. On the other hand, it is to regulate many electrical properties of the filler-matrix interface region, especially the trap distribution characteristics. Conventional coupling agent treatment usually emphasize the first aspect, which can refine the modification effect of nano fillers by improving the dispersibility and compatibility of fillers. And treatments such as fluorination and amination modulation offer both of these capabilities simultaneously. Taking fluorination as an example, fluorination can not only enhance the dispersibility of fillers, but also introduce deep traps at the interface of fillers and inhibits the development of discharge and secondary electron emission at the interface. The dielectric parameters at the junction of filler-matrix-vacuum are significantly different, which will lead to obvious electric field distortion effect. This causes the triple junction to become a weak link in the flashover development, and easily excite a large number of secondary electrons under the initial electrons. Fluorinated nanofillers introduce substantial fluorine-containing groups in the interface region. These fluorine-containing groups can provide massive deep trap energy levels, which effectively inhibit the development of discharge in the interface region and improve the dielectric strength at the filler-matrix interface. On the other hand, the fluorine-containing groups often possess high reactivity, which facilitate their further reaction with the epoxy resin, thereby establishing a chemical bond between the filler and the resin. This eliminates the situation where the carriers cannot be transported due to the lack of effective bonding at the filler interface. Therefore, when the filler concentration reaches a certain threshold, the charge dissipation rate on the surface of the EP composite will also be improved obviously. This provides a good path for the dissipation of local charges on the surface of the composite material, alleviating the field distortion effect due to charge accumulation. The two mechanisms act on the filler side and the interface layer respectively and the surface pressure resistance of the composite is enhanced synergistically.

7 Conclusion

This chapter systematically and comprehensively introduces methods of nanofiller functional modification and their effect rule and mechanism on the electrical properties of epoxy composite. By assessing the current research regarding epoxy composite nanomodification research, methods of functional modification of nanofiller surface are proposed to improve the dispersity and compatibility of filler in matrix. Meanwhile, the interface properties of filler-matrix can be targeted adjusted by controlling the grafting of surface functional groups. Furthermore, the effect mechanism of nanofiller functional modification was analyzed and summarized by combining experiment results and simulation results of MD and DFT. The technology of nanofiller functional modification can enhance the modification effect of traditional inorganic nanoparticle on the insulation performance of epoxy composite, and optimize the preparation of epoxy nanocomposite, which has a broad industrial application prospect. The main conclusions of this chapter are as follows:

(1) This chapter introduced a systematic overview of the surface functional modification for nanofiller in epoxy composite insulation material research. And the platforms and methods of nanofiller surface coupling agent grafting, hydrothermal fluorination and one-step method of amination modification were elaborately discussed. Moreover, various types of functional inorganic nanofiller were prepared successfully.

(2) The experiments were conducted to study the influence law of nanofiller surface functional modification on microstructure and electrical properties of epoxy composite. The dispersity and compatibility of nanofiller in matrix were improved by coupling agent graft, fluorination and amination modification all, so as to increase the modification effect of nanofiller on insulating property of epoxy resin. In addition, fluorine-containing groups and amino groups could influence the trap distribution of composite surface and targeted adjust the aggregation and dispersion of material surface charge, which was essential for the improvement of epoxy composites surface insulation.

(3) Based on the nanointerface model and simulation results of MD and DFT, this study examined the effect mechanism of nanofiller functional modification on insulating property of epoxy composite. It could be considered that groups grafted on nanofiller surface can boost macro electric properties of epoxy composite by modifying filler- matrix interfacial properties. Filler surface fluorination modification could effectively inhibit the nanoparticle agglomeration effect. Furthermore, fluorine-containing groups could increase the energy gap of molecule chain at interface, thus high level deep traps were introduced to the internal of materials to improve the insulating property of materials.

References

1. Li, S., Li, J.Y.: Condition monitoring and diagnosis of power equipment: review and prospective. High Volt. **02**(02), 82–91 (2017)
2. Yang, S., Xiang, D., et al.: Condition monitoring for device reliability in power electronic converters: a review. IEEE Trans. Power Electron. (2010)
3. Fan, B.H., Zha, J.W., Wang, D., et al.: Size-dependent low-frequency dielectric properties in the $BaTiO_3$/poly (vinylidene fluoride) nanocomposite films. Appl. Phys. Lett. **100**(1), 012903 (2012)
4. Zha, J.W., Dang, Z.M., Li, W.K., et al.: Effect of micro-Si_3N_4-nano-Al_2O_3 co-filled particles on thermal conductivity, dielectric and mechanical properties of silicone rubber composites. IEEE Trans. Dielectr. Electr. Insul. **21**(4), 1989–1996 (2014)
5. Landry, C., Coltrain, B.K., Landry, M.R., et al.: Poly(vinyl acetate)/silica-filled materials: material properties of in situ vs fumed silica particles. Macromolecules **26**(14), 3702–3712 (1993)
6. Giannelis, E.P.: Polymer layered silicate nanocomposites. Adv. Mater. **8**(1), 1–9 (1996)
7. Lewis, T.J.: Interfaces: nanometric dielectrics. J. Phys. D Appl. Phys. **38**(2), 202 (2005)
8. Tanaka, T., Kozako, M., Fuse, N., et al.: Proposal of a multi-core model for polymer nanocomposite dielectrics. IEEE Trans. Dielectr. Electr. Insul. **12**(4), 669–681 (2005)

9. Heid, T., Fréchette, M., David, E.: Enhanced electrical and thermal performances of nanostructured epoxy/POSS composites. IEEE Trans. Dielectr. Electr. Insul. **23**(3), 1732–1742 (2016)
10. Valentini, L., Puglia, D., Carniato, F., et al.: Use of plasma fluorinated single-walled carbon nanotubes for the preparation of nanocomposites with epoxy matrix. Compos. Sci. Technol. **68**(3–4), 1008–1014 (2008)
11. Yin, Z., Sun, P., Sima, W., et al.: Synergistic enhancement of arc ablation resistance and mechanical properties of epoxy resin insulation. IEEE Trans. Dielectr. Electr. Insul. **27**(3), 748–756 (2020)
12. Jiyuan, Y.A.N., Liang, G., Hongliang, L., et al.: Effect of plasma step gradient modification on surface electrical properties of epoxy resin. Plasma Sci. Technol **23**(6), 064012 (2021)
13. Lei, W., Mochalin, V., Liu, D., et al.: Boron nitride colloidal solutions, ultralight aerogels and freestanding membranes through one-step exfoliation and functionalization. Nat. Commun. **6**, 8849 (2015)
14. Simmons, J., Tam, M.: Theory of isothermal currents and the direct determination of trap parameters in semiconductors and insulators containing arbitrary trap distributions. Phys. Rev. B **7**(8), 3706–3713 (1973)
15. Lv, F.C., Yin, K., Fu, K.X., et al.: Effect of fluorination and exfoliation filler on the surface flashover voltage of boron nitride/epoxy resin composites. High Volt. Eng. **43**(9), 8 (2017)
16. Xie, Q., Zhang, Y.J., Duan, Q.J., et al.: Effect of fluorinated modified graphene nanoplatelets on surface voltage resistance properties of epoxy resin composites. Proc. CSEE
17. Wang, Y.N., Lu, X., Yan, L.D., et al.: Effect of amino modified boron nitride nanosheets on surface insulation properties of epoxy resin. Insul. Mater. **54**(09), 48–54 (2021)
18. Zhang, S., Chen, W., Zhao, Y., et al.: Surface NH_2-functionalized by C doping of boron nitride nanotube to improve the thermal conductivity of epoxy composites. Compos. B Eng. **223**, 109106 (2021)
19. Li, J., Liang, H., Xiao, M., et al.: Mechanism of deep trap sites in epoxy/graphene nanocomposite using quantum chemical calculation. IEEE Trans. Dielectr. Electr. Insul. **26**(5), 1577–1580 (2019)

Research on the Influence of Nanoparticles and Surface Microstructure on the Hydrophobic and Electrical Properties of Silicone Rubber Materials

Peng Wang, Qizhi Chen, Jiaxuan Zhang, and Zinan Wang

1 Introduction

The concept of “fluorination pretreatment, nanoparticles, polyamide mesh micron-scale structure, and insulating substrate” is proposed in the design. The fluorinated nano-alumina/PA/SR composite material’s surface was formed by connecting the fluorinated low surface energy nano-alumina to the surface of the polyamide mesh (PA) and fixing it to the surface of the silicone rubber material (SR). This paper tested and analyzed the surface properties of composite materials. A preparation method of superhydrophobic material with high flashover performance was determined by analyzing the properties of the samples before and after treatment from the aspects of monitoring the changes of functional groups by analyzing the chemical elements of the surface structure using surface morphology tests, x-photoelectron spectroscopy analysis, FTIR infrared spectroscopy analysis, and other means.

The influence of binary nano-structures on the surface characteristics of fluorinated nano-alumina/PA/SR composite materials is investigated in this work. Controlling the number of PA net regulations of the composite material surface micron structure, analyzing the different the composite material surface microstructure, surface roughness, hydrophobic properties, the change of the flash data characteristics, and further attempting to construct the surface flash model mechanism interpretation through surface potential attenuation and trap distribution.

The influence of nano-structure on the surface of fluorinated nano-alumina/PA/SR composites at the micron scale was investigated further. The nano-particle blending experiment was carried out by dissolving and resolidifying nano-fluoride Al_2O_3/

P. Wang (✉) · Q. Chen · J. Zhang · Z. Wang
School of Energy, Power and Mechanical Engineering, North China Electric Power University, Baoding 071000, China
e-mail: wang.peng.ncepu@foxmail.com

Q. Xie (ed.), *Electrical Materials*, Engineering Materials,
https://doi.org/10.1007/978-981-99-9050-4_5

MWCNT in the PA network structure. The effects of various mass fractions of nano-fluorinated Al_2O_3 and MWCNT on the hydrophobic characteristics of the composite surface were investigated, and a physical model was developed to attempt to explain the mechanism.

2 Preparation and Performance Characterization of Nano-alumina, Polyamide Mesh, Silicone Rubber Composites

This work attempted to build a macroscopic-micro dual-scale surface structure to achieve a composite material with both superhydrophobic and high flashover capabilities. According to research, the material surface morphology and composition have a significant impact on the flashover and hydrophobic properties of the material surface. As a result, this section was built by dissolving and resolidifying nano-alumina particles as filler and polyamide mesh as the skeleton of binary micro-nanostructures for composite surfaces. Based on this preparatory plan, this chapter will build on the discussion. Meanwhile, the surface characteristics of the composite were characterized using a scanning electron microscope surface morphology test, an X-ray photoelectron spectroscopy test, an FTIR Fourier infrared spectroscopy test, and the hydrophobic properties of the flashover properties, as well as the effect of modified nanoparticles on the surface physical and chemical properties of polyamide mesh/silicone rubber composite.

2.1 Preparation of Modified Nano-alumina, Polyamide Mesh, Silicone Rubber Composites

(1) Preparation of the experimental materials

The materials prepared for the experiment included: polyamide mesh (40 mesh, 100 mesh, 160 mesh, 300 mesh, 400 mesh, 400 mesh, 500 mesh, and 600 mesh, purchased from Jiangsu Honghao Silk Grid Co., Ltd.); silicone rubber (adhesive with back) purchased from Shanghai Taozhe Products Co., Ltd.; 1H, 1H, 2H, 2H-perfluorinatedtriethoxlosilane (C8F13H4Si(OCH2CH3)3, FAS) were purchased from Aladin reagent (Shanghai) Co., Ltd.; formic acid (85%), ethanol (99%), and acetone (99%) were purchased from Tianjin Comio Chemical Reagent Co., Ltd.; Al_2O_3 nanoparticles (about 30 nm in diameter, China Research Institute of Metal Metallurgy) and carbon nanotubes (TNM 7, Chengdu Organic Chemistry Co., LTD.) as nanofillers. All chemicals were analytical-grade reagents.

(2) Fluorination of the nanoparticles

Firstly, acetone and FAS mixed solutions (25 (wt)% FAS and 1 (wt)% Al_2O_3) were produced. The nano-alumina particles were added to the mixing solution and well stirred to ensure homogeneity. The modified superhydrophobic powder suspension was achieved after 16 h of 50 °C reaction. The upper solvent was removed after the suspension had been allowed to layer up and down. To obtain the superhydrophobic powder, the fluid was dried in an 80 °C drying oven for 24 h.

(3) Experimental preparation

A mixture of 20 g of formic acid and ethanol was prepared with a mass ratio of 3.5:6.5. After stirring for 10 min until uniform, modified nano-alumina powder and carbon nanotubes were added to the mixed solution. The mass percentage of the modified nano-alumina, carbon nanotube mass, and the mixed solution of formic acid and ethanol were defined as, respectively, γAl_2O_3 and γCNT. Before use, the suspension is stirred further for 60 min to uniformity.

Place the polyamide mesh in a sealed container with the suspension to ensure that it is completely immersed in the suspension. After sealing the container, set it in a drying oven at 60 °C for 1 h. Finally, the polyamide mesh was removed and allowed to air-dried. The air-dried polyamide mesh is directly adhered to the surface using the silicone rubber product's own glue (Fig. 1).

In the experiment, 40, 100, 160, 300, 400, 500, and 600 mesh and $\gamma Al_2O_3 = 5\%$ were prepared, and various preparation degrees were prepared in the experimental procedure for further micron-level experimental examination. The surface of

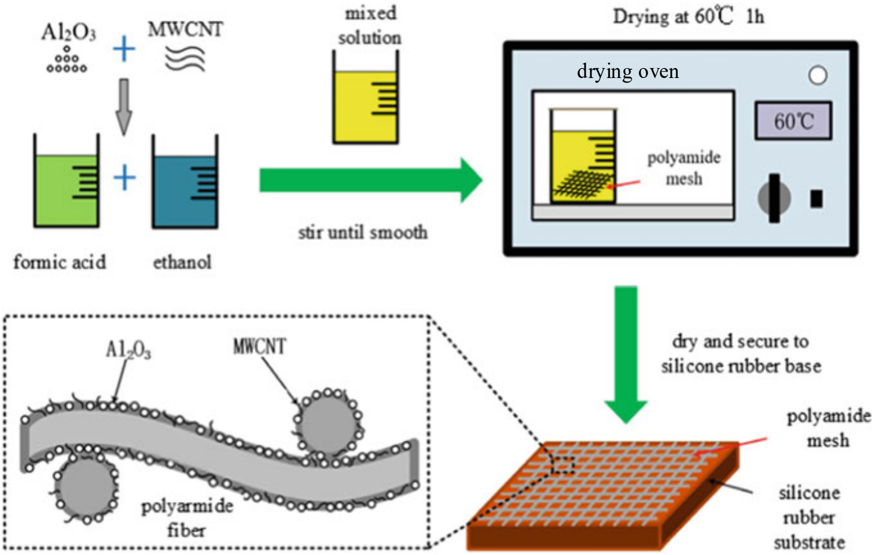

Fig. 1 Schematic diagram of the experimental sample preparation process

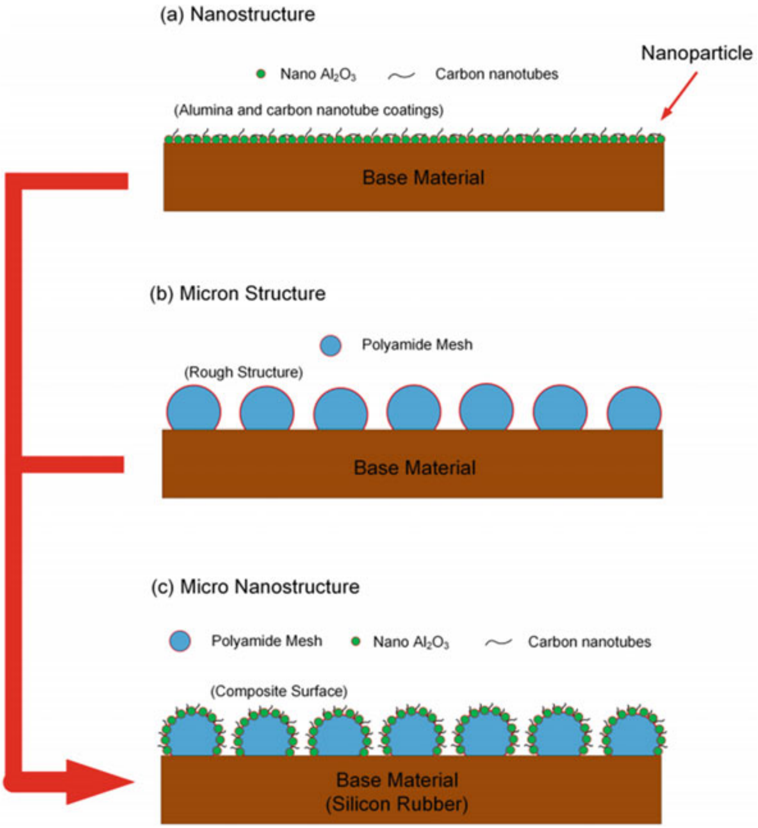

Fig. 2 Dual micro-nanostructures

the composite material under varying mass fraction nanoparticles was created for the future nanoscale structure studies by manipulating the γAl_2O_3 and γCNT. The schematic diagram of the dual micro-nano structure is shown in Fig. 2.

2.2 Surface Properties of Modified Nano-alumina/Polyamide Mesh/Silicone Rubber Composites

In this section, 300 mesh polyamide mesh composite surfaces are used as an example for experimental material fabrication and testing for key physicochemical properties [1]. The nanoparticles used in the experiment were a 5% mass fraction of nano-alumina, with silicone rubber serving as the insulating substrate. The composite

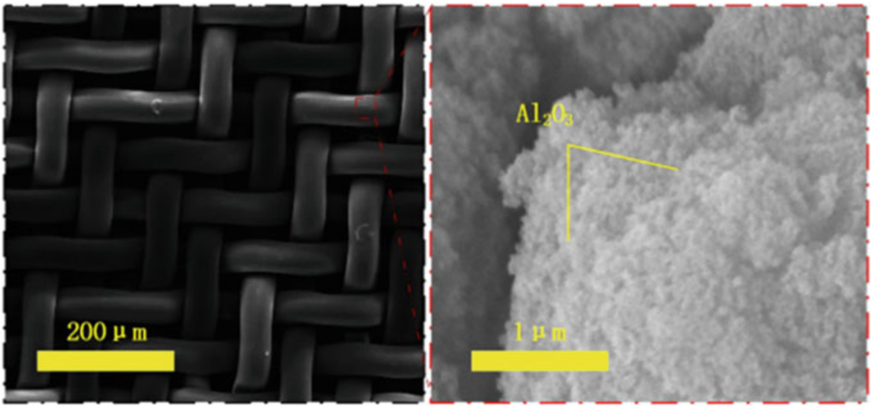

Fig. 3 Surface structure of 300 mesh polyamide mesh composite

surface's surface morphology, X-ray photoelectron, FTIR Fourier infrared spectroscopy, hydrophobic characteristics, and surface flashover qualities were also investigated.

(1) Surface morphology test

Figure 3 depicts the surface morphology of the polyamide mesh/silicone rubber composite surface. It depicts the electron microstructure of a sample of 300-mesh polyamide mesh composite. Low-power electron microscopy can reveal the interwoven structure of the polyamide mesh wire. Surface-attached aggregate nano-alumina particles can be seen using high-power electron microscopy.

(2) X-ray optoelectronic test

As shown in Fig. 4, the surface of the composite material was examined for chemical components, and the treated samples were evaluated using the XPS equipment. When dissolved and resolidified, a prominent peak develops at the binding energy 74.49 eV, which corresponds to the distinctive peak of Al 2p, which originates from the nano-alumina particles on the surface of the composite material, as shown in Fig. 4a. We achieve the outcomes depicted in Fig. 4b. The C1s on the sample surface became multimodal after surface fluorination, revealing four peaks at 284.50, 285.49, 286.94, and 291.32 eV, corresponding to the typical peaks of –CH, C–O, C–CF, and –CFx, respectively. This indicates that after FAS fluoridation, element F is successfully grafted on the surface of nanoparticles on the surface of composite materials. It is worth noting that C–CF and –CFx are crucial for providing low surface energy.

(3) The FTIR infrared spectroscopy test

The Fourier spectra of the several experimental control groups are shown in Fig. 5. We attempt to investigate the changes and effects of the composite surface during the experimental treatment by comparing the Fourier spectra of the composite surface in different experimental treatment phases. The three curves are the composite surface of

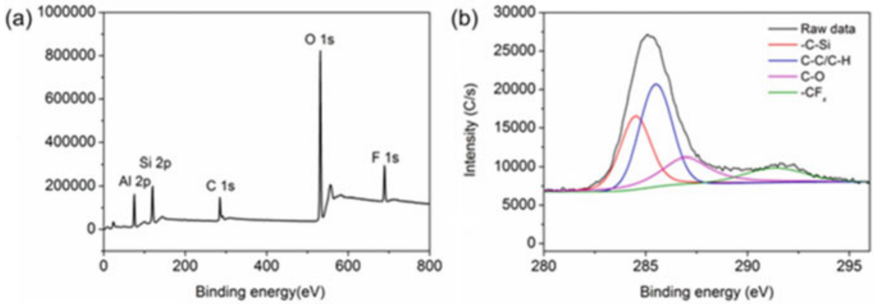

Fig. 4 An X-ray photoelectron test map of the experimental samples

untreated polyamide mesh and silicone rubber, the composite surface of polyamide mesh formed with silicone rubber that has been soaked in formic acid, and the composite surface of polyamide mesh and silicone rubber that has been dissolved and solidified after being soaked in formic acid. Experimental different samples prepared in the process of processing Fourier spectrum approximate, namely formic acid etching polyamide mesh and nano-alumina by dissolving solidification technology attached in the process of polyamide mesh, functional group basic no change, the two processes are given priority with physical change.

Fig. 5 The X-ray photoelectron test map of the experimental samples

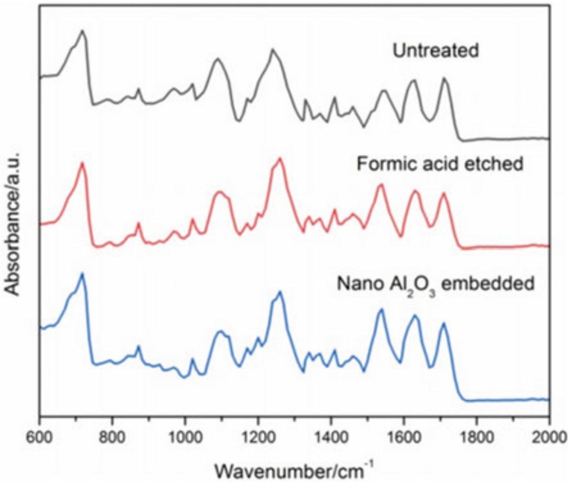

2.3 Electrical Characteristics of Modified Nano-alumina/ Polyamide Mesh/Silicone Rubber Composites

Figure 6 depicts the surface hydrophobicity test results. The hydrophobic Angle of the composite surface increased from 105 to 152 after the experiment treatment, indicating that the superhydrophobic function of the composite surface can be effectively realized by constructing the micro-nano dual-scale surface topography and reducing the surface energy of the composite surface with fluorinated fillers.

The test results of flashover characteristics along the surface of silicone rubber material before and after treatment are given in Fig. 6. The flashover voltage along the surface of the composite material was increased by about 20% after the experimental treatment, demonstrating that the flashover performance could be improved to some extent by modifying the surface topography of the composite material and doping nanoparticles.

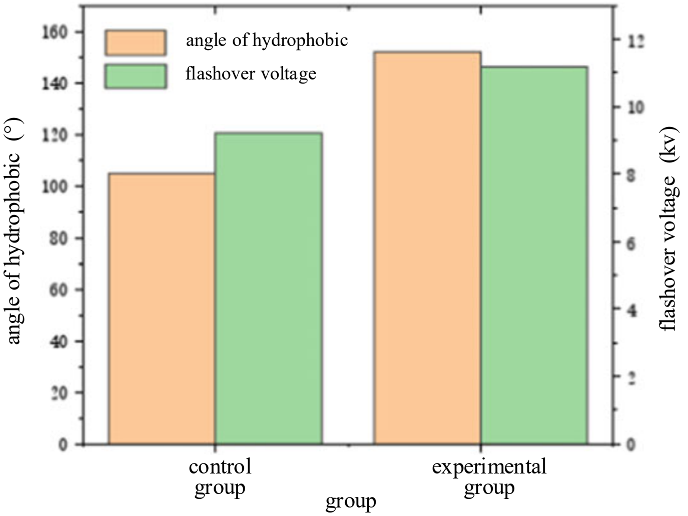

Fig. 6 The changes of hydrophobic characteristics and flashover characteristics before and after treatment of composite samples

3 Study on the Influence of the Micrometer-Scale Structure of the Polyamide Mesh on the Hydrophobic and Electrical Properties of the Composites

The experimental preparation idea of "small molecule nanostructure (nano-Al_2O_3 particles) + micron structure of polyamide mesh (300-mesh polyamide mesh) + insulating substrate (silicone rubber)" was preliminarily constructed in previous experimental studies, and the realization of the superhydrophobic properties of the composite surface and the improvement of the flashover properties along the surface were preliminarily proven. The surface characteristics of composite materials are explored using polyamide mesh of various mesh numbers based on the experimental investigation in the preceding chapter. The optical microscope observation test, water contact Angle test, and flashover performance test were performed on polyamide mesh/silicone rubber composite surfaces of 40 mesh, 100 mesh, 160 mesh, 300 mesh, 400 mesh, 500 mesh, and 600 mesh. Surface profile test, roughness test, surface potential attenuation test, and surface trap distribution calculation were used to analyze the physical and chemical properties of the composite surface, and the process of the composite surface was explained. The mass fraction of nano-alumina remains at 5% in this chapter.

3.1 Physicochemical Characteristics of the Composite Surface Under the Influence of the Micron-Scale Structure of Polyamide Mesh

3.1.1 Optical Microscopic Characteristics of the Composite Materials Under the Influence of the Micrometer-Scale Structure of the Polyamide Mesh

The optical microscopic observation findings of the surface of polyamide mesh composites with 40 mesh, 100 mesh, 160 mesh, 200 mesh, 300 mesh, 400 mesh, 500 mesh, and 600 mesh are presented in Fig. 7a–g, respectively. The diameter and spacing of 40 mesh polyamide mesh are the greatest among them. The mesh diameter and mesh spacing of the polyamide mesh reduced continually during the process from 40 to 600 mesh. Further measurement and analysis can yield the changing table of mesh diameter and mesh spacing of polyamide mesh with the number of mesh sizes displayed in Table 1.

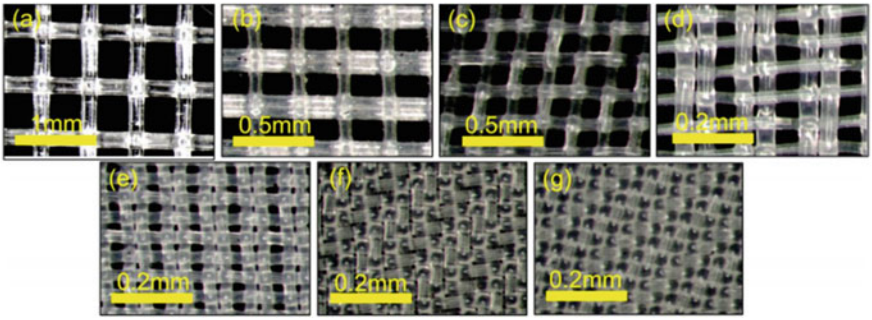

Fig. 7 40–600 polyamide mesh/silicone rubber composite test samples

Table 1 Table of diameter/spacing variation of 40–600 mesh polyamide mesh wire

Serial number	Number of grids	Average mesh diameter (μm)	Average wire spacing (μm)	Area fraction
1	40	195	410	0.566
2	100	88	171	0.654
3	160	70	113	0.679
4	300	48	52	0.815
5	400	35	30	0.890
6	500	–	–	–
7	600	–	–	–

3.1.2 Surface Profile Characteristics of the Composite Materials Under the Influence of the Micron-Scale Structure of the Polyamide Mesh

The surface profile of a 40–600 mesh polyamide mesh composite surface is evaluated to examine the surface morphology of composites qualitatively and quantitatively, and the two-dimensional and three-dimensional test results are presented in Figs. 8 and 9, respectively.

The surface roughness of the material surface is frequently expressed in experimental study by Sa (arithmetic mean height), and the basic calculation formula is stated in Eq. (1). Where A represents the computed surface roughness area, Z indicates the material's surface height, and x and y represent the material's position in the horizontal direction, respectively.

$$Sa = \frac{1}{A}\iint_A |Z(x, y)|dxdy \tag{1}$$

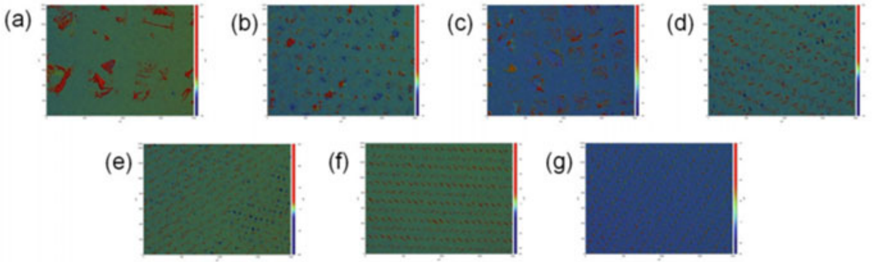

Fig. 8 40–600 2D surface profile of a mesh polyamide mesh/silicone rubber composite sample

The surface profiler can present the surface structure of polyamide mesh composite, as illustrated in Figs. 8 and 9, and the specific value of surface roughness of polyamide mesh composite is shown in Fig. 9h. The composite surface of 40-mesh polyamide mesh has the coarsest filament diameter and the greatest filament distance, while the material surface has the roughest and highest roughness of 9.8 μm. Simultaneously, as the number of polyamide meshes increases, the diameter of the mesh lowers, the distance of the mesh decreases, and the surface of the composite gradually smooths. The surface roughness of the composite is reduced to 6.8 μm when the number of polyamide meshes reaches 600. The results of the composite surface surface profile reveal that managing the composite surface morphology quantitatively may make the number of the composite surface simple and effective.

3.1.3 Water Contact Angle Characteristics of Composites Under the Influence of Micrometer Structure of Polyamide Mesh

Multiple linkages are used in the experiment to prepare the composite surface. In this paper, the contact angle of the polyamide mesh composite surface was measured for each production stage to clearly and quantitatively analyze the influence of the composite material's surface hydrophobicity [2]. "B-SR" is the blank silicone rubber test group; "B-PA" is the composite surface of the untreated polyamide mesh and silicone rubber substrate; "B-Al_2O_3" is the composite surface of the polyamide mesh and re-solidified; and "F-Al_2O_3" is the composite surface of fluorinated graft before "B-Al_2O_3" is dissolved and solidified. The following figure depicts the test results.

Among them, "hydrophobic crucial" is a 90° contact angle, a contact angle less than 90° is called hydrophilic material, a contact angle greater than 90° is called hydrophobic material, and a contact angle greater than 150° is called superhydrophobic material.

The silicone rubber substance itself has a strong hydrophobicity, according to the test, and its hydrophobic angle has been regularly recorded around 105° (Fig. 10). Although the polyamide mesh/silicone rubber composite material has a complex rough structure, the improvement in hydrophobic performance due to the better hydrophobic silicone rubber material is not visible. The polyamide mesh/silicone

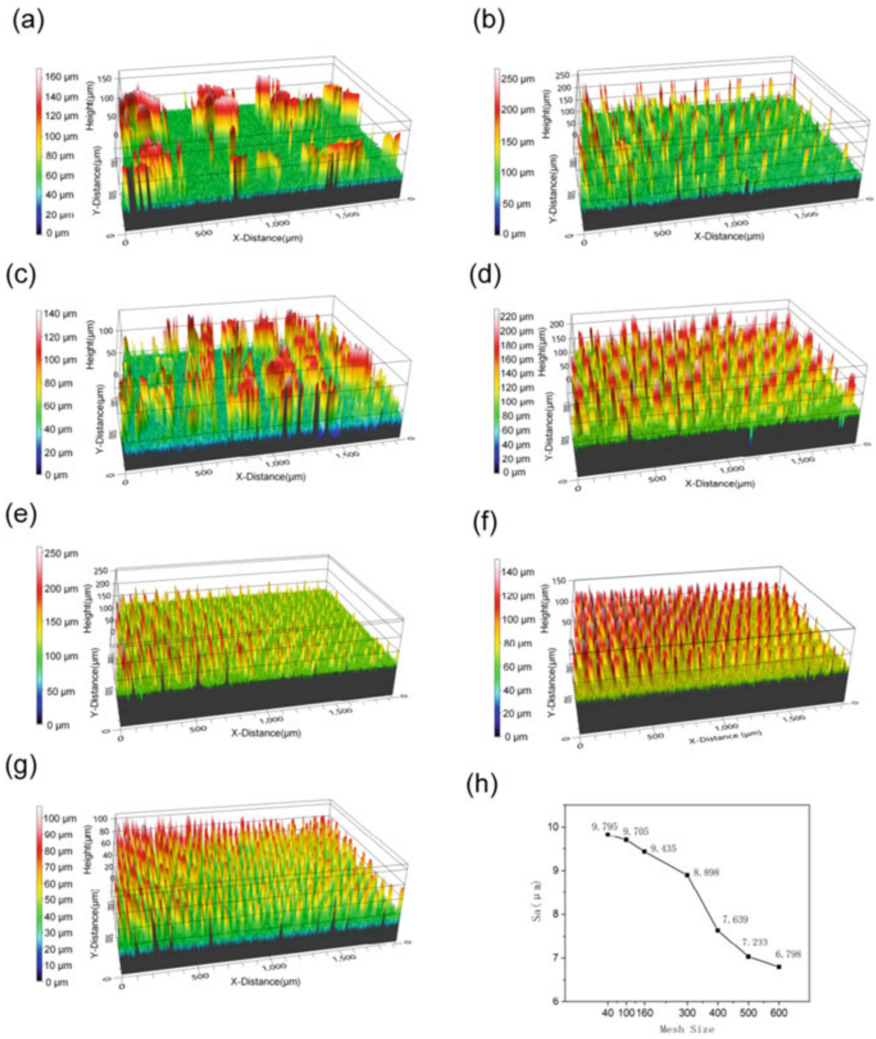

Fig. 9 **a**–**g** 40–600 mesh polyamide mesh/silicone rubber composite **h** surface roughness of 40–600 mesh polyamide/silicone rubber composite

rubber composite offers the best hydrophobic characteristics at 300 mesh. The hydrophobic performance of the 40 mesh polyamide mesh/silicone rubber composite is slightly worse, which is due to the rough texture of the composite material's surface. Because the 40-mesh polyamide mesh spacing is too widely apart and the mesh diameter is too high, the surface roughness of the composite material is the greatest at this time. At 400 mesh, the hydrophobic properties of the polyamide mesh composite material decrease sharply, and the hydrophobicity is lower than that of ordinary silicone rubber material; at 500 mesh, the composite material surface loses

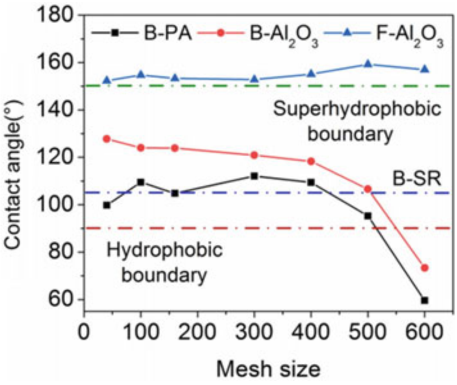

Fig. 10 40–600 water contact angle of mesh polyamide mesh/silicone rubber composite samples

the hydrophobic characteristics; and at 600 mesh, the hydrophobic characteristics on the surface of the polyamide mesh composite material are the lowest, and the contact Angle is as low as 60°. This is due to the fact that when the order number of polyamide mesh increases, the polyamide mesh filament distance decreases, the polyamide mesh dominates the surface of the composite material, and the polyamide mesh is overall relatively smooth. This experiment examined the surface hydrophobic properties of the polyamide mesh/silicone rubber composite to determine the effect of the micron-scale structure on the hydrophobic properties of the composite surface, which was not affected by the higher hydrophobic properties of the silicone rubber material itself.

Furthermore, the nano-alumina particles were connected to the polyamide mesh by using the recoagulation technique on the polyamide mesh/silicone rubber composite surface [3]. The experimental group with the addition of nano-alumina particles had a trend of decreasing contact angle with increasing polyamide mesh number, and the total contact angle was similar to the polyamide mesh/silicone rubber composite. However, the nanostructure of the nanoparticles improves the hydrophobic properties of the composite surface, resulting in an increasing contact angle of the composite surface following the introduction of the nanoparticles, and this promotion is more visible when the number of polyamide mesh is lower. The contact angle of the 40-mesh composite surface is the greatest at this point, reaching about 130°. However, at 400–600 mesh, the hydrophobic characteristics of the composite material will still fall dramatically. The contact angle of the composite surface remains at 106° for 500 mesh; at 600 mesh, the contact angle of the composite surface lowers to 70°. In this experiment, the binary micro-nanostructures significantly improved the hydrophobic characteristics of the composite surface, demonstrating that the binary micro-nanostructures can improve the hydrophobic characteristics of the composite and that the regulation can be adjusted by changing the number of polyamide mesh.

The surface of superhydrophobic materials should be further prepared, according to the experimental concept. The qualitative shift of the composite from hydrophobic to superhydrophobic is obtained by grafting the nano alumina particles and lowering the surface energy of the composite. The nanoparticles were fluorinated in this work using nano alumina particles/polyamide mesh/silicone rubber composites. The findings of the experimental tests demonstrate that the nanoparticles in the fluorinated composite have outstanding superhydrophobic characteristics. As shown in Fig. 10, after fluoride of nanoparticles, the number of polyamide mesh in 40–600 attained superhydrophobic function and displayed a shifting pattern with increasing polyamide mesh number and composite material surface contact angle. The contact Angle of the 40-mesh composite surface is the lowest, but still more than 150°, reaching 152°. The hydrophobic Angle of the 500–600 mesh composite surface is reaching 156°. The mesh spacing and mesh diameter become smaller as the number of polyamide meshes increases, giving the high-order polyamide mesh a higher specific surface area and more opportunities for fluorinated nanoparticles to adhere. The addition of more low surface energy nanoparticles improves the composite's hydrophobic characteristics [4, 5]. Based on the previous chapter's experimental concept of "small molecule nanostructure (nano-Al_2O_3 particles) + polyamide mesh micron structure (300 mesh polyamide mesh) + insulating substrate (silicone rubber)," the influence of binary micro-nanostructure composed of fluorine nanoparticles on the hydrophobic characteristics of the composite surface was investigated in this experiment.

3.2 Electrical Characteristics of the Composite Surface Under the Influence of the Micron-Scale Structure of Polyamide Mesh

3.2.1 Flashover Properties of Composites Under the Influence of Micrometer Structure of Polyamide Mesh

In this section, several techniques are involved in the surface preparation of polyamide mesh composites. The flashover characteristics of different sets of control groups were evaluated to conduct out analysis in order to dynamically monitor the influence of each process on the flashover characteristics of composite materials. "B-SR" was the untreated polyamide mesh and silicone rubber substrate composite surface; "B-PA" was the blank silicone rubber test group. After dissolving and resolidification of untreated nano-alumina, "B-Al_2O_3" is the composite surface of polyamide network and silicone rubber substrate; "F-Al_2O_3" was fluorinated grafted, and then B-Al_2O_3 was dissolved and coagulated on the composite surface of nano-alumina particles. The outcomes are as follows (Fig. 11).

The "B-SR" was the first to be tested in the experiment. The average flashover voltage after ten flashover tests was 9.2 kV. The flashover voltage on the surface of the "B-PA" polyamide mesh/silicone rubber composite is somewhat greater than that of the blank silicone rubber, fluctuating at around 9.5 kV. The flashover voltage increased with the number of polyamide mesh, slightly increasing and then gradually reducing, with the flashover voltage of 300 mesh polyamide mesh composite surface being the highest, reaching 9.8 kV.

Fig. 11 Flashover properties of the 40–600 mesh polyamide mesh/silicone rubber composite samples

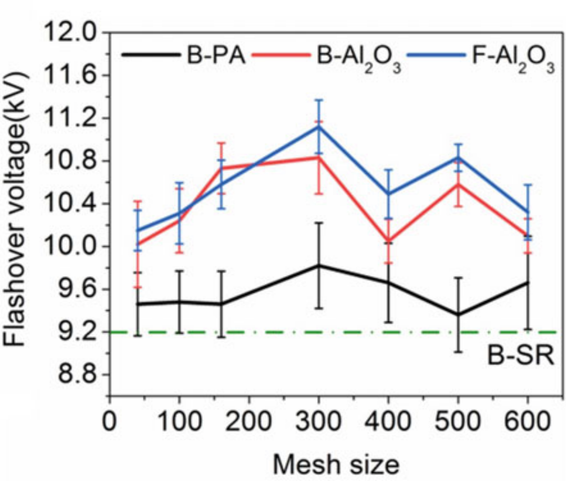

Non-conductive nanoparticles are commonly employed as fillers to increase the flashover voltage [6]. As a result, the surface flashover voltage of the composite material is dissolved and swiftly and dramatically raised after solidification during the composite material's surface treatment. The surface flashover voltage of the material corresponding to each mesh exceeded 10 kV in the test, the flashover voltage of the 300 mesh polyamide mesh remained the highest, reaching nearly 11 kV, and the flashover characteristic increased by more than 20% when compared to the untreated silicone rubber material. The overall variation pattern of the "B-Al_2O_3" experimental group's flashover voltage was comparable to that of the "B-PA," which displayed a shifting tendency of rising initially and then lowering. Simultaneously, the flashover voltage of different-order composite material surfaces changes more dramatically, which may be related to the alumina material's dissolution and resolidification efficiency and the change in discharge distance along the surface caused by the material's surface roughness.

Following fluorination of the composite material, the flashover voltage on the composite surface is increased once more. The overall flashover property of the test material continued to change with the number of polyamide mesh, first rising and then falling, but the increase in flashover voltage in the low-number test group was not obvious, whereas the increase in flashover voltage in the high-number polyamide mesh test group was more obvious. The flashover voltage of the composite surface of the 40 mesh polyamide mesh was 10.2 kV, whereas the mesh 300 experimental group's flashover value was 11.2 kV. This could be related to the fluoridation-induced trap modification and the improved attachment efficiency of nanoparticles by high order number polyamide mesh.

3.2.2 Surface Potential Attenuation Characteristics of the Composites Under the Influence of the Micrometer-Scale Structure of the Polyamide Mesh

This research continues to investigate the surface charge decay properties of the composite material before and after nanoparticle incubation using the surface charge decay test platform, which corresponds to the order polyamide mesh. “B-100,” “B-300,” and “B-600” correspond to the experimental groups of 100 mesh polyamide mesh, 300 mesh polyamide mesh, and 600 mesh polyamide mesh, respectively; “F-100,” “F-300,” and “F-600” correspond to the fluorinated group of nano-alumina particles of 100 mesh polyamide mesh, 300 mesh polyamide mesh, and 600 mesh polyamide mesh, respectively.

The charge dissipation rate in this study is defined as the ratio of the potential difference between the beginning and end, and the potential after the withdrawal (formula 2 and 3).

$$V = \frac{U_{(\mathrm{o})} - U_{(t)}}{U_{(\mathrm{o})}} \times 100\% \tag{2}$$

$$L = \frac{U_{(t\mathrm{o})}}{U_{(\mathrm{o})}} \tag{3}$$

In formula (2), V represents the surface charge dissipation rate, $U_{(0)}$ represents the test zero surface charge, and $U_{(t)}$ represents the material’s surface charge at the end of the test. The surface charge normalization results are examined here to emphasize the dissipation rate of the surface charges. At each time, the normalization is the ratio of the surface potential to the initial potential (such as formula 3).

When illustrated in Fig. 12, the surface charge decay of the nonfluorinated group (“B-100,” “B-300,” and “B-600”) and the fluorinated group (“F-100,” “F-300,” “F-600”) accelerates as the polyamide mesh number increases. When the surface charge stabilizes, the amount of residual charge decreases. However, the proportion of surface charge decreasing at the same moment is growing. At the same time, the surface potential decay of the fluorinated composite is faster than the surface potential decay of the nonfluorinated composite (e.g., “B-100” is faster compared to “F-100”). This could be due to the trapping effects of fluoride of nanoparticles on the composite surface.

3.3 Mechanism Analysis of Composite Surface Affected by the Micron Structure of Polyamide Mesh

This work primarily employs two ways of creating binary micro-nano surface structure and dissolving and resolidification of nanoparticles for the surface preparation of polyamide mesh composite. The surface structure of composite materials with binary

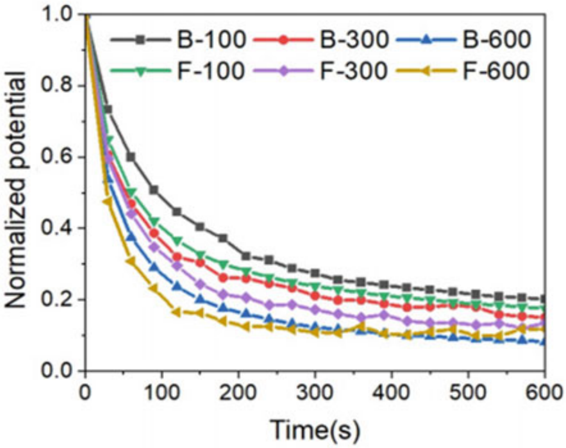

Fig. 12 Surface charge dissipation curve of 100–600 mesh polyamide mesh/silicone rubber composite samples

micro-nano structure has been tested in this paper. On the one hand, the optical fiber structure was used to measure the wire diameter and wire distance of polyamide mesh with varied mesh numbers. The results reveal that a lower polyamide mesh has a greater wire diameter and a longer wire distance. The surface profile test, on the other hand, assessed the surface roughness of the composite surface as it varied with the mesh number of polyamide mesh. The results reveal that a polyamide mesh with a low mesh number has a higher roughness, which corresponds to the optical microscopic observations. On the one hand, the length of the discharge channel along the composite surface flashover is lengthened. On the other hand, significant electric field distortion occurs. The surface trap calculation approach is utilized in this section to examine the effect of nanoparticle introduction on the surface of composite materials throughout the experimental preparation phase. In addition, try to develop a model to describe the mechanism of synergy.

3.3.1 Polyamide Mesh Structure's Influence on Surface Trap Distribution in Composites

The distribution of trap energy levels is determined using Eqs. (4) and (5) based on the surface potential decay curve and the isothermal surface potential decay theory (Isothermal Surface Potential Decay, ISPD) (5).

$$E_{\mathrm{t}} = k_B T \ln(V_{ATE} t) \tag{4}$$

$$Q_{\mathrm{s}}(t) = t \frac{\varepsilon_0 \varepsilon_t}{q_e L} \frac{d\varphi_s(t)}{dt} \tag{5}$$

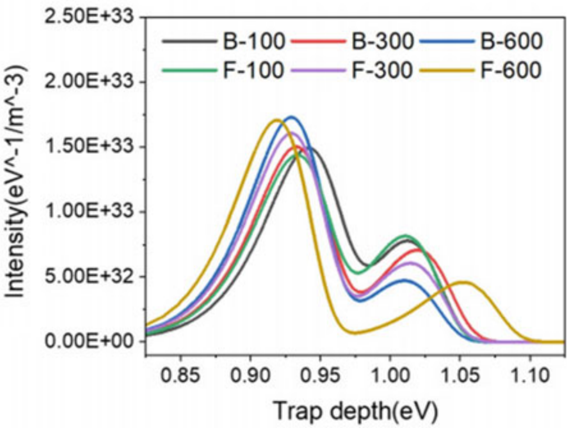

Fig. 13 Surface trap distribution curve of 100–600 mesh polyamide mesh/silicone rubber composite samples

Et is the trap energy level; Qs is the trap charge density; k_B is the Boltzmann constant; T is the temperature of the sample; νATE is the escape frequency of the trapped charge (taking 4.17 × 1013 s^{-1}); L is the thickness of the sample; $\varphi_s(t)$ is the surface potential.

Figure 13 depicts the composite surface's trap level study results. The deep trap energy levels and shallow trap energy levels on the surface of 100 mesh, 300 mesh, and 600 mesh polyamide mesh composites did not change appreciably in the non-fluorinated group. Deep trap energy levels are all about 1.02 eV; shallow trap energy levels decreased from 0.942 eV for 100 mesh to 0.928 eV for 600 mesh. The trap level of the surface of the polyamide mesh composite in different orders changed dramatically in the fluoride experiment group. The deep trap level of the polyamide mesh composite increases dramatically after fluoride, from 1.01 eV for 100 mesh to 1.053 eV for 600 mesh; the shallow trap level decreases marginally, from 0.934 eV for 100 mesh to 0.918 eV for 600 mesh.

It has been proposed that the change in trap depth on the composite surface is connected to the chemical bonding on the surface. The FTIR test in the material preparation process shows that there is no obvious peak change in the Fourier spectra in the process of soaking in formic acid mixed solution and in the process of dissolving and resolidification of nano-alumina particles, so physical changes are primarily used in these two processing processes. As a result, even if the number of polyamide meshes changes, the change in specific surface area caused by thinning the polyamide mesh and shorter wire distances only influences the dissolution efficiency of the polydactyl mesh and the efficiency of attaching the nano-alumina particles. It will not alter the surface chemical bond of the composite material. This results in a negligible change in trap depth on the composite surface.

On the one hand, the fluorinated group had a higher deep trap depth and a lower shallow trap density. On the other hand, there is a decrease in deep trap density as well as an increase in shallow trap density. The previous X-ray photoelectron spectroscopy test (Fig. 3) effectively confirmed fluorinated group grafting and nanoparticle introduction on the polyamide mesh skeleton. Meanwhile, past research indicates that the composite surface fluoride frequently expands the deep trap level on the material's surface, raising the flashover voltage. As a result, the fluorine-containing group reduces the surface energy of the composite material and accomplishes the superhydrophobic function, which is also the fundamental reason for the material's increased deep trap energy level. At the same time, the composite material surface deep trap depth increases as the polyamide mesh number increases, implying that a greater polyamide mesh number results in a higher fluorinated nanoparticle attachment rate on the composite surface. This supports the previously stated explanation: increasing the polyamide mesh number and surface area enhances each process in the processing efficiency process. It is evident in the dissolution and resolidification of nanoparticles, and its attachment efficiency improves.

The difference in the trap surface of the composite material of the polyamide mesh was primarily reflected in the trap density in the experimental test, as illustrated in Fig. 14. "B-D" is the non-fluoridated experimental group's deep trap density; "F-D" is the fluoridated experimental group's deep trap density; "B-S" is the non-fluoridated experimental group's shallow trap density; and "F-S" is the fluoridated experimental group's shallow trap density. The deep trap density of 100, 300, and 600 mesh polyamide mesh composites decreased successively in the non-fluoridated experimental group, with values of 8.31, 6.02, and 4.54 (all units are 10^{32} eV^{-1}/m^{-3}); the shallow trap density increased successively, with values of 1.44, 1.60, and 1.71 (all units are 10^{32} eV^{-1}/m^{-3}). The deep trap density of 100, 300, and 600 mesh composite reduced gradually, with values of 7.76, 6.93, and 4.71 (all units are 10^{32} eV^{-1}/m^{-3}); the shallow trap density grew successively, with values of 1.49, 1.51, and 1.73 (all units are 10^{32} eV^{-1}/m^{-3}). The trap density of the composite surface changed significantly during the experiment due to the change in polyamide mesh number.

The shallow trap density of the composite surface grew as the number of polyamide mesh increased, but the deep trap density fell dramatically. Previous research has found that shallow traps on the surface of composite materials are more affected by surface physical imperfections, while deep traps are frequently related to chemical defects. Two major adjustments are examined in this experiment: (1) On the one hand, when the number of polyamide meshes grows, the larger specific surface area contacts the polyamide more fully during the dissolution soaking process, generating more physical defects due to the increase in the density of shallow traps; (2) There were some researches found that the interfacial layer on the surface of the composite material is more prone to form deep traps. The nanofillers are partially incorporated in the polyamide fabric in this paper using a dissolving and resolidification technique. The interfacial layer of the nanoparticle polyamide mesh is subsequently created, introducing deep traps to the composite material's surface. When the polyamide mesh number is increased, the specific surface area increases, giving the nanoparticles more possibilities to attach. As a result, there is a possible tendency toward greater deep trap density in the composite surface. However, the solution concentration and material processing time continue to limit the embedding of the nanofillers. The

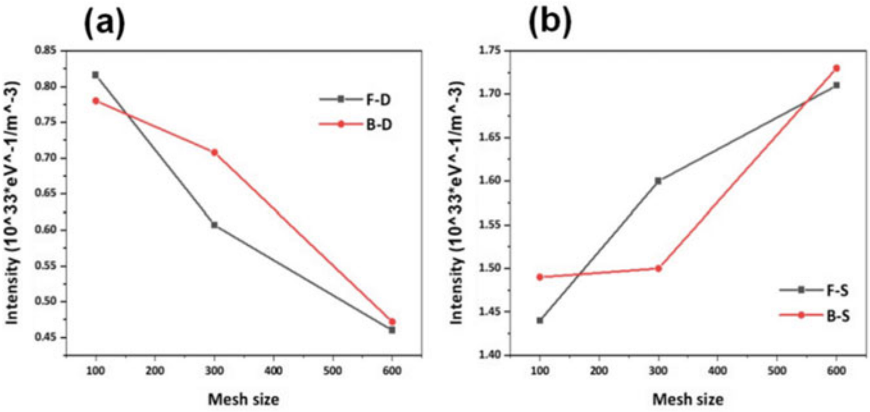

Fig. 14 Deep-depth trap density of 100–600 mesh polyamide mesh/silicone rubber composite samples

findings of the experimental tests demonstrate that the polyamide mesh is physically dissolved in the formic acid solution, and the process of generating a shallow trap takes precedence, resulting in an increase in shallow trap density and a decrease in deep trap density.

3.3.2 Flashover Model of Composite Material Under the Influence of the Micron-Scale Structure of Polyamide Mesh

To attempt to explain changes in the flashover properties of composite surfaces, a physical model is constructed (Fig. 15). The network structure of polyacrylamide is important at the macroscopic level. According to the roughness statistics (Fig. 15), decreasing the grid size causes an increase in roughness. The effect of roughness on material flashover is separated into two categories. On the one hand, high roughness causes lengthy discharge lengths along the surface, preventing the flashover from developing further and increasing the flashover voltage. Increased roughness, on the other hand, creates severe local electric field distortion, which causes a flashover along the surface and reduces the flashover voltage on the composite surface. As a result, the composite demonstrated the best surface flashover performance at the required roughness.

At the same time, the effect of nanoscale fillers (Al_2O_3 nanoparticles and carbon nanotubes) and surface modification is critical from a microscopic standpoint. Because they improve the thermal stability, mechanical characteristics, and corona resistance of composites, Al_2O_3 nanoparticles are frequently used in industrial applications [7, 8]. Further research revealed that a large number of unpaired atoms and flaws on the surface of the nano-packing can trap carriers and limit charge transport in the nanoscale polymer. The inclusion of CNTs raises surface conductivity. A

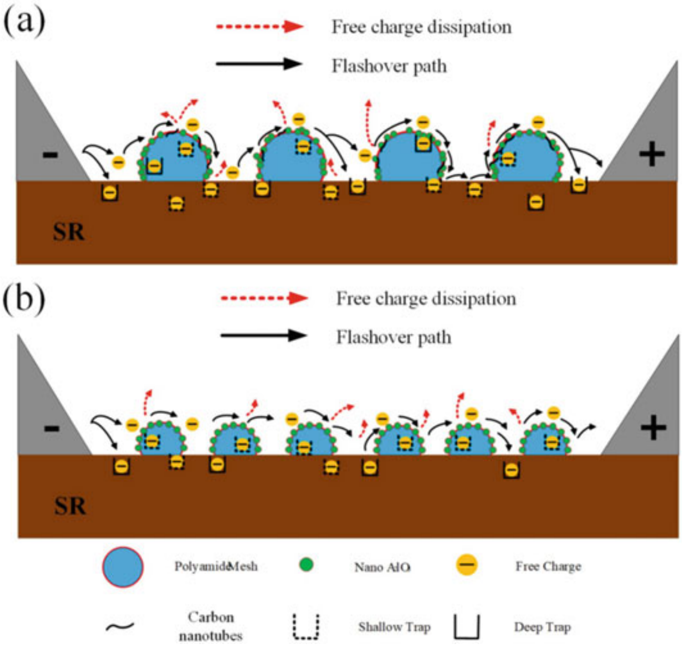

Fig. 15 Physical model of polyamide mesh/silicone rubber composites with different mesh sizes

proper increase in surface conductivity aids in the acceleration of charge dissipation, which in turn increases the flashover voltage. Previous research has demonstrated that correct fluoride adjustment can reduce surface charge accumulation and boost flashover tolerance voltage.

4 Study on the Influence of Nanostructures on the Surface Properties of Composite Materials Under the Mixed Modification of Nano Alumina and Carbon Nanotubes

Based on the preceding section of this chapter, the composite surface will be attempted to increase further electrical performance based on the ideal 300 mesh polyamide meshsilicone rubber composite surface. As a result, carbon nanotubes (CNTs) were injected as a modified filler during the dissolving and resolidification process to combine carbon nanotubes with nano-alumina particles. The water contact Angle test, flashover performance test, surface potential attenuation test, and surface trap distribution calculation of the composite surface were carried out by modifying the blending ratio of the two nano-fillers, and the method was attempted to explain.

In the experiment, 300 mesh polyamide mesh, fluorinated modified nano-alumina particles, and a silica rubber substrate were used. Nanoparticle doping studies were carried out with alumina particles of 0%, 2%, 4%, 4%, 6%, 8%, and 10% mass fraction and carbon nanotubes of 0%, 0.05%, 0.1%, 0.15%, and 0.2% mass fraction, respectively. In the experiment, 300 mesh polyamide mesh, fluorinated modified nano-alumina particles, and a silica rubber substrate were used. Nanoparticle doping studies were carried out with alumina particles of 0%, 2%, 4%, 4%, 6%, 8%, and 10% mass fraction and carbon nanotubes of 0%, 0.05%, 0.1%, 0.15%, and 0.2% mass fraction, respectively.

4.1 Effect of Nanostructures on the Hydrophobic Properties of Composite Surfaces

Figure 16 depicts the results of the hydrophobic properties test on nanoparticles. The doping of fluorinated nano alumina particles significantly affects the surface hydrophobic properties of the composite material, although the influence on the varied doping of carbon nanotubes is not obvious. The experimental group of nonfluorinated nano-alumina particles demonstrated the worst hydrophobic qualities of the composite surface, with a contact angle of roughly 120°, corresponding to the experimental group of mass fraction of each carbon nanotube. The surface hydrophobic characteristics of the composite material increased fast after the addition of partly fluorinated nano-alumina particles to the surface, surpassing 150°. When the fluorinated nano-alumina particles' mass fraction exceeds 4%, the surface of the composite material becomes stable and exhibits a superhydrophobic function.

The contact Angle of the composite material's surface varies depending on the type of nanoparticle. On the one hand, the doping amount of carbon nanotubes is thought to be modest, resulting in no substantial changes in the hydrophobic qualities

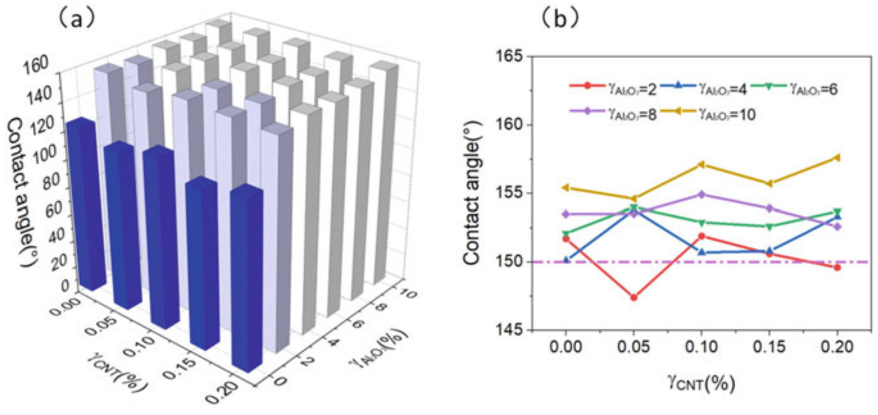

Fig. 16 Water contact angle characteristics of composite surface for nano-Al_2O_3 and MWCNT blend doping

of the material surface. Conversely, increasing the mass fraction of fluorinated nano-alumina enhances the ultimate adhesion amount of nano-alumina particles during the dissolving and resolidification process. The bigger the amount of nano alumina attachment, the lower the surface energy of the composite. As a result, for superior hydrophobic qualities, the composite surface with a greater mass fraction of fluorinated nano alumina is used, and can stably display superhydrophobic capabilities once the mass fraction exceeds 4%.

4.2 Effect of Nanostructures on the Electrical Characteristics of Composite Surfaces

4.2.1 Surface Flashover Properties of Composites Modified by Nanoparticle Blending

(1) Flashover test results of nanoparticle blend composite surface

The surface flashover test results of fluorinated nano-alumina particles on 300 mesh polyamide mesh composite surface and carbon nanotubes are illustrated in Fig. 17. The overall flashover property of the composite material increased with the amount of doping of both nanoparticles, with a trend of increasing initially and then decreasing. The surface flashover properties of a composite material made with 6% nanoscale alumina particles and 0.15% carbon nanotubes were the best among them. At this point, the flashover voltage on the composite material's surface reaches 12.3kV, the flashover performance improves by 10%, and the cumulative flashover performance improves by more than 30%.

4.2.2 Surface Potential Attenuation Characteristics of Composites Under Mixed Modification of Nanoparticles

Using 6% nano-alumina and 0.15% nano-carbon nanotubes in the mixed solution, the composite surface demonstrated the best flashover performance in the blending experiment. This paper investigated the charge dissipation of the composite surface with varying mass fractions of carbon nanotubes and alumina nanoparticles at $Al_2O_3 = 6\%$ and 0.15% CNT to further understand the microscopic characteristics of the composite surface and the changing mechanism of flashover qualities. The test results are depicted in Fig. 18.

Figure 18 depicts the normalized potential dissipation test results. When γCNT was 0.15%, the charge dissipation on the surface of the composite material displayed a rapid changing trend. When γAl_2O_3 reaches 6%, charge dissipation on the surface of the composite material first slows and then accelerates as the mass fraction of carbon nanotubes increases.

Fig. 17 Flashover properties of composite materials with nano-Al_2O_3 and MWCNT

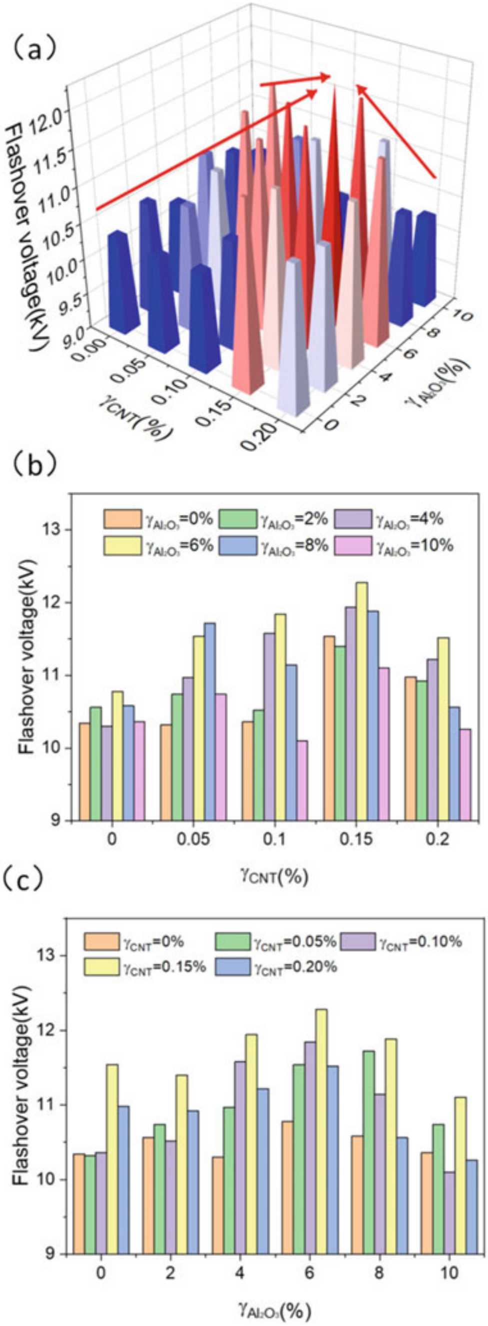

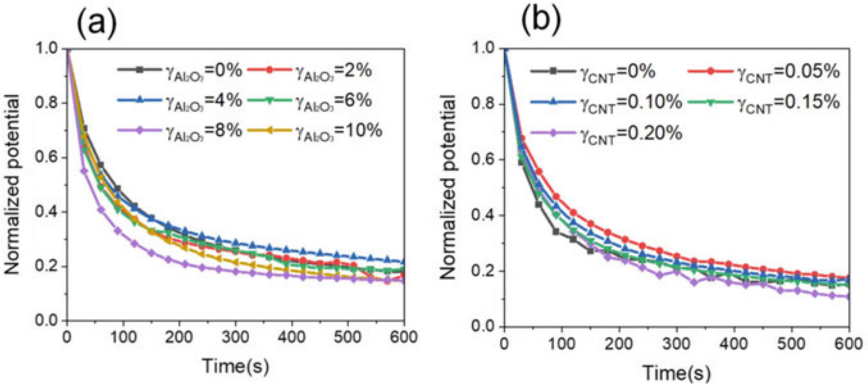

Fig. 18 Charge dissipation properties of composite materials at nano-Al_2O_3 and MWCNT blend doping

4.3 Mechanism Analysis of the Influence of Nanostructure on the Surface Characteristics of Composite Materials

4.3.1 Surface Trap Distribution of Composites Under Mixed Modification of Nanoparticles

Based on the surface potential dissipation test of the nanoparticle blend sample, the surface trap distribution is further calculated.

(1) Energy level distribution characteristics of the composite surface of alumina particles in different proportions.

The surface trap distribution of the composite material was under varied nano alumina doping mass fractions when γ CNT was 0.15% in Fig. 19a. Deep trap levels on the composite surface are centered at 1.02 eV, while shallow trap levels are concentrated around 0.93 eV. The change in nano-alumina was not significant.

Changes in the trap density of the composite surface are also obtained, as seen in Fig. 19b. It is discovered that the scenario is comparable to that which occurs when the polyamide mesh number changes. Surface trap modifications are mostly reflected in trap density when the surface of the composite is physically modified. In this experiment, when the nano-alumina mass fraction grows, the density of the deep trap increases while the density of the shallow trap drops. From $\gamma Al_2O_3 = 0\%$ to $\gamma Al_2O_3 = 4\%$, the deep trap density grew from 0.81 (10^{33} eV^{-1}/m^{-3}) to a maximum of 1.07 (10^{33} eV^{-1}/m^{-3}), whereas the shallow trap density declined from 1.48 (10^{33} eV^{-1}/m^{-3}) to a minimum of 1.22 (10^{33} eV^{-1}/m^{-3}). Subsequently, when the γAl_2O_3 was further increased to 10%, the deep trap density decreased to a minimum of 0.7 (10^{33} eV^{-1}/m^{-3}), the shallow trap density was increased to a maximum of 1.57 (10^{33} eV^{-1}/m^{-3}).

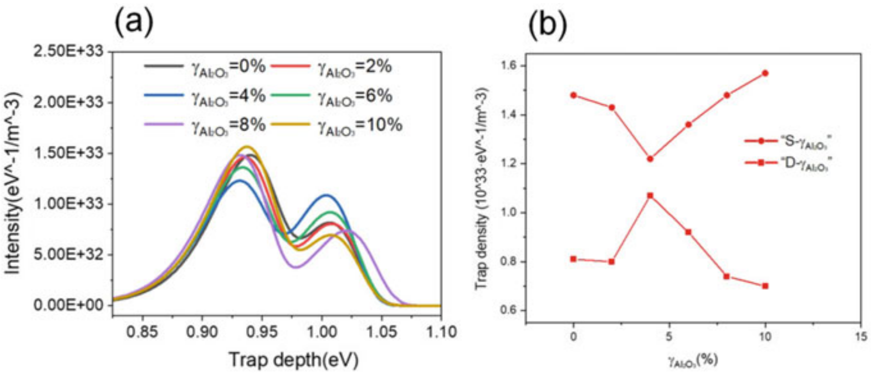

Fig. 19 Surface trap distribution of nano-Al_2O_3 composites with different mass fractions

(2) Energy level distribution characteristics of the composite surface of carbon nanotube particles with different proportions.

Figure 20a shows the distribution of composite surface traps at different nano-alumina doping mass fractions when γAl_2O_3 was 6%. The deep trap level on the composite surface is found to be concentrated at around 1.02 eV, whereas the shallow trap level is concentrated at around 0.93 eV. The corresponding change in CNT mass fraction did not occur.

Furthermore, as illustrated in Fig. 20b, the trap density fluctuates on the composite surface. It is discovered that the condition is identical to that which occurs when the mass fraction of nano alumina changes. Surface trap modifications are mostly reflected in trap density when the surface of the composite is physically modified. In this experiment, when the mass fraction grew, the density of the deep trap increased little at first, then rapidly declined. The change in shallow trap density on the material surface is the inverse. From γCNT = 0% to γCNT = 0.05%, the deep trap density

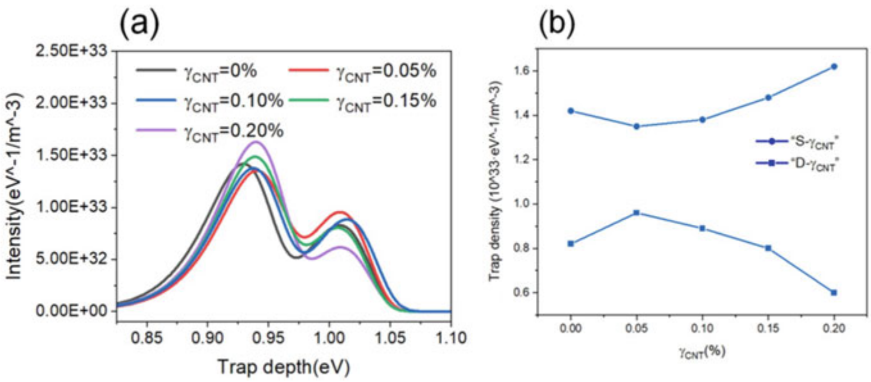

Fig. 20 Surface trap distribution for different mass fractions of MWCNT composites

increased from 0.82 (10^{33} eV^{-1}/m^{-3}) to a maximum of 0.96 (10^{33} eV^{-1}/m^{-3}). The shallow trap density fell from 1.42 (10^{33} eV^{-1}/m^{-3}) to a low of 1.35 (10^{33} eV^{-1}/m^{-3}). When the γCNT content was increased to 10%, the deep trap density declined to a minimum of 0.6 (10^{33} eV^{-1}/m^{-3}), while the shallow trap density grew to a maximum of 1.62 (10^{33} eV^{-1}/m^{-3}).

4.3.2 Flashover Model of Composites Under Mixed Modification of Nanoparticles

The grouping test of the surface qualities of the composite material reveals that the composite material has a high hydrophobicity structure built on a silicone rubber hydrophobic material substrate, polyamide mesh, and nanoparticles. Although increasing the mass fraction of fluorinated nano-alumina particles can improve the composite surface's superhydrophobic characteristics, the overall impact is small. The impact of nanoparticles on the surface properties of composite materials is most visible in the flashover properties along the surface.

Figure 21 depicts a tiny representation of the composite surface. Cheng K and others discovered the phenomena of nanoparticle introduction in their research. The researchers expected that introducing nanoparticles onto the surface of the composite material would result in the formation of an interface zone between distinct components [9]. Deep traps on the composite surface are mostly caused by the interface region between these distinct media. Along with being connected to the composite material surface, the nano-alumina particles attached to the polyamide mesh/silicone rubber composite material surface initially created the interface area with the composite material, resulting in a significant number of deep traps. Further doping of nano-alumina results in the formation of a loose layer on the surface of the composite material made of nano-alumina particles, which is the primary cause of the decrease in the deep trap density of the composite surface in the second stage [10].

Concerning the influence of carbon nanotubes on the composite surface, the researchers believe that the high electrical conductivity of carbon nanotubes increases the pace of charge dissipation of the composite surface, which is related to the improvement of the composite surface's trap distribution [11]. Carbon nanotube introduction can be divided into three steps. To begin, the addition of a very modest amount of carbon nanotubes causes the deep trap on the surface of the composite material to rise. Carbon nanotubes with increasing mass fraction improve trap distribution on the surface of composite materials, accelerate surface charge dissipation, hinder the creation of surface flashover discharge route, and eventually raise flashover voltage [12]. As the number of carbon nanotubes increases, they lap to form a local or via bridging network, resulting in a dramatic drop in the composite's surface flashover voltage.

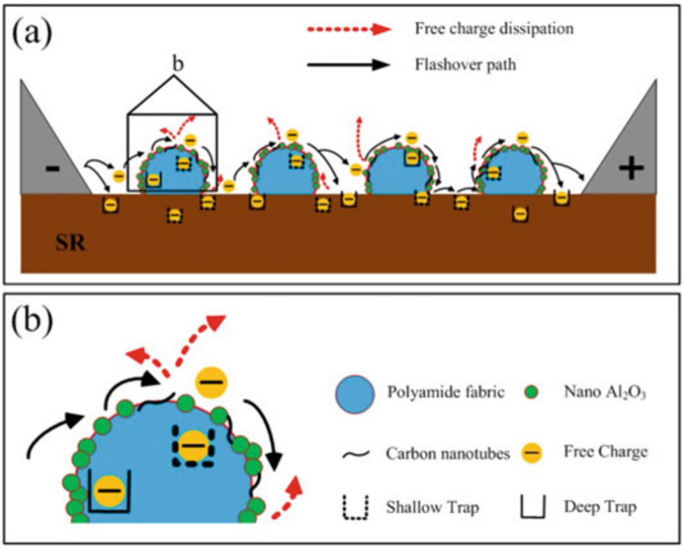

Fig. 21 Model of the flashover mechanism along the surface of the composite material

References

1. Touko, L.S.K.K., Vasuki, D., et al.: Protein adsorption and its effects on electroanalytical performance of nanocellulose/carbon nanotube composite electrodes. Biomacromolecules (2023)
2. Guannan, J., Lei, Z., Jiao, L., et al.: Robust metallic-based superhydrophobic composite with rigid micro-skeleton structure for anti-icing/frosting. J. Mater. Process. Tech. **316** (2023)
3. Assaedi, H.S., Olawale, D.M.: Impact of nano-alumina on the mechanical characterization of PVA fibre-reinforced geopolymer composites. J. Taibah Univ. Sci. **16**(1) (2022)
4. Jianwen, Z., Xinyu, P., Jinquan, H., et al.: Construction of hierarchical micro/nanostructured ZnO/Cu-ZnMOFs@SA superhydrophobic composite coatings with excellent multifunctionality of anticorrosion, blood-repelling, and antimicrobial properties. ACS Appl. Mater. Interfaces (2022)
5. Niu, L., Cai, L., Xinyu, X., et al.: Highly reliable transparent superhydrophobic composite by organosilane/denture base resin-modified alkylated silica nanoparticles against contaminants. Surf. Interfaces **35** (2022)
6. Qin, X., Luyao, W., Wenfang, F., et al.: Ratiometric electrochemical sensor based on polythionine/multiwalled carbon nanotube composite for butylated hydroxyanisole determination. J. Alloys Compd. **925** (2022)
7. Xiaoguang, Z., Dean, P., Gangqiang, Z.: Preparation and characterization of form-stable phase-change materials with enhanced thermal conductivity based on nano-Al_2O_3 modified binary fatty acids and expanded perlite. Energy Build. **271** (2022)
8. Ke, L., Chao, Y., Siyuan, Z., et al.: Laser direct writing of a multifunctional superhydrophobic composite strain sensor with excellent corrosion resistance and anti-icing/deicing performance. Mater. Des. **218** (2022)
9. Cheng, K., Yifan, F., Zheng, Z., et al.: Superhydrophobic composite coating with excellent mechanical durability. Coatings **12**(2) (2022)

10. Ke, L., Chao, Y., Siyuan, Z., et al.: Multifunctional slippery polydimethylsiloxane/carbon nanotube composite strain sensor with excellent liquid repellence and anti-icing/deicing performance. Polymers **14**(3) (2022)
11. Sansotera, M., Talaeemashhadi, S., Gambarotti, C., et al.: Comparison of branched and linear perfluoropolyether chains functionalization on hydrophobic, morphological and conductive properties of multi-walled carbon nanotubes. Nanomaterials **8**(3) (2018)
12. Mathur, A., Wadhwa, S., Byrne, A.J., et al.: Experimental demonstration of hydrophobicity variation in carbon nanotubes by surface modifications. e-J. Surf. Sci. Nanotechnol. **7** (2009)

Molecular Dynamics Simulation of the Effect of Water Intrusion on the Epoxy Resin/glass Fiber Interface of Composite Insulator Core

Jun Xie, Ke Chen, Qing Xie, and Fangcheng Lü

1 Introduction

1.1 Background of the Topic Selection and Research Significance

Composite insulators have the advantages of being lightweight, resistant to pollution, and exhibiting excellent flashover performance, making them widely used in power systems. According to the investigation, the number of standard composite insulators used in domestic grid lines in our country has exceeded 8 million. However, composite insulators are typical organic insulation devices that operate for long periods in high-temperature and high-pressure environments, often under harsh conditions. Various factors such as wind, sunlight, rain, ultraviolet radiation, and strong electric fields can cause aging in composite insulators, leading to a decrease in pollution flashover performance and even serious accidents like insulation breakdown and core rod fracture. Statistical data shows that dozens of 500 kV composite insulator stringing accidents have already occurred in the eastern coastal areas of our country.

Therefore, studying the aging mechanism of composite insulators under different environmental conditions is of great significance for improving their material properties and ensuring the safety and stability of the power system.

Currently, most of the research on the aging characteristics of composite insulators is based on artificial accelerated aging methods. Silicone rubber is an essential factor contributing to the excellent pollution flashover performance of composite insulators. The aging mechanism of silicone rubber materials is primarily studied through methods such as wet-heat aging, corona aging, and ultraviolet radiation

---

J. Xie (✉) · K. Chen · Q. Xie · F. Lü
Department of Electrical Engineering, North China Electric Power University, Baoding, China
e-mail: junxie@ncepu.edu.cn

Q. Xie (ed.), *Electrical Materials*, Engineering Materials,
https://doi.org/10.1007/978-981-99-9050-4_6

aging. The core rod is another important factor contributing to the excellent mechanical strength of composite insulators. However, factors like surface damage leading to moisture ingress can cause aging and overheating in the core rod, ultimately leading to accidents such as fractures [1].

In addition, besides studying silicone rubber and core rods, an increasing number of scholars have been focusing on the interface issues of composite insulating materials. The interface is a vulnerable link in composite insulation devices. In order to study the interface, Yang [2] investigated the impact of moisture ingress on the crimping interface of composite insulators, while Wang [3, 4] studied the boiling aging characteristics of the silicone rubber and cycloaliphatic epoxy resin interface in composite insulators and the effect of insulator mold joints on water diffusion tests.

The interface of composite insulators includes both macroscopic and microscopic interfaces. The macroscopic interfaces of composite insulators mainly include silicone rubber sheath/skirt, silicone rubber sheath/core rod, and end fittings/core rod. The representation of the microscopic interface is the interface between the core rod epoxy resin and glass fiber. The performance of the epoxy resin/glass fiber interface will significantly influence the overall performance of the composite insulator core rod. Therefore, conducting relevant research on the degradation characteristics of the epoxy resin/glass fiber interface is of great importance in understanding the aging mechanism of the core rod at the micro level.

Molecular simulation, as an important method for studying the microscopic properties of materials, has been widely applied in various fields. Compared to traditional experiments, molecular simulation methods have the advantages of high accuracy, low cost, and high efficiency. They are consistent with experimental results and can be flexibly and efficiently applied in polymer materials, synthetic chemistry, biology, and other fields. Molecular simulation methods integrated into the field of insulating materials can provide better insights into the material's changes and mechanisms in different environmental conditions.

Therefore, in order to clarify the degradation mechanism of the epoxy resin/glass fiber interface under moisture ingress, this study employs molecular simulation methods to analyze the impact characteristics of moisture ingress on the epoxy resin/glass fiber interface under different electric fields and environments. The research findings can contribute to a better understanding of the deterioration mechanism of composite insulators and provide theoretical and engineering guidance for enhancing the performance of composite insulators.

1.2 Research Status at Home and Abroad

1.2.1 Research Progress on Epoxy Resin/Fiber Interface Properties

Rain et al. [5] found that when moisture infiltrates the epoxy resin and penetrates into the quartz, it leads to the separation of interconnected epoxy resin and quartz, creating an interface. Other related studies have shown that moisture entering the interior of composite materials can cause damage and severe degradation of the epoxy resin/fiber interface [6], and may also result in matrix plasticization [7]. In the wet-heat aging process, the synergistic effect of moisture and temperature on the epoxy resin/fiber interface is primarily due to the high temperature causing the interface to fracture, and the post-curing reaction of the alkoxy material further deepens the fracture plane [8], resulting in a significant accumulation of moisture in the cross-sectional area. It is generally believed that the phenomenon of interface fracture in composite materials is mainly caused by the swelling or expansion stress resulting from moisture infiltration into the interface. Xu et al. [9–11], in their study of epoxy resin/fiber composite materials in a humid high-temperature and high-pressure environment and under the influence of an electric field, found that under conditions where other electrical parameters remain the same, the dielectric loss and dielectric constant of the composite material are directly proportional to the experimental treatment time and temperature, inversely proportional to the electric field intensity. Furthermore, with an increase in the experimental duration, the material's resistivity gradually decreases, indicating a deterioration in its insulating properties.

According to relevant studies, epoxy resin in composite materials may undergo hydrolysis reactions in a humid and hot environment, resulting in the rupture of the epoxy resin chain structure [12, 13]. FTIR analysis of the epoxy resin/fiber interface material after wet-heat aging reveals changes in the characteristic peaks of carboxyl and hydroxyl groups [14]. When composite materials absorb water, hydrolysis reactions occur between the epoxy resin and water, generating C–O bonds and N–CO–N bonds, accompanied by the cleavage of epoxy groups [15]. Furthermore, FTIR analysis of the water solution after immersing the composite material shows a characteristic peak at 1012 cm^{-1}, indicating the precipitation of some substances from the epoxy resin/fiber material after aging in a humid and hot environment, and this characteristic peak corresponds to Si–O bonds. However, the original composite material does not contain the mentioned chemical bonds, providing strong evidence of hydrolysis reactions occurring in composite materials under wet-heat conditions [16]. Additionally, the FTIR scan of the material after wet-heat aging shows a characteristic peak at 1735 cm^{-1}, indicating that the wet-heat environment can cause oxidation of the composite material [17]. Soles et al. [18] found that after wet-heat aging, samples develop polar hydroxyl groups that form hydrogen bonds. Since epoxy resin molecules do not contain amino groups, the formation of hydrogen bonds in the samples is likely due to hydroxyl groups interacting with ether groups or self-interactions.

In conclusion, researchers usually conduct simulated aging experiments on epoxy resin/fiber interfaces under conditions of wet-heat and applied external electric fields. However, the actual aging process of the interface is influenced by factors such as the ambient temperature during long-term operation, operating voltage, electric field, and electrochemical heating. The simulation experiments conducted by researchers only consider the effects of wet-heat and discharge, and the macroscopic experimental results cannot fully reflect the aging deformation process of the material's internal structure. Therefore, it is essential to explore characteristic values that indicate significant changes in the microscopic structure of epoxy resin/glass fiber materials in environments with moisture ingress. By using molecular dynamics methods, the macroscopic properties of the material can be organically linked to the microscopic structure and characteristics of the internal structure. This will provide a more comprehensive understanding of how the material behaves in the presence of moisture infiltration and its impact on the microstructure.

1.2.2 Molecular Simulation for Epoxy/Fiber Interface Properties

Lau et al. [19] conducted a molecular simulation analysis at the microscopic level to study the adhesion characteristics at the interface between fiber-reinforced resin composite materials and wood. They also analyzed the interfacial free energy. They found that the mechanism of hydrogen bond formation differs at different water molecule concentrations. At higher water molecule concentrations, water molecules tend to form larger clusters connected by hydrogen bonds, whereas at lower concentrations, smaller clusters connected by hydrogen bonds are formed with the composite organic materials. The entry of water molecules into the interface between epoxy resin and single-walled carbon nanotubes significantly affects the adhesion of the two molecules, leading to a decrease in the material's mechanical strength [20]. The internal water content of epoxy resin composite materials is positively correlated with their density but negatively correlated with the Young's modulus. As the water content increases, the Young's modulus initially increases and then decreases, with the lowest value being as low as 94.5% of the original performance. Other studies have found that the hydrogen bonding forces between water molecules and composite materials severely affect the movement of water molecules within the composite structure [21]. Additionally, through the analysis of root mean square displacement, volume expansion rate, and radial distribution function, it was observed that in the early stage of wet-heat aging, the moisture uptake is small, and the hydrogen bonding between water molecules and the composite material is the dominant form. As water molecules continue to increase, they bind together, enhancing their diffusion ability [22]. Due to the topological constraints of the spatial distribution of amino and hydroxyl groups, they are not affected by temperature limitations. However, the diffusion coefficient of water molecules shows a positive correlation with temperature [23]. Analyzing the simulation results, it was observed that water molecules enter the interior of the composite material and condense in the interface region between epoxy resin and carbon fiber. They form hydrogen bonds with the chemical bonds present in the interface, thereby reducing the surface free energy between epoxy resin and carbon fiber [24]. When the water content in the interface material is 0 wt%, the free volume accounts for 5.1% of the total volume. As the internal water content increases from 4 to 7 wt%, the proportion of free water decreases from 4.4 to 4.0%. This indicates that water molecules entering the interface interior occupy the free volume in the interface analysis [25, 26]. Xiao [27] studied water molecule infiltration into the epoxy resin/carbon fiber interface and found that water molecules enter the gaps between the epoxy resin and carbon fiber surfaces. Through intermolecular forces, they further expand the gaps between epoxy resin and carbon fiber molecules at the interface, resulting in reduced adhesion at the interface.

The basic properties of the composite material were analyzed using Material Studio software [28]. The simulation results obtained the glass transition temperature of the material, which showed a high degree of agreement with experimental results. However, the glass transition temperature calculated from the diffusion coefficient was found to be higher compared to experimental results [29–31]. Incorporating carbon nanotubes with high aspect ratios into the epoxy resin composite material can enhance the material's stiffness, leading to an early occurrence of tensile yield phenomena. Consequently, adding carbon nanotubes with high aspect ratios to the epoxy resin composite material significantly reduces its thermal stability [32, 33]. Research has indicated a negative correlation between the mechanical properties of epoxy resin and its moisture absorption and environmental temperature. However, the mechanical properties can be improved by increasing the crosslinking density of the epoxy resin [34, 35]. Therefore, in a humid and hot environment, epoxy resin composite materials tend to undergo accelerated aging, resulting in a decrease in their basic mechanical properties. The infiltration of water into the interior of composite materials leads to a reduction in their physical and chemical properties, subsequently affecting their fundamental insulating properties and mechanical strength [36–38].

In conclusion, scholars worldwide have mainly focused on studying the physicochemical properties of epoxy resin composite materials at the macroscopic level after water infiltration at the interface. There has been limited research on the microscopic structural changes of water molecules at the interface. Therefore, we need to shift our perspective and conduct comprehensive research from the perspectives of temperature and electric fields to study the changes in the epoxy resin/fiber interface after water infiltration in different environments. Subsequently, we can delve into the investigation and analysis of the movement patterns of microscopic molecules within the interface and their correlation with the macroscopic fundamental properties, as well as the variations and mechanisms of the interfacial bonding performance.

1.3 What This Article Examines

This paper aims to investigate the impact and failure mechanism of water infiltration on the epoxy resin/glass fiber interface using molecular dynamics methods. Considering the actual working conditions of composite insulators, this study focuses on the effects of temperature, electric fields, and their combined influence on the characteristics of water at the epoxy resin/glass fiber interface. The main tasks of this study are as follows:

(1) Based on the production process of composite insulator core rod epoxy resin/glass fiber interface, the composition ratios and reactions occurring during the preparation process are studied. The molecular-level model of the epoxy resin/

glass fiber interface is constructed and optimized, and water molecules are introduced as the working environment. After appropriate treatment, a stable conformational molecular model is obtained.

(2) Molecular simulations are performed on the epoxy resin/glass fiber interface in a water environment, and the results are compared with simulations conducted in a dry environment. Interface binding energy, ester group quantity, radial distribution function, and hydrogen bond quantity are selected as indicators to study the effects of water infiltration on the epoxy resin/glass fiber interface under the influence of temperature and electric fields.

(3) By simultaneously varying temperature and electric field parameters, the study investigates the impact of temperature/electric field synergistic effects on the epoxy resin/glass fiber interface in the presence of water infiltration. The variations in interface binding energy, ester group quantity, radial distribution function, and hydrogen bond quantity are analyzed to elucidate the degradation mechanism of the epoxy resin/glass fiber interface after water infiltration.

2 Establishment and Optimization of Epoxy/Glass Fiber Interfacial Molecular Models

Composite insulators commonly use glass fiber and epoxy resin as the core rod material, preparing fiber-reinforced composite materials with a certain proportion and processing method to combine the advantages of both materials. The adhesive performance of the epoxy resin/glass fiber interface in the core rod of composite insulators greatly affects the overall performance of the core rod. Therefore, establishing a simulation model for the epoxy resin/glass fiber interface and studying its changes in interface performance under different environments is of great significance.

In this chapter, we first analyze the composition and structure of the epoxy resin/glass fiber interface based on the production process of composite insulator core rods. Using the Material Studio simulation software, we construct a simulation model for the epoxy resin/glass fiber interface. By employing molecular dynamics theory, we perform energy optimization and relaxation operations on the interface model to establish a stable epoxy resin/glass fiber interface structure model. Subsequently, we place the model in environments with water molecules and dry conditions, laying the foundation for the study of interface performance under different environments.

2.1 Fundamentals of Molecular Dynamics Simulation

The molecular dynamics theory was initially proposed by Alder and Wainwright in the late 1950s. The earliest model of molecular dynamics was a simple hard sphere fluid model, which gradually developed into a mature theory through a series of optimization methods such as constant pressure and constant temperature simulations [39–42]. Using molecular dynamics methods, one can determine the molecular kinetic properties of materials during static equilibrium and physical deformation, and thus understand the macroscopic changes in material properties arising from the microscopic movements of molecules.

To simplify the calculations, the theory ignores the free movement of electrons and assumes that the forces acting on the atoms within the molecular material depend solely on the interatomic distances of neighboring nuclei. Therefore, the main calculation process of molecular dynamics involves calculating the acceleration of each atom based on Newton's second law under the same system constraints (as shown in Eq. 1). The potential energy of the molecular system is then calculated using fundamental mechanical parameters, and the first-order partial derivatives of the atomic coordinates are obtained for force analysis (as shown in Eq. 2). Multiple iterations are performed to compute the coordinates and velocities of all atoms in the system, resulting in the comprehensive trajectory of molecular motion.

$$\frac{\partial^2 r_i}{\partial t^2} = \frac{F_i}{m_i} = a_i \tag{1}$$

$$F_i = \frac{\partial U}{\partial r_i} \tag{2}$$

In the equations, t represents time; mi denotes the mass of atom i; ri is the coordinate of atom i; Fi represents the force acting on atom i; ai is the acceleration of atom i; and Ui stands for the potential energy of atom i.

During the calculation of molecular motion trajectories, the initial values of parameters directly affect the deviation between simulation results and actual results. To address this, ensemble theory can be used to adjust the overall computation process of atoms by controlling the system temperature and pressure. An ensemble refers to the sum of independent microscopic systems in different motion states under the same macroscopic conditions. The state of the atoms includes the coordinates, velocities, and momenta of all atoms. Common ensembles include the microcanonical ensemble (NVE), canonical ensemble (NVT), grand canonical ensemble (μVT), Gibbs ensemble (NPT), and isobaric-isenthalpic ensemble (NPH). The NVE ensemble has the constraint of a microsystem collection with the same number of molecules N, volume V, and temperature T, while the NPT ensemble has the constraint of a microsystem collection with the same number of molecules N, pressure P, and temperature T.

Furthermore, due to computational limitations, the scope of molecular dynamics research is limited to a collection of molecules in a finite space. Therefore, the boundary effects have a significant impact on the computational results. To reduce the boundary restrictions and computational complexity, the method of analyzing multi-atomic systems under force is often employed. Additionally, periodic boundary conditions are commonly used in molecular dynamics simulations to simplify computations and force analysis.

Taking the example of molecular dynamics simulations using the NVE ensemble with the same number of molecules, pressure, and temperature, the main computational steps are as follows:

(1) Determine the initial values of running parameters (number of molecules, velocities, structural density, integration time step, and running time).
(2) Initialize the system by determining the initial coordinates and velocities of atoms.
(3) Analyze the forces on atoms based on the system's initial set of basic mechanical parameters. Calculate the accelerations and potential energies of the atoms using Newton's second law and atomic nuclear distances.
(4) Calculate the velocities of atoms and iteratively integrate to calculate the velocities at the present time step based on the previous time step's velocities and forces on atoms.
(5) Calculate the system's kinetic energy and system temperature based on the forces on atoms, velocities, and potential energies. Optimize the running velocities of atoms accordingly.
(6) Calculate the coordinates of atoms and iteratively integrate to calculate the coordinates at the present time step based on the previous time step's coordinates and forces on atoms.
(7) Repeat steps 2–6 in a loop to compute the complete trajectories of atoms and the basic atomic structure of the system at its static equilibrium state. Analyze the statistical thermodynamic parameters of the system based on molecular dynamics theory.

2.2 Establishment and Optimization of Molecular Models

2.2.1 Establishment and Optimization of the Molecular Model for Epoxy Resin

Epoxy resin refers to a high molecular weight oligomer with two or more epoxy groups in its molecular structure and a backbone of aromatic, cyclic, or aliphatic compounds. It can form thermosetting products through the mutual reaction of epoxy groups. The epoxy resin used in composite insulator core rods is mainly composed of diglycidyl ether of bisphenol A (DGEBA) as the base resin and methyl tetrahydrophthalic anhydride (MTHPA) as the curing agent. The molecular structures of DGEBA and MTHPA are shown in Figs. 1 and 2, respectively.

The epoxy resin cured product obtained using anhydride exhibits excellent heat resistance and chemical stability. Its main cross-linking reaction mechanism is as follows:

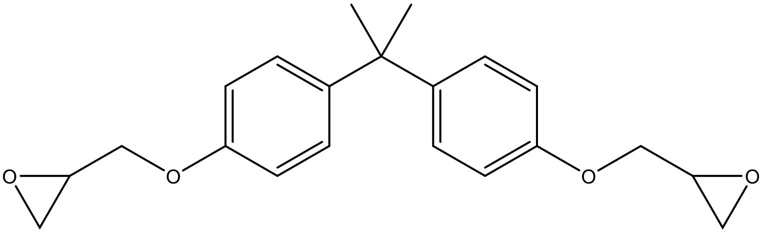

Fig. 1 Molecular structure of DGEBA

Fig. 2 MTHPA molecular structure

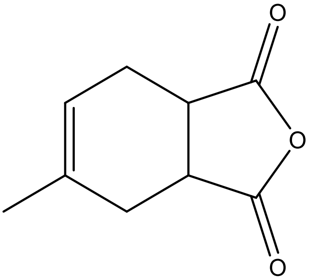

(a) Water molecules cause the epoxy resin's epoxy groups to open, generating hydroxyl groups.
(b) Anhydride groups react with hydroxyl groups in the epoxy resin, forming ester and carboxyl groups.
(c) Carboxyl groups undergo addition reaction with epoxy groups, producing new ester groups.
(d) In an acidic environment, epoxy groups undergo etherification reaction with hydroxyl groups.

The specific reaction mechanism is illustrated in Fig. 3.

Based on the above principles, the molecular configurations of DGEBA and MTPHA were established using Materials Studio simulation software, as shown in Fig. 4 and Fig. 5, respectively.

In the actual production process of curing the DGEBA resin with MTHPA, the mass ratio of the curing agent to epoxy resin is typically 80:100. Given the molecular masses of MTHPA (166) and DGEBA (330), the required quantity ratio of DGEBA to MTHPA is calculated as 83:132. Considering the computational limitations of the computer, the final epoxy resin model in this study includes 35 DGEBA molecules and 56 MTHPA molecules.

Based on the cross-linking mechanism of epoxy resin, a cross-linking program was written in Perl language to facilitate the automated cross-linking of DGEBA and MTHPA using the Amorphous Cell module of Materials Studio software. The resulting cross-linked model is shown in Fig. 6.

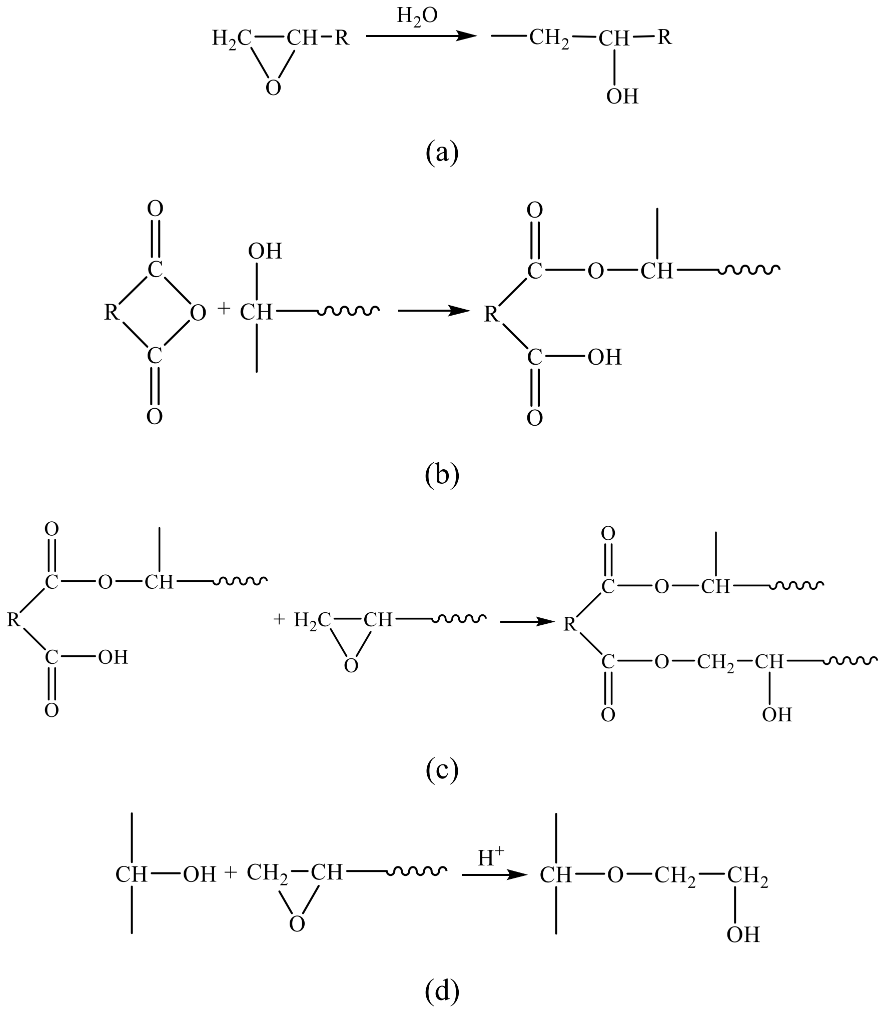

Fig. 3 Crosslinking reaction mechanism of DGEBA and MTHPA

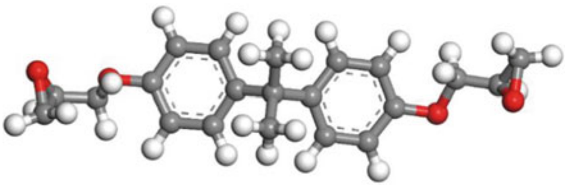

Fig. 4 DGEBA molecular model

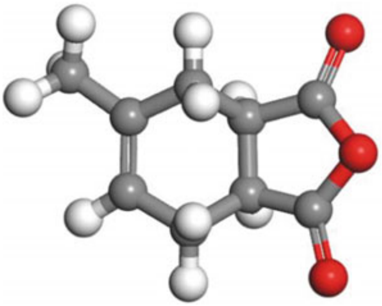

Fig. 5 MTHPA molecular model

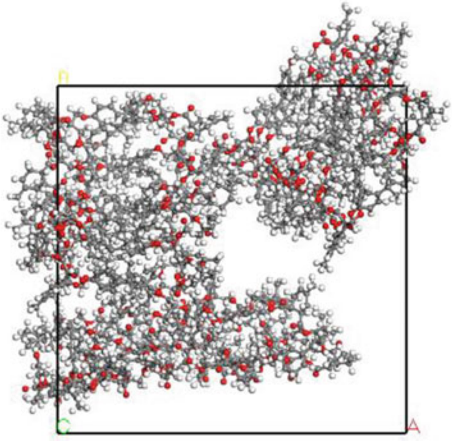

Fig. 6 Molecular model after crosslinking of DGEBA and MTHPA

To ensure that the cross-linked model aligns with the real situation, it needs to be optimized to obtain the lowest and most stable molecular structure. The optimization process of the model includes the following steps:

(1) Energy minimization optimization: The cross-linked epoxy resin is structurally optimized using the "Geometry Optimization" function in the Forcite module of Materials Studio. The COMPASS force field is employed, and the Smart algorithm is iterated for 50,000 steps to achieve energy minimization optimization of the model.

(2) High-temperature relaxation optimization: After performing energy minimization optimization on the molecular model, the COMPASS force field and NPT ensemble are used to simulate the system at an elevated temperature of 600 K. The simulation is iterated for 500,000 steps with a time step of 1 fs. The pressure is controlled using the Berendsen method, and the temperature is controlled using the Nose method. The molecular configuration is obtained based on Newton's second law and iterative calculations after 500.0 ps of simulation at high temperature.

(3) Annealing optimization: Annealing is performed to gradually stabilize the molecular model by continuously heating and cooling it. The Anneal function in the Forcite module is used for this optimization, with the COMPASS force field. The annealing process includes cycles of gradually raising the temperature from 300 to 600 K and then cooling it back to 300 K. The simulation is cycled 5 times, and each temperature gradient is simulated with 10,000 dynamic steps. The NPT ensemble is also used. The model's structure becomes relatively stable after annealing.

(4) NPT and NVT optimizations: The COMPASS force field is used, and the temperature is set to 300 K for both optimizations to ensure that the model is at its lowest and most stable energy state under normal temperature conditions. The time step is set to 1 fs, and the pressure is set to 0.1 MPa. The NPT optimization is performed with 500,000 steps, and the NVT optimization is performed with the same number of steps.

The optimized epoxy resin molecular model is shown in Fig. 7. It can be observed that the optimized model is more compact compared to the model just after cross-linking, with a significant reduction in voids, indicating a lower energy state and better alignment with actual conditions. The comparison of energy characteristic values before and after molecular model optimization is presented in Table 1. It can be observed that the optimized model exhibits considerable improvement in energy characteristic values compared to the non-optimized model, indicating that the optimized molecular model has reached a more stable state.

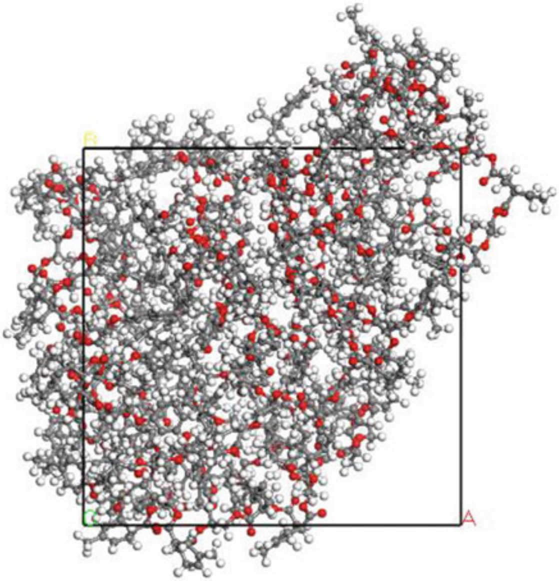

Fig. 7 Optimized epoxy resin molecular model

Table 1 Comparison of energy characteristic values before and after epoxy resin molecular model optimization

Energy (kcal/mol)	Before optimization	After optimization
Total energy	12,585.512	7447.213
Bond angle bending energy	3096.446	2036.045
Dihedral angle torsion energy	1032.854	896.637
Bond length stretching energy	2296.233	1432.258
Non-bonded interaction energy	856.414	422.174

2.2.2 Establishment of Glass Fiber Molecular Model

Glass fibers exhibit excellent corrosion resistance, heat resistance, and insulation properties. They are mainly made from natural minerals through processes such as high-temperature melting, drawing, spinning, and weaving. In molecular simulations, to simplify computations, the silica (SiO_2) structure can be used to model the surface of glass fibers.

The SiO_2 structure is retrieved from the Materials Studio software library and then trimmed to a size of 42.789742.789710.5853 $Å^3$ with a density of 2.254 g/cm^3. To enhance the simulation's authenticity and reliability, the SiO_2 surface undergoes hydrogenation treatment to simulate the oxidation process of SiO_2. The unsaturated O atoms on the SiO_2 surface are paired with H atoms, and the unsaturated Si atoms are bonded with –OH, resulting in the specific molecular model shown in Fig. 8.

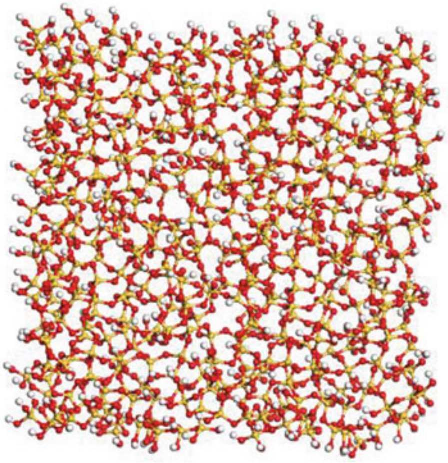

Fig. 8 SiO_2 amorphous molecular model

2.2.3 Establishment of Epoxy/Glass Fiber Molecular Model

The optimized epoxy resin and SiO_2 models are combined into a layered structure using the Amorphous Cell module in Materials Studio software. To eliminate the unwanted interface binding energy due to periodicity, a vacuum layer of 30 Å is added above the epoxy resin molecules. The final box size is set to 42.789742.789790.2477 $Å^3$, with SiO_2 at the bottom, epoxy resin in the middle, and a vacuum layer at the top. The initial model's interface binding performance is not satisfactory and does not represent the actual situation accurately. Hence, further optimization of the model is required. Following the epoxy resin optimization method and parameters, the interface model is optimized. The optimized Epoxy Resin/SiO_2 molecular model before and after optimization is shown in Fig. 9. It can be observed that the optimized epoxy resin molecules are closer to the SiO_2 interface, indicating improved interface binding performance, laying the foundation for studying the effect of water molecules on interface binding performance.

Composite insulator core rods often work in humid environments. Therefore, it is crucial to investigate the basic mechanical properties and adhesion interface free energy changes of epoxy resin/glass fiber composites under humid conditions. To simulate the water molecule's action mechanism at the epoxy resin/glass fiber interface, water molecules are randomly added inside the aforementioned simulation model. Considering the hydrophobic nature of glass fiber and the adsorption behavior of epoxy resin towards water molecules, according to the research results in reference [42], as shown in Fig. 10, the moisture absorption process of epoxy resin can be divided into several stages, and the saturation moisture absorption rate can generally

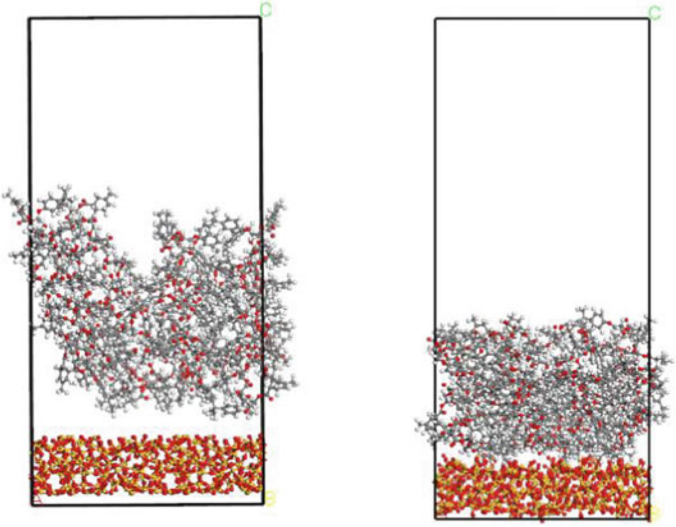

Fig. 9 Epoxy/SiO_2 interface model before and after optimization

reach 2.4% [42]. Based on these results, the model is randomly supplemented with 56 water molecules, and the water molecule model follows the TIP4P model proposed by Abascal, Jose LF, and Carlos Vega. Specific parameters of the water molecule model are shown in Table 2.

Following the above-mentioned method, the molecular model of the epoxy resin/glass fiber interface was established in the presence of water molecules. Subsequently, the model was optimized using the previously described approach. The optimized model is shown in Fig. 11.

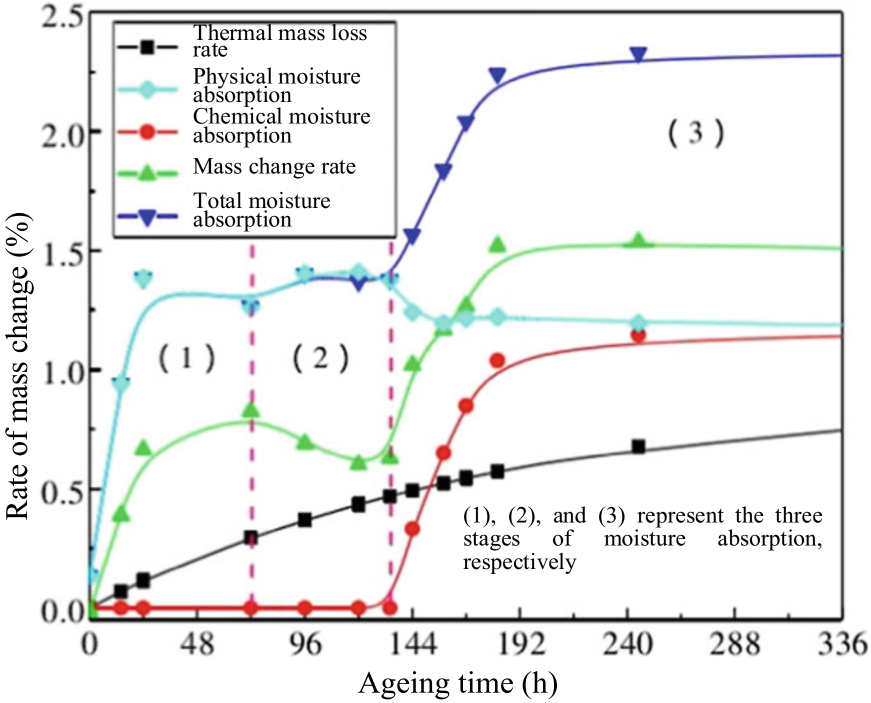

Fig. 10 Change law of moisture absorption of epoxy resin [42]

Table 2 TIP4P water model parameters

Oxygen atom mass	Hydrogen atom mass	Oxygen atom charge	Hydrogen atom charge	Hydroxyl bond length (A)	HOH bond angle (deg)	OM distance (A)
15.9994	1.008	−1.0484	−1.0484	0.9572	104.52	0.1250

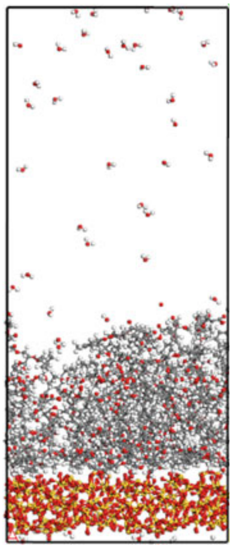

Fig. 11 Represents the molecular model of the epoxy resin/SiO_2 interface in the presence of water molecules

2.3 Summary

Based on the fundamental theory of molecular dynamics, this chapter establishes the molecular models of epoxy resin and glass fiber. The epoxy resin model represents the DGEBA/MTPHA cross-linked structure, while the glass fiber model adopts an amorphous SiO_2 structure. Additionally, using the Amorphous Cell module, the interface model of epoxy resin/glass fiber is constructed, and an appropriate amount of water molecules is added to create the molecular model of epoxy resin/glass fiber interface in a water environment. Furthermore, to match the models with the real system, energy minimization, relaxation, annealing, and NVT/NPT molecular dynamics optimizations are conducted. The establishment of these various molecular models in this chapter serves as a foundation for the research in subsequent chapters.

3 Considers the Influence of Water Intrusion on the Epoxy Resin/Glass Fiber Interface Under Temperature Effect

The high altitude and cold environment in some regions of China have significantly different requirements for transmission equipment and lines compared to other regions, which is also a major challenge in the construction of ultra-high voltage projects in China. In the case of moisture intrusion, the composite insulator core rod may experience abnormal heating, and in extreme cases, partial discharge may occur, leading to a further increase in the temperature around the core rod. Different environmental temperatures may cause varying degrees of damage to the interface after water intrusion. Therefore, it is important to study the microstructure and interfacial bonding performance changes of the epoxy resin/glass fiber interface under different temperature conditions. Therefore, this chapter mainly studies the impact of water molecules invading the epoxy resin/glass fiber interface in different temperature environments, summarizes and summarizes the simulation results, and finally obtains the factors and mechanisms of water molecules affecting the interface, providing reference for the causes of composite insulator core rod failures at the molecular level.

3.1 Temperature Selection Basis and Parameter Settings

In terms of temperature selection, this study mainly relies on the following two criteria.

(1) According to the Meteorological Bureau, extreme weather below −40 °C has occurred in Inner Mongolia and Heilongjiang Province in northeast China. The lowest winter temperature in the northernmost Heihe region of China can reach −45 °C.

(2) Epoxy resin undergoes hydrolysis reactions in water molecular environments, with hydrolysis reactions and epoxy resin degradation occurring at temperatures ranging from 400 to 500 °C. The air gap between the sheath and the core rod will be generated due to aging, and the air gap is easy to conduct due to the invasion of moisture, which will lead to partial discharge. In serious cases, it will lead to the carbonization of epoxy resin. Generally, this reaction occurs at 400–580 °C [43].

Considering the above environmental temperature and the additional temperature caused by the partial discharge phenomenon in the core rod area and other factors, the possible temperature range of the composite insulator core rod is analyzed, and a certain margin is reserved. The simulation temperature range is 213–853 K, and the interval is 60 K. Simulate and calculate the changes in the internal microstructure and basic microscopic properties of the epoxy resin/glass fiber interface when water invades at different environmental temperatures. The simulation takes the standard atmospheric pressure of 0.1 MPa. According to the constraint theory of NVT ensemble, the number, volume, and temperature of molecules in the system are kept constant. The integration step size is 1 fs, and the number of iterations is set to 20,000, totaling 20.0 ps. Considering that the interface model contains C, H, O, and Si atoms, and that the Dreiding universal force field is suitable for calculating the structure and other basic properties of polymer polymers, this simulation uses the GULP/Dreiding module to simulate and statistically calculate the interface model. This also establishes a foundation for the subsequent study of the GULP module on the impact of water molecule invasion on the epoxy resin/glass fiber interface in temperature and electric field synergistic environments.

3.2 Analysis of the Influence of Water Intrusion on the Epoxy Resin/Glass Fiber Interface Under Temperature Effect

3.2.1 Interface Structure Changes

This article first uses molecular simulation technology to analyze the changes in the interface structure of epoxy resin/glass fiber under the action of water molecules at different temperatures.

From the results of Fig. 12, it can be seen that in a water molecule environment, at low temperatures (213–293 K), the epoxy resin/glass fiber interface is tightly bonded, and the number of water molecules entering the interface through epoxy resin is very small; As the temperature increases, the tightness of the epoxy resin structure decreases, and holes gradually form inside. A small amount of water gradually enters the epoxy resin/glass fiber interface through the epoxy resin; As the temperature continues to rise, the bonding degree of epoxy resin becomes more and more loose, and the number of holes in the top epoxy resin increases. When the temperature rises to 453 K, the epoxy resin molecular chain in the water molecule environment undergoes fracture, and the bottom epoxy resin shows slight bulging, and the number of water molecule accumulation at the epoxy resin/glass fiber interface increases significantly; As the temperature continues to rise, when the temperature exceeds 613 K, the epoxy resin begins to decompose and disperse around; When the temperature reaches 693 K, water molecules gather on the surface of the decomposed epoxy resin group, and the interface has been completely destroyed.

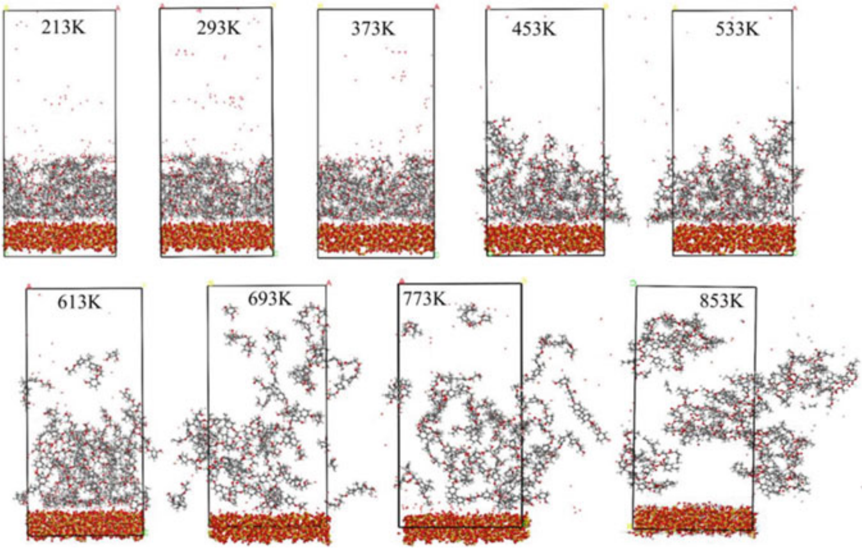

Fig. 12 Changes in interface structure of epoxy resin/glass fiber under water molecular environment

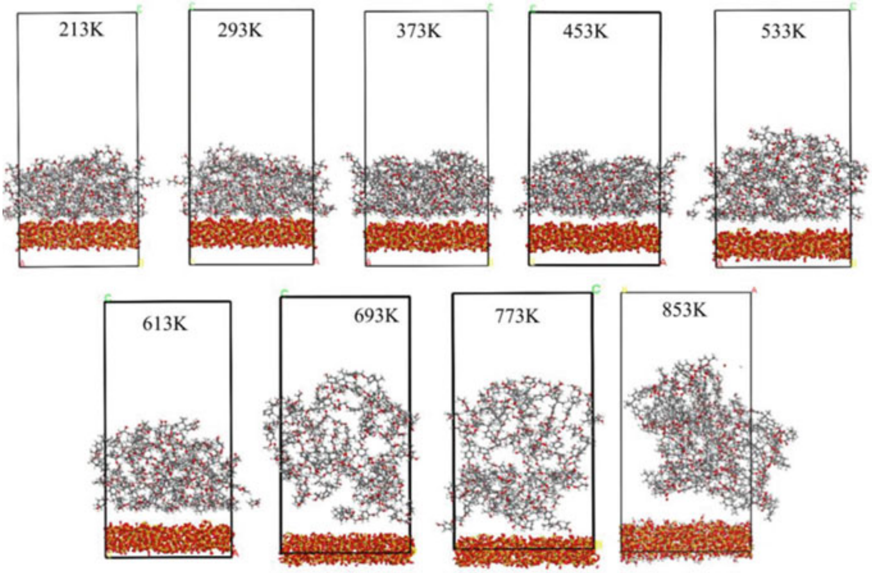

Fig. 13 Changes in the interface structure of epoxy resin/glass fiber in a dry environment

In order to further illustrate the destructive effect of temperature on the epoxy resin/glass fiber interface, this article also presents the results of the structural changes of the epoxy resin/glass fiber interface in a dry environment under temperature changes, as shown in Fig. 13.

From the results in Fig. 13, it can be seen that in a dry environment, as the temperature increases, the tightness of the epoxy resin structure gradually decreases, and the number of internal holes in the epoxy resin gradually increases. But when the temperature reached 853 K, there was no significant fracture of the epoxy resin molecular chain, and the epoxy resin/glass fiber interface was not completely destroyed.

Figure 14 shows the change of molecular structure of epoxy resin/glass fiber interface model with time at 853 K, in water molecular environment and dry environment. From the results of this figure, it can be further observed that spontaneous separation occurs at the epoxy resin/glass fiber interface at high temperatures, as shown in Figs. 14 and 15; The presence of water molecules will break the Chemical bond of epoxy resin and decompose the epoxy resin, thus further promoting the migration of water to the epoxy resin/glass fiber interface, and ultimately accelerating the destruction process of the interface.

In summary, after water intrusion, water molecules will enter the epoxy resin/glass fiber interface, promoting interfacial debonding; When the temperature increases, the epoxy resin/glass fiber also exhibits debonding behavior; When the temperature increases, the tightness of the epoxy resin molecular chain decreases, and the internal

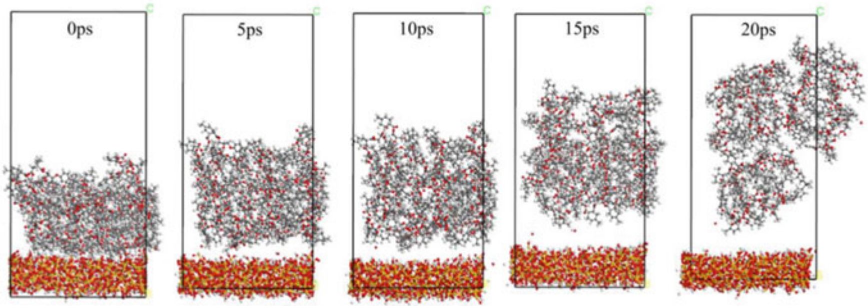

Fig. 14 Changes in interface structure of drying environment

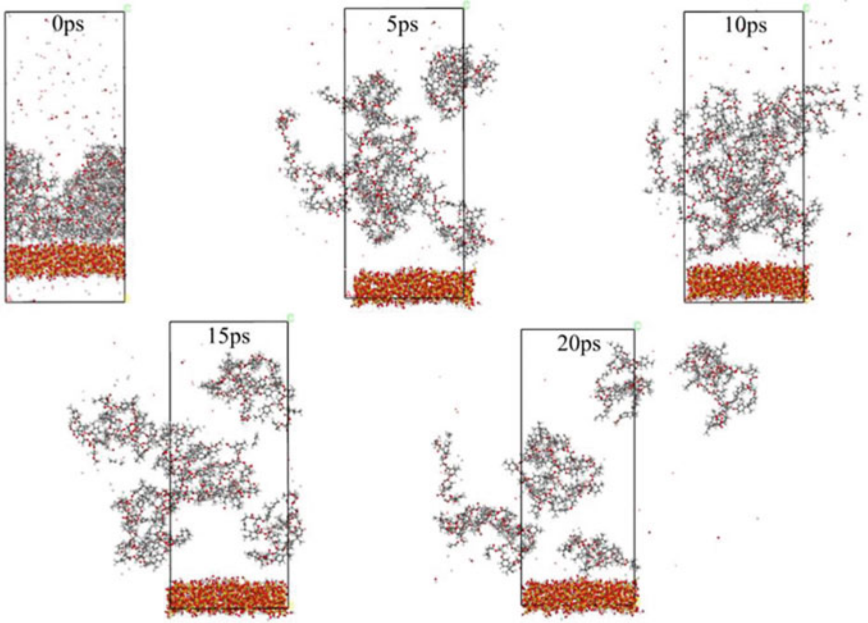

Fig. 15 Changes in interface structure under water molecular environment

holes gradually increase, accelerating the migration process of water towards the interface. In addition, under the combined action of high temperature and moisture, the molecular chains of epoxy resin break, further damaging the bonding degree of the interface.

3.2.2 Interface Adhesion Ability

Interface binding energy refers to the energy released to make the system more stable when atoms or other particles combine with each other. It is a parameter of the interaction energy of different components in a mixed system. Based on the changes in interface structure in last section, it can be seen that the interface between epoxy resin and silicon dioxide has undergone separation and damage in different environments. Studying interface binding energy can quantitatively explore the specific changes in interface binding performance. The calculation method for interfacial binding energy in water molecular environments is as follows:

$$E_{Epoxy\&\mathrm{SiO_2}} = \left[\begin{array}{l} \mathrm{E_{Total}} - \left(E_{Epoxy} + E_{\mathrm{SiO_2+H_2O}}\right) + \mathrm{E_{Total}} \\ -\left(E_{\mathrm{SiO_2}} + E_{Epoxy+\mathrm{H_2O}}\right) - \mathrm{E_{Total}} + \left(E_{\mathrm{H_2O}} + E_{Epoxy+\mathrm{SiO_2}}\right) \end{array}\right] \tag{3}$$

$E_{Epoxy\&\mathrm{SiO_2}}$	Interface Binding energy of epoxy resin and silica;
E_{Epoxy}	Epoxy resin energy;
$E_{\mathrm{SiO_2}}$	Silicon dioxide energy;
$E_{\mathrm{H_2O}}$	Water molecular energy;
$E_{\mathrm{SiO_2+H_2O}}$	The total energy of water molecules and silica;
$E_{Epoxy+\mathrm{H_2O}}$	Total energy of water molecules and epoxy resin;
$E_{Epoxy+\mathrm{SiO_2}}$	Total energy of silica and epoxy resin;
E_{Total}	Total energy of the system.

Before calculating the interface Binding energy, the above parameters were calculated by deleting the epoxy resin, silica and water molecules in the model. The interfacial Binding energy of epoxy resin/glass fiber interface changing with temperature under the water molecular environment was calculated by introducing the formula.

See Eq. 4 for the calculation formula of Binding energy of interface in dry environment. Similarly, delete the epoxy resin and silica from the model separately, and calculate the relevant parameters in the formula.

$$E_{Epoxy\&\mathrm{SiO_2}} = \left(E_{Epoxy} + E_{\mathrm{SiO_2}}\right) - E_{Total} \tag{4}$$

$E_{Epoxy\&\mathrm{SiO_2}}$	Interface Binding energy of epoxy resin and silica;
E_{Epoxy}	Epoxy resin energy;
$E_{\mathrm{SiO_2}}$	Silicon dioxide energy;
E_{Total}	Total energy of the system.

Based on the above calculation method, the changes in interfacial binding energy of epoxy resin/glass fiber in water molecular environment and dry environment were calculated at different temperatures. The results are shown in Figs. 16 and 17, respectively.

From the results in Fig. 16, it can be seen that in the water molecular environment, the interfacial binding energy of epoxy resin/glass fiber shows a trend of first increasing and then decreasing. The interfacial binding energy is relatively small in

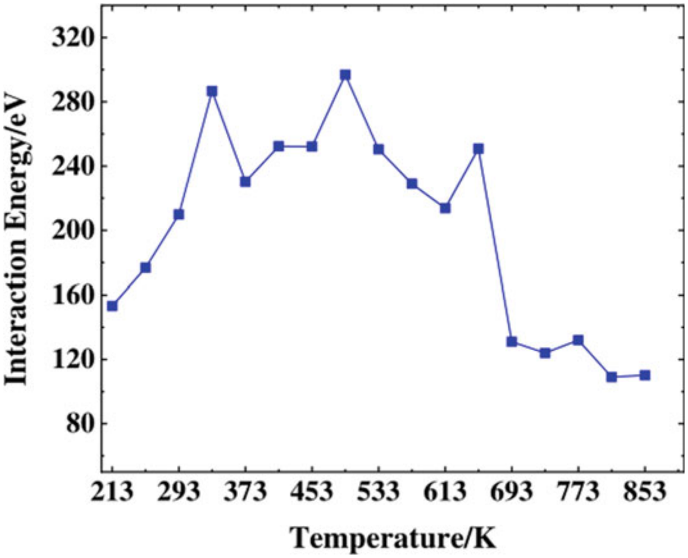

Fig. 16 Change of interface binding energy in water molecular environment

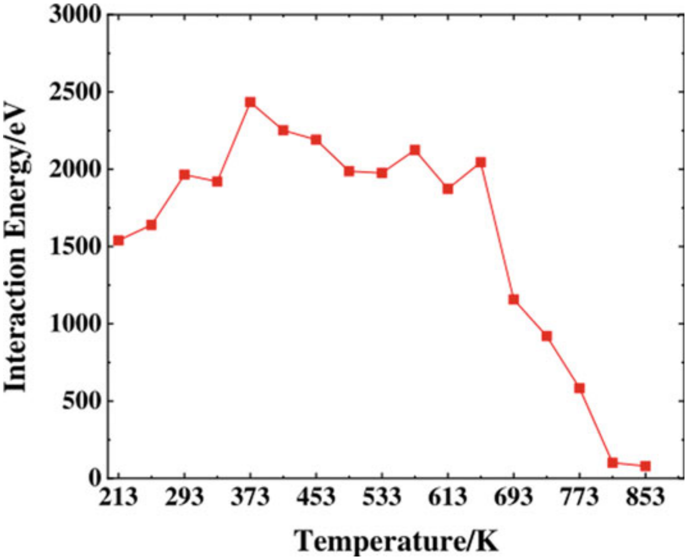

Fig. 17 Interface binding energy change in dry environment

low temperature environments, and increases rapidly with increasing temperature. When the temperature is between 373 and 653 K, the interfacial binding energy shows a fluctuating pattern and remains basically stable. When the temperature exceeds 653 K, the interfacial binding energy rapidly decreases. Afterwards, due to the severe damage of the epoxy resin/glass fiber interface, as the temperature further increased, the binding energy of the interface remained at a lower level without significant change.

It can be seen from the results in Fig. 17 that the change trend of the Binding energy of the epoxy resin/glass fiber interface in the dry environment is similar to that in the water molecular environment, but the value of the Binding energy of the interface is significantly higher than that in the water molecular environment at the same temperature, so the water molecule has an obvious role in destroying the interface. In addition, in dry environment, when the temperature is higher than 373 K, the fluctuation of interfacial Binding energy decreases, and when the temperature is higher than 653 K, the interfacial Binding energy decreases significantly.

In summary, as the temperature increases, the interface binding energy will show a trend of first increasing and then decreasing. Based on the changes in the interface structure mentioned earlier, it can be seen that when the temperature is around 373 K, the epoxy resin will expand due to the influence of temperature and water molecules entering the holes, causing the epoxy resin in the interface area to approach SiO_2, making the interface bonding more tight, and thus increasing the interface binding energy. This indicates that the increase of temperature does not necessarily lead to the decrease of interface bonding ability. Only when the temperature is higher than a certain limit value, will the decrease of interface Binding energy be caused in the anhydrous environment, which will reduce the degree of interface bonding. When water is present, it will significantly reduce the interfacial binding energy and affect the degree of interfacial bonding.

3.2.3 Microstructural Changes

Composite insulators often operate in humid environments, and the epoxy resin in the core rod spontaneously absorbs water in the humid environment. During the operation of the composite insulator core rod, it may encounter high-temperature environments, where the epoxy resin undergoes hydrolysis reactions in the water molecule environment. From Fig. 12, it can be observed that epoxy resin molecules undergo cracking when the temperature reaches a certain value. The specific hydrolysis reaction equation is shown in Fig. 18.

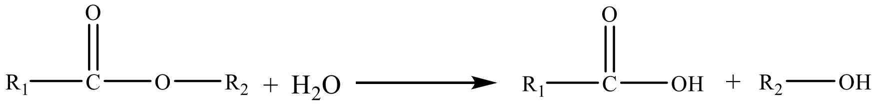

$$R_1-\overset{\overset{\displaystyle O}{\|}}{C}-O-R_2 + H_2O \longrightarrow R_1-\overset{\overset{\displaystyle O}{\|}}{C}-OH + R_2-OH$$

Fig. 18 Epoxy resin hydrolysis reaction equation

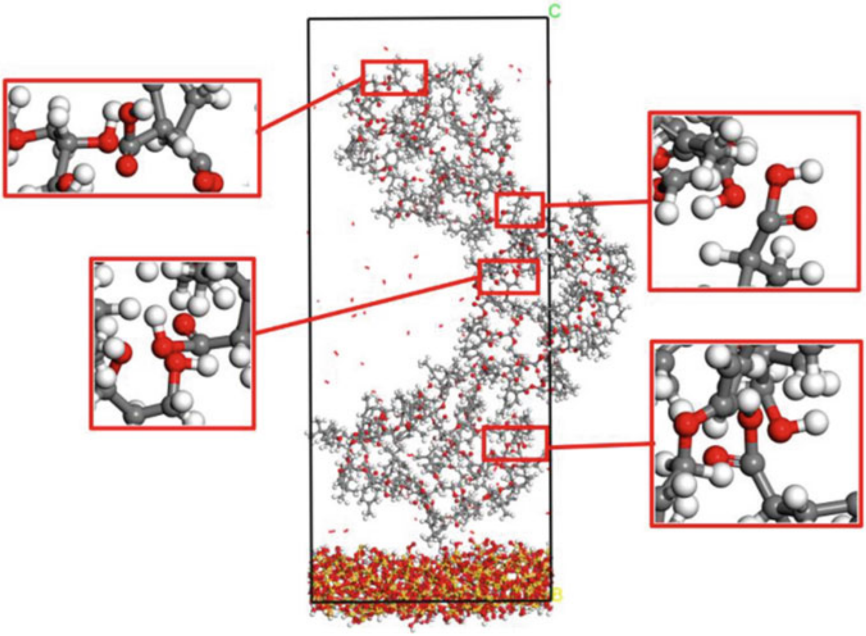

Fig. 19 693 K interface model ester group fracture diagram

From the previous analysis results, it can be seen that in the water molecule environment, as the temperature increases, the epoxy resin undergoes chemical bond breakage and gradually generates holes. Figure 19 shows an enlarged view of the local structure inside the epoxy resin at a temperature of 693 K. It can be seen from the figure that the ester group inside the epoxy resin breaks and generates carboxyl and hydroxyl groups. The above hydrolysis reaction did indeed occur.

From Fig. 19, it can be seen that the ester groups formed by cross-linking in the epoxy resin components will react with water molecules to generate carboxyl and hydroxyl groups, leading to the breaking of cross-linking bonds and the overall cracking of the epoxy resin. From Fig. 19, it can be observed that the degree of molecular cleavage of epoxy resin varies under different temperature environments. Therefore, the degree of hydrolysis reaction can be determined by counting the number of ester groups inside the epoxy resin.

According to statistics, the previously established molecular model contains a total of 56 ester groups. Due to the absence of water molecules in the model in a dry environment and the absence of conditions for hydrolysis reactions to occur, this statistical analysis only covers the ester group breakage in a humid environment. The statistical results of the number of ester groups in the interface model of water molecules at different temperatures are shown in Fig. 20.

From Fig. 20, it can be seen that there is no significant change in the number of ester groups at temperatures below 373 K; When the temperature is greater than 373

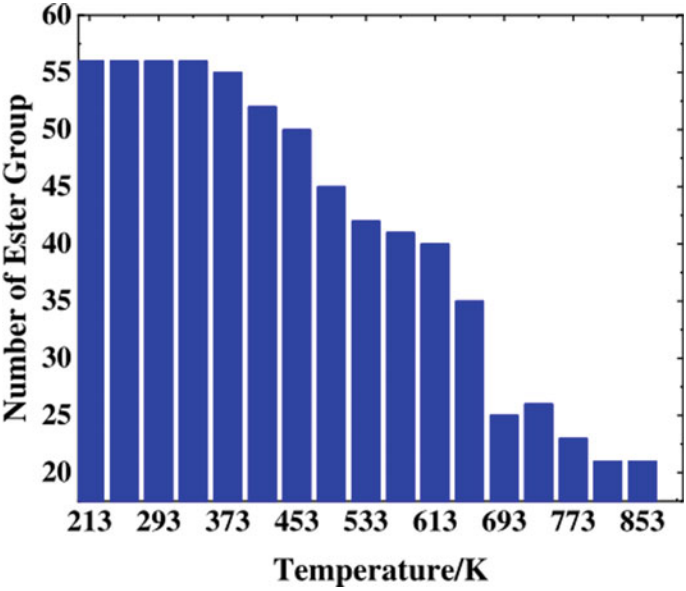

Fig. 20 Changes in the number of ester groups

K, the number of ester groups begins to decrease; When the temperature exceeds 613 K, the number of ester groups rapidly decreases; When the temperature reaches 693 K, the number of ester groups remains basically unchanged.

Based on the changes in the interface model at different temperatures mentioned above, it can be concluded that when the temperature is below 373 K, the number of ester groups does not change, indicating that this temperature environment does not comply with the temperature at which the epoxy resin hydrolysis reaction occurs, and the epoxy resin does not undergo significant hydrolysis. When the temperature reaches 373 K, reaching the hydrolysis temperature of the epoxy resin, the number of ester groups gradually decreases. As the temperature further increases, the molecular structure of the epoxy resin gradually relaxes, and water molecules are more likely to enter the epoxy resin to participate in the reaction. Therefore, as the temperature increases, the number of ester groups rapidly decreases. As the temperature further increases, the broken epoxy resin molecules drift freely in the system, causing water molecules to be too far away from the epoxy resin and making it difficult to react. Therefore, the ester base amount is relatively stable at this time.

In summary, based on the previous analysis results, it can be seen that the epoxy resin/glass fiber interface begins to undergo hydrolysis reaction at 373 K, leading to a decrease in interfacial binding energy. As the temperature continues to rise, a large number of water molecules enter into the epoxy resin molecules, leading to more intense hydrolysis reaction, which eventually causes the epoxy resin molecules to gradually crack and disperse, leading to a sharp drop in the interface binding energy, further damaging the interface.

3.2.4 Hydrogen Bond Changes

Figure 21 is a schematic diagram of the enlarged interface area between epoxy resin and silica. It can be seen that there is aggregation of water molecules in the interface area, which can increase the distance between epoxy resin and silica. The hydroxyl groups in silica will form hydrogen bonds with water molecules, which may affect the formation of hydrogen bonds between epoxy resin and silica, thereby affecting interface bonding. So studying the formation of hydrogen bonds in water molecular environments is very important.

Firstly, investigate the possible formation of hydrogen bonds in the interface region. In a dry environment, the oxygen atoms in the epoxy resin/silica interface area and the hydroxyl groups in the silica may form hydrogen bonds, resulting in stronger interfacial bonding performance. In humid environments, hydrogen bonding between hydroxyl atoms in silica and oxygen atoms in water may also occur at the interface. In humid environments, there are numerous water molecules, and the hydrogen bonds generated may affect the interfacial bonding performance.

The radial distribution function (RDF) can determine the distribution probability of other particles in space based on the given coordinates of a certain particle. Based on RDF, the probability density of another molecule appearing at a distance of r from a certain molecule can be achieved. By using the RDF method, the distance between atoms that may form hydrogen bonds at the epoxy resin/glass fiber interface and the overall distance between epoxy resin molecules and silica molecules can be analyzed.

Based on the possible forms of hydrogen bonds mentioned above, the main research objects of this section are as follows:

(1) Hydrogen bonds formed by O_{epoxy}—$H_{silicon}$ in water molecular environments;
(2) Hydrogen bonds formed by O_{water}—$H_{silicon}$ in water molecular environments;
(3) Hydrogen bonding formed by O_{epoxy}—$H_{silicon}$ in a dry environment.

The distance at which the peak appears in the RDF spectrum represents the fixed distance from one of the studied atoms, find the distance corresponding to the highest probability of finding another atom. Figure 22 shows the RDF analysis of hydrogen atoms in silicon dioxide and oxygen atoms in water molecules at a temperature of 253 K. It can be seen from the figure that the probability of oxygen atoms appearing is the

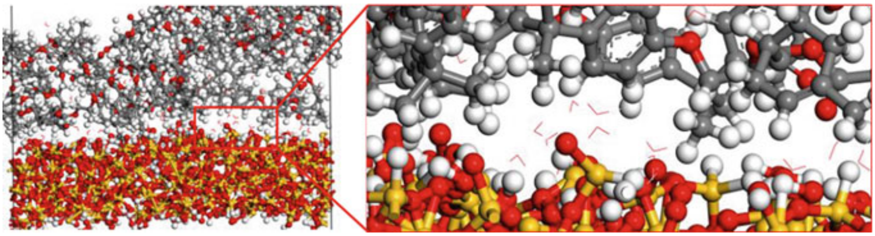

Fig. 21 Schematic diagram of water molecule aggregation in the interface area

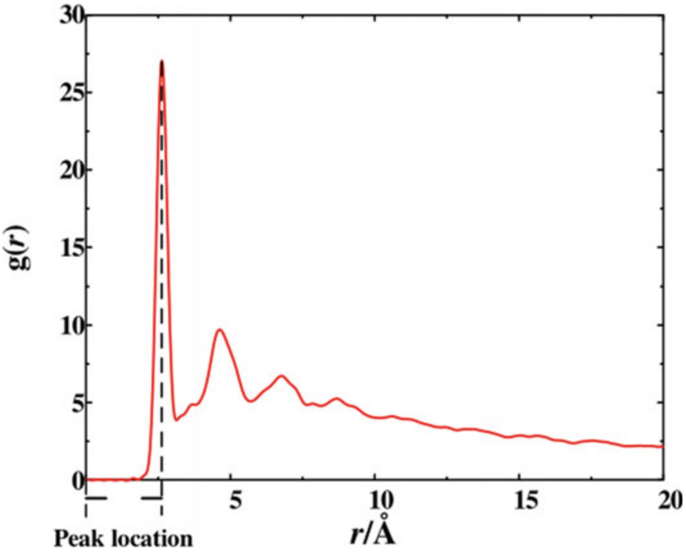

Fig. 22 RDF diagram of $H_{silicon}$—O_{water} at 253 K

highest at a distance of 2.5 Å from the hydrogen atom. Therefore, the most important parameter in the RDF study in this section is the distance from the peak, which is the abscissa of the peak. By studying the distance between peaks, it is possible to study both the distance between interfaces and the sequence of hydrogen bond formation between interfaces.

The research statistical results are shown in Fig. 23. It can be seen that the RDF peak distance of $H_{silicon}$—O_{epoxy} under different environments shows an overall upward trend with the increase of temperature, and the increasing speed of the peak distance increases when the temperature is greater than 653 K. Among them, at temperatures ranging from 373 to 653 K, the distance from the peak of $H_{silicon}$—O_{epoxy} to the peak of $H_{silicon}$—O_{water} is generally larger than that of $H_{silicon}$—O_{water}, indicating that the formation of hydrogen bonds between water molecules and silica occurs earlier than that between epoxy resin and silica, which inevitably leads to a decrease in the mechanical properties of the interface between epoxy resin and glass fiber. As the temperature continues to rise, water molecules disperse in high-temperature environments, leading to a rapid increase in the distance from the peak. In a dry environment, the distance between $H_{silicon}$—O_{epoxy} first remains stable and then rapidly increases, indicating that even without the presence of water, the hydrogen bonding between epoxy resin and glass fiber will weaken as the temperature increases.

From the changes in interface structure mentioned earlier, it can be seen that water will gradually migrate through epoxy resin to the epoxy resin/glass fiber interface. The accumulation of water molecules at the interface will lead to the formation of hydrogen bonds between water molecules and silicon dioxide molecules, hindering

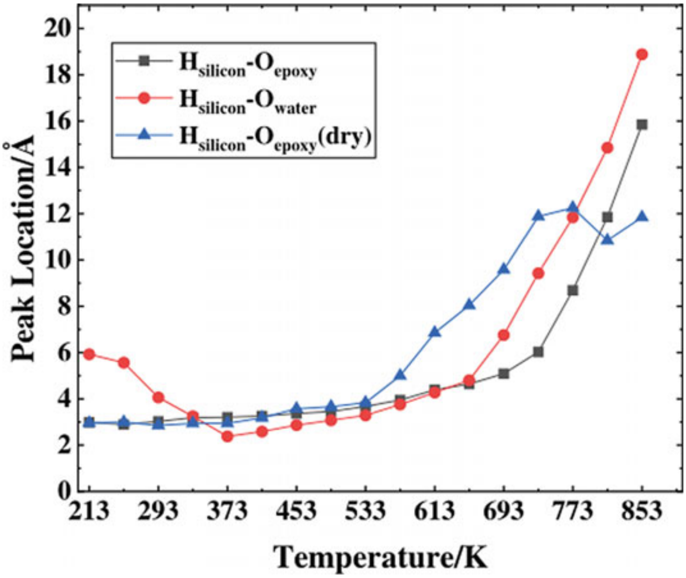

Fig. 23 RDF peak occurrence distance

the formation of hydrogen bonds between epoxy resin molecules and silicon dioxide molecules, thereby affecting the interface bonding performance.

The phenomenon of water accumulation at the interface indicates that water molecules and silica adhere to each other, which leads to more hydrogen bonds forming in the interface area than in dry environments. Therefore, counting the number of hydrogen bonds has an important impact on explaining the changes in interface bonding performance. Using Perl language to write a script for counting the number of hydrogen bonds, this script combines the trajectory file of the interface under water molecules with temperature changes to obtain the average value of hydrogen bonds generated by the interface over time, which can accurately determine the number of hydrogen bonds in the system. The statistical results are shown in Fig. 24.

From Fig. 24, it can be seen that in the water molecule environment, the number of hydrogen bonds increases at 373 K, and begins to decrease when the temperature exceeds 493 K. The number of hydrogen bonds decreases significantly when the temperature exceeds 653 K, and remains stable at 693 K.

Based on the changes in interface structure mentioned earlier, it can be seen that when the temperature is below 373 K, water molecules do not move violently and cannot enter the interface area due to the lower temperature. As the temperature increases (above 373 K), epoxy resin molecules begin to hydrolyze, causing damage to the overall structure of epoxy resin molecules, causing water molecules to enter the internal holes of epoxy resin, leading to epoxy resin expansion, making the epoxy resin in the interface area slightly move downwards, making the interface fit more

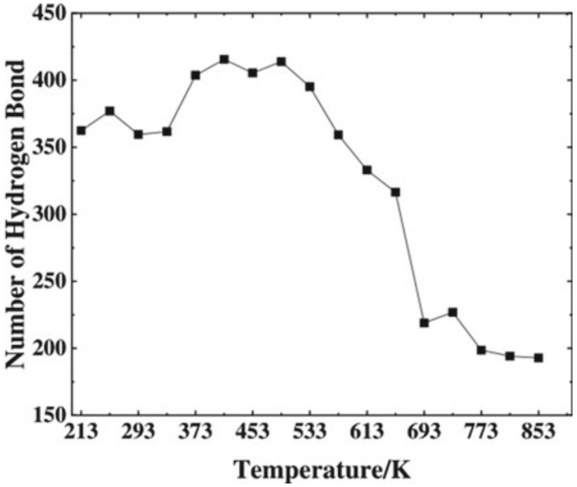

Fig. 24 Changes in the number of hydrogen bonds

tightly, leading to an increase in hydrogen bonding. Afterwards, as the temperature continues to rise, water molecules adhere to the surface of SiO_2 under the action of temperature, forming hydrogen bonds with them. At this time, the hydrogen bonds formed by O_{epoxy}-$H_{silicon}$ break, and the hydrogen bonds formed by O_{water}-$H_{silicon}$ remain stable at this temperature. As the temperature continues to rise (greater than 653 K), water molecules begin to break free from the binding of hydrogen bonds and leave the surface of silica under the influence of temperature, resulting in a sharp decrease in the number of hydrogen bonds. When the temperature is above 693 K, the distance between each component in the system is relatively far, and hydrogen bonds cannot be formed, resulting in a stable number of hydrogen bonds.

In summary, epoxy resin undergoes expansion and cracking under the influence of temperature and hydrolysis reaction, causing water molecules to pass through the epoxy resin to reach the interface area and form hydrogen bonds with silica molecules, hindering the formation of hydrogen bonds between epoxy resin and silica molecules, resulting in a decrease in interfacial binding energy. This is manifested in a decrease in interfacial binding energy at temperatures ranging from 493 to 613 K.

3.3 Summary

In this chapter, the influence of water intrusion on the epoxy resin/glass fiber interface under the consideration of temperature effect was studied, and the changes of interface structure, interface Binding energy, ester group number and hydrogen bond were emphatically analyzed. From the results of this chapter, it can be seen that as the temperature gradually increases, the molecular structure of epoxy resin gradually relaxes, water molecules are easy to enter the internal and interface areas of epoxy resin molecules. After water molecules invade the interface, hydrogen bonds are formed between epoxy resin and silica molecules, hindering the formation of hydrogen bonds between O_{epoxy}-$H_{silicon}$ and subsequently hindering the bonding of epoxy resin/glass fiber interface. When the temperature reaches the hydrolysis temperature (373 K), as the temperature increases, the hydrolysis reaction of the epoxy resin intensifies, causing the epoxy resin to gradually crack and accelerating the process of interface damage. The hydrolysis of epoxy resin promotes the easier entry of water into the interface area, further hindering the formation of hydrogen bonds between epoxy resin and silica molecules, resulting in a significant decrease in the bonding ability of epoxy resin/glass fiber interface. When the temperature reaches 653 K, the hydrolysis reaction of the epoxy resin is basically completed, and the interface has been basically completely destroyed.

4 Considers the Influence of Water Intrusion on the Epoxy Resin/Glass Fiber Interface Under Electric Field Effect

Under working conditions, composite insulators bear the effect of electric fields. In addition, due to water intrusion and other reasons, the interface between the core rod and the sheath and the inside of the core rod are prone to field strength distortion. Due to the polarity of water molecules, their migration behavior within the core rod is inevitably influenced by the strength of the electric field. In view of this, this chapter focuses on studying the changes in the epoxy resin/glass fiber interface after water intrusion under the electric field effect.

4.1 Selection Basis and Parameter Settings for Electric Field Strength

According to the research results of Ref. [44], due to stray capacitance and other reasons, the axial potential and electric field distribution of composite insulators exhibit significant non-uniformity, with a prominent manifestation being the high field strength on the wire side, which can reach a value of 3.9 kV/cm. The field strength in the middle of the insulator is the lowest, with a value of approximately 0.8 kV/cm. The field strength in the middle is relatively low. In addition, due to the infiltration of moisture at the interface of the core rod/sheath, the 15–20 cm electric field at the defect site will undergo distortion. When the field strength distortion occurs on the high-voltage side, the maximum field strength can reach 33.14 kV/cm.

According to the above principles, when conducting molecular simulation, the electric field intensity range is set to 1 kV/cm–33 V/cm, with an interval of 2 kV/cm. According to the research conclusion in last chapter, when the temperature is higher than 373 K, the epoxy resin will undergo a hydrolysis process, causing the interface performance to gradually decay. Therefore, during the simulation in this chapter, the temperature is still set at 373 K.

In summary, the parameter settings in this chapter are: temperature is 373 K; the air pressure is standard atmospheric pressure (0.1 MPa); the integration step size is 0.1 fs; 20,000 iterations; the total simulation time is 20.0 ps; the simulation module is GULP/Dreiding.

In addition, due to the extremely short molecular simulation time, usually calculated in femtoseconds (fs), which is much smaller than the alternating period of the AC electric field, the electric field can be equivalent to a constant electric field during simulation.

4.2 Analysis of the Influence of Water Intrusion on the Epoxy Resin/Glass Fiber Interface Under the Consideration of Electric Field Effect

4.2.1 Interface Structure Changes

This article first uses molecular simulation technology to analyze the changes in the interface structure of epoxy resin/glass fiber in a water molecular environment under the action of an electric field. The results are shown in Fig. 25.

From the results of Fig. 25, it is not difficult to find that when the electric field intensity is low (1 kV/cm), the number of water molecules entering the epoxy resin

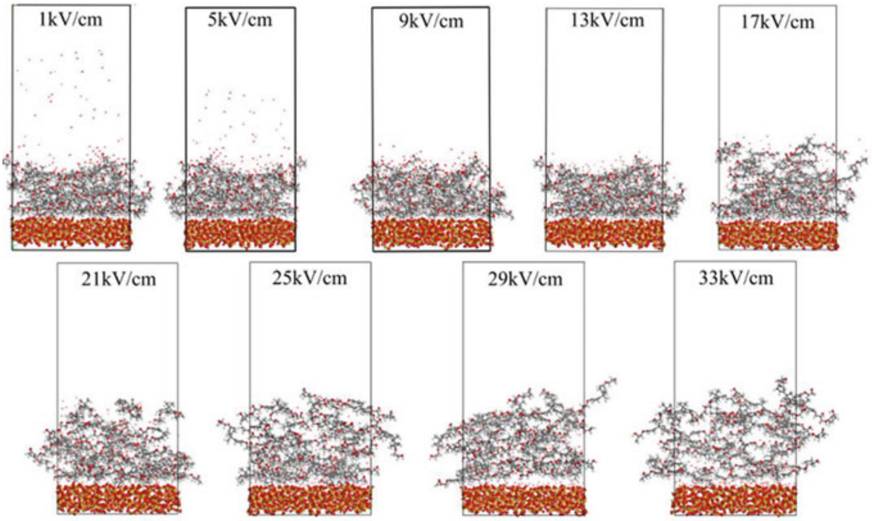

Fig. 25 Changes in the interface structure of epoxy resin/glass fiber in water molecular environments under different electric fields

is relatively small, and there is no significant change in the structure at the interface. When the electric field is 5–9 kV/cm, the number of water molecules attached to the epoxy numerical surface gradually increases, but there are still no obvious holes inside the epoxy resin, and the structure at the epoxy numerical/glass fiber interface remains unchanged. When the electric field strength exceeds 9 kV/cm, the top of the epoxy resin undergoes splitting and creates holes, through which water molecules can enter the interior of the epoxy resin. As the electric field strength further increases, the splitting phenomenon of epoxy resin intensifies, and the number of internal holes in epoxy resin increases. The number of water molecules entering the epoxy value and entering the interface through epoxy resin gradually increases. When the field strength reaches 29 kV/cm, the vast majority of water molecules have reached the interface area and attached to the SiO_2 surface.

To further analyze this phenomenon, this article presents the evolution results of the interface structure between epoxy resin and glass fiber in a water molecular environment at a field strength of 29 kV/cm, as shown in Fig. 26. During the 0–5 ps process, water molecules shift from random distribution to directional movement towards epoxy resin molecules, with a large number of water molecules adhering to the surface of the epoxy resin and some entering the interior of the epoxy resin. At 10 ps, the water molecules in the space have completely entered the interior of the epoxy resin, and the epoxy resin above begins to split, creating holes, and some water molecules reach between the epoxy resin and silica. At 15 ps, the number of water molecules at the interface increases, and the epoxy resin at the interface also decomposes. At 20 ps, a large number of water molecules have entered the interface area and the interface has been basically destroyed.

After analyzing the above rules, it can be concluded that after water intrusion, water molecules will gradually migrate towards the epoxy resin/glass fiber interface. When the electric field intensity is low, the main inducement of water molecule migration is molecular Thermal motion. As the electric field strength increases, water molecules move directionally under the action of electric field force and adhere to the surface of epoxy resin. Due to the temperature of 373 K during the simulation in this article, which has reached the hydrolysis temperature, the top of the epoxy resin first hydrolyzes under the action of water molecules and forms holes. At this time, water molecules are prone to pass through the holes and enter the interior of the epoxy resin under the action of an electric field. However, some of the water molecules entering the interior of the epoxy resin are easily blocked by the hydrolysis products and stop migrating. As the electric field strength further increases, the number of water molecules entering the interior of epoxy resin increases, the degree of hydrolysis of epoxy resin deepens, and the number of internal holes gradually increases. Under the strong electric field force, water molecules are more likely to overcome the obstruction of epoxy resin and its hydrolysis products and reach the interface.

To compare and illustrate the destructive effect of moisture on the interface, this article also presents the changes in the interface structure of epoxy resin/glass fiber under different electric fields in a dry environment. As shown in Fig. 27.

From the results in Fig. 27, it can be seen that due to the fact that both epoxy resin and silica are non-polar molecules and have no functional groups available for

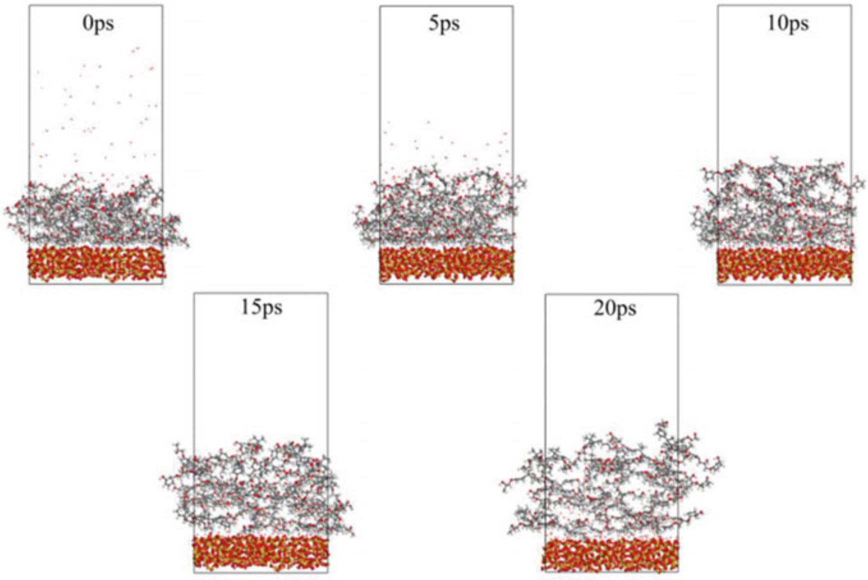

Fig. 26 Changes in interface model under a 29 kV/cm electric field environment

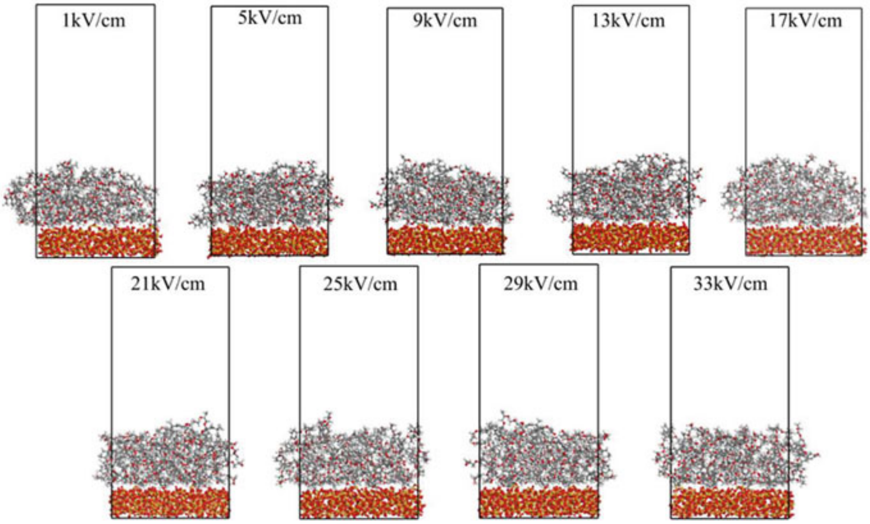

Fig. 27 Changes in the interface structure of epoxy resin/glass fiber in dry environments under different electric fields

electric field action, there is no significant change in the interface structure under the electric field in a dry environment.

In summary, the effect of electric field on the interface structure of epoxy resin/glass fiber after water intrusion is mainly due to the directional movement of water molecules and the increase in the number of water molecules entering the epoxy resin. At the temperature allowed by the hydrolysis reaction, the electric field can trigger the hydrolysis reaction and generate holes. In addition, water molecules can cause more water molecules to enter the interface area under the action of an electric field, affecting the binding of the interface.

4.2.2 Interface Adhesion Ability

The interface adhesion can be quantitatively characterized by the interface Binding energy. With the increase of electric field strength, the change rule of interface Binding energy under different environments is shown in Fig. 28.

It can be seen from the results of Fig. 28a. In the water molecular environment, the Binding energy of the epoxy resin/glass fiber interface shows a decreasing trend. When the electric field intensity is low (1–9 kV/cm), the interface Binding energy value is high and basically stable. When the electric field intensity is 9–25 kV/cm, the interface Binding energy shows a gradual decline trend. When the electric field intensity is greater than 25 kV/cm, the interface Binding energy decreases rapidly. When the electric field strength reaches 29 kV/cm, the epoxy resin/glass fiber interface has been severely damaged at this time, and the water molecules have basically covered the surface of silica. Therefore, with the further increase of the electric field strength, the interface Binding energy remains at a low level.

It can be seen from the results in Fig. 28b that the Binding energy of the epoxy resin/glass fiber interface is basically stable in a dry environment with small fluctuations, and the average value is 2017.98 eV. Compared with water molecule environment, the interface Binding energy in dry environment is significantly higher, which also confirms that water molecules in electric field environment will damage the epoxy resin/glass fiber interface.

According to the analysis of the above rules, when the electric field intensity is low in the water molecule environment, the amount of entering the epoxy resin interior and interface is still small, at this time, the interface Binding energy remains at a high value. With the increase of electric field strength, water molecules begin to move directionally and enter into the epoxy resin. Under the action of water molecules, the epoxy resin undergoes hydrolysis reaction and generates holes. Water molecules entering the interface also increase, and the interface Binding energy gradually decreases. With the further increase of the electric field strength, the water entering the epoxy resin gradually becomes more and more, the degree of hydrolysis of the epoxy resin deepens and the holes increase. Under the strong electric field, water molecules are more likely to break through the barriers of the epoxy resin and its hydrolysates and enter the interface, which greatly reduces the interface Binding energy and severely damages the epoxy resin/glass fiber interface.

Fig. 28 Electric field intensity

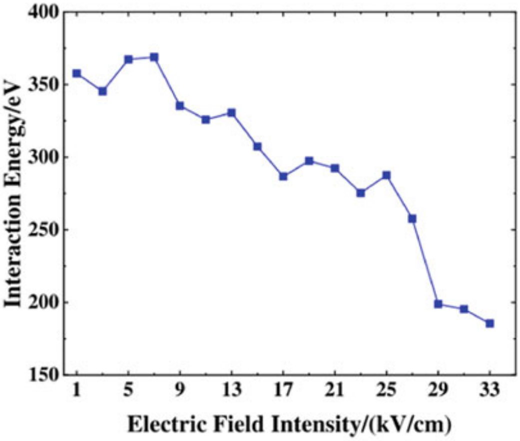

(a) Water Molecular Environment

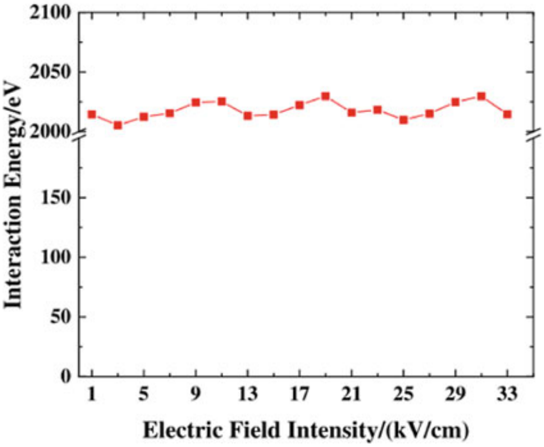

(b) Dry environment

4.2.3 Microstructural Changes

As the electric field strength increases, the internal moisture of the epoxy resin gradually increases and hydrolysis occurs. Therefore, this section follows the method in last chapter and characterizes the degree of hydrolysis reaction based on the number of ester groups. The results are shown in Fig. 29.

From Fig. 29, it can be seen that as the electric field intensity increases, the overall number of ester groups shows a decreasing trend. When the electric field intensity is less than 9 kV/cm, there is no significant change in the number of ester groups. When the electric field intensity is greater than 9 kV/cm, the number of ester groups

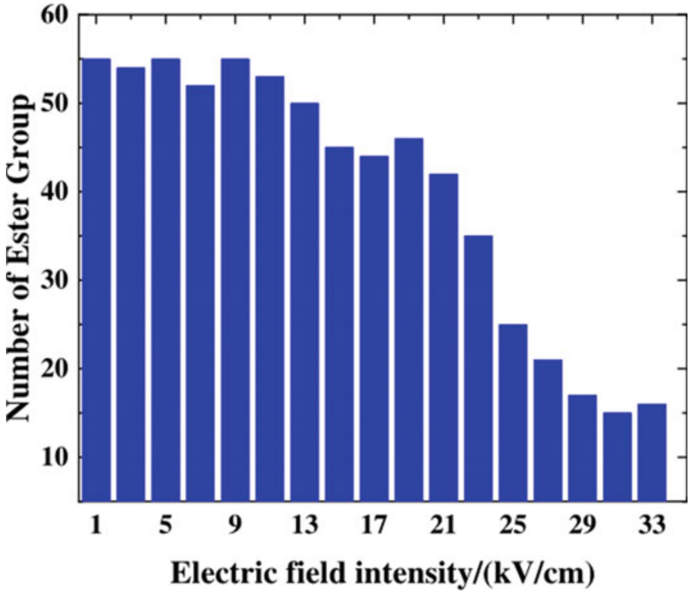

Fig. 29 Changes in the number of ester groups

gradually decreases. When the electric field intensity is greater than 19 kV/cm, the number of ester groups rapidly decreases. When the electric field intensity is greater than 25 kV/cm, the trend of decreasing the number of ester groups slows down and remains basically stable.

Based on the analysis of the changes in interface results in the previous text, it is found that when the electric field strength is below 9 kV/cm, the water molecules have not yet reached the interior of the epoxy resin, the degree of hydrolysis reaction is relatively low, and the number of ester groups remains basically unchanged. When the electric field intensity exceeds 9 kV/cm, water molecules reach the interior of the epoxy resin and begin to undergo hydrolysis, resulting in a decrease in the number of ester groups. When the electric field is greater than 19 kV/cm, a large amount of water molecules enter the interior of the epoxy resin, causing a large number of ester groups to fracture. As the electric field intensity continues to increase, when it reaches 25 kV/cm, most of the water molecules have reached the surface of silica with the strong electric field effect, so the ester base amount is relatively stable.

4.2.4 Hydrogen Bond Changes

According to the analysis results in Sect. 4.2.1, when the electric field strength is high, a large number of water molecules pass through the epoxy resin and reach the interface area. According to the analysis of hydrogen bond formation, oxygen atoms in water molecules are prone to form hydrogen bonds with hydrogen atoms on the

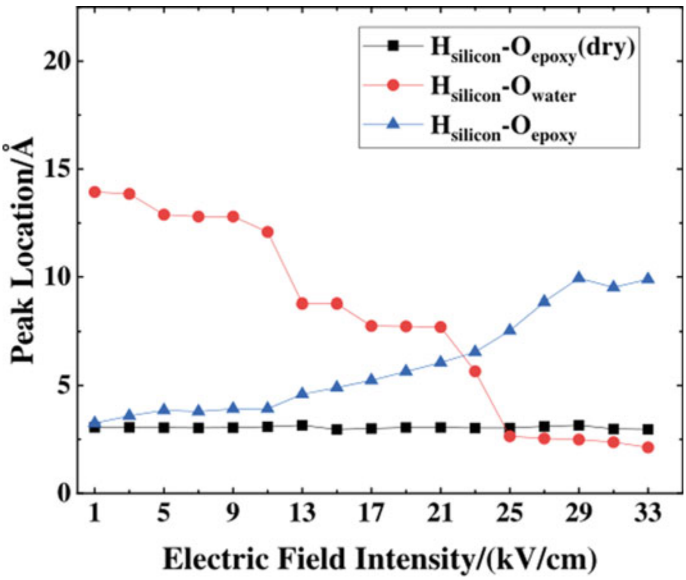

Fig. 30 RDF peak distance

surface of silica, hindering the formation of hydrogen bonds between epoxy resin and silica, and damaging the interface bonding. Therefore, consistent with the method in Sect. 3, RDF analysis can be performed on the relevant atoms in the interface region under electric field environment. This section also conducts RDF analysis on the relevant atoms, and the results are shown in Fig. 30.

From the results in Fig. 30, it can be seen that the distance from the peak RDF of $H_{silicon}$-O_{epoxy} (dry) in a dry environment remains basically unchanged with the change of electric field intensity. This indicates that the distance between epoxy resin and silica in a dry environment does not change significantly. This is consistent with the conclusion that electric field intensity has no significant effect on the epoxy resin/glass fiber interface in a dry environment when analyzing the changes in interface structure in the previous section. In the water molecule environment, as the electric field intensity increases, the distance from the peak RDF of $H_{silicon}$-O_{epoxy} gradually increases, while the distance from the peak RDF of Hsilicon-O_{water} gradually decreases. In addition, in the water molecule environment, when the electric field intensity exceeds 25 kV/cm, the RDF peak distance of $H_{silicon}$-O_{water} is already smaller than that of $H_{silicon}$-O_{epoxy}. This indicates that in the water molecule environment, when the electric field intensity exceeds 23 kV/cm, hydrogen bonds will preferentially form between the water molecule and silicon dioxide.

In summary, as the electric field strength increases, water molecules gradually accumulate at the interface and preferentially form hydrogen bonds with SiO_2, thereby hindering the formation of hydrogen bonds between SiO_2 and epoxy resin, resulting in a decrease in the degree of bonding between epoxy resin and glass fiber.

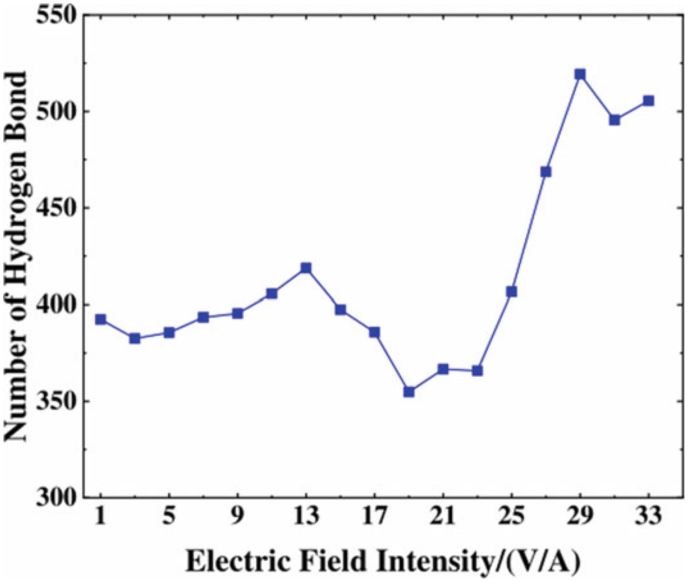

Fig. 31 Changes in the number of hydrogen bonds at the interface under different environments

Therefore, analyzing the changes in the number of hydrogen bonds can help clarify the destructive effect of water intrusion on the epoxy resin/glass fiber interface under the action of an electric field. Figure 31 show the changes in the number of hydrogen bonds when the electric field changes.

From Fig. 31, it can be seen that in the water molecular environment, the overall number of hydrogen bonds shows a trend of first decreasing and then increasing. When the electric field intensity is between 1–13 kV/cm, the number of hydrogen bonds in the interface remains basically stable. When the electric field intensity is greater than 13 kV/cm, the number of hydrogen bonds decreases. When the electric field intensity is greater than 19 kV/cm, there is a significant increase in the number of hydrogen bonds. When the electric field intensity is greater than 29 kV/cm, the number of hydrogen bonds reaches its peak and remains stable.

Based on the analysis of the above rules, it can be concluded that when the electric field strength is low, the main form of hydrogen bonding at the interface is O_{epoxy}-Hsilicon. However, there is less O_{epoxy} near the interface area, resulting in less hydrogen bonding with SiO_2. Additionally, there are fewer water molecules at the epoxy resin and interface, which do not participate in the formation of hydrogen bonds. As the electric field strength increases, water molecules enter the interior of the epoxy resin. At this point, a small amount of water molecules reach the bottom epoxy resin and undergo hydrolysis reactions with it, breaking some hydrogen bonds. Most water molecules are blocked by the hydrolysis products of the epoxy resin and cannot continue to move. When the electric field strength continues to increase, water molecules break through the barrier of epoxy resin hydrolysis products and reach the surface of silica, forming hydrogen bonds with them. The higher the electric field strength, the more water molecules reach the surface of silica, and the more hydrogen bonds can be formed. The final manifestation is that there are more hydrogen bonds formed when the electric field intensity is high than when the electric field intensity is low.

In summary, when the environmental temperature reaches the hydrolysis temperature of the epoxy resin, water molecules migrate directionally to the interior of the epoxy resin under the action of an electric field, causing the epoxy resin to undergo hydrolysis. When water molecules reach the interface area and form hydrogen bonds with silica, the formation of hydrogen bonds between epoxy resin and SiO_2 is hindered, which leads to the reduction of interface Binding energy.

4.3 Summary

In this chapter, the influence of water intrusion on the epoxy resin/glass fiber interface under the effect of electric field was studied, and the change laws of interface structure, interface Binding energy, ester group number, hydrogen bond number, etc. were emphatically analyzed. From the results of this chapter, it can be seen that: (1) In a dry environment, the electric field has no significant effect on the epoxy resin/glass fiber interface; (2) In the environment of water molecules, an electric field will cause water molecules to migrate directionally through epoxy resin to the interface, and when the environmental temperature reaches the hydrolysis temperature of epoxy resin, it will cause the epoxy resin to undergo hydrolysis and generate holes; (3) The hydrolysis of epoxy resin and the generation of holes promote the migration process of water molecules, and under strong electric fields, water molecules are more likely to break through the binding of epoxy resin and its hydrolysis products and migrate to the interface; (4) As the electric field strength increases, the moisture at the interface gradually increases, promoting the hydrolysis of epoxy resin and hindering the formation of hydrogen bonds between epoxy resin and silica molecules. Under the combined effect of the above effects, the epoxy resin/glass fiber interface gradually damages.

5 Effect of Moisture Intrusion on Epoxy Resin/Glass Fiber Interface Considering Synergistic Effects of Temperature and Electric Field

The temperature and electric field at the insulator rod are variable due to environmental factors and local defects. Therefore, in this chapter, based on the previous paper, molecular simulation techniques will be used to investigate the characteristics of the moisture intrusion on the epoxy resin/glass fiber interface characteristics when considering the synergistic effect of temperature and electric field. Combining the principles of temperature and electric field settings in Sects. 3 and 4, this chapter determines that the temperature range of the simulation experiment is 213–853 K, with an interval of 80 K; the electric field strength range is 1–33 kV/cm, with an interval of 4 kV/cm.

5.1 Considering the Synergistic Effect of Temperature and Electric Field, the Influence of Water Intrusion on the Interface of Epoxy Resin/Glass Fiber Was Analyzed

5.1.1 Interface Structure Changes

Firstly, the epoxy resin/glass fiber interface in a water molecule environment is analyzed when the temperature and electric field change synergistically. Figure 32 shows the results of the interfacial structure changes in the water molecule environment at temperatures of 213 K, 453 K, 613 K, and 853 K with electric field strengths of 1 kV/cm, 13 kV/cm, 21 kV/cm, and 33 kV/cm, respectively.

The results in Fig. 32 can be summarized as follows:

At low temperatures (typically 213 K), with the increase of electric field strength, water molecules can migrate to the surface of epoxy resin, but the structure of epoxy resin and epoxy resin/glass fiber interface do not change significantly.

At medium and high temperatures (typically 431 K), the hydrolysis of the epoxy resin gradually appears, resulting in the expansion of the epoxy resin structure, and along with the increase in the electric field strength, water is more likely to migrate to the interior of the epoxy resin and the interface, resulting in the destruction of the structure of the epoxy resin and the interface between the epoxy resin and the glass fibers.

At high temperatures (typically 613 K), the internal and interface structures of epoxy resin are basically similar under different electric fields, and the effect of the electric field on the epoxy resin/glass fiber interface is relatively small, even if the strength of the electric field is low, the moisture exists more around the epoxy resin and at the epoxy resin/glass fiber interface.

For comparison, this paper gives the temperature and electric field in Fig. 32, dry environment, epoxy resin/glass fiber interface structure change rule, the results are shown in Fig. 33:

In the dry environment, the electric field strength had no significant effect on the epoxy resin/glass fiber interface at different temperatures.

In dry environments, as the temperature rises, the holes in epoxy resin increase gradually.

In summary, when moisture intrusion occurs, the epoxy resin/glass fiber interface structure will be co-influenced by the electric field and the temperature. At lower

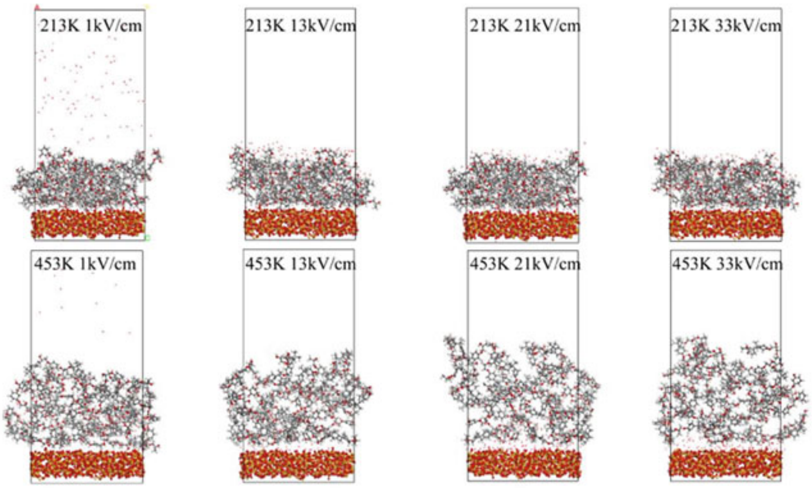

(a) 213K-453K

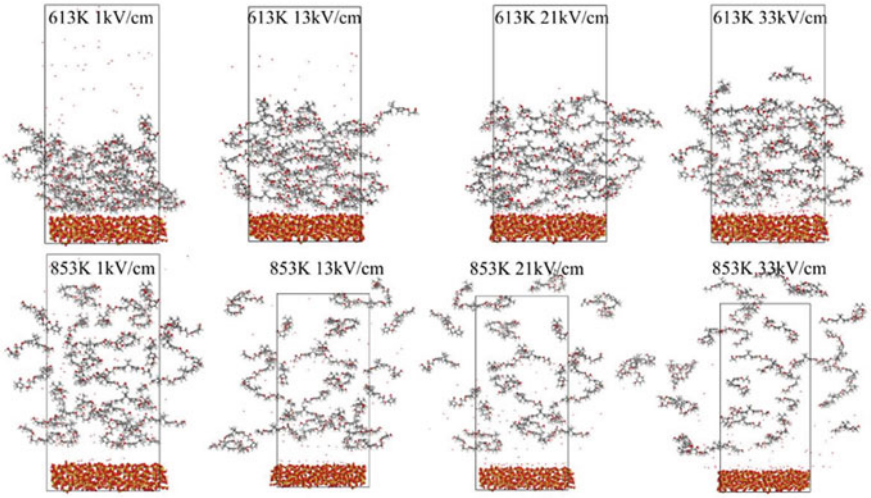

(b) 213K-853K

Fig. 32 Interfacial structure change underwater molecule environment

temperatures (below the hydrolysis temperature), the electric field has no significant effect on the interfacial structure. When the temperature is higher than the hydrolysis temperature, the electric field will make the water molecules move directionally and promote the migration process of water molecules inside the epoxy resin, therefore, the electric field promotes the destruction process of water on the interface at this temperature. When the temperature is further increased, the molecular thermal movement is intensified, the migration of water will be mainly affected by the molecular thermal movement, and the hydrolysis of the epoxy resin is also stronger, at the

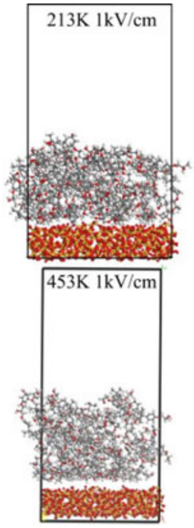

(a) 213K-453K

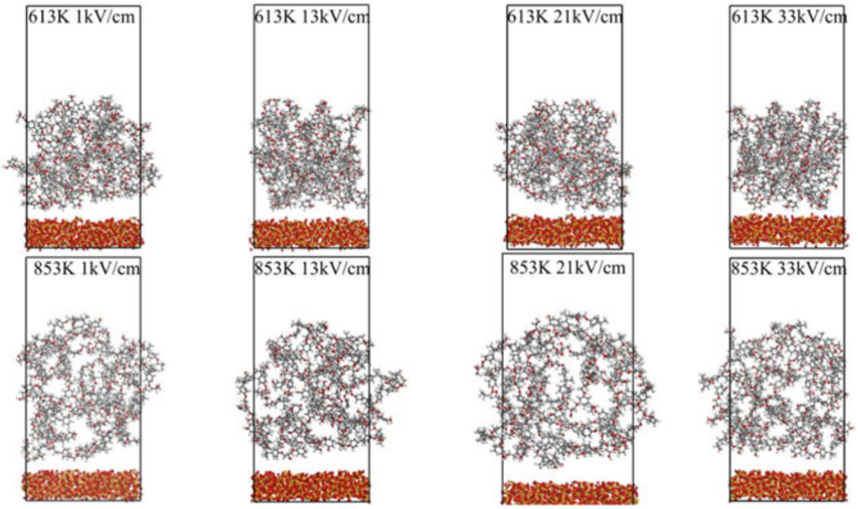

(b) 613K-853K

Fig. 33 Changes in the interfacial structure under a dry environment

same time, the thermal effect under the action of the epoxy resin itself will produce cavities, the structure of the epoxy resin expands, resulting in a lower temperature when the interfacial region of the epoxy resin is closer to the interface. And when the temperature is further increased, at this time the epoxy resin can epoxy resin/glass fiber interface will be extremely easy to be damaged, at this time the electric field on the epoxy resin/glass fiber interface structure influence effect will become weaker.

5.1.2 Interface Adhesion Ability

In this paper, we analyze the adhesion capacity of epoxy resin/glass fiber interface under a water molecule environment at different temperatures and electric fields. Consistent with the analytical approach in Sects. 3 and 4, the interface adhesion capacity is still characterized by calculating the interface binding energy. Also, for comparison, the epoxy resin/glass fiber interface bonding energies are given together in this paper for dry environments.

As can be seen in Fig. 34, the interface binding energy in the water molecule environment decreases at different temperatures and with the increase of electric field strength. Among them, the interface bonding energies at low and high temperatures (213, 693, 773, 853 K) are lower than those at other temperatures. At 453–613 K, the decrease of interface binding energy with the increase of electric field strength is larger, while the decrease of interface binding energy with the increase of electric field strength is smaller at 213 K and 693–853 K, and the higher the temperature, the slower the decrease of interface binding energy with the increase of electric field.

Combined with the analysis of the interfacial structure change in Sect. 5.1.1, it can be seen that the effect of electric field on the interface bonding energy is mainly due to the directional movement of water molecules by the electric field, which will cause water molecules to enter the internal cavities of the epoxy resin and lead to its expansion, and also trigger the hydrolysis of the epoxy resin and the formation of hydrogen bonds with silica. Therefore, the interface binding energy tends to decrease as the electric field strength increases. The reason for the smaller magnitude of change in interface binding energy at low temperatures may be that the

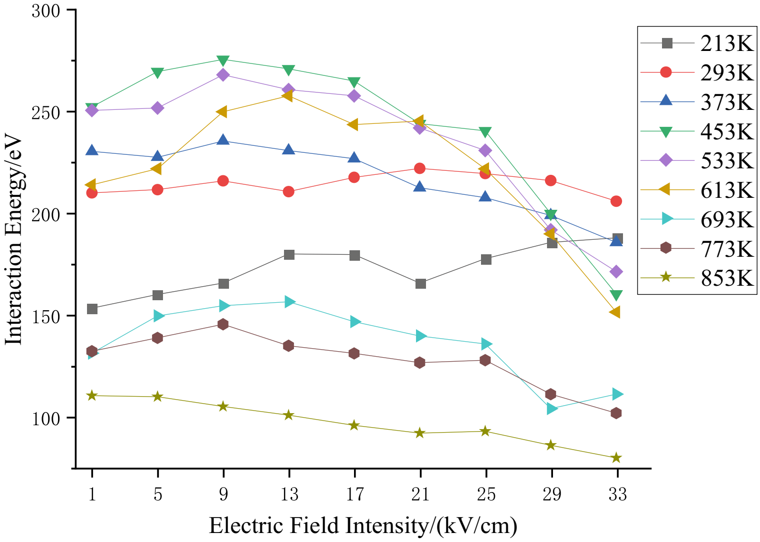

Fig. 34 The change of interface binding energy in the water molecular environment

epoxy molecules are more compact in this environment due to the lower temperatures, and thus it is difficult for water molecules to pass through the epoxy to enter the interfacial region even at higher electric fields. The movement of water molecules is mainly affected by temperature under high temperature environment, the electric field for water molecules is small, resulting in high-temperature environments interface binding energy with the increase in the electric field does not change much. In the temperature range 453–613 K, water molecules are similarly affected by temperature and electric field, and are able to diffuse with the increase of temperature and move along the direction of electric field. In this temperature environment and the electric field strength is low, a large number of water molecules into the interior of the epoxy resin and hydrolysis reaction, but due to the low electric field, the water molecules by the electric field is less affected by the electric field, it is difficult to continue to move to the surface of the SiO_2, resulting in a large number of water molecules in the interior of the epoxy resin cavities build up and trigger the expansion of the epoxy resin, so that the interface region of the epoxy resin is closer to the SiO_2, resulting in the improvement of interface bonding properties in this environment, when the electric field strength continues to rise, water molecules continue to move in the environment of the strong electric field and attach to the surface of the silicon dioxide, which affects the interface bonding performance. It shows that the change of interface binding energy is more obvious with the increase of electric field strength in this temperature environment, the interface binding energy is higher when the electric field is lower, and the interface binding energy decreases obviously when the electric field is higher.

As can be seen from Fig. 35, the interface binding energy is higher in a dry environment than in a water molecule environment. When the temperature is fixed, the interface binding energy does not change significantly with the gradual increase of electric field strength. When the temperature is 213 K, the interface binding energy is lower.

In summary, when the temperature is fixed, the gradual increase of the electric field strength mainly affects the movement law of water molecules. It has little effect on epoxy resin and silica. At low and high temperatures, the interface bonding energy is generally lower but less affected by the electric field; at other temperatures, the interface bonding energy is generally higher but more affected by the electric field.

5.1.3 Microstructure Change

To further analyze the hydrolysis reaction law of the epoxy resin when the temperature and electric field were changed synergistically, the number of ester groups inside the system at each temperature and electric field was counted, and the results are shown in Fig. 36.

Comparison by the 213 and 293 K in Fig. 36 when the change rule of ester group can be seen; in the low temperature, the number of ester group in the system is basically stable, and the value is higher, and with the electric field strength is not related. This analysis shows that at low temperatures, there is no obvious hydrolysis

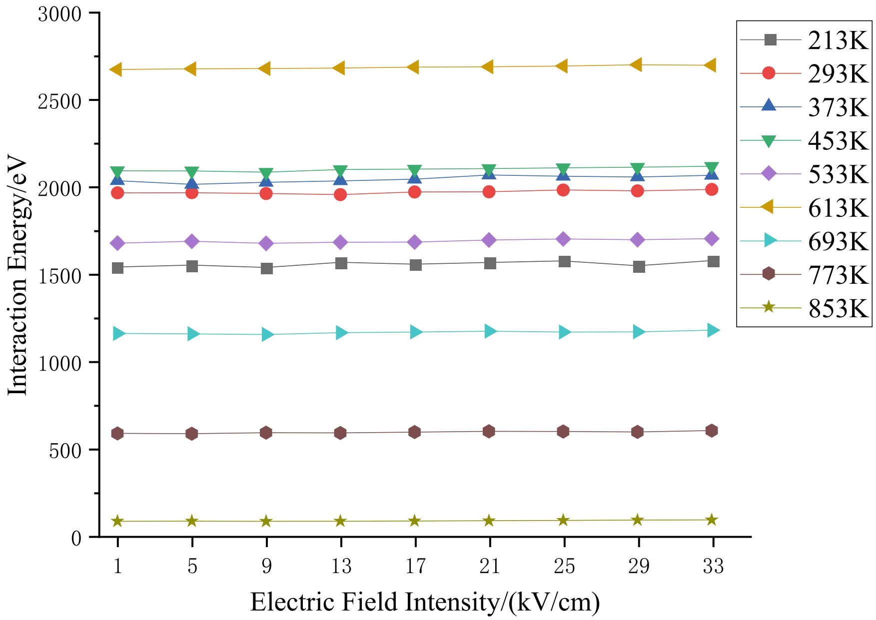

Fig. 35 The change of interface binding energy in a dry environment

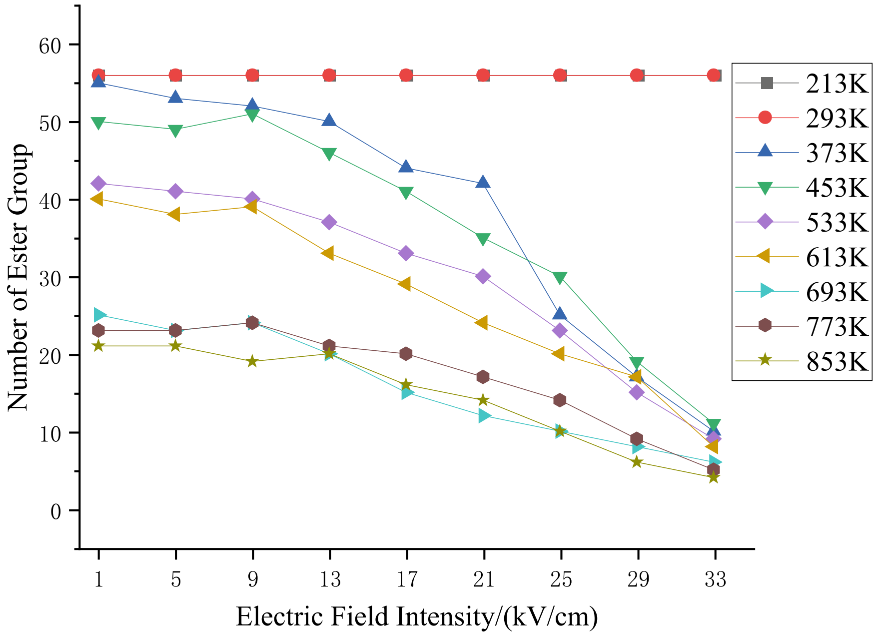

Fig. 36 Changes in the number of ester groups

reaction, so the electric field and temperature have no obvious effect on the ester group.

Comparison of other temperatures in Fig. 36 under the change rule of the ester group can be seen, when the temperature is not lower than 373 K, with the increase of electric field strength, the number of ester groups gradually declines. Analysis of this can be seen, water molecules will move directionally under the action of the electric field, resulting in water molecules that can more easily enter the rest of the epoxy resin molecules that did not react and react with them.

Comparison of Fig. 36 in 693, 773, and 853 K when the change rule of ester group can be seen, high-temperature environment, due to the hydrolysis of epoxy resin has been very intense, so at this time the temperature on the number of ester group has no obvious effect.

In summary, when the ambient temperature does not reach the hydrolysis temperature, the change of the electric field has no obvious effect on the number of ester groups; when the ambient temperature exceeds the hydrolysis temperature, the increase of the electric field will promote the migration of water, and exacerbate the hydrolysis behavior of the epoxy resin; after further elevating the temperature, the electric field will play a dominant role in the migration of water molecules, at this time, the epoxy resin will be hydrolyzed under the action of water molecules, which will lead to the destruction of the interface.

5.1.4 Hydrogen Bond Changes

Combined with the changes in the interfacial structure in Sect. 5.2.1, it can be seen that, except for the lower temperature when the number of water molecules reaching the interfacial region is very small, there are different numbers of water molecules attaching to the silica interface and forming hydrogen bonding with it in the rest of the temperature environments. Therefore, it is necessary to carry out an RDF analysis of O_{water}-$H_{silicon}$ and O_{epoxy}-$H_{silicon}$ at the interfaces under different environments, and the results of the RDF analysis are shown in Fig. 37.

From Fig. 37a, it can be seen that in the low-temperature environment (213–293 K), the peak distance of O_{epoxy}-$H_{silicon}$ is stable with the increase of the electric field strength; when the temperature is greater than 293 K, with the increase of the electric field strength, the increase of the peak distance of O_{epoxy}-$H_{silicon}$ is faster and faster; when the temperature is greater than 773 K, the peak distance is increasing rapidly. As can be seen from Fig. 37b, the O_{epoxy}-$H_{silicon}$ peak distance at a gradually increasing distance and fluctuates with increasing temperature. As can be seen in Fig. 37c, the O_{water}-$H_{silicon}$ peak distance at temperatures below 293 K at a gradually decreasing distance to near 8 Å and then remains stable. The O_{water}-$H_{silicon}$ peak distance decreases to around 2.5 Å at temperatures greater than 373 K and then stabilizes, but the O_{water}-$H_{silicon}$ peak distance varies at lower field strengths: at 373–453 K, the peak distance decreases from the higher value to around 2.5 Å; at 533–693 K, the peak distance reaches around 2.5 Å after a small decrease; at 773–853 K, the peak distance does not start to decrease until the electric field strength is at 13 kV/cm,

Fig. 37 RDF analysis of interfaces in different environments

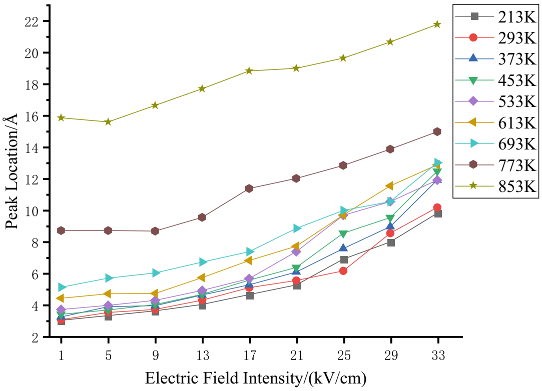

(a) O_{epoxy}-$H_{silicon}$

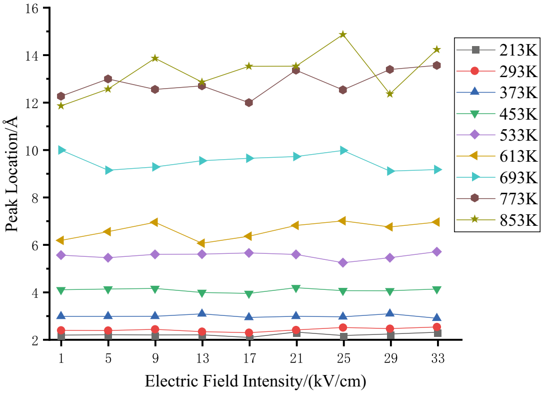

(b) O_{epoxy}-$H_{silicon}$(dry)

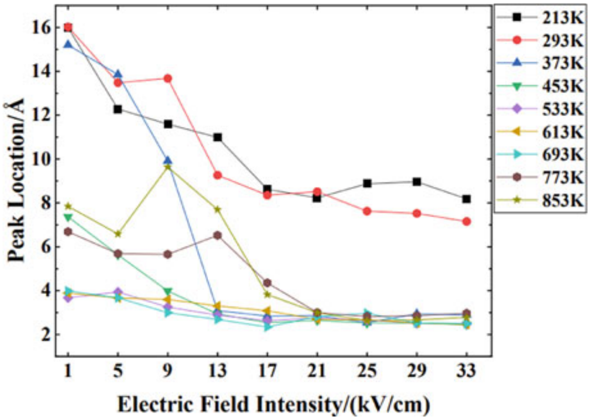

(c) O_{water}-$H_{silicon}$

and the peak distance decreases to 2.5 Å when the electric field strength increases to 21 kV/cm. The peak distance decreases to 2.5 Å when the electric field strength increases to 21 kV/cm.

Combining the study in Sect. 5.2.1 with Fig. 37a, it can be seen that at low temperatures, water molecules are unable to enter the interfacial region, and the epoxy resin is kept at a distance from SiO_2. When the temperature rises, water molecules can enter the epoxy resin with the electric field and make it crack and expansion, epoxy resin and silica are keep at a distance when the electric field strength is low, with the increase of the electric field, the hydrolysis reaction is more intense, at this time, the distance between the epoxy resin and the silica has increased, and some of the water molecules arrive at the interface area will also make the interface separation. At temperatures greater than 773 K, the epoxy resin is dispersed into the spatial region by the effects of temperature, increasing the distance to the peak significantly.

Combining the study in Sect. 5.2.1 with Fig. 37b, it can be seen that the epoxy resin swells in a dry high-temperature environment. The groups inside the epoxy resin affected by high temperature vibrate violently, resulting in large fluctuations in the peak distance from the peak in the high-temperature environment.

Combined with the previous study of interfacial structure analysis and Fig. 37c, it can be seen that at low temperature, water molecules can not enter into the epoxy resin, and can only attach to the surface of the epoxy resin. As the temperature rises above 373 K, water molecules are able to enter the hydrolyzed epoxy resin and stay inside the cavities, causing the epoxy resin to expand as a whole, and as the electric field increases further, the water molecules can reach the surface of the silica. When the temperature is above 533 K, the epoxy resin molecules are subjected to hydrolysis and swelling to produce cavities, and the water molecules reach the interfacial region under the influence of a stronger electric field and temperature. As the temperature continues to rise, water molecules are only able to reach the interfacial region in environments with higher electric field strengths.

The synergistic effect of electric field and temperature on the water molecules invading the interface is a complicated mechanism, in which the change of hydrogen bonds affects the bonding performance of the interface under different environments. Therefore, in this paper, the method of counting the number of hydrogen bonds in the interface is also used to investigate the bonding degree of the interface under different environments. The variation in the number of hydrogen bonds is shown in Fig. 38.

As can be seen from Fig. 38, the number of hydrogen bonds did not change significantly when the temperature was 213–293 K; when the temperature was 373–613 K, the trend of the number of hydrogen bonds with the increase of the electric field strength was a small increase when the electric field strength was 9–13 kV/cm, and then decreased, and then increased, and then reached the lowest point at 21 kV/cm. As the electric field strength continues to increase, there is a large overall decrease in the number of hydrogen bonds; as the temperature increases, the curve of the number of hydrogen bonds with the electric field strength flattens out.

Combined with the structural change of the interface in Sect. 5.2.1 and the RDF analysis, it can be seen that in the lower temperature environment, there is no water

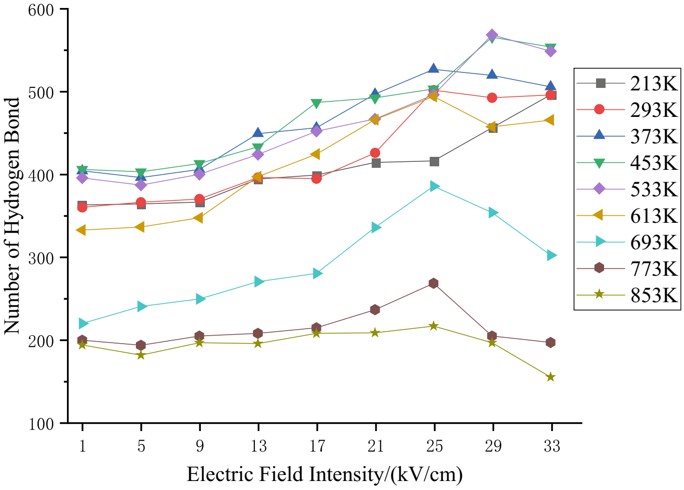

Fig. 38 The change of the number of hydrogen bonds at the interface under the environment of water molecules

molecule entering into the interface region, so the number of hydrogen bonds has not changed significantly. The temperature continued to increase above 373 K. At the lower electric field strength, water molecules hydrolyzed with the top epoxy resin, resulting in the expansion of the epoxy resin after the creation of cavities at the top of the epoxy resin, and the epoxy resin in the interface region bulged out to the SiO_2, and hydrogen bonds was formed, at which time the number of hydrogen bonds increased slightly. With the increase of the electric field, a small number of water molecules into the bottom of the epoxy resin area and hydrolysis reaction with it, destroying part of the hydrogen bond, most of the water molecules by the epoxy resin hydrolysis products blocking, can not reach the SiO_2 surface, at this time, the number of hydrogen bonds show a gradual decrease in the trend. When the electric field strength is large, the water molecules break through the barrier in the strong electric field environment and continue to move to the surface of SiO_2 and form hydrogen bonds with it, at which time the trend of the number of hydrogen bonds shows a gradual increase. When the temperature is high, epoxy resin due to hydrolysis reaction and high temperature, gradually cracked and dispersed to the space region, at this time, the number of hydrogen bonds drops dramatically, the interface is damaged.

In summary, the water molecules in the electric field and temperature under the synergistic effect of the law of motion and distribution of the main: in the low temperature and low electric field environment, water molecules are mainly distributed in the space region; when the electric field is raised, the water molecules move directionally to the surface of the epoxy resin and cannot enter the inside of the epoxy resin. When the temperature is raised to 373 K and above, the water molecules still exist in the space region under the low electric field environment. When the electric field strength increases, the water molecules begin to hydrolyze with the top epoxy resin first, resulting in part of the cavity, and other water molecules continue to enter the inside of the epoxy resin resulting in expansion of the epoxy resin, but due to the low electric field, some of the water molecules are blocked by the hydrolysis products of the epoxy resin, and can't continue to move, at this time, a large number of water molecules gathered in the inside of the epoxy resin. When the electric field strength continues to increase, the water molecules continue to move under the action of the strong electric field until they reach the surface of SiO_2. When the temperature is further increased, the epoxy resin by the influence of high temperature first generated cavities, so that most of the water molecules can enter the epoxy resin and hydrolysis reaction, hydrolysis reaction of the epoxy resin is more relaxed, so that more water molecules can reach the surface of the SiO_2. When the temperature is further increased, the movement of water molecules at this time is mainly affected by the temperature, part of the water molecules exist in the space, part of the water molecules into the epoxy resin and hydrolysis reaction occurs, resulting in the epoxy resin is cracked and dispersed in the space region, and a part of the water molecules attached to the surface of SiO_2.

5.2 Destruction Mechanism of Moisture on Epoxy Resin/Glass Fiber Interface of Composite Insulator Rod

The process of moisture intrusion at the epoxy/fiberglass interface of composite insulator mandrels considering the synergistic effects of temperature and electric field is summarized.

As the temperature rises, the epoxy resin expands and creates cavities, while the water molecules move irregularly in response to the heat. When the temperature reaches 373 K, the epoxy resin and water molecules will produce a hydrolysis reaction, the hydrolysis reaction further caused by the epoxy resin structure, resulting in an increase in the number of cavities within the epoxy resin, and leading to a decrease in the interfacial bonding properties. In addition, due to the increase of cavities inside the epoxy resin, the migration process of water molecules to the epoxy resin/glass fiber interface can be facilitated, and the water molecules at the interface will first form hydrogen bonds with SiO_2 and hinder the formation of hydrogen bonds between epoxy resin-SiO_2. Under the combined effect of hydrolysis and hydrogen bonding disruption, the bonding ability of the epoxy resin/glass fiber interface decreases, and the interface is gradually destroyed.

The migration process of water inside the epoxy resin is affected by both temperature and electric field. When the temperature is low, the water molecules can be directed to move inside the epoxy resin by increasing the strength of the electric field, but because the temperature is too low to reach the hydrolysis conditions of the epoxy resin, and the structure of the epoxy resin is relatively dense, it is difficult for the water molecules to destroy the epoxy resin and the structure of the interface even under the action of the electric field, so there is no significant effect of the electric field on the interface of the epoxy resin/fiberglass when the temperature is low.

With the increase of temperature, when the temperature reaches the hydrolysis temperature of the epoxy resin (the simulation result in the paper is 373 K), under the action of low electric field, the water molecules are still dominated by the irregular thermal movement, and the number of water molecules entering the interior of the epoxy resin is relatively small. However, as the electric field strength increases, the electric field force on the water molecules gradually increases, which leads to more water molecules attaching to the surface of the epoxy resin or entering into the interior of the epoxy resin, and hydrolyzes the epoxy resin. Under the combined effect of hydrolysis reaction and spontaneous expansion of epoxy resin at high temperature, the number of cavities inside the epoxy resin increases. The increase of cavities and promote the migration of water inside the epoxy resin, but the epoxy resin and its hydrolysis products on the migration of water molecules have a certain impediment to the water molecules, when the water molecules are not enough to break through the above impediment to the electric field, the number of water molecules into the interface at the interface did not significantly increase, so the interface bonding energy decreases slowly at this time. As the field strength is further increased, the majority of water molecules can break through the epoxy resin and its hydrolysis products and reach the interface. Hydrolysis of the epoxy resin at the interface, and the presence of water molecules destroy the formation of hydrogen bonds between the epoxy resin and SiO_2, which further reduces the degree of interface bonding. Therefore, at this time, the increase of electric field strength has an accelerating effect on the destruction of the epoxy resin/glass fiber interface.

With the further increase of temperature, the irregular thermal movement of water molecules is the dominant factor for its migration, and the degree of hydrolysis damage to the epoxy resin has been more serious, the interface can be basically destroyed, so at this time to increase the electric field on the epoxy resin/glass fiber interface bonding degree has no significant effect.

In summary, when considering the synergistic effect of electric field and temperature, the damage mechanism of epoxy resin/glass fiber interface by moisture intrusion is analyzed from the molecular nanoscopic level as follows:

Temperature causes the epoxy resin to expand, and as the temperature rises, there are more cavities within the epoxy resin, which affects the bonding properties of the epoxy resin/glass fiber interface;

The destructive effect of moisture on the epoxy resin/glass fiber mainly exists: moisture makes the epoxy resin undergo hydrolysis, and moisture at the interface affects the formation of hydrogen bonds between the epoxy resin/glass fiber;

The electric field itself has no significant effect on the epoxy resin/glass fiber interface, but the electric field will cause the moisture to migrate directionally. When the temperature reaches the hydrolysis temperature of the epoxy resin, increasing the electric field can accelerate the migration process of the moisture and aggravate the damage process of the moisture on the body of the epoxy resin and the interface of the epoxy resin/glass fiber;

When the temperature is high enough, the hydrolysis reaction of the epoxy resin itself has been more obvious, and at this time increasing the electric field on the epoxy resin/glass fiber interface damage process has no obvious effect.

5.3 Summary

This section investigates the electro-thermal synergetic environment at the epoxy resin/fiberglass interface based on the studies in Sects. 3 and 4. At the beginning of this chapter, the selection of parameters is first described. Subsequently, the study of interfacial structure change, interface binding energy, number of ester groups, radial distribution function, number of hydrogen bonds, and the damage mechanism of moisture intrusion into the epoxy/fiberglass interface are summarized. The results show that the interface under an electrothermal synergistic environment undergoes a hydrolysis reaction with increasing temperature epoxy resin and the interface separates under high temperature environment. Under the influence of an electric field, water molecules begin to enter into the epoxy resin in large quantities in the internal and interfacial areas, which promotes the expansion and hydrolysis of the epoxy resin. From the molecular structure microscopic changes, the mechanism of the synergistic effect of the electric field and temperature on the interface and water molecules can basically be considered as the superposition of the separate effects of the electric field and temperature.

References

1. Xie, J., Chen, K., Yan, M., et al.: Effect of temperature and water penetration on the interfacial bond between epoxy resin and glass fiber: a molecular dynamics study. J. Mol. Liq. **350**, 118424 (2022)
2. Yang, C., Xu, C., Yan, N., et al.: The impact of water intrusion into the crimping interface on composite insulators. Power Grid Technol. **43**(5), 1841–1848 (2019)
3. Wang, Y., Liu, Y., Fan, H., et al.: Water boiling aging characteristics of the interface between silicone rubber and alicyclic epoxy resin composite insulators. High Volt. Technol. 1–8
4. Fan, H., Liu, Y., Wang, L., et al.: The effect of epoxy resin insulator mold joint on water diffusion test. Power Grid Technol. 1–8
5. Rain, P., Brun, E., Guillermin, C., et al.: Experimental model of a quartz/epoxy interface submitted to a hygrothermal ageing: a dielectric characterization. IEEE Trans. Dielectr. Electr. Insul. **19**(1), 343–351 (2012)
6. Li, Y., Li, R., Huang, L., et al.: Effect of hygrothermal aging on the damage characteristics of carbon woven fabric/epoxy laminates subjected to simulated lightning strike. Mater. Des. **99**, 477–489 (2016)
7. Deng, S.: Study on the Assembly Behavior and Interfacial Properties of Grafted Polymer Chains at the Fiber/Resin Interface. East China University of Science and Technology, Shanghai (2013)
8. Patel, S.R., Case, S.W.: Durability of hygrothermally aged graphite/epoxy woven composite under combined hygrothermal conditions. Int. J. Fatigue **24**(12), 1295–1301 (2002)

9. Xu, R., Cui, C., Wang, J., et al.: The effect of high-temperature and high-pressure humid heat treatment on the electrical properties of epoxy resin composite materials. Fiber Compos. Mater. **25**(1), 32–34 (2008)
10. Huang, Y., Yi, L.: Effect of thermal aging on the dielectric properties of epoxy resin in dry-type transformers. Insul. Mater. **60**(009), 53–56 (2016)
11. Yin, Q., Gao, W., Ye, K., et al.: The influence of different effects on the development of electrical tree branches in insulating materials. High Volt. Technol. (4), 766–771 (2009)
12. Bao, L.R., Yee, A.F.: Moisture diffusion and hygrothermal aging in bismaleimide matrix carbon fiber composites-Part I: uni-weave composites. Compos. Sci. Technol. **62**(16), 2099–2110 (2002)
13. Bao, L.R., Yee, A.F.: Effect of temperature on moisture absorption in a bismaleimide resin and its carbon fiber composites. Polymer **43**(14), 3987–3997 (2002)
14. Haghighi-Yazdi, M., Lee-Sullivan, P.: FTIR analysis of a polycarbonate blend after hygrothermal aging. J. Appl. Polym. Sci. **132**(3) (2015)
15. Xiao, G.Z., Delamar, M., Shanahan, M.E.R.: Irreversible interactions between water and DGEBA/DDA epoxy resin during hygrothermal aging. J. Appl. Polym. Sci. **65**(3), 449–458 (2015)
16. Sun, B., Li, Y.: Study on the damp heat aging behavior and durability prediction of composite materials. Fiberglass/Compos. Mater. (4), 28–34 (2013)
17. Wang, X., Liang, G., Zhang, W., et al.: The effect of damp heat aging on the properties of high performance composite materials. Solid Rocket Technol. **29**(4), 301–304 (2006)
18. Soles, C.L., Yee, A.F.: A discussion of the molecular mechanisms of moisture transport in epoxy resins. J. Polym. Sci. Part B: Polym. Phys. **38**(5), 792–802 (2015)
19. Zhou, A., Tam, L.H., Yu, Z., Lau, D.: Effect of moisture on the mechanical properties of CFRP-wood composite: an experimental and atomistic investigation. Compos. Part B: Eng. **71**, 63–73 (2015)
20. Tam, L.H., Wu, C.: Molecular mechanics of the moisture effect on epoxy/carbon nanotube nanocomposites. Nanomaterials **7**(10), 324–343 (2017)
21. Tam, L.H., Lau, D.: Moisture effect on the mechanical and interfacial properties of epoxy-bonded material system: an atomistic and experimental investigation. Polymer **57**, 132–142 (2015)
22. Pandiyan, S., Krajniak, J., Samaey, G., et al.: A molecular dynamics study of water transport inside an epoxy polymer matrix. Comput. Mater. Sci. **106**, 29–37 (2015)
23. Lee, S.G., Ji, I.C., Koh, W., et al.: Effect of temperature on water molecules in a model epoxy molding compound: molecular dynamics simulation approach. IEEE Trans. Compon. Packag. Manuf. Technol. **1**(10), 1533–1542 (2011)
24. Xiao, Y., Xian, G.: Effects of moisture ingress on the bond between carbon fiber and epoxy resin investigated with molecular dynamics simulation. Polym. Compos. **1**, 1–10 (2017)
25. Lee, S.G., Jang, S.S., Kim, J., et al.: Distribution and diffusion of water in model epoxy molding compound: molecular dynamics simulation approach. IEEE Trans. Adv. Packag. **33**(2), 333–339 (2010)
26. Li, H., Fan, X., Yue, S., et al.: Molecular dynamics simulation of water diffusion in epoxy resin. Comput. Appl. Chem. **31**(06), 696–700 (2014)
27. Xiao, Y.: Molecular Dynamics Simulation of the Interfacial Bonding Effect of Water on Carbon Fiber/Epoxy Resin. Harbin Institute of Technology, Harbin (2017)
28. Zhang, W., Li, Z., Wu, T., et al.: Molecular simulation research and progress on the crosslinking structure and macroscopic properties of epoxy resin and its composite materials. J. Compos. Mater. **36**(02), 269–276 (2019)
29. Wang, Z., Lv, Q., Chen, S., et al.: Glass transition investigations on highly crosslinked epoxy resins by molecular dynamics simulations. Mol. Simul. **41**(18), 1515–1527 (2015)
30. Zhang, M., Wang, R., Lin, Y., et al.: Molecular dynamics simulation of glass transition temperature and mechanical properties of crosslinked fluorosilicone rubber. Polym. Mater. Sci. Eng. **31**(04), 68–72 (2015)

31. Yang, Q., Sui, G., Xu, D., et al.: Molecular simulation research on the structure and properties of epoxy resins. In: Proceedings of the 17th National Composite Materials Academic Conference (Composite Materials and Raw Materials Sub Forum), Chinese Aerospace Society: Beijing AVIC Era Culture Communication Co., Ltd., p. 4 (2012)
32. Sul, J.H., Prusty, B.G., Kelly, D.W.: Molecular dynamics study on effects of aspect ratio of carbon nanotubes in thermosetting epoxy based nanocomposites including modeling of crosslinking process. Adv. Manuf. Polym. Compos. Sci. **9**(2), 94–104 (2015)
33. Chen, S., Sun, S., Gwaltney, S.R., et al.: Molecular dynamics simulation of the interaction between carbon nanofibers and epoxy resin monomers. J. Polym. Sci (10), 1158–1164 (2015)
34. Han, Q.: A molecular dynamics investigation on the compression of cross-linked epoxy resins. Mol. Simul. **41**(18), 1509–1514 (2015)
35. Chen, X.: Experimental and Molecular Dynamics Simulation of Thermodynamic Properties of Epoxy/SiO_2. Wuhan University, Wuhan (2017)
36. Lin, Y.C., Chen, X.: Moisture sorption-desorption-resorption characteristics and its effect on the mechanical behavior of the epoxy system. Polymer **46**(25), 11994–12003 (2005)
37. Li, D.: Performance Evolution and Molecular Dynamics Simulation of Epoxy Resin Under Water Alkali Immersion Conditions. Harbin Institute of Technology, Harbin (2015)
38. Lin, J.: Simulation of Mechanical Properties of Polymer Based Nanocomposites Based on Materials Studio. Jinan University, Guangzhou (2013)
39. Alder, B.J., Wainwright, T.E.: Studies in molecular dynamics. I. General method. J. Chem. Phys. **31**, 459–466 (1959)
40. Parrinello, M., Rahman, A.: Crystal structure and pair potentials: a molecular-dynamics study. Phys. Rev. Lett. **45**, 1196 (1980)
41. Nose, S.: A unified formulation of the constant temperature molecular dynamics methods. J. Chem. Phys. **81**, 511–519 (1984)
42. Liu, Y.: Study on the Aging Characteristics of Epoxy Resin in Humid and Hot Environments. Chongqing University, Chongqing (2018)
43. Liang, X., Gao, Y.: Research on composite insulator crumb fracture (1): main characteristics, definition, and criteria of crumb fracture. Chin. J. Electr. Eng. **36**(17), 4778–4786 (2016)
44. Xie, C., Liu, S., Liu, Q., et al.: The influence of internal defects in AC 500 kV composite insulators on axial electric field distribution. High Volt. Technol. **38**(04), 922–928 (2012)

Preparation and Thermal–Mechanical Property Evaluation of Cellulose Insulation Paper with Differing Nano-SiC Contents

Yiyi Zhang, Chuqi Xu, Shuangxi Nie, and Junwei Zha

1 Introduction

Oil-immersed transformers play an important role in power systems and their insulating properties are determined by the internal insulation consisting of insulating oil and insulating paper [1–3]. Because of its intrinsic mechanical and electrical qualities, cellulose pressboard is utilized as transformer insulation paper. During long-term operation, cellulose insulation paper will cause local thermal ageing due to uneven heat dissipation, which will lead to irreversible deterioration of mechanical strength and insulation properties, and greatly reduce the service life of insulation paper. In the actual operation of the transformer, the insulation oil can be updated by changing the oil, but the insulation paper cannot be replaced. As a result, the service life of the cellulose insulation paper directly determines the service life of transformers [4].

Although cellulose insulation paper has excellent properties in comparison to other insulation materials, it is still deficient in some specific aspects. In recent years, many experts have studied different aspects of improving the properties of cellulose insulation paper. Among them, the combination of polymers and nanoparticles is the preferred method for improving material properties. Tang et al. [5] prepared modified insulation paper doped with nano-Al_2O_3, the results showed that the addition of nano-Al_2O_3 had a positive effect on AC breakdown voltage and improved the thermal ageing performance of cellulose insulating paper. Liao et al. [6] have found that the addition of nano-TiO_2 changed the contact interface between the insulation paper and oil, created a large number of shallow traps, the AC breakdown strength of

---

Y. Zhang (✉) · C. Xu · S. Nie
School of Electrical Engineering, Guangxi University, Nanning, China
e-mail: zdsizyy@126.com

J. Zha
School of Chemistry and Biological Engineering, University of Science & Technology Beijing, Beijing, China

Q. Xie (ed.), *Electrical Materials*, Engineering Materials,
https://doi.org/10.1007/978-981-99-9050-4_7

oil-impregnated insulation paper increased by 20.8% when the nano-TiO_2 content reached 3%. Chen et al. [7] prepared transformer insulation paper using cellulose nanocrystals modified by citric acid crosslinking and melamine amidation, found that the tensile strength of the modified paper increased by 17.30% and the breakdown strength in oil increased by 40.28%. Sequeira et al. [8] prepared Nano-SiO_2 composite cellulose paperboard, the result showed that when the content was 40–60% SiO_2 in the paperboard, the hydrophilicity was reduced, but the thermal stability is greatly improved.

In comparison to other nanoparticles, nano-SiC particles have a high thermal conductivity and thermal stability, as well as a low dielectric constant and dielectric loss. So far, it has been an excellent filler. Park et al. [9] found that liquid silicone resin composites doped with 20% SiO_2 and 3% SiC had a more evenly distributed space charge than materials with other contents. Pu et al. [10] enhanced the properties of 7075Al alloy with nano-SiC particles, demonstrating that nano-SiC particles can strengthen the tensile properties of Al when containing a less amount.

Experimental approaches for polymer modification are prone to being influenced by experimental circumstances and equipment, and they can be time-consuming and costly. Molecular simulation technology has become widely used in the calculation and investigation of molecular micro-mechanisms as computer technology has advanced [11]. Yang et al. [12] established the pure cellulose model and the modified cellulose with three kinds of polyhedral oligomeric silsesquioxane derivatives by molecular dynamics. The addition of polyhedral oligomeric silsesquioxane derivatives can effectively reduce the polarizability of cellulose, and can improve the electric field distribution in the oil-paper insulation system. Du et al. [13] investigated the effects of carbon nanowires with three different structures on the thermodynamic properties of cellulose insulation paper by molecular dynamics simulation technology. The simulation results showed that the addition of carbon nanowires can increase the number of intermolecular hydrogen bonds and improve the thermodynamic performance.

Although the properties and applications of composite modified materials have received a lot of attention in recent years, there are few studies on the effects of nano-SiC particles on the properties of insulating paper.

In summary, in this paper, nano-SiC particles were doped into cellulose, and molecular dynamics was used to establish SiC/cellulose composite models with different contents to determine the feasibility of the experiment. Simultaneously, nano-SiC composite papersheets were prepared, the thermal conductivity, thermal stability, and mechanical properties of cellulose with different contents were studied; and the modification mechanism of nano-SiC on cellulose was investigated by using microscopic parameters such as free volume and mean square displacement. The aim is to investigate a method of enhancing the performance of cellulose insulation paper by combining theoretical calculations with practical experimental results.

2 Methods and Characterizations

2.1 *Methods*

In this paper, in order to study the effect of different contents of nano-SiC on the thermal–mechanical properties of cellulose insulation paper. Firstly, a pure cellulose model and nano-SiC modified models were established by molecular dynamics, and the changes of the thermal–mechanical properties of the models at different contents were simulated; then, according to the simulation results, the nano-SiC modified insulation papersheets at different contents were prepared experimentally and the properties were tested.

2.2 *Characterizations*

2.2.1 Mechanical Properties

The generalized Hooke's law [14] can be used to define the stress–strain relationship of solid materials, as shown in Eqs. (1) and (2).

$$\sigma_i = \boldsymbol{C}_{ij}\varepsilon_j \tag{1}$$

$$\begin{bmatrix} \sigma_1 \\ \sigma_2 \\ \sigma_3 \\ \sigma_4 \\ \sigma_5 \\ \sigma_6 \end{bmatrix} = \begin{bmatrix} C_{11} & C_{12} & C_{13} & C_{14} & C_{15} & C_{16} \\ C_{21} & C_{22} & C_{23} & C_{24} & C_{25} & C_{26} \\ C_{31} & C_{32} & C_{33} & C_{34} & C_{35} & C_{36} \\ C_{41} & C_{42} & C_{43} & C_{44} & C_{45} & C_{46} \\ C_{51} & C_{52} & C_{53} & C_{54} & C_{55} & C_{56} \\ C_{61} & C_{62} & C_{63} & C_{64} & C_{65} & C_{66} \end{bmatrix} \cdot \begin{bmatrix} \varepsilon_1 \\ \varepsilon_2 \\ \varepsilon_3 \\ \varepsilon_4 \\ \varepsilon_5 \\ \varepsilon_6 \end{bmatrix} \tag{2}$$

In Eqs. (1) and (2), σ_i is the stress, $\boldsymbol{C_{ij}}$ is the calculated elastic stiffness coefficient matrix, and ε_j is the strain tensor. λ and μ are lame constants. As shown in Eqs. (3) and (4).

$$\lambda=\frac{1}{3}(C_{11} + C_{22} + C_{33}) - \frac{2}{3}(C_{44} + C_{55} + C_{66}) \tag{3}$$

$$\mu = \frac{1}{3}(C_{44} + C_{55} + C_{66}) \tag{4}$$

Mechanical properties are important indicators of macroscopic strength that can be reflected by various moduli. Elastic modulus E is the ratio of stress to strain, the greater the value, the stronger the stiffness and deformation resistance of the material;

shear modulus G is the ratio of shear stress to strain, the higher the value, the better the ability to resist shear stress and the less likely it is to be damaged under external stress; bulk modulus K, a physical quantity describing the connection between strain and average stress, can reflect the macroscopic mechanical properties of materials.

The elastic modulus, shear modulus, and bulk modulus are calculated by molecular dynamics, and the calculation formulas are as follows:

$$E = \frac{\mu(3\lambda + 2\mu)}{\lambda + \mu} \tag{5}$$

$$G = \mu \tag{6}$$

$$K = \lambda + \frac{2}{3}\mu \tag{7}$$

In the experiment, a tensile strength tester (Lorentzen and Wettre, Stockholm, Sweden) was used to measure the tensile index of papersheets according to the GB/T453-1989 standard.

2.2.2 Thermal Conductivity

Molecular dynamics has been used to calculate the thermal conductivity of polymeric materials in many ways [15, 16]. The reverse non-equilibrium molecular dynamics (RNEMD) method has been widely used because of its faster convergence time of temperature gradient [17].

The calculation of the thermal conductivity is based on Fourier's Law of Heat Conduction:

$$\lambda = -\frac{Q}{\mathrm{dT/dx}} \tag{8}$$

where Q is the energy flux in the x-direction, dT/dx is the temperature gradient, and the negative sign indicates that the energy flux is in the direction opposite to the gradient.

In the RNEMD method, the hot and cold regions are formed in the simulated system by simulating the exchange of atomic center-of-mass velocities in different regions of the system in the ideal state. Then, by averaging the kinetic energy exchange between the coldest particle in the hot layer and the hottest particle in the cold layer several times, a stable temperature gradient and energy flux in the system is achieved, and the thermal conductivity is finally obtained by calculation. The energy flux is imposed by exchanging the energy ΔE between two fixed layers in the system at each time interval Δt, the equation is as follows:

Fig. 1 Model diagram of RNEMD method

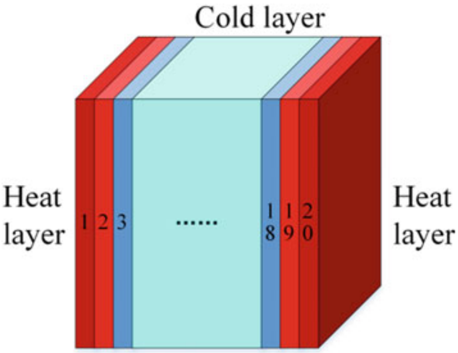

$$Q = \frac{1}{2A}\frac{\Delta E}{\Delta \mathrm{t}} \tag{9}$$

where *A* is the area perpendicular to the flux direction and the factor *2* is due to the periodic boundary condition.

As shown in Fig. 1, the RNEMD method divides the model into 20 regions in one direction. The hot layer is in the left and right boundary layers, and the cold layer is in the middle. Heat is transferred by kinetic energy exchange between the hot and cold layers. After multiple exchanges, a stable temperature gradient is finally formed in the system. To calculate the thermal conductivity in one direction, the model is first simulated for 100 ps in the NVT ensemble and then 100 ps in the NPT ensemble.

The RNEMD method can only calculate thermal conductivity by balancing the temperature gradient in a single direction. To calculate the overall thermal conductivity of the composite material, it is necessary to calculate the thermal conductivity of the model in the x, y, and z directions, and take the average value as the thermal conductivity of the model [18].

In the experiment, the thermal conductivity of the papersheets was measured using LFA467HT HyperFlash (Netzsch Ltd.).

2.2.3 Microscopic Topography

In the experiment, the microstructure and morphology were observed by the field emission scanning electron microscope (GeminiSEM 300), with a beam accelerating voltage of 10 kV. Energy-dispersive X-ray spectroscopy (EDS) is an accessory used on scanning electron microscope for micro-area analysis of components energy spectrum. The specimens were broken in liquid nitrogen and the cross-sections were sputtered with gold before observation.

2.2.4 Thermal Stability

In the molecular simulation, the thermal stability of a material can be characterized by glass transition temperature (T_g) and mean square displacement (MSD). In this simulation, three models with contents of 0, 3, and 6% are used to calculate the T_g and MSD.

T_g is the transition temperature from a glass state to a high elastic state of polymer materials. Cellulose insulation paper can meet engineering requirements before glass transition, when the temperature exceeds T_g, many properties will change significantly, such as mechanical, thermal, optical, and electrical properties [19]. Therefore, T_g is taken as a criterion to evaluate the stability of materials.

The molecular dynamics simulation of stage cooling treatment was carried out at temperatures ranging from 650 to 200 K, with each step lowering the temperature by 50 K. The starting conformation for the next stage was taken from the final equilibrium conformation simulated in the previous stage. First simulated for 100 ps at each temperature in an NPT ensemble, then for 200 ps under 0.0001 GPa in an NPT ensemble is performed for data analysis and calculation of various properties.

The temperature is plotted against the specific volume derived from the NPT molecular dynamics simulation. Taking the inflection point of the specific volume as the boundary point, linear fitting was performed before and after the boundary point respectively. The boundary point is the glass transition point.

The entire movement of the center of the molecular chain can be described by MSD. The stronger the molecular chain motion, the higher the MSD value [20]. Its calculation is expressed as:

$$MSD = \left\langle |r_i(t) - r_i(0)|^2 \right\rangle \tag{10}$$

Among them: $r_i(t)$ is the position of i molecule or atom at t time; $r_i(0)$ represents the position of i molecule or atom at 0 time; < > represents the average of all atoms in the group.

In the experiment, a simultaneous thermal analyzer (NETZSCH STA 449F3) was used for thermogravimetric experiments. The samples were cut into 1 mm * 1 mm particles with a mass of about 5 mg. The heating rate of the sample was 10 °C/min, the temperature was raised from 20 to 800 °C, the purge gas and the protective gas were nitrogen.

2.2.5 Internal Structure

In the simulation, according to the free volume theory, the free volume (V_f) is the gap between molecules, and the occupied volume is the space occupied by the molecular chains (V_0). The free volume provides space for the movement of molecular chains. The smaller the free volume fraction (FFV), the smaller the inner space of the material, the smaller the tendency of molecular chains to move at the molecular level, and the relatively stable structure of the material [21].

The calculation of FFV is expressed as follows:

$$FFV = \frac{V_f}{V_0 + V_f} \tag{11}$$

In the experiment, the pore size distributions and porosities of the papersheets were measured using Mercury Intrusion Porosimeters (MicroActive AutoPore V9600, Micromeritics Instrument Corporation). The sample of no less than 2 g was degassed under vacuum degree less than 1 Pa to remove the adsorbed substance before the experiment.

2.2.6 Thermal Ageing Resistance

In the experiment, papersheets with the nano-SiC content of 9% and unmodified papersheets are used for thermal ageing experiments. Karamay NO. 25 naphthenic mineral oil was chosen as the insulation oil. Dry the oil for 48 h under vacuum at 90 °C. The papersheets are immersed for 48 h in degassed and dewatered insulating oil.

Regular sampling is done to measure the degree of polymerisation (DP) of cellulose in papersheets during an accelerated heat ageing experiment at 130 °C. The viscosity method is used to measure the DP of paper in the laboratory. The fibers are dissolved in copper ethylene diamine, and the outflow time of the obtained solution in the capillary determines the DP of the paper.

3 Results and Discussions

3.1 Model Establishment and Parameter Setting

Cellulose models with a DP of 10, an initial density of 0.6 g/cm^3, and spherical nano-SiC particles with a radius of 5 Å were established in Materials Studio [22]. In the Amorphous cell module, nano-SiC/cellulose composite models with different contents of 0%, 2%, 3%, 4%, 5% and 6% were established, which were recorded as 0%-SiC, 2%-SiC, 3%-SiC, 4%-SiC, 5%-SiC and 6%-SiC respectively.

Geometry optimization of the models is carried out by using Forcite module for energy minimization calculation, followed by annealing treatment with six cycles between 300 and 900 K. After such treatment, the internal stress of the models is decreased, the simulation system is in a stable state, and the distribution of voids in the models is closer to the real material. Then, the models were simulated by dynamics, which included simulations in an NVT ensemble for 100 ps, an NPT ensemble for 100 ps under 1 GPa, and an NPT ensemble for 100 ps under 0.0001 GPa successively. Compass force field [23], Nose temperature control method [24], Ewald electrostatic

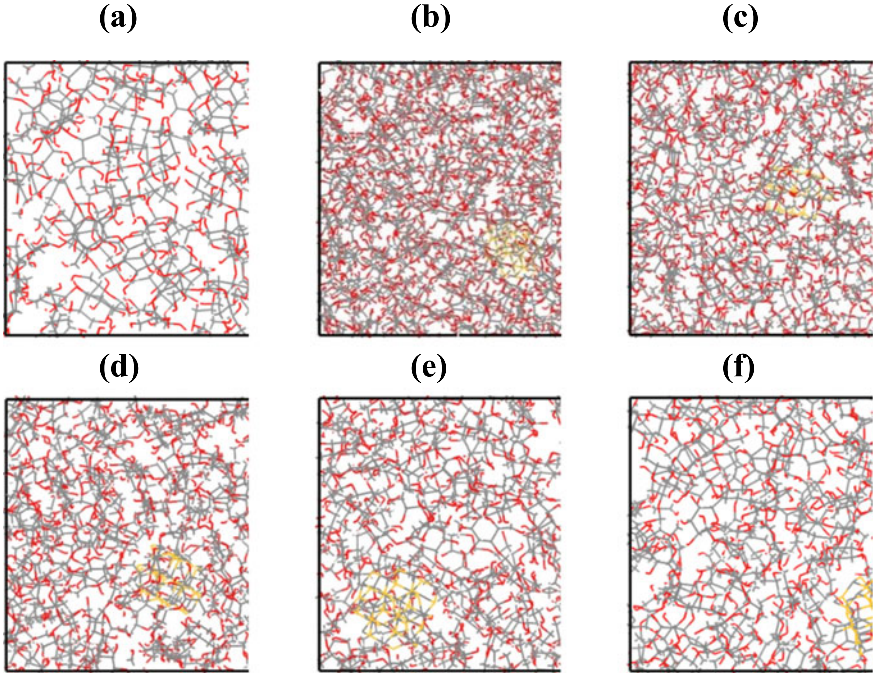

Fig. 2 Models of OAB surface **a** 0%-SiC/cellulose model. **b** 2%-SiC/cellulose model. **c** 3%-SiC/cellulose model. **d** 4%-SiC/cellulose model. **e** 5%-SiC/cellulose model. **f** 6%-SiC/cellulose model

method [25], Atom Based method for Vander Waals, and Berendsen method for pressure control are employed in the process of energy optimization and molecular dynamics simulation. After the above optimizations, the density and energy of the models can converge, and the models can be considered as close to the real cellulose. The models are shown in Fig. 2.

3.2 Sample Preparation

In this paper, the laboratory papersheet forming method was used. T4 pressboards (manufactured by Taizhou Weidmann High Voltage Insulation Co., Ltd., Taizhou, China) were employed to prepare Laboratory papersheets. Nano-SiC was produced by Beijing Xingrongyuan Technology Co., Ltd. with an average particle size of 50 nm and a purity of 99.99%. First, soak T4 pressboard and tear it into small pieces, the small pieces were stirred by a Messmer pulp disintegrator (Mavis Engineering Ltd., London, UK) at 3000 rpm for 10 min.

In order to investigate the effect of different nano-SiC contents on the variation of insulating paper properties, five groups of papersheets with 0%, 3%, 6%, 9%, and 12% were prepared based on the molecular simulation results, 0%-SiC, 3%-SiC, 6%-SiC, 9%-SiC, 12%-SiC were recorded as P0, P1, P2, P3 and P4, respectively.

Different contents of nano-SiC particles were added to deionized water and stirred magnetically. Then, different contents of insulating pulp and nano-SiC particles were mixed and diluted with deionized water to reach a final concentration of 1 wt%. Then the mixture was filtered, moulded, pressed, and dried to obtain papersheets in a normalized Rapid-Köthen papersheet former (PTI, Vorchdorf, Austria) according to ISO 5269/2 (2004). Finally, the papersheets were hot-pressed at 15 MPa and 90 °C to achieve densification and internal bonding. The papermaking process is shown in Fig. 3.

Finally, circular papersheets with an average thickness of 0.27 mm, a basis weight of 240 g/m^2, and a diameter of 16 cm were produced. After the papermaking was completed, they were dried at 90 °C for 48 h, and then sealed in a sample bag for storage.

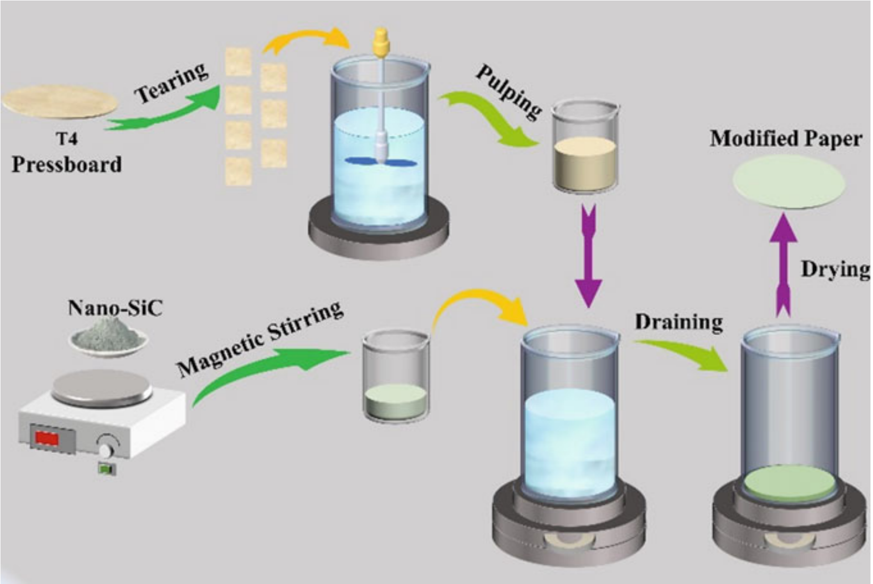

Fig. 3 Schematic diagram of the preparation process

3.3 Performance Analysis

3.3.1 Mechanical Properties Analysis

In the simulation, the relationships between bulk modulus, shear modulus, elastic modulus, and different contents of nano-SiC in the models are obtained, as shown in Fig. 4a.

The moduli of the modified models are higher than those of the unmodified model, the addition of nano-SiC particles can improve the bulk modulus, shear modulus, and elastic modulus, indicating an increase in stiffness and resistance to deformation, with the greatest increase in properties occurring at a content of 3%. When the content exceeds 3%, the mechanical properties begin to decline.

In the experiment, the tensile strength of pure cellulose papersheet and nano-SiC composite papersheets was studied, the curves of the stress–strain and the maximum tensile strength are shown in Fig. 4b, c, respectively.

The tensile strength of the pure cellulose papersheet is 35.87 MPa, when the content is 9%, the maximum tensile strength reaches 51.22 MPa, which is 42.8% higher than the strength of the pure cellulose papersheet. The mechanism of adding nano-SiC to enhance the tensile strength of insulation paper is mainly due to the existence of van der Waals forces between them, and also due to the large specific surface area of nano-SiC, the number of atoms on the surface of the particles increases, and many active dots are formed on the surface of the particles, so the interface

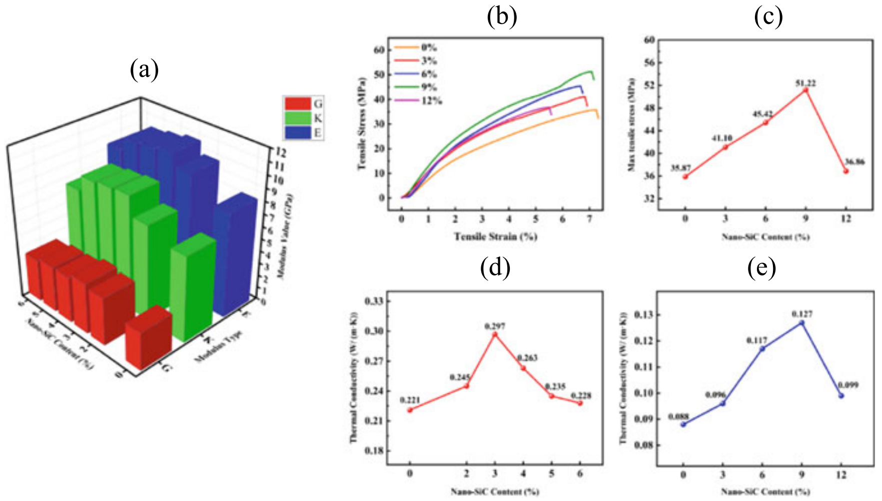

Fig. 4 **a** Bulk modulus (G), shear modulus (K) and elastic modulus (E) of SiC/cellulose models with different nano-SiC contents. **b** Stress–strain curves of papersheets with different nano-SiC contents. **c** Max tensile stress of papersheets with different nano-SiC contents. **d** Thermal conductivity of SiC/cellulose models with different nano-SiC contents in the simulation. **e** Thermal conductivity of papersheets with different nano-SiC contents in the experiment

between nano-SiC and cellulose is well bonded, thus improving the tensile strength of insulation paper.

With the further increase of nanoparticles, when the nano-SiC content exceeds 9%, it can be considered that the nano-SiC particles appear to agglomerate, at which time the particle size of nano-SiC becomes larger, the specific surface area becomes smaller, the unpaired atoms on its surface become fewer, the surface activity becomes lower, and the bond with cellulose becomes relatively weaker, which leads to a decrease in the mechanical properties of the insulation paper, which is the reason for the peak in tensile strength, which is also consistent with the trend obtained from molecular simulation.

Wrapping and winding copper conductors to act as electrical insulation is an important application for cellulose insulation paper in transformer insulation. If the mechanical properties of the cellulose insulation paper deteriorate, it will be liable to fracture when the conductor coil is subjected to mechanical stress, which affects the insulation performance of the transformer. As a result, improving the mechanical properties of cellulose insulation paper can enhance the insulation performance from a different perspective, extending the service life of transformers.

3.3.2 Thermal Conductivity Analysis

The normal operating temperature of power transformers is around 343 K, but due to various factors such as operating environment and load, the temperature of certain parts inside the transformer can sometimes soar to around 393 K, so 363 K was chosen in this paper to study the thermal conductivity of cellulose insulation paper.

Figure 4d shows the simulation results of the thermal conductivity at 363 K. It can be seen from Fig. 4d, with the addition of nano-SiC, the thermal conductivity first increases and then decreases. When the content is 3%, the thermal conductivity of cellulose pressboard increases the most, which is 34.4% higher than that of unmodified model.

In the experiment, the thermal conductivity of composite papersheets with different nano-SiC contents at 363 K was measured, the results are shown in Fig. 4e. It can be seen from the figure that the thermal conductivity of pure cellulose papersheet is 0.088. When the content of nano-SiC is 9%, the thermal conductivity reaches 0.127, which is 44.3% higher than unmodified papersheet. With the increase of nano-SiC content, the thermal conductivity first increases and then decreases, which is also the same as the simulation trend.

According to heat conduction pathway theory, with the addition of thermally conductive fillers, because of the high thermal conductivity of SiC, and some thermally conductive fillers begin to contact each other and form local thermal conductive chains or networks, accelerating the heat diffusion within the paper, resulting in an increase in the thermal conductivity. When the addition of fillers exceeds 9%, as the number of fillers continues to increase, the distribution of thermally conductive fillers in the paper becomes wider, the probability that the fillers are distributed on the surface gradually increases. The addition of thermally conductive fillers increases the surface roughness of papersheets, which increases the thermal resistance of the insulating paper interface, generates more phonon scattering, and hinders the propagation of phonons inside the insulating paper, so it results in a decrease in the thermal conductivity of papersheets.

3.3.3 Microscopic Topography Analysis

Figure 5a–e shows the SEM image of the cellulose/nano-SiC. Figure 5f, g shows the types of trace elements in cellulose, and the presence of silicon is found, indicating that nano-SiC was added successfully.

It can be roughly seen that the paper fibers are intertwined in a disorderly manner to maintain a certain mechanical strength. At the same time, it can be seen that the small particles (nano-SiC) are attached to the surface of the fibers, filling the voids in the cellulose network, and can form a network structure with the fibers, which enhances the mechanical properties of the composite paper.

When the content is small, the nanoparticles are dispersed in the fiber surface without obvious agglomeration. When the content is 12%, it can be seen that the

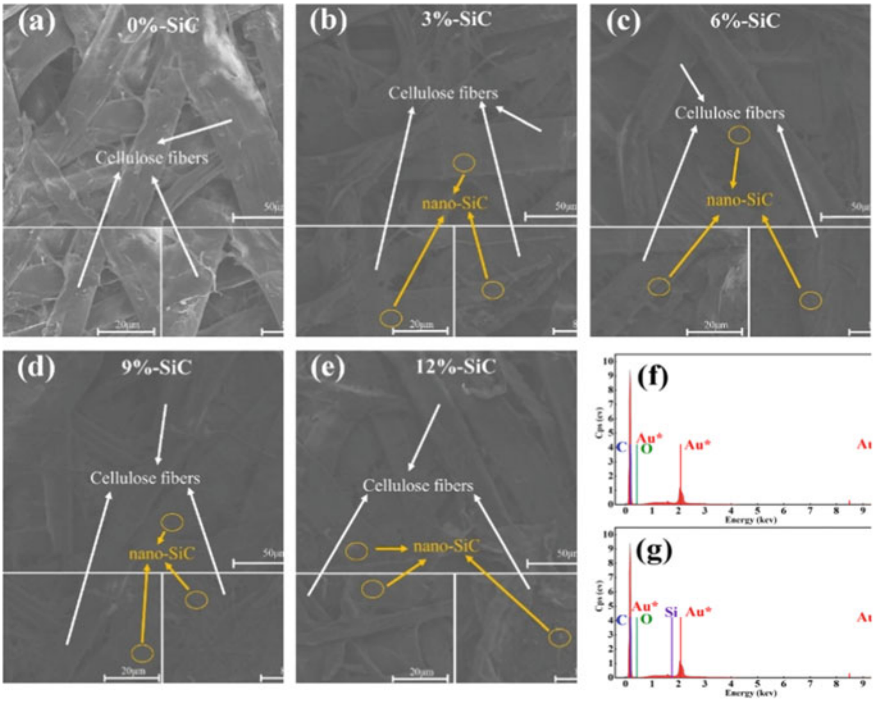

Fig. 5 **a** SEM image of P0 (0%-SiC). **b** SEM image of P1 (3%-SiC). **c** SEM image of (6%-SiC). **d** SEM image of P3 (9%-SiC). **e** SEM image of P4 (12%-SiC). **f** EDS image of P0 (0%-SiC). **g** EDS image of P3 (9%-SiC)

distribution range of the globules attached to the fiber surface becomes wider, and the particle size becomes larger. It shows that when the content is 12%, slight agglomeration occurs. The degradation of thermal–mechanical properties of insulation paper may be caused by the agglomeration of nanoparticles.

3.3.4 Thermal Stability Analysis

The simulation curves of T_g are shown in Fig. 6a–c. T_g of the unmodified model is 439 K, and that of the pure cellulose model obtained by Wang et al. is 448 K [26]. The result of this paper is not much different from 448 K, which verifies the accuracy of the models.

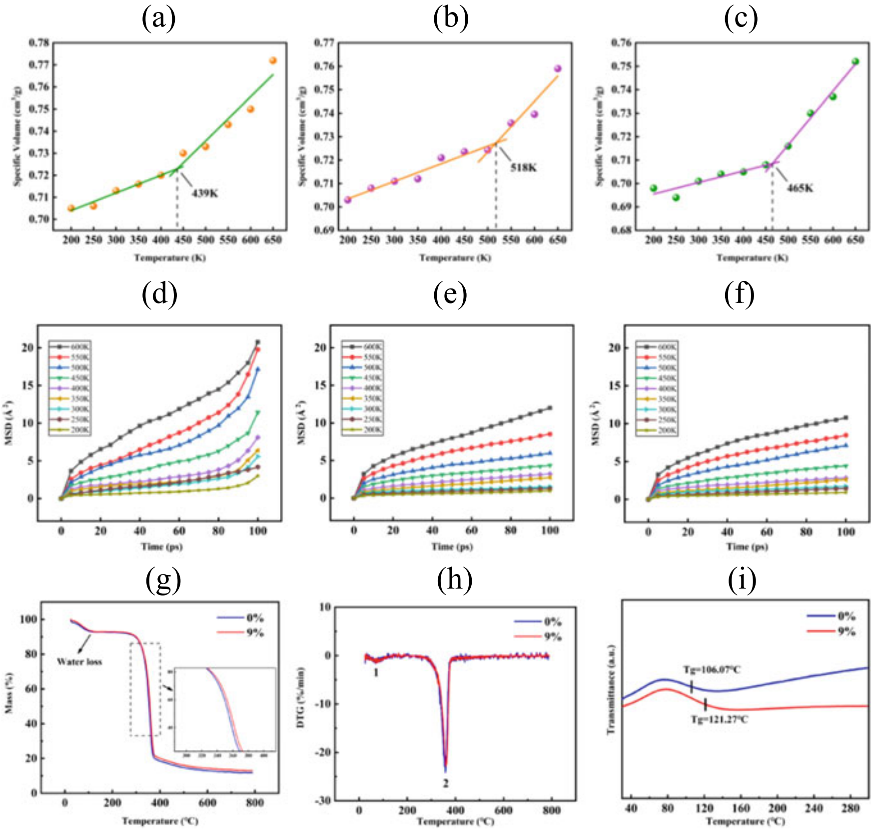

Fig. 6 **a** Glass transition temperature of 0% SiC unmodified model. **b** Glass transition temperature of 3% SiC modified model. **c** Glass transition temperature of 6% SiC modified model. **d** MSD curve of 0% unmodified model. **e** MSD curve of 3% modified model. **f** MSD curve of 6% modified model. **g** TGA curves of P0 (0%-SiC) and P3 (9%-SiC). **h** DTG curves of P0 (0%-SiC) and P3 (9%-SiC). **i** T_g curves of P0 (0%-SiC) and P3 (9%-SiC)

T_g of the modified model with 3%-SiC is 518 K and that of the modified model with 6%-SiC is 465 K. The T_g of the modified model with 3%-SiC is 79 K higher than that of the unmodified model, and T_g of the modified model with 6%-SiC is 26 K higher than that of the unmodified model. It shows that adding nano-SiC particles to cellulose insulation paper can increase T_g. The mechanical characteristics and thermal stability of composites are inextricably linked to T_g. Therefore, nano-SiC can improve the thermal–mechanical properties of cellulose insulation paper.

The MSD curves of cellulose chains are shown in Fig. 6d–f. As shown in Fig. 6d–f, the MSD value in 0%-SiC model is relatively small before 400 K, around 0–8 Å^2, and the temperature at which the MSD value jumps is between 400–450 K, this temperature range corresponds to the glass transition temperature of 0%-SiC model, after 450 K, the MSD value increases rapidly, reaching a maximum of 21 Å^2. While in the 3%-SiC model, the MSD value is lower before 500 K, around 0–6 Å^2, the temperature of the transition occurs between 500–550 K, which also corresponds to the glass transition temperature of 3%-SiC model, the MSD value increases after 550 K, but the magnitude of the increase is relatively small, with values between 8–12 Å^2. In the 6%-sic model, the MSD value is lower than the above two models, before the glass transition temperature, the value is 0–4 Å^2, and after the glass transition temperature, the MSD value is around 7–11 Å^2.

Overall, the MSD curves at adjacent temperatures in the low-temperature region are not significantly different, but as the temperature rises, there are varying degrees of jumps, because the elevation of temperature helps to overcome the interaction forces between molecular chains and aggravates the chain movement, which also complies with Laws of thermodynamics. At the same time, it can be seen that the MSD values in the modified models are much lower than the MSD value in the unmodified model. In the modified models, the temperatures at which the jump occurs are higher than that of the unmodified model, indicating that the addition of nano-SiC particles can weaken the motion of molecular chains, as well as improve the thermal stability of cellulose.

In the experiment, according to the experimental results of the tensile strength and the thermal conductivity, it is found that the performance improvement of P3 is the largest Therefore, P0 (0%-SiC) and P3 (9%-SiC) were measured by the simultaneous thermal analyzer.

The thermogravimetric Analysis (TGA), derivative thermogravimetry (DTG), and T_g curves of the papersheets are shown in the Fig. 6g–i.

Figure 6g shows that the samples have two significant weight losses in the measurement temperature range, corresponding to the two peaks in Fig. 6h. The first weight loss is around 100 °C, which corresponds to the loss of water. After 100 °C, all the water evaporates, corresponding to the area “1” in Fig. 6h. The primary reaction stage of cellulose thermal cracking is the second weight loss stage, and the main reaction temperature range for cellulose thermal cracking is 300–400 °C. In this process, the glycosidic bonds of cellulose are broken by ring-opening, small-molecule volatile compounds are generated, resulting in a significant decrease in quality at this stage, and the reaction rate reaches the maximum, corresponding to the “2” area in Fig. 6h.

Comparing the TGA curves of 0 and 9%, it can be seen that the final residual amount of P0 is 11.73%, while the final residual amount of P3 is 13.03%.

Figure 6h shows that the maximum reaction rate of P0 is higher than that of P3, indicating that the degradation rate of the papersheets becomes slower after adding nano-SiC, and the thermal stability of cellulose is improved.

In this paper, the glass transition temperature of the sample was measured by differential scanning calorimetry, and the results are shown in Fig. 6i. It can be seen that the T_g of P0 is 106.07 °C (379.22 K), while the T_g of P3 is 121.27 °C (394.42 K), which is 15.2 °C higher than that of the unmodified papersheet. It shows that adding nano-SiC to cellulose can increase the glass transition temperature, which is consistent with the conclusion drawn from the simulation.

3.3.5 Internal Structure Analysis

At 298 K, the free volume distributions of different models under the OAB surface are shown in Fig. 7. The blue area is V_f and the gray area is V_0. The *FFV* of each model under different contents is shown in Table 1.

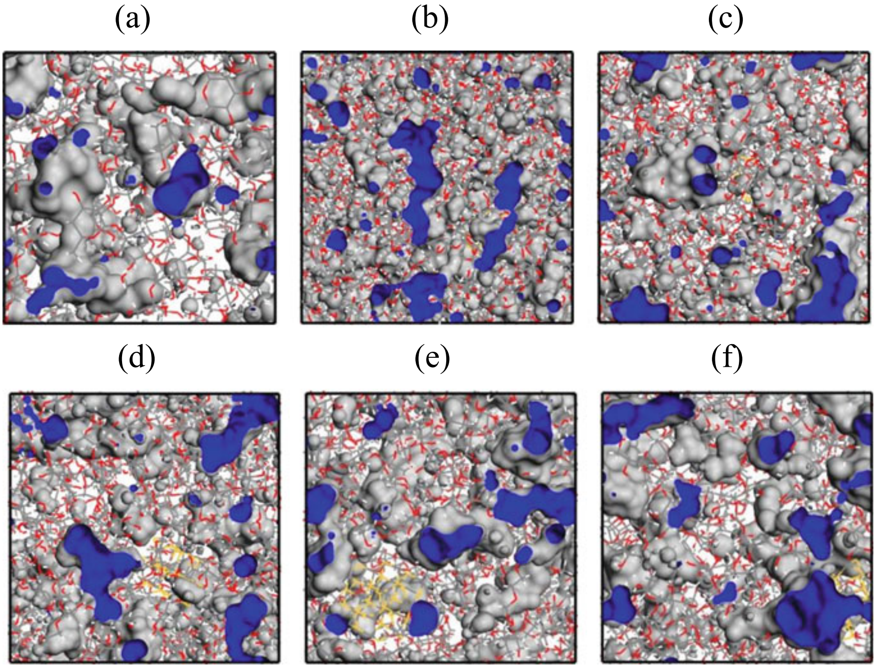

Fig. 7 The free volume distribution of OAB surface in models **a** free volume distribution of 0% unmodified model. **b** Free volume distribution of 2% modified model. **c** Free volume distribution of 3% modified model. **d** Free volume distribution of 4% modified model. **e** Free volume distribution of 5% modified model. **f** Free volume distribution of 6% modified model

Table 1 The proportion of the free volume of SiC/cellulose models under different nano-SiC content

Content	0%	2%	3%	4%	5%	6%
V_0	18,528	49,145	31,790	24,195	19,101	16,291
V_f	4578	9804	5258	3867	3569	2785
FFV	0.198	0.166	0.142	0.138	0.158	0.146

It can be seen from the data in Table 1, with the increase of nano-SiC particles gradually, the *FFV* of cellulose first decreases, then fluctuates up and down. When the content is between 3–4%, the *FFV* is relatively low.

Due to the addition of nano-SiC particles, the whole molecular structures of cellulose are combined more closely, and the gaps between molecule chains can be filled, resulting in a reduction in free volume and effectively weakening the movement of molecular chains. As a result, adding nano-SiC in cellulose can slow down the movement of molecular chains.

From the perspective of thermal conductivity and tensile strength, when the content of nano-SiC is 9%, the performance improvement is the largest. Therefore, in this paper, the pore distribution and porosity of P0 (0%-SiC) and P3 (9%-SiC) were measured.

Figure 8 is the log-differential intrusion image, showing the pore size distribution and quantity of papersheets. In Table 2, the porosity of P0 is 40.96%, the average pore size is 2599.38 nm, and the pore size distribution is obvious (361 and 2 μm). After adding nano-SiC particles, the porosity and average pore size of cellulose decreased to 40.23% and 2203.41 nm, respectively, and the pore size distribution decreased at 361 μm and 2 μm. It can also be seen from the Table 2 that the total pore area has decreased from 6.359 to 4.506 m^2/g. All show that the nano-SiC particles were attached to the surface of cellulose, filled the voids of the fiber network and reduced the number of pores.

Fig. 8 Log differential intrusion image of P0 (0%-SiC) and P3 (9%-SiC)

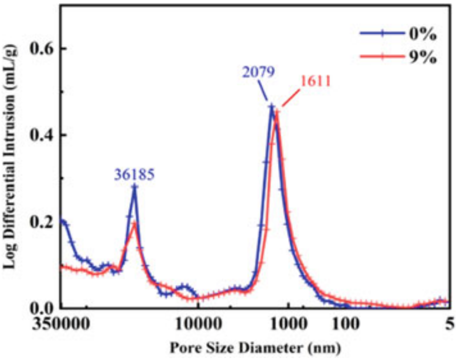

Table 2 Porosity, average pore diameter and total pore area of papersheets with 0%-SiC and 9%-SiC

Sample	Porosity (%)	Average pore diameter (nm)	Total pore area (m^2/g)
P0	40.96	2599.38	6.359
P3	40.23	2203.41	4.506

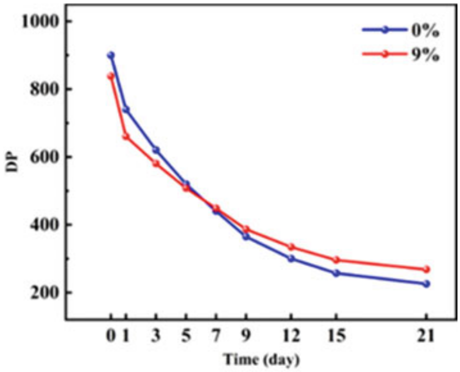

Fig. 9 The change curve of the DP of P0 (0%-SiC) and P3 (9%-SiC) with ageing time

3.3.6 Thermal Ageing Analysis

The variations of the DP of modified and unmodified paper with ageing time are shown in Fig. 9.

It can be seen from Fig. 9 that the DP of the modified papersheet is slightly smaller than that of the unmodified papersheet when they are not aged. This may be due to the fact that the same mass is taken from each sample when measuring the DP. The addition of nano-SiC makes the relative content of cellulose lower than that of the unmodified paper, resulting in a smaller viscosity and DP.

Before ageing for seven days, the DP of the unmodified papersheet was higher than that of the modified papersheet. As the ageing continued, the DP of the modified papersheets began to be gradually higher than that of the unmodified papersheets, indicating that the nano-SiC modified papersheets had excellent thermal stability.

The mechanism by which the addition of nano-SiC can enhance the anti-ageing performance is analyzed. In Fig. 10, the yellow lines represent cellulose molecules and the green spheres represent nano-SiC. Figure 10a shows fibers in insulation paper that are haphazardly intertwined. Figure 10b shows the schematic of the addition of a small number of nanoparticles, it can be seen that the small amount of added nano-SiC adheres to the surface of the cellulose and forms a thermal conductivity pathway. From Fig. 10c, there forms a thermally conductive network inside the cellulose with the further addition of nano-SiC particles.

A comprehensive analysis shows that there are two reasons why nano-SiC can improve thermal ageing resistance: One is that the addition of nano-SiC can fill the intermolecular gaps and the thermal conductivity network can greatly accelerate the

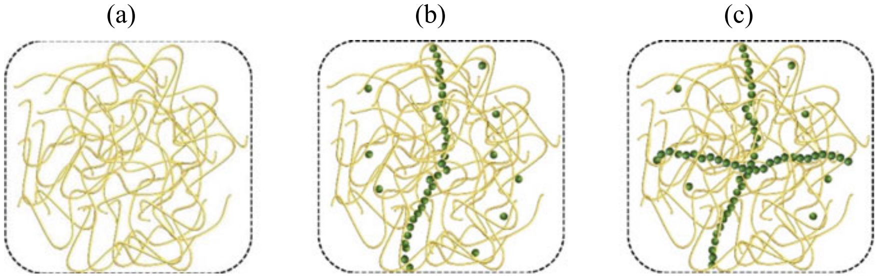

Fig. 10 Ageing retardation mechanism of nano-SiC modified insulation paper **a** Cellulose model. **b** Thermal conductivity path. **c** Thermal conductivity network

heat transfer inside the insulation paper and improve the local overheating. Another one is that the close connection between nano-SiC and cellulose molecules weakens the damage to cellulose by thermal stress.

Therefore, in the oil-paper insulation system, the insulation paper with faster thermal dispersion can transfer more heat to the insulation oil, so the DP of the modified paper decreases more slowly. This also indicates that the nano-SiC-modified insulation paper has better anti-ageing properties and can meet the requirements of long-term operation of transformers, which has potential application significance.

4 Conclusions

In summary, we have shown that the thermal–mechanical properties of cellulose insulation paper could be improved by adding nano-SiC particles. In comparison with that of unmodified papersheet, the tensile strength and thermal conductivity can be increased by 42.8% and 44.3%, respectively. The performance of cellulose insulating paper was simulated by molecular dynamics. Based on the simulation results, nano-silicon carbide modified insulating paper with different contents was prepared experimentally, and its performance was tested to verify the accuracy of the simulation. Because of the free settling of nanoparticles and cellulose during the experiment, and part of nanoparticles flow out with water, the optimal content of nano-SiC in the experiment is larger than that in the simulation. In the case of ignoring the experimental error, when the nano-SiC content is 9%, the thermal–mechanical performance can be improved the most. Our research provides a reference for the practical application of nanomaterials in the improvement of cellulose insulation paper.

References

1. Zhang, Y., et al.: Preparation and thermal-mechanical property evaluation of cellulose insulation paper with differing nano-SiC contents. High Volt. **8**(3), 599–610 (2023)
2. Liao, R., et al.: Influence of the copper ion on aging rate of oil-paper insulation in a power transformer. IET Electr. Power Appl. **3**(5), 407–412 (2009)
3. Oommen, T.V., Prevost, T.A.: Cellulose insulation in oil-filled power transformers: part II maintaining insulation integrity and life. IEEE Electr. Insul. Mag. **22**(2), 5–14 (2006)
4. Huang, M., et al.: Influence of voltage reversal on space charge behavior in oil-paper insulation. IEEE Trans. Dielectr. Electr. Insul. **21**, 331–339 (2014)
5. Tang, C., et al.: Molecular simulation and experimental analysis of Al_2O_3-nanoparticle-modified insulation paper cellulose. IEEE Trans. Dielectr. Electr. Insul. **24**(2), 1018–1026 (2017)
6. Liao, R., et al.: The insulation properties of oil-impregnated insulation paper reinforced with nano-TiO_2. J. Nanomater. **4**, 373–959 (2013)
7. Chen, Q., et al.: Effect of melamine modified cellulose nanocrystals on the performance of oil-immersed transformer insulation paper. Cellulose **27**, 7621–7636 (2020)
8. Sequeira, S., et al.: Synthesis and characterisation of cellulose/silica hybrids obtained by heteropoly acid catalysed sol–gel process. Mater. Sci. Eng. C **27**(1), 172–179 (2006)
9. Park, J.-J., Lee, J.-Y.: Effects of SiC nanoparticles on space charge behaviors of LSR/ nano-SiO_2/nano-SiC composites for insulating material of HVDC cable joints. Mater. Chem. Phys. **270** (2021)
10. Pu, B., et al.: Effect of SiC nanoparticles on the precipitation behavior and mechanical properties of 7075Al alloy. J. Mater. Sci. **55**, 6145–6160 (2020)
11. Tang, C., et al.: Thermal stability of polyphenylsilsesquioxane-modified meta-aramid insulation paper. High Volt. **5**(3), 264–269 (2020)
12. Yang, L., et al.: Cellulose insulation paper with high thermal stability and low polarizability: influence of different substituents on POSS modified cellulose insulating paper. Cellulose **28**, 6023–6033 (2021)
13. Du, D., et al.: Molecular simulation on the mechanical and thermal properties of carbon nanowire modified cellulose insulating paper. Compos. Struct. **261**, 113283 (2021)
14. Tanaka, F., Okamura, K.: Characterization of cellulose molecules in bio-system studied by modeling methods. Cellulose **12**, 243–252 (2005)
15. Jund, P., Jullien, R.: Molecular-dynamics calculation of the thermal conductivity of vitreous silica. Phys. Rev. B **59**(21), 13707 (1999)
16. Yang, X., et al.: Atomic-scale insights into interface thermal resistance between epoxy and boron nitride in nanocomposites. Int. J. Heat Mass Transf. **159**, 120105 (2020)
17. Liu, X., Rao, Z.: Molecular dynamics simulations on the heat and mass transfer of hyper-crosslinked shell structure of phase change nanocapsules as thermal energy storage materials. Int. J. Heat Mass Transf. **132**, 362–374 (2019)
18. Xie, Y., et al.: Research progress of thermal conductive epoxy resin matrix composites for electronic packaging. Eng. Plast. Appl. **46**(12), 143–147 (2018). J-GLOBAL ID:201902241552662274
19. Chang, K., et al.: Free volume and alcohol transport properties of PDMS membranes: insights of nano structure and interfacial affinity from molecular modeling. J. Membr. Sci. **417–418**, 119–130 (2012)
20. Yi, Z., et al.: Derivation of mean-square displacements for protein dynamics from elastic incoherent neutron scattering. J. Phys. Chem. B **116**(16), 5028–5036 (2012). https://doi.org/10.1021/jp2102868
21. Yin, F., et al.: Effect of moisture on mechanical properties and thermal stability of meta-aramid fiber used in insulating paper. Polymers **9**(10), 537 (2017)
22. Tang, C., et al.: Molecular dynamics simulations of the effect of shape and size of SiO_2 nanoparticle dopants on insulation paper cellulose. AIP Adv. **6**, 125106 (2018). https://doi.org/10.1063/1.4971280

23. Theodorou, D.N., Suter, U.W.: Detailed molecular structure of a vinyl polymer glass. Macromolecules **18**(7), 1467–1478 (1985)
24. Nose, S.: Constant temperature molecular dynamics method. Prog. Theor. Phys. Suppl. (103), 1–46 (1991)
25. Berendsen, H.J.C., et al.: Molecular dynamics with coupling to an external bath. J. Chem. Phys. **81**, 3684–3690 (1984).https://doi.org/10.1063/1.448118
26. Wang, Y.Y., et al.: Molecular dynamics simulation of glass transition in amorphous region of insulating paper. Gaodianya Jishu/High Volt. Eng. **38**(05), 1199–1206 (2012)